THE COORDINATION CHEMISTRY OF FUNCTIONALISED POLY(PYRAZOL-1-YL)BORATE LIGANDS AND THE PHOTOPHYSICAL PROPERTIES OF CYANIDE-BRIDGED D-F HYBRIDS

Graham M. Davies

A Thesis submitted to the University of Sheffield in partial fulfilment of the requirements for the Degree of Doctor of Philosophy

Department of Chemistry
University of Sheffield
Sheffield S3 7HF

December 2006
59,970 words

ABSTRACT

The content of this thesis is concerned with two distinctly independent areas of research: (i) the synthesis and study of new poly(pyrazol-1-yl)borate ligands and their metal complexes; (ii) crystallographic and photophysical studies of new *d-f* hybrid complexes.

Chapter One is divided into three parts: Part one gives a general introduction to poly(pyrazol-1-yl)borate chemistry along with a concise and up-to-date review of those ligands containing substituents in the C_3 position of the pyrazolyl ring; part two provides a brief introduction into the physical properties of lanthanide(III) metal ions, as well as describing the practical applications of their individual spectroscopic properties; and part three contains a brief review on the structural chemistry of cyanide-bridged coordination polymers.

Chapter Two describes the syntheses of four new scorpionates: dihydro-bis[3-(4-pyridyl)pyrazol-1-yl]borate (Bp^{4py}); dihydro-bis[3-(3-pyridyl)pyrazol-1-yl]borate (Bp^{3py}); hydro-tris[3-(4-pyridyl)pyrazol-1-yl]borate (Tp^{4py}) and hydro-tris[3-(3-pyridyl)pyrazol-1-yl]borate (Tp^{3py}). A series of X-ray crystallographic studies reveals a range of mononuclear, dinuclear and polymeric coordination complexes with various metal ions.

Chapter Three describes a range of structural and photophysical studies on lanthanide(III) complexes of poly(pyrazol-1-yl)borate ligands. New mixed-ligand lanthanide(III) complexes with various combinations of the anionic ligands Tp^{2py}, Bp^{2py} and dibenzoylmethane (dbm) were prepared and structurally characterised. Photophysical studies on the isostructual series $[Ln(Bp^{2py})(dbm)_2]$ (Ln = Pr, Nd, Er, Yb) show characteristic near-IR luminescence from the lanthanide ion. Near-IR luminescence was also demonstrated from the complexes $[Ln(Bp^{2py})_2(NO_3)]$ and $[Ln(Tp^{2py})(NO_3)_2]$ (Ln = Pr, Er), upon suitable excitation of the ligand chromophores.

Chapter Four describes the structural and photophysical properties of new cyanide-bridged *d-f* coordination polymers. Structural and photophysical studies are presented for a series of Ru-Ln complexes based on the $[Ru(bipy)(CN)_4]^{2-}$ donor unit connected to a Ln(III) energy-acceptor *via* cyanide bridges (where bipy is 2,2'-bipyridine and Ln = Pr, Nd, Er, Yb). Structural and photophysical studies were also performed on $[Cr(CN)_6][Ln(DMF)_4(H_2O)_2]$ complexes, in which the lanthanide ion (Ln = Nd, Yb) acts as the energy acceptor from the hexacyanochromate chromophore. The structures of $[Cr(CN)_6][Ln(H_2O)_2]$ (Ln = Gd, Yb) and $K_2[Ru(phen)(CN)_4]$ (where phen = 1,10-phenanthroline) are also presented.

Chapter Five gives a brief review of the field of X-Ray Crystallography with analysis of the history and theory of the technique, as well as an overview of its practical aspects used in this work. A few crystal structures solved by the author, and independent of the topics in this thesis, are also reported.

For Mum, Dad and Claire, for helping me get this far…

ACKNOWLEDGEMENTS

Firstly, I must extend heartfelt thanks to my supervisor Mike Ward for his enthusiasm and support over the course of this research; and for being an unlimited resource for good ideas (I guess you really could classify cheese & onion crisps as brain food).

Thanks also to Steve, Simon and Rebecca for performing the photophysical measurements on my complexes, without which this thesis would just be a catalogue of crystal structures; and to John and Harry for introducing me to X-ray Crystallography, and putting up with me whilst I try to unravel its mysteries (respectively).

There are just too many members of the research group to list here, but to you all, past and present, I thank you for being a great bunch of guys to work with, for all your friendship and support, and for putting up with my 'eclectic' music selections at work.

Outside of the lab I've made some great friends to whom I am thankful for relieving the intermittent burdens of strain that a Ph.D brings. To Dan, Will, Wayne, Jon, Matt, Lorna, Aoife, Sarah, Simone and Camilla: 'Thank you.'

To my Mum and Dad, who gave me this opportunity in the first place by enabling me to study chemistry at Warwick. For all your support during those years and these ones, thank you so much and I love you both (p.s. the first instalment will be with you next month).

And finally to Claire, who's made these past three years fly by and made them the best I've known. Thanks for all your love and support during the difficult times and for making the rest of them so much fun. Two years of journeying the M1-M42-M5 circuit has been well worth it! xxx

DECLARATION

The work described in this Thesis was carried out in the School of Chemistry at the University of Bristol between October 2002 and August 2003 and in the Department of Chemistry at the University of Sheffield between August 2003 and June 2005. It is the original work of the author, unless otherwise acknowledged within the text, and it has not been submitted previously for a degree at this or any other University. The views expressed in this Thesis are entirely those of the author, and not those of either University.

Graham M. Davies
March 2006

TABLE OF CONTENTS

Chapter One - Ligands, Lanthanides and Cyanides

Chapter Two - New Scorpionates

Chapter Three - Lanthanides and Scorpionates

Chapter Four - Cyanide-Bridged *d-f* Hybrids

Chapter Five- X-ray Crystallography: History, Theory and Technique

LIST OF FIGURES

LIST OF TABLES

LIST OF SCHEMES

PUBLICATION LIST

The following publications contain work that has been submitted as part of this thesis and was performed at the University of Sheffield and the University of Bristol.

Chapter 2 – New Scorpionates

- **Chiral coordination polymers based on thallium(I) complexes of new bis- and tris(pyrazolyl)borate ligands with externally-directed 4-pyridyl groups**
  Graham M. Davies, John C. Jeffery and Michael D. Ward
  New Journal of Chemistry, 2003, **27**, p1550

- **New bis-, tris- and tetrakis(pyrazolyl)borate ligands with 3-pyridyl and 4-pyridyl substituents: synthesis and coordination chemistry**
  Harry Adams, Stuart R. Batten, Graham M. Davies, Martin B. Duriska, John C. Jeffery, Paul Jensen, Jinzhen Lu, Graham R. Motson, Simon J. Coles, Michael B. Hursthouse and Michael D. Ward
  Dalton Transactions, 2005, p1910

- **Dichlorotetrakis[3-(4-pyridyl)-1*H*-pyrazole]cobalt(II) acetonitrile tetrasolvate: an infinite hydrogen-bonded network, in an instant**
  Graham. M. Davies, Harry Adams and Michael D. Ward
  Acta Crystallographica Section C, 2005, **61**, m485

Chapter 3 – Lanthanides and Scorpionates

- **Structural and near-IR photophysical studies on ternary lanthanide complexes containing poly(pyrazolyl)borate and 1,3-diketonate ligands**
  Graham M. Davies, Rebecca J. Aarons, Graham R. Motson, John C. Jeffery, Harry Adams, Stephen Faulkner and Michael D. Ward
  Dalton Transactions, 2004, p1136

- **Bis(1,3-diphenylpropane-1,3-dionato-κ^2 *O,O'*){hydrotris[3-(2-pyridyl)pyrazol-1-yl]borato}praseodymium(III): another member of an unpredictable series**

  Graham M. Davies, Harry Adams and Michael D. Ward

  Acta Crystallographica Section C, 2005, **61**, m221

- **Photophysical properties of Pr(III) and Er(III) complexes of poly(pyrazolyl)borates**

  Graham M. Davies, Harry Adams, Simon J. A. Pope, Stephen Faulkner and Michael D. Ward

  Photochemical & Photobiological Sciences, 2005, **4**, p829

Chapter 4 – Cyanide-bridges Ru(II)-Ln(III) Complexes

- **Structural and photophysical properties of coordination networks combining $[Ru(bipy)(CN)_4]^{2-}$ anions and lanthanide(III) cations: Rates of photoinduced Ru-to-lanthanide energy transfer and sensitised near-infrared luminescence**

  Graham M. Davies, Simon J. A. Pope, Harry Adams, Stephen Faulkner and Michael D. Ward

  Inorganic Chemistry, 2005, **44**, p4656

  Front Cover Feature Article – Vol. 44, Issue 17

- **New members of the $[Ru(diimine)(CN)_4]^{2-}$ family: structural, electrochemical and photophysical properties**

  Harry Adams, Wassim Z. Alsindi, Graham M. Davies, Martin B. Duriska, Timothy L. Easun, Hazel E. Fenton, Juan-Manuel Herrera, Michael W. George, Kate L. Ronayne, Xue-Zhong Sun, Michael Towrie, and Michael D. Ward

  Dalton Transactions, 2006, p39

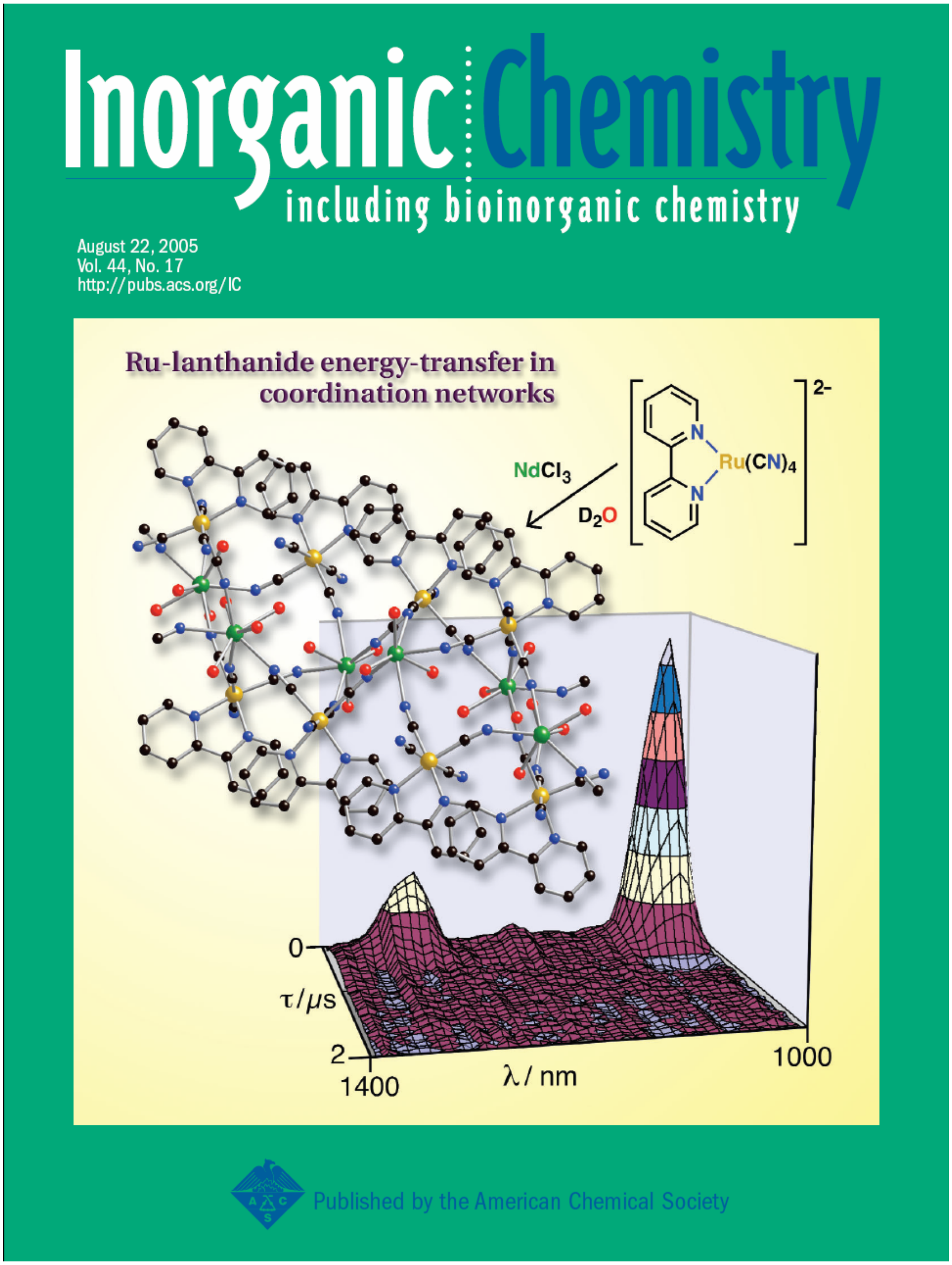

Inorganic Chemistry

including bioinorganic chemistry

August 22, 2005
Vol. 44, No. 17
http://pubs.acs.org/IC

Ru-lanthanide energy-transfer in coordination networks

Published by the American Chemical Society

ABBREVIATIONS - General

Chemicals

M	Metal
L	Ligand
R	Alkyl, aryl
Pypz	pyridyl-pyrazole
bipy	2,2'-bipyridyl
bpym	2,2'-bipyrimidinyl
DMF	*N,N*'-dimethyl formamide
Ln	lanthanide
Me	Methyl
Et	Ethyl
i-Pr	*iso*-Propyl
t-Bu	*tertiary*-Butyl
Ph	Phenyl
Tol	Tolyl
Ant	9-anthryl
Z	Effective nuclear charge
MeCN	acetonitrile
MeOH	methanol
phen	1,10-phenanthroline
THF	tetrahydrofuran
Et_3N	triethylamine

Other terms

k_{ET}	Rate constant of energy transfer
LMCT	Ligand to metal charge transfer
MLCT	Metal to ligand charge transfer

Experimental techniques and terms

EI	electron impact
ES	electrospray
FAB	fast atom bombardment
m/z	Mass to charge ratio
IR	infra red
NIR	near infra red
UV/Vis	ultraviolet/visible
br	broad
d	doublet
dd	doublet of doublets
δ	chemical shift (ppm)
m	multiplet
s	singlet
t	triplet
τ	Luminescence lifetime
q	Number of coordinated water molecules
(h,k,l)	Miller indices
Å	Ångstoms (10^{-10} m)
Z	Formula units per cell
μ	Linear absorption coefficient
a,b,c	Unit cell dimensions
α,β,γ	Unit cell angles
U	Unit cell volume
U	Thermal parameter
F(000)	No. electrons per unit cell
S	Goodness-of-fit
F_o, F_c	Observed and calculated structure factors
R_1, wR_2	R-indicis (based on F and F^2 respectively)

ABBREVIATIONS - Poly(pyrazolyl)borates

The initial abbreviation system for poly(pyrazolyl)borates by was introduced by Curtis.[1] Tp and Tp* are used to depict $[HB(pz)_3]^{-}$ and $[HB(3,5\text{-}Me_2pz)_3]^{-}$ respectively, for they are the most widely used members of the ligand system. Following the introduction of the 'second generation' poly(pyrazolyl)borates, the system was expanded by Trofimenko[2] to accommodate the rapid growth of new ligands that were being synthesised.

Homoscorpionates: The basic tris(pyrazolyl)borate core is represented by Tp, with any non-hydrogen substituents in the 3-position denoted by a superscript. For example, Tp^{Me} is $[HB(3\text{-}Mepz)_3]^{-}$ and $Tp^{i\text{-}Pr}$ is $[HB(3\text{-}isopropylpz)_3]^{-}$; a 5-substituent follows the 3-substituent in superscript, separated by a comma (e.g. $Tp^{i\text{-}Pr,Me}$ is $[HB(3\text{-}isopropyl\text{-}5\text{-}methylpz)_3]^{-}$. When both 3- and 5-substituents are identical, the R group is followed by a '2' (e.g. $[HB(3,5\text{-}Ph_2pz)_3]^{-} = Tp^{Ph2}$); 4-substituents are denoted by a superscript 4R, which follows the 3-substituent by a comma (e.g. $[HB(3\text{-}isopropyl\text{-}4\text{-}bromopz)_3]\text{-} = Tp^{i\text{-}Pr,4Br}$.

Heteroscorpionates: These ligands are abbreviated 'Bp' with 3-, 4- and 5-substituents catalogued in an analogous manner to those of Tp as above. **NB**: Any non-hydrogen substituents on the boron atom of either scorpionate system are denoted *before* the abbreviation (e.g. diethylbis(pyrazolyl-1-yl)borate = Et_2Bp). Reference to scorpionate systems in general are denoted by a superscript 'x' (e.g. Tp^x and Bp^x).[3]

X-Ray Structures

Within this report, pictorial representations of crystal structures have been shown without hydrogen atoms as an aid to clarity. Full lists of both bond lengths and angles are contained within the rich text format (.rtf) files of Appendix 3.

1. M. D. Curtis, K. –B. Shlu, W. M. Butler. *Organometallics*, 1983, **2**, 1475.
2. S. Trofimenko, *Chem. Rev.*, 1993, **93**, 943.
3. There remain a few scorpionate systems that do not follow this abbreviation system. For example Tp^a is used to describe hydrotris(4,5-dihydro-2*H*-benz[g]-indazol-2-yl)borate.

‘You never truly understand something until you can explain it to your grandmother.’

-- Albert Einstein

Chapter One

Ligands, Lanthanides & Cyanides

Introduction

This chapter provides a general introduction to the various fields concerned with the works of this thesis. *Section One* deals with the nature and synthesis of the poly(pyrazolyl)borate ligands, charting the history of their coordination chemistry with a particular focus on the development of the second-generation ligands. *Section Two* introduces the lanthanide ions, describing the physical properties of those in the +3 oxidation state and how these can be harnessed for use in practical applications; whilst *Section Three* covers a brief review of coordination polymers based on the cyanide-bridge motif.

Any specific topics that have not been addressed in this introduction will be discussed at the beginning of the relevant chapter.

1.1 Poly(pyrazolyl)borates

1.1.1 The Ligand

Poly(pyrazolyl)borates were first introduced to the literature in 1966 by Trofimenko.[1] They are a unique class of ligand in that the multiple binding sites they offer are enhanced by the negative charge on the boron atom, making them especially attractive for metal ion coordination. This, along with the simplicity of their system, has made them a popular and well-established class of ligand, whose library to date consists of over 200 individual, novel members, spanning almost 2000 publications.[2]

At the heart of the poly(pyrazolyl)borate system is a tetra-substituted boron atom, accommodating between two and four pyrazole rings through boron-nitrogen bonds in a tetrahedral array. Coordination to a metal ion then occurs through those nitrogen atoms occupying the 2-position of the individual pyrazole rings, with the most commonly synthesised systems being the bis- and tris-(pyrazolyl)borate ligands (n = 2 and 1 respectively, **Fig. 1.1.1**).

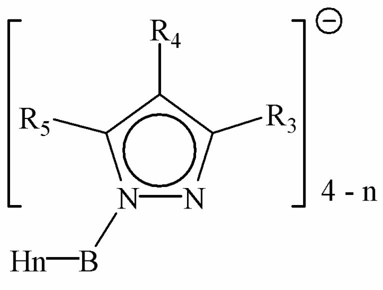

Fig. 1.1.1 – General formula of a poly(pyrazolyl)borate (n = 0, 1, 2)

1.1.2 Substitution Rights

In addition to the boron atom, the pyrazole rings offer a vast number of substitutable positions, making the poly(pyrazolyl)borates incredibly versatile. Substitution at the 3-, 4- or 5-positions of the rings with different R-groups has a significant bearing on the coordination number and geometry of their metal complexes, as well as directly influencing their physical and chemical properties. Thus, poly(pyrazolyl)borates can often be designed to meet the requirements or limitations of a particular metal.

The most obvious effects are seen with substituents at the 3- and 5-positions (**Fig. 1.1.1**). Those at the former offer steric hindrance to the ligand's central cavity, restricting metal ion coordination; or, once a metal is coordinated, these substituents can also serve to 'screen' the metal, controlling its accessibility to external reagents. Those at the C^5 position provide steric protection to the boron atom, and as the boron-hydrogen bond(s) are susceptible to chemical attack,[3] this may help to stabilise the ligand and its complexes. In addition to this, repulsion between 5R-substituents may serve to narrow the 'bite' angle of the nitrogens available for metal coordination. No immediate steric effects are transformed from substitution at the 4-position as it is equally remote from both metal ion and boron atom.

1.1.3 The Synthesis

1.1.3.1 Poly(pyrazolyl)borates

Poly(pyrazolyl)borates may be prepared from a variety of boron sources, yet the most convenient route is through the borohydride ion.[4] Synthesis proceeds by thermolysis of the appropriate pyrazole and an alkali metal borohydride (e.g. KBH_4) to form a melt.[5] The degree of boron substitution is temperature dependent, and by using an appropriate excess of pyrazole and heating for long enough in the correct temperature range, one can synthesise bis-, tris- and (in the case of 5-unsubstitued pyrazoles) tetrakis(pyrazolyl)borates (**Fig. 1.1.2** and **Table 1.1.1**). The bis-substitution reaction is the first to occur - even with a pyrazole molar deficiency, the mono-substituted boron analogue $[H_3B(pz)]$ is never formed.

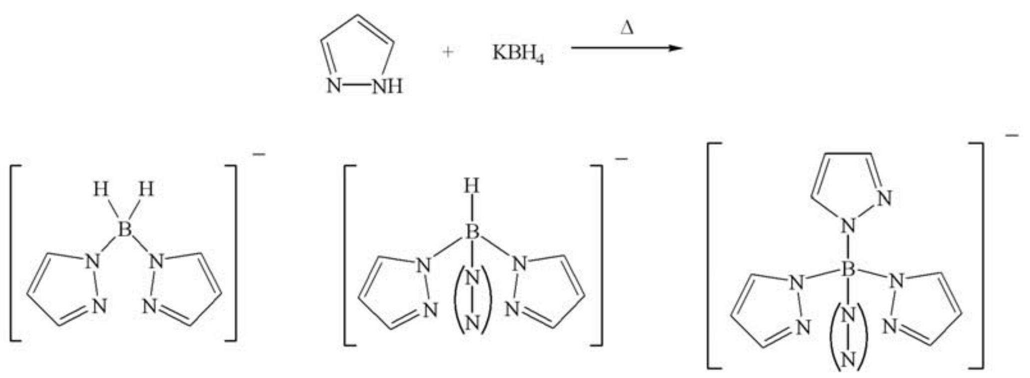

Fig. 1.1.2 – Synthesis of the poly(pyrazolyl)borates
- (N-N) represents the third pyrazole ring seen edge-on

Equivalents of Pyrazole	Reaction Temp /°C (melt)	Product	IR B-H Stretch /cm^{-1}
3	≤ 125	$[H_2B(pz^x)_2]^-$	2200-2500
3.5	≤190	$[HB(pz^x)_3]^-$	2500
4	> 220	$[B(pz^x)_4]^-$	N/A

Table 1.1.1 – General conditions for subsequent pyrazolyl substitution

Hydrogen gas is liberated as reaction proceeds, and the synthesis of many poly(pyrazolyl)borates involves measuring the quantity of gas evolved to follow the reaction rate, as well as its extent of completion.[4] The pure product is obtained by sonicating the melt with toluene to remove the excess pyrazole, and filtering. In addition to the melt pathway, the ligands may be formed by refluxing the reagents in a solvent with an appropriate boiling point. This serves to prevent over-substitution, which is commonplace in a melt due to the build up of localised heat.

The degree of substitution and the success of the reaction can also be checked in the final product by IR spectroscopy, as each poly(pyrazolyl)borate has a characteristic B-H vibration pattern at *ca*. 2500 cm^{-1} (**Table 1.1.1**)

1.1.3.2 Pyrazoles

Cyclo-condensation of the appropriate 1,3-dicarbonyl compound with hydrazine is typically employed in this synthesis, and pyrazoles are usually obtained in excellent yield (**Fig. 1.1.3**).

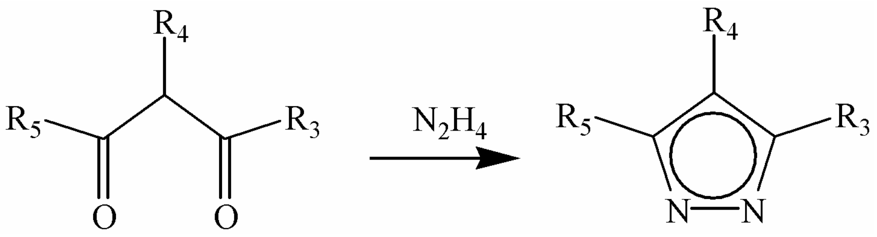

Fig. 1.1.3 – Pyrazole synthesis

4R-substituents can be introduced to the isolated pyrazole *via* electrophilic substitution,[6] whilst 3R- and 5R-groups are introduced in the preparation of the dicarbonyl reagent. This is typically a Claisen condensation of the appropriate ketone and ester, employing NaOMe as a base (**Fig. 1.1.4**).[5]

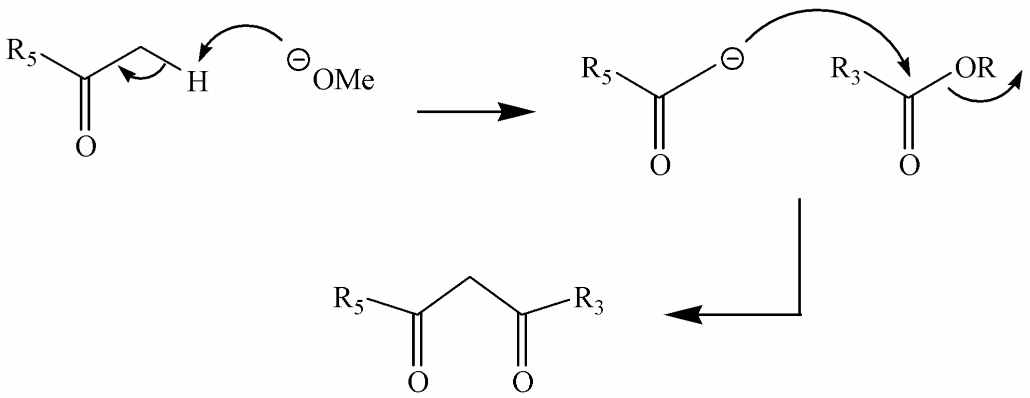

Fig. 1.1.4 – 1,3-dicarbonyl synthesis *via* Claisen condensation

It is important to remember that poly(pyrazolyl)borates are, when isolated, the anion components of an alkali metal salt. Consequently, they are soluble in alcohols and polar solvents (Bp^x more so than Tp^x), fairly soluble in water, and pretty much insoluble in alkanes and non-polar aromatics (again, Bp^x more so than $Tp^{x,}$ where x is any pyrazole substituent). The nature of the 3-, 4-, and 5-substituents may be changed to vary these degrees of solubility, and the solubility in organic solvents is enhanced when the alkali metal is replaced with Tl(I).[4]

1.1.4 Steric Effects

1.1.4.1 The Cone Angle (α)

Many steric influences arise from varying the nature of the R-substituents. The most widely used method of characterising these 'steric effects' is the 'cone angle' – a system originally developed by Tolman for describing symmetric phosphine ligands, in which the apex angle of the cylindrical cone is 2.28 Å from the phosphine atom (**Fig. 1.1.5a**).[7] Its application to poly(pyrazolyl)borates (**Fig. 1.1.5b**) does provide a useful measure of the steric effect, but as with the phosphines, occasional intermeshing of substituents can warp the ligand's shape, distorting it from ideal symmetry.

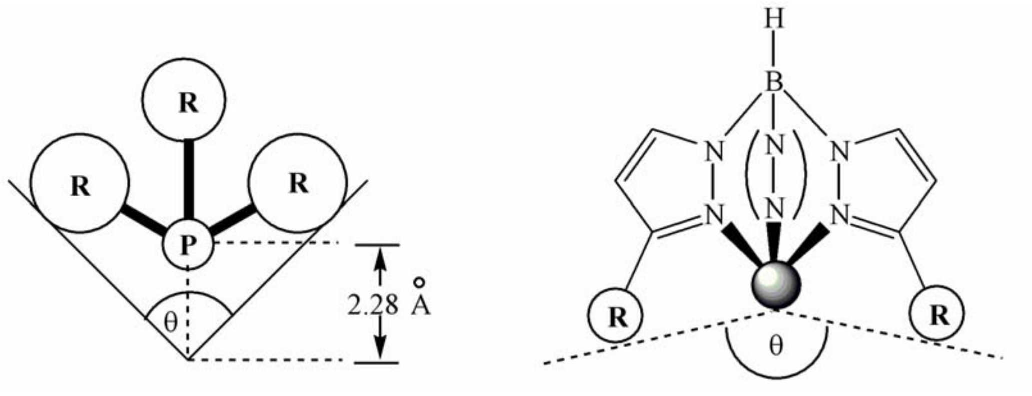

(a) **(b)**

Fig. 1.1.5 – (a) Tolman's original cone angle (α = 2θ) and
(b) The poly(pyrazolyl)borate cone angle (α = 360 - θ)

Trofimenko and co-workers have determined analogous 'cone angles' for Tp^{x} derivatives containing 3R substituents and established a steric hierarchy for the various Tp^{x} ligands.[4,8,9] The size of a cone angle is not only ligand dependent, but is also affected by the length of the bonds between nitrogen donors and metal ions. Because of this metal ion dependence, and the fact that transition metals can adopt different geometries with these ligands, Trofimenko employed Tl(I) as the reference metal in these structural characterisations.[10] This is further justified by the fact that all Tp^{x}Tl complexes - expect for [Tl(Tp^{Cpr})], see later - are monomeric and isostructural.[4]

A small cone angle indicates large steric repulsion from the 3R substituents, and subsequently suggests that the metal is more susceptible to approach from external reagents. This degree of steric crowding is mirrored in the cone angle scale when the 3R substituents are of a non-planar nature, yet the case is not so simple when planar substituents are employed. Hydrotris(4,5-dihydro-2*H*-benz[*g*]-indazol-2-yl)borate (Tp^{a}) for example, has a rather large cone angle (262°), which is almost equal to that of hydrotris(3-t-butylpyrazol-1-yl)borate, Tp$^{t\text{-Bu}}$ (265°). However, it readily forms complexes in the form of [Tp$^{a}_{2}$M] with octahedral metals, in preference to those of [Tp^{a}MX] where X is a coordinated anionic counter ion.[8] Tp$^{t\text{-Bu}}$ on the other hand, forms solely complexes of the latter type, containing only one Tp ligand (**Fig. 1.1.6**).[11]

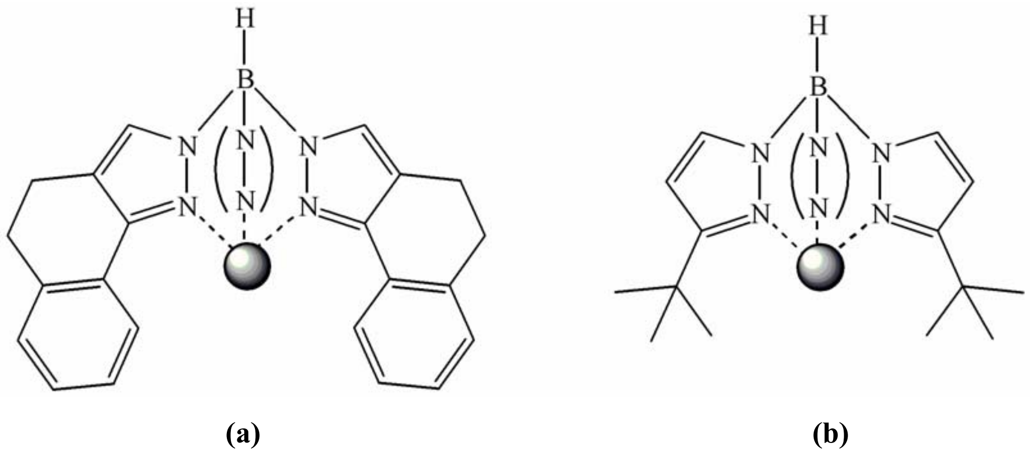

Fig. 1.1.6 – Metal complexes of (a) Tp^a and (b) Tp^{t-Bu}

1.1.4.2 The Wedge Angle (β)

As we have seen, ligands that may have similar cone angles do not necessarily display the same chemistry, and the cone angle principle is limited to use of the non-planar 3R substituents. There is however, a more suitable alternative in the 'wedge angle'. This is a quantitative measure of the wedge-shaped space between pyrazole rings - the space where nucleophilic attack upon a coordinated metal is permitted (**Fig. 1.1.7**). A bulky substituent will minimise the wedge angle, decreasing the chance of approach by external reagents.

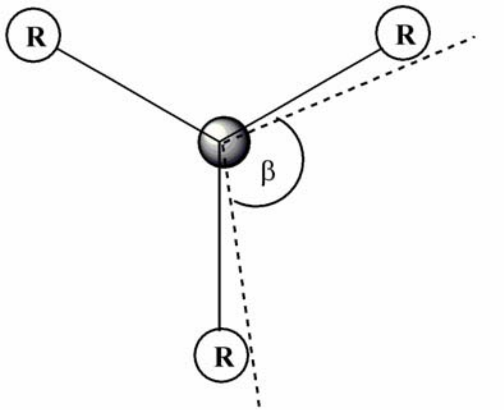

Fig. 1.1.7 – The wedge angle (β) viewing down the B-M bond

The preferential dimer formation of Tp^a is now justified by a large wedge angle of 44°,[8] whilst that of $Tp^{t\text{-}Bu}$ is a mere 29°.[4]

Planar substituents are free to rotate about the σ-bond and so complicate the measuring of wedge angles. Nonetheless, once measured, the wedge angle correlates more effectively with the properties of such ligands although most early publications quote cone angles.[4]

1.1.5 Shake Hands with a Scorpion!

When coordinated, poly(pyrazolyl)borates are always at least bidentate and consequently, display a characteristic mode of binding upon complexation: a six membered ring formed by the apical boron, the 1- and 2-nitrogen atoms and the metal centre. Because of the varying bond angles and distances involved, this ring is consistently in a boat formation of varying depth. Whilst the pseudoequatorial R group points away from the metal (and we have an approximately linear R-B-M axis), the pseudoaxial R^1 group is able to curl towards the metal where it will serve to: i) bond to the metal, or ii) interact with the metal in an agostic fashion, or iii) screen the metal (**Fig. 1.1.8a**)

On the basis of this model, Trofimenko[10] coined the term ‘Scorpionate’ likening the coordination behaviour of the pyrazolylborates to the hunting manners of the scorpion: the creature grabs its prey with its two identical claws $[(pz^x)_2]$ before it may, or may not, proceed to ‘sting’ its prey with its tail (R^1), **(Fig. 1.1.8b)**.

The close relationship between bis- and tris(pyrazolyl)borates is clearly evident from this analogy, and the versatility of poly(pyrazolyl)borate chemistry can therefore be related to the varying nature of the sting.

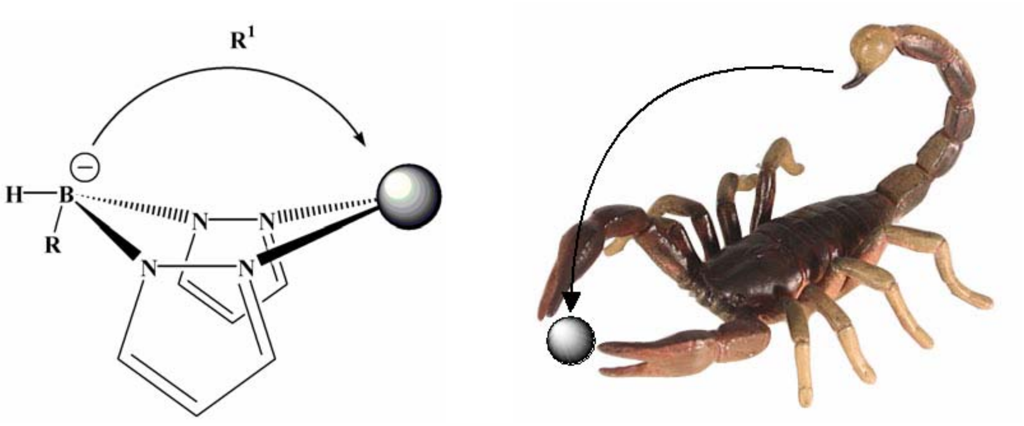

(a) **(b)**

Fig 1.1.8 – (a) The coordination mode of poly(pyrazolyl)borates (b) the scorpion analogy

The scorpionate family can be divided into two distinct groups:

- *Homoscorpionates* – in which the pseudoaxial group R^1 is identical to the other two 'claws' giving the ligand local C_{3v} symmetry.

- *Heteroscorpionates* – The 'sting' is performed (if at all) by an R^1 group that is different from those that form the 6-membered boat ring. Remarkably, despite the wealth of controllable variables available in heteroscorpionates, these remain the lesser studied of the family groups by a large margin. Although activity has increased over the past decade, up until 1993 only 5% of all known scorpionate publications dealt with this family group.[10]

1.1.6 Homoscorpionates

The ease with which scorpionates could be synthesised made them extremely popular after their introduction in 1966. Such was the extent of this popularity, that research for the next 20 years was confined to the roles of Tp and Tp* alone (**Fig. 1.1.9a** and **1.1.9b** respectively). It was not until 1986 that 3R substituents (other than Me) were incorporated into Tp ligands for the first time.[12]

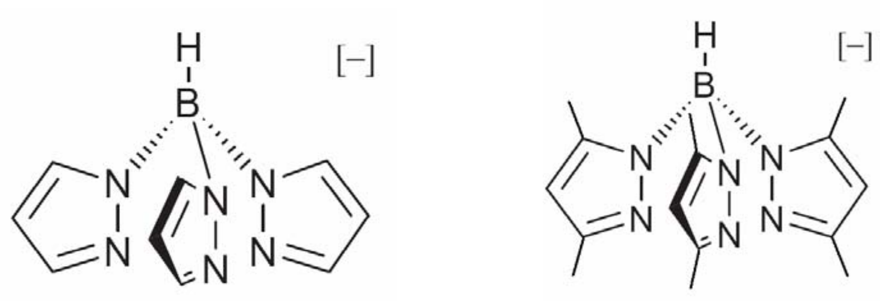

(a) **(b)**

Fig. 1.1.9 – (a) Tp and (b) Tp*

The work in this thesis is concerned with scorpionates bearing 3R substituents (the so-called 'second generation' scorpionates), and so a more detailed review of their chemistry will follow.

1.1.6.1 Tp and Tp* - First Generation Scorpionates

The coordination behaviour of these first-generation scorpionates is entirely metal dependent. Due to the large wedge angles they possess (*ca*. 70° each), divalent octahedral transition metals readily form the full-sandwich Tp_2M complexes, and their tetrahedral complexes [TpMX] show great tendency to self-convert to the sandwich form as well.[13]

The reason is the complexes are extremely labile, and gentle heating of the reaction mixtures is, at most, enough to induce the transformation.[14] For example, the complex [TpCoCl] is formed under anhydrous conditions using $CoCl_2$ and KTp, yet after standing for 30 minutes at room temperature in DCM, starts to precipitate $CoCl_2$ and reverts to the $[Tp_2Co]$ sandwich (**Fig. 1.1.10**).[15]

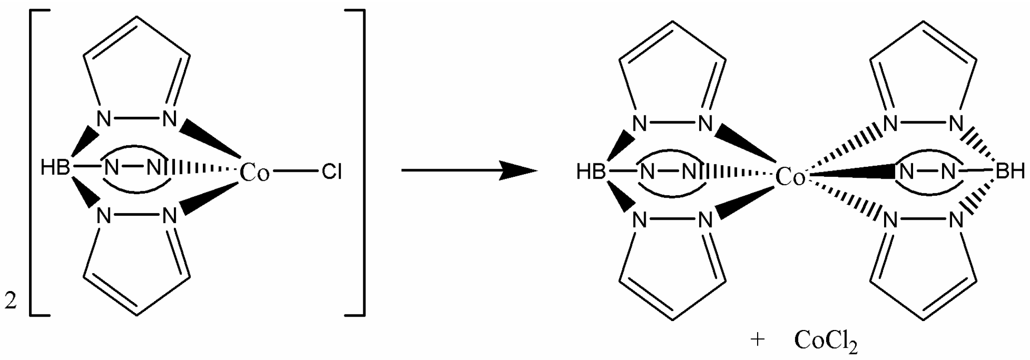

Fig. 1.1.10 – Disproportionation of [Tp_2Co]

The tridentate nature of the ligands is removed upon coordination with square planar metals, leaving one pyrazole arm pendant in such complexes as [Tp_2Pd].[16] The ligands' lability is evident in solution however as rapid interchanging of coordinating pyrazole rings results in only one pyrazole group being observed in the NMR spectrum.

Whilst their chemistry with first-row transition metals appears limited, the first-generation scorpionates have found considerable popularity as spectator ligands with the remaining d-block metals. Scorpionates function as nitrogen σ-donors with little tendency to accept electron density from the metal,[17] and offering this uniquely large amount of electron density has enabled Tp and Tp* to form stable complexes with metals of unusually high oxidation states. For example, complexes ranging from $Mo^{(0)}$ in [$TpMo(CO)_3$]$^-$ to $Mo^{(VI)}$ in [$TpMoO_2X$] have been synthesised with relative ease.[18, 19]

Once coordinated, the ligands have no tendency to interfere with any further reaction(s) at the metal centre, and this permits the use of their complexes in catalytic cycles. For example, [$RuTp(PhCN)_2Cl$] is catalytically active in the hydrogenation of methyl acrylate;[20] [RuTp*(COD)H] catalyses the reduction of unactivated ketones to alcohols by hydrogen transfer from alcohols in basic media;[21] and [$RuTp(PPh_3)_2H$] is an effective catalyst for the dimerization of terminal alkynes to give enynes.[22]

1.1.6.2 The Second Generation

The ‘second-generation’ scorpionates were ‘born’ in 1985 with the synthesis of hydrotris(3-methylpyrazoyl-1-yl)borate (Tp^{Me}) in an attempt to avoid formation of the recurring octahedral sandwich complexes, although the methyl bulk proved insufficient to prevent this.[23] Sufficient bulk was found however in $Tp^{t\text{-}Bu}$, providing the first examples of stable tetrahedral coordination with a tris(pyrazolyl)borate ligand (**Fig. 1.1.11**).[11]

Such [$Tp^{t\text{-}Bu}$MX] complexes were formed with all first row transition metals earning the ligand the nickname of ‘tetrahedral enforcer’, although 5-coordination was later observed by using bidentate anions such as nitrate.[24] Whilst no full-sandwich complexes were observed with the first row transition metals, the importance of the cavity’s degree of encapsulation became apparent when octahedral dimer complexes were formed on reaction with the larger d-block metals of molybdenum and tungsten.[4]

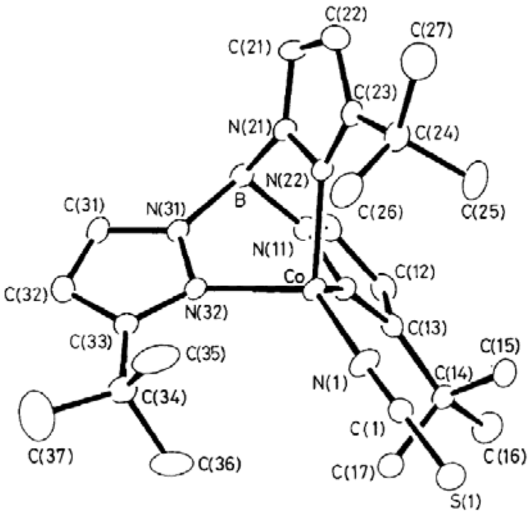

Fig. 1.1.11 – Crystal structure of [($Tp^{t\text{-}Bu}$)Co(NCS)]

The addition of a methylene spacer in hydrotris(3-neopentylpyrazol-1-yl)borate (Tp^{Np}), permitted a greater flexibility for the substituents *via* rotation about three C^3-CH_2 bonds, allowing the *t*-butyl group to either crowd the metal, or face away from it (**Fig. 1.1.12**).

On coordination, the latter was preferable, and sandwich complexes were evident,[25] but by tethering the *t*-butyl groups in hydrotris(7-*tert*-butylindazol-2-yl)borate [$\mathrm{Tp}^{3\mathrm{Bo},7t\mathrm{Bu}}$], it was possible to force their direction towards the cavity.[26]

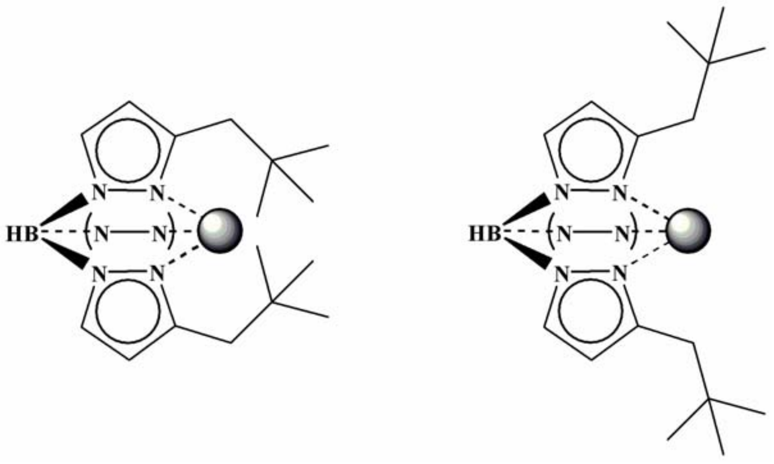

Fig. 1.1.12 – Potential coordination modes of $\mathrm{Tp}^{\mathrm{Np}}$

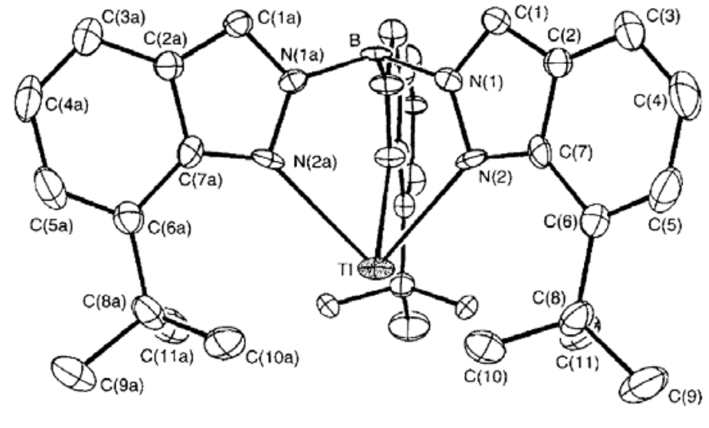

Fig. 1.1.13 – Crystal structure of [($\mathrm{Tp}^{3\mathrm{Bo},7\mathrm{tBu}}$)Tl]

From the structure of the Tl(I) complex (**Fig. 1.1.13**), this gave a large calculated cone angle of 261°, mainly due to steric repulsions, and because the thallium(I) ion was completely surrounded by the substituents, further reaction with additional metal salts was reluctant to occur under similar conditions.

Reaction with $Co(SCN)_2$ under elevated temperatures, however, resulted in metamorphosis of the ligand to give [HB(3-*tert*-butyl-indazol-2-yl)$_2$(3-*tert*-butyl-indazol-1-yl)] ($Tp^{3Bo,7tBu*}$). Here, one of the ligand's arms undergoes rearrangement, coordinating to the boron atom *via* the N^2 atom of the pyrazole ring (**Fig. 1.1.14**), forming a less hindered isomer that can accommodate the metal ion in a [($Tp^{3Bo,7tBu*}$)Co(NCS)] complex. Such ligand rearrangement had already been seen in some octahedral second-generation homoscorpionates, such as hydrotris(3-isopropylpyrazol-1-yl)borate ($Tp^{i\text{-}Pr}$)[6] and (Tp^{Np})[25] but this was the first example of such behaviour on formation of a tetrahedral complex.

The cone angle for this complex was calculated at 305° (using the two un-rearranged 7-*tert*-butylindazolyl groups). Whilst this value suggests no sandwich complexes can form, from the fact that reaction conditions have to be made more vigorous to induce any reaction, and that the ligand must rearrange in order to accommodate the metal, it was proposed[26] that in this ligand, the steric limit for effective coordination with the scorpionates had now been reached and that this ligand was a true 'tetrahedral enforcer.'

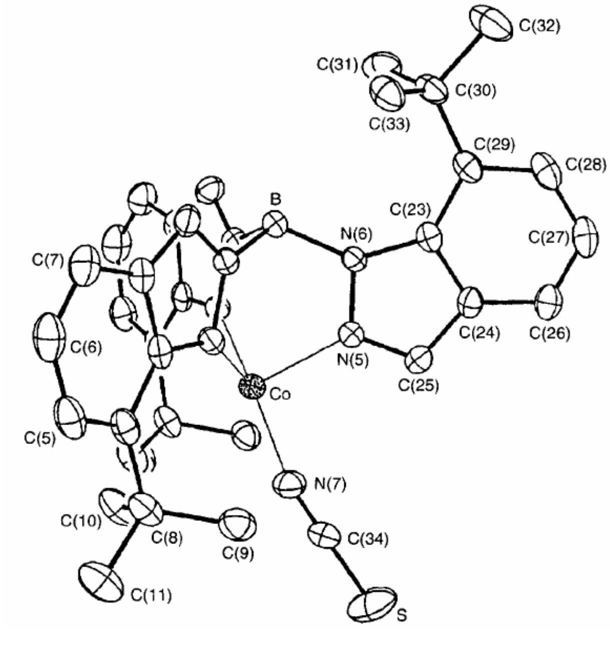

Fig. 1.1.14 – Crystal structure of Tl[$Tp^{3Bo,7tBu*}$]

The first planar 3R-substituents were employed in the synthesis of hydrotris(3-phenylpyrazol-1-yl)borate (Tp^{Ph}). The freedom of rotation about the pyrazolyl-phenyl bonds provided a less hindered environment for the metal ion than the $Tp^{t\text{-Bu}}$ ligand, and although monomeric complexes were formed, they were of a solvated nature (e.g. [Tp^{Ph}Co(SCN)(THF)], **Fig. 1.1.15**),[12] with full-sandwich complexes still apparent in some instances.[27]

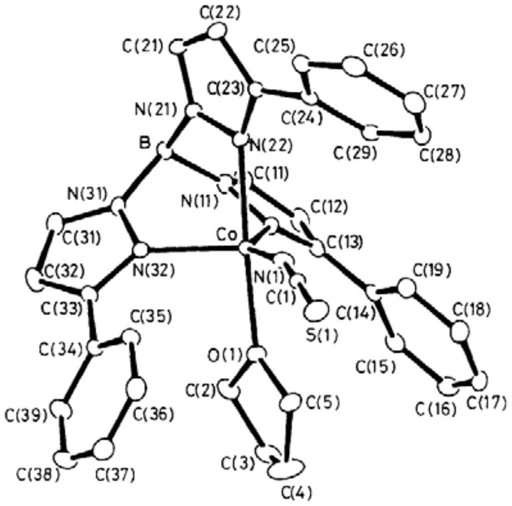

Fig. 1.1.15 – Crystal structure of [(Tp^{Ph})Co(NCS)(THF)]

The ligand of hydrotris(3-{*p*-tolyl}pyrazol-1-yl)borate (Tp^{Tol}), in which the 3R substituent is a *para*-methyl substituted phenyl ring, was analogous to Tp^{Ph}, but the methyl group protruded slightly further beyond the coordinated metal ion. Surprisingly though, this extra methyl bulk was sufficient enough to prevent coordination of a second Tp^{Tol} ligand, and monomeric [Tp^{Tol}MX] complexes were readily formed.[28] Whilst no full sandwich complexes were observed, it was evident that close approach by additional Tp^{Tol} ligands was still possible (**Fig. 1.1.16**).[29]

In order to reduce the phenyl-pyrazole rotation, mesitylene substituents were incorporated into hydrotris(3-mesitylpyrazol-1-yl)borate (Tp^{Ms}), with the additional methyl groups successfully ensuring that only tetrahedral complexes were obtained.[30] To date, this ligand still has the smallest wedge angle of all the second-generation scorpionates (7°).

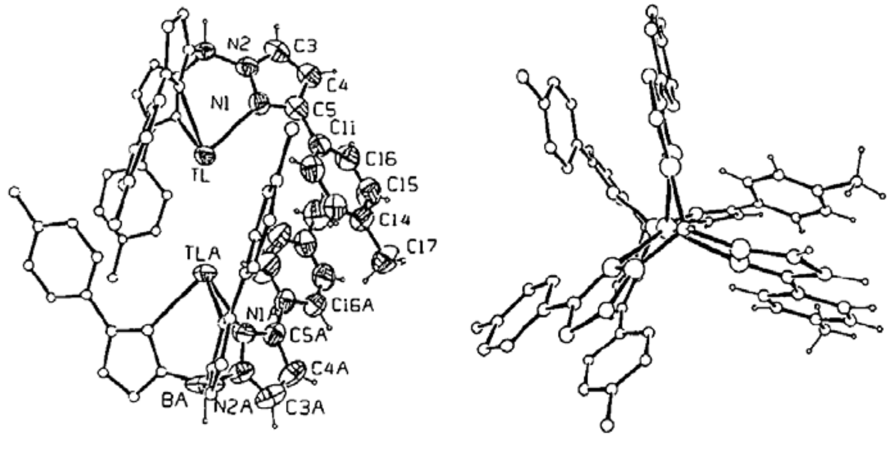

(a) **(b)**

Fig. 1.1.16 – Crystal structure of [Tp^{Tol}Tl].
(a) Scenic view, (b) 3-fold Axial View

Another way of restricting the phenyl-pyrazole rotation was to tether the rings together with –(CH$_n$)- linkers, forcing the rings to be coplanar, and lead to a more predictable environment about the metal centre. An ethene tether did not provide strict coplanarity as it zig-zagged across the plane of the pyrazolyl ring; a methylene tether achieved coplanarity, but the resulting expansion of the 'bite' in this manner assured coordination by external reagents.[8]

Strict coplanarity without bite angle change was eventually obtained with an ethyne spacer (**Fig. 1.1.17**), making each pyrazolyl arm totally rigid, although the resultant chemistry was altered. For whilst the reaction of Tp^{Ph} with [Mo(CO)$_2$(MeCN)$_2$Cl(η^3-CH$_2$CMeCH$_2$)] permitted the formation of [Mo(CO)$_2$(Tp^{Ph})(η^3-methallyl)] with κ^3-coordination, the ethyne-tethered analogue showed only κ^2-coordination behaviour in the same complex, with an agnostic B-H-Mo interaction to achieve an 18-electron structure (**Fig 1.1.17**),[2,9] with the steric bulk of the η^3-methallyl group preventing κ^3-coordination.

Coplanarity between the phenyl substituents and the pyrazole rings was removed altogether in the ligands of hydrotris(3-(9-anthryl)pyrazol-1-yl)borate (Tp^{Ant}), and hydrotris(3-(1-napthyl)pyrazol-1-yl)borate (Tp^{Nt}) (**Fig. 1.1.18**).[3, 31, 32]

The shear steric vastness of these substituents eliminated any possibility of full-sandwich complex formation, forming solely [Tp^{x}MX] species.

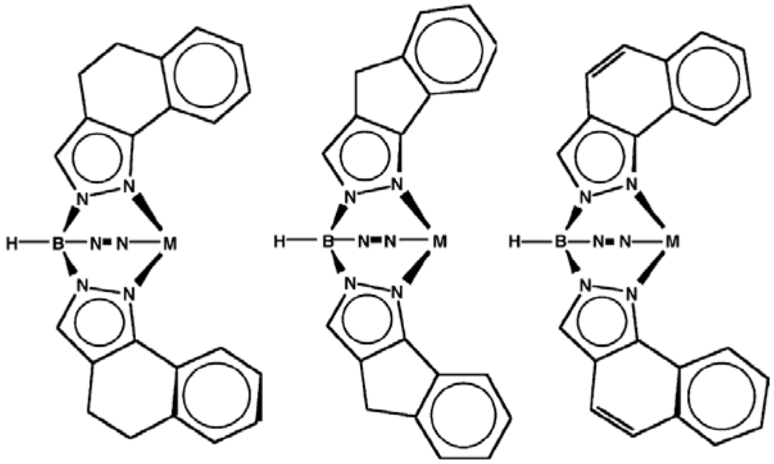

Fig. 1.1.17 – Ethene, methylene, and ethyne spacers: Tethering of the phenyl substituents

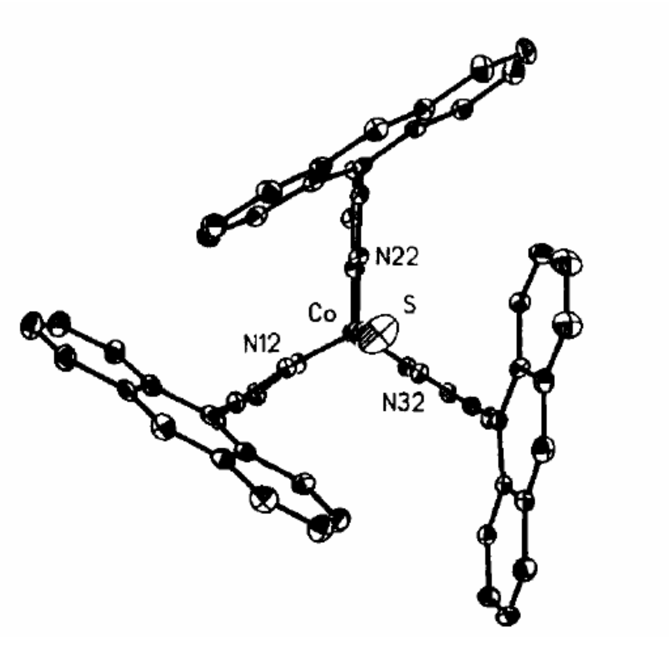

Fig. 1.1.18 – Tp^{Ant}

In attempts to change the solubility of the ligands and their complexes, Tp^{Cpr},[33] Tp^{Cbu}, Tp^{Cpe},[34] and Tp^{Cy},[35] were synthesised offering various sizes of hydrophobic pockets to the metal ion (the superscript refers to 3-*C*yclo-*pr*opyl, *bu*tyl, *pe*ntyl, and hex*y*l 3R substituents respectively).

Little steric hindrance was offered by the cyclopropyl groups (β = 68°), regularly affording octahedral dimers, whilst the cyclohexyl groups (β = 46°) required higher temperatures to achieve the same feat, namely κ^2-coordination in square planar $[Cu(Tp^{Cy})_2]$,[36] and κ^3-coordination in $[Co(Tp^{Cy})_2]$ in which all three substituents' tertiary hydrogens pointed away from the central cavity in the solid state.[35] Tp^{Cpr} gave a unique result[37] in its structure with Tl(I), of a perfect Tl_4 tetrahedron with each face capped by a Tp^{Cpr} (**Fig. 1.1.19**).

The intermediate ligands Tp^{Cbu} and Tp^{Cpe} (β = 51 and 46° respectively), afforded regular mixtures of both tetrahedral and octahedral complexes, the latter being mostly heteroleptic with other Tp-based ligands with smaller substituents.[34] As found with Tp^{Cy}, excessive heating of dimeric complexes often resulted in the isomerism of the ligands' arms to the 5-position of the pyrazole ring.

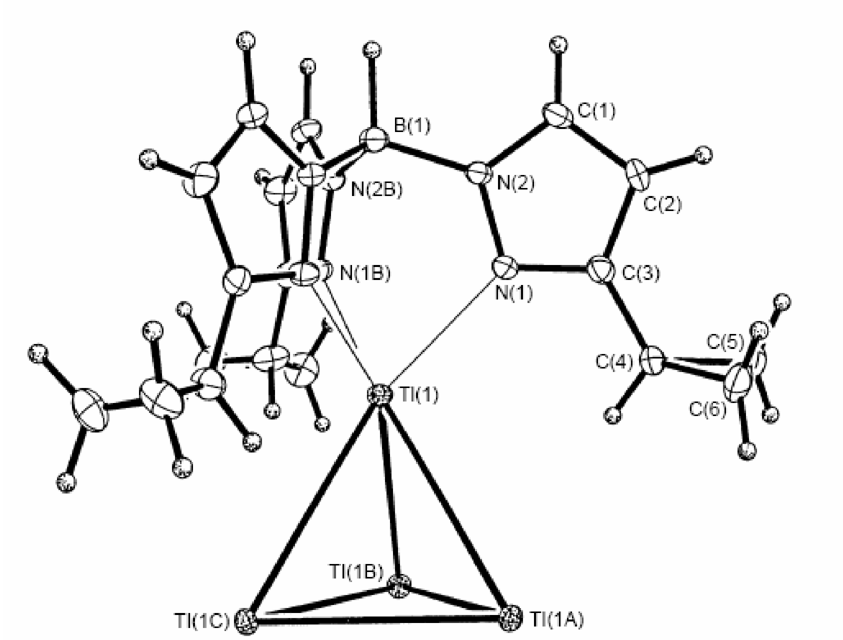

Fig. 1.1.19 – Crystal structure of $[(Tp^{Cpr})_4Tl_4]$

1.1.6.3 Additional Donors – the Next Generation?

Initially, a lot of emphasis had been placed on using 3R substituents to promote the formation of monomeric species, and the aliphatic nature of such substituents had ensured that the scorpionates would continue to coordinate in bidentate (Bp) or tridentate (Tp) fashion.

The inclusion of additional donors in the substituents offers even more scope for variation in the coordination behaviour of poly(pyrazolyl)borates. Hydrotris(3-(2'-thienyl)pyrazol-1-yl)borate ($\mathrm{Tp}^{\mathrm{Tn}}$) was the first example of this new area.[38] The pyrazolyl nitrogens still functioned as donor atoms, but no interaction was observed between the coordinated metal and the sulphur atoms. In the solid state, the thienyl rings remained in a transoid relationship to the pyrazolyl rings, and formation of sandwich complexes was still evident with octahedral metals (**Fig. 1.1.20**).

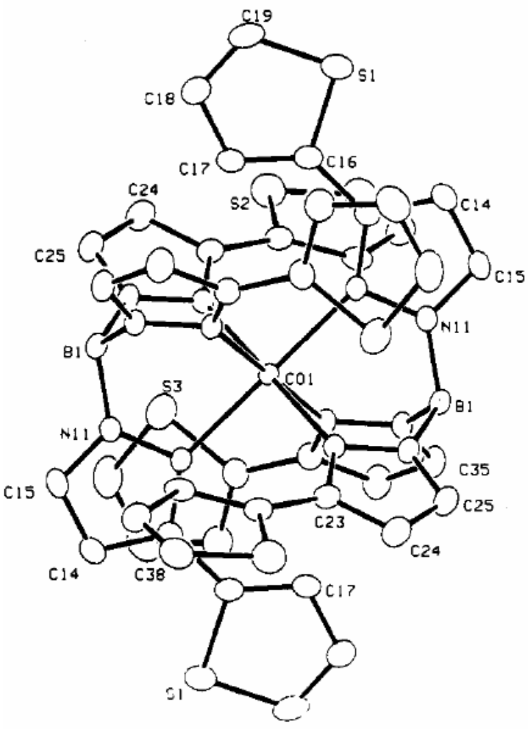

Fig. 1.1.20 – Crystal structure of [$(\mathrm{Tp}^{\mathrm{Tn}})_2\mathrm{Co}_2$]

Hydrotris(3-(2-pyridyl)pyrazol-1-yl)borate (Tp^{Py}) however, has three additional nitrogen donors that do result in the ligand being hexadentate. This was demonstrated in several complexes, most notably in those of lanthanides and actinides, as they seemed to be an ideal fit for the cavity.

The first reported example of the hexadentate behaviour of Tp^{Py} was in the complex $[Tp^{Py}Eu(MeOH)_2F][PF_6]$ where the six donor atoms of the ligand satisfy two thirds of the metal's coordination requirements.[39] Some high coordination numbers have been obtained with Tp^{Py} - for reaction of an f-block metal with two equivalents of the ligand results in a cation with an icosahedral N_{12} coordination environment (**Fig. 1.1.21**).[40]

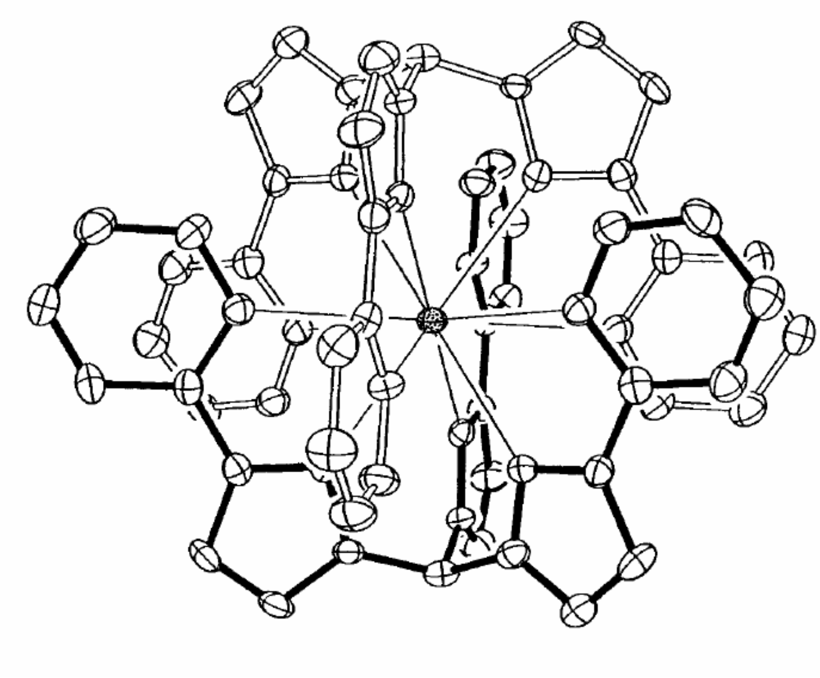

Fig. 1.1.21 – Crystal structure of the cation of $[(Tp^{Py})_2U]I$

Complexation of the ligand with d-block metals offers some nice examples of unusual coordination modes as well. A tetranuclear tetrahedron $[Tp^{Py}{}_4Mn_4]^{4+}$ is formed on reaction with $Mn(OAc)_2$,[41] whilst Cu(I) induces formation of a $[Tp^{Py}{}_2Cu_3][PF_6]$ structure (**Fig. 1.1.22**).[42] The structure of $[Tp^{Py}Cu(H_2O)][PF_6]$ shows a square pyramidal copper(II) ion with the base formed by two coordinated arms of the ligand, whilst the third chelates with the proton of an axial water molecule instead of coordinating to the metal (**Fig. 1.1.23**).[43]

Monomeric complexes with Co(II),[44] Pb(II),[45] and Tl(I),[46] are also known, and an $[Ag_3Tp^{Py}{}_2]^+$ cluster exists with silver.[46]

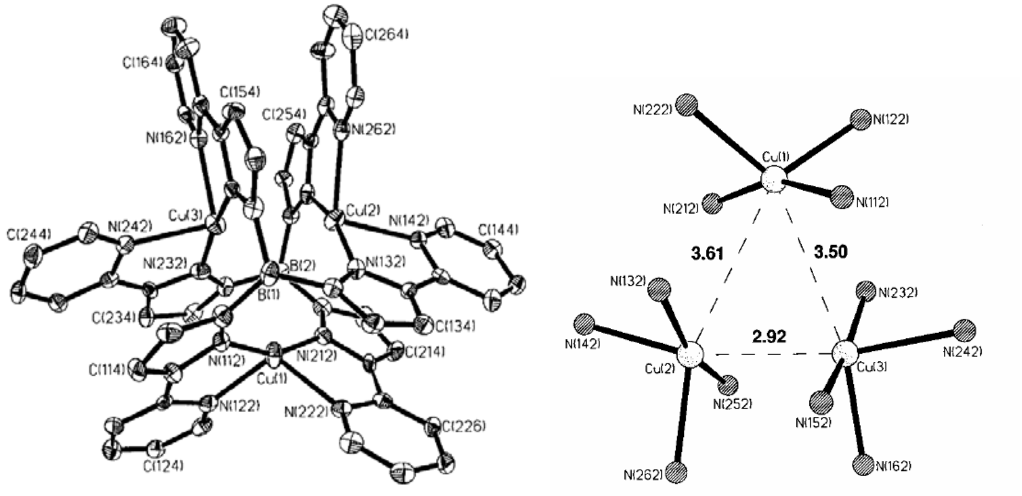

Fig. 1.1.22 – Crystal structure of the cation of $[(Tp^{Py})_2Cu_3][PF_6]$

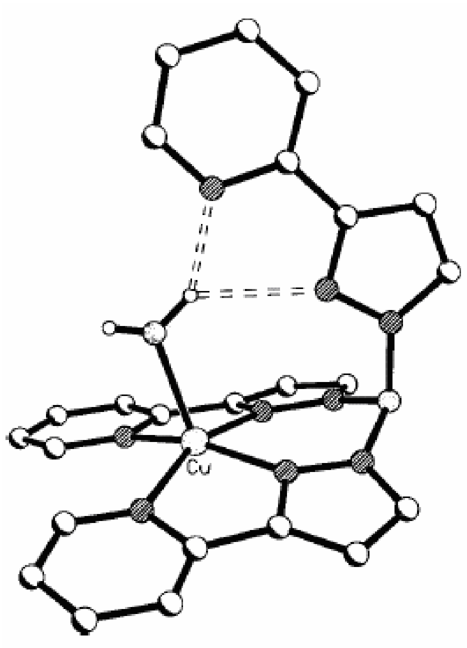

Fig. 1.1.23 – Crystal Structure of the cation of $[(Tp^{Py})Cu(H_2O)][PF_6]$

The use of additional donor 3R substituents has become increasingly popular over recent years and remains an important part of the future of poly(pyrazolyl)borates.

Mixed-donor species are now regularly synthesised, incorporating sulphur and oxygen atoms in addition to the pyrazolyl nitrogen donors. κ_6-coordination is not always observed however. Tp^{An} for example, where Tp^{An} is hydrotris[3-(2-methoxyphenyl)pyrazol-1-yl]borate, shows some unique trinucleating behaviour with Ag(I), but in none of the complexes with d-block metals do the methoxy groups participate in coordination (**Fig. 1.1.24**).[47] With the sulphur analogue, coordination is observed by two of the three sulphur atoms in a complex with Cu(II).[48]

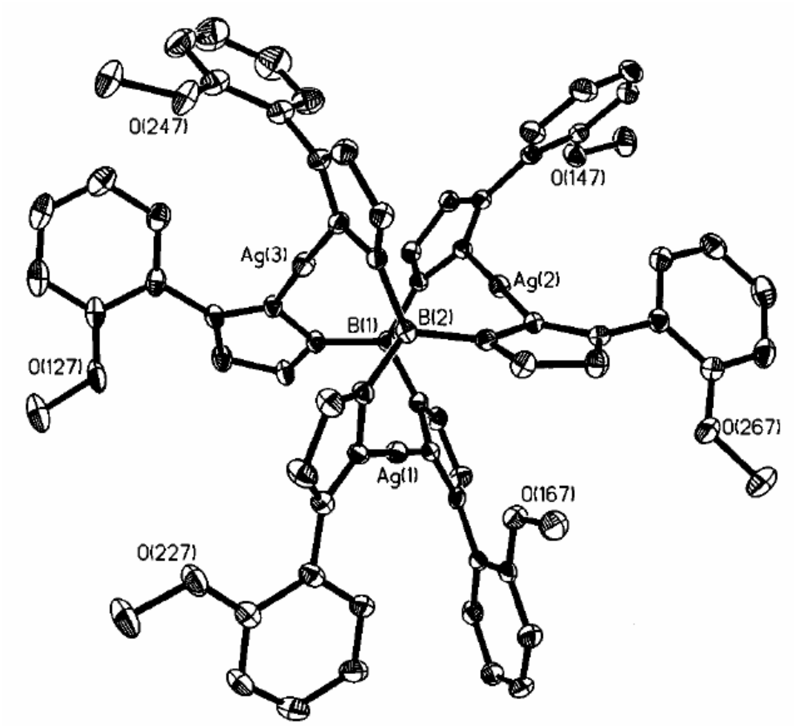

Fig. 1.1.24 – Crystal structure of the cation of $[(Tp^{An})_2Ag_3][ClO_4]$

Again, the coordination behaviour is clearly metal dependent, for the Tl(I) complex of hydrotris[3-(carboxypyrrolidido)pyrazol-1-yl]borate (Tp^{Cpd}) cannot show hexadentate coordination with a tetrahedral metal. However the same ligand readily fulfils its potential with samarium, forming a $[(Tp^{Cpd})_2Sm]^+$ species, albeit with one of the six arms pendant due to steric crowding (**Fig. 1.1.25**).[49]

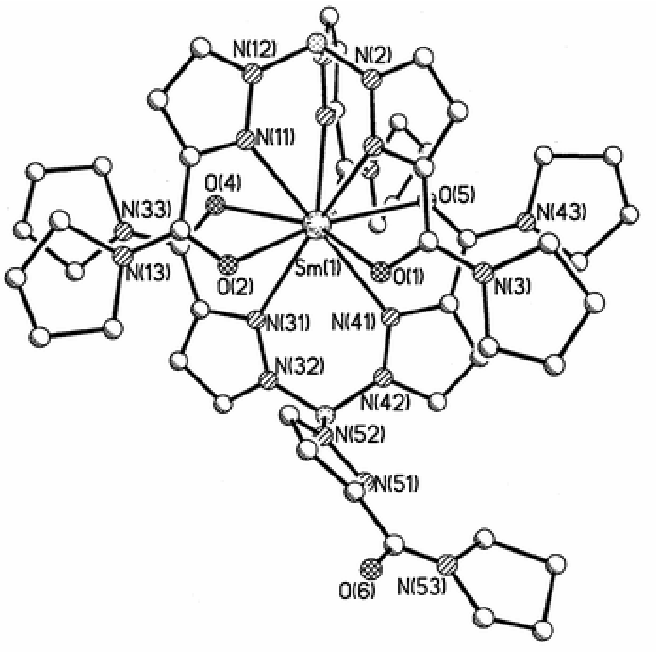

Fig. 1.1.25 – Crystal structure of the cation of $[(\mathrm{Tp}^{\mathrm{Cpd}})_2\mathrm{Sm}][\mathrm{PF}_6]$

A new approach to the incorporation of additional donor atoms into the Tp core is the inclusion of hydrogen bonding substituents. The ester groups employed in $\mathrm{Tp}^{\mathrm{CO_2Et,Me}}$, where the methyl 5R-substituents are present solely to protect the B-H bond, provide both steric bulk and hydrogen bonding groups which can be directed towards the central cavity.[50] On reaction with divalent metal ions, this leads to the stabilisation of discrete, well-defined metal-aquo complexes, with a counter anion in close proximity. Water molecules are held within the cavity between the pyrazolyl-ester arms, and share their hydrogen atoms between a mixture of carbonyl oxygens and nearby perchlorate ions (**Fig. 1.1.26**) (*cf* the behaviour of a pendant pyrazolyl-pyridine arm in **Fig. 1.1.23**).

The inclusion of water molecules in the cavity of second-generation Tp^{x} ligands is a common occurrence[43,48,51] and promotes these complexes as good examples of model compounds for the study of metalloenzymes and enzymes of the vicinal oxygen chelate (VOC) superfamily. This superfamily comprises structurally related proteins that provide a metal coordination environment with two or three open (vacant) or readily accessible coordination sites to promote direct electrophilic involvement of the metal ion in catalysis.[52]

Such coordination sites are not always vacant in aqueous media, often being occupied by metal-bound water molecules, although these are generally labile and can easily be displaced from the metal ion by incoming substrates.

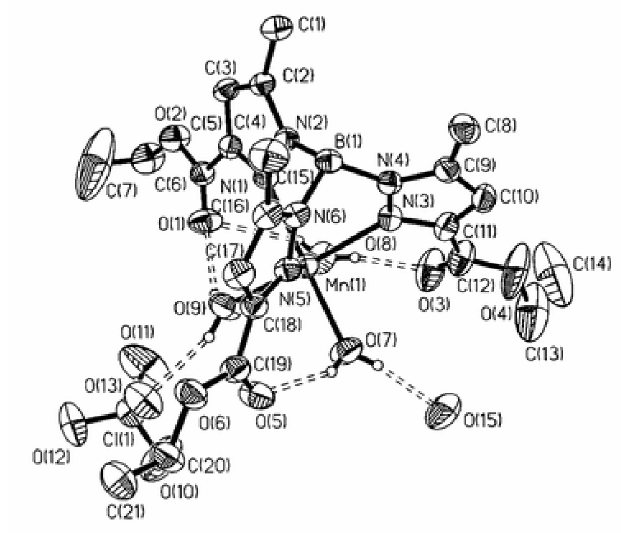

Fig. 1.1.26 – Crystal structure of $[(\mathrm{Tp}^{\mathrm{CO}_2^{\mathrm{Me,Me}}})\mathrm{M}(\mathrm{H_2O})_3][\mathrm{ClO_4}]$
(only one perchlorate ion is shown in full)

On the other hand, metal-bound water molecules are potential nucleophiles, but metal-bound hydroxides are much more powerful as such, and are generally thought to be the active species involved in hydrolytic metalloenzymes. In attempts[51] to convert the $[(\mathrm{Tp}^{\mathrm{CO_2Me,Me}})\mathrm{M}(\mathrm{H_2O})_x][\mathrm{ClO_4}]$ complexes to metal-hydroxo species by *in vivo* deprotonation, L_2M sandwich complexes were formed - although this result was metal ion dependent, with Ni(II), Co(II) and Mn(II) all forming the $[L_2M]$ dimer, whilst Zn(II) and Cu(II) forming a hydroxo-bridged $[LM(OH)]_2$ dimer.

1.1.7. Heteroscorpionates

In the absence of a pyrazole arm, the Tp^x ligands undoubtedly lose a degree of functionality. However, the resultant heteroscorpionate ligands Bp^x offer a greater versatility with the two substituents at the boron atom, in addition to the 3-, 4-, and 5-positions of the pyrazole rings.

There are three main sub-areas of heteroscorpionate ligands: $H_2B(pz)_2$, $HRB(pz)_2$, and $R_2B(pz)_2$, where R can either be an alkyl or aryl group which may, or may not, contain a heteroatom. This area of scorpionate chemistry has remained largely untapped since the first synthesis of KBp,[53] although the last few years have seen an increase in its exploration – made all the more popular with the introduction of the analogous poly(pyrazolyl)methane system,[54] in which the boron atom is replaced by a carbon, thus removing the ligand's negative charge. This section gives a comprehensive review of the recent advances in the heteroscorpionates, with a focus on those with heteroatom-containing 3R substituents.

1.1.7.1 $H_2B(pz)_2$

The earliest Bp^x systems were synthesised using identical conditions to their Tp^x counterparts, by adjusting the stoichiometry of the pyrazole and borohydride sources accordingly. Bp equivalents of most of the 3-substituted Tp^x systems discussed in **Sections 1.1.6.1** and **1.1.6.2**, have been synthesised with similar steric effects being observed (**Table 1.1.2**), but due to the lack of the ligands' functionalities, such studies have been largely restricted to structural investigations.

Heteroscorpionate	Reference
Bp	53
Bp*	13
$Bp^{i\text{-Pr}}$	6
Bp^{Me}	6
$Bp^{t\text{-Bu}}$	11
Bp^{Ph}	11
Bp^{Ph2}	55

Table 1.1.2 – Early Bp^x ligands

First-row transition metals readily form $[(Bp)_2M]$ complexes with Bp^x ligands, with both square planar (Cu^{2+}, Ni^{2+}) and tetrahedral (Co^{2+}, Zn^{2+}, Mn^{2+}, Fe^{2+}) geometries being observed,[6,13,53] whilst larger trivalent lanthanide ions form $[(Bp)_3Ln]$ complexes with the smaller 3R-substituted pyrazoles.[56]

An interesting observation is made in the complex of [$Bp^*Mo(CO)_2(C_3H_5)$] where Bp^* is hydrobis(3,5-dimethylpyrazol-1-yl)borate,[57] for whilst it initially appears to be a 16-electron complex, (Bp^*, 2CO, allyl, and Mo each contributing 4 electrons respectively using a 'charged ligand' count), an agostic B-H-Mo interaction is seen to occur (**Fig. 1.1.27**). This is quite favourable in complexes with a multiply hydrogen-substituted boron,[58] and this B-H-Mo bond can be considered a hydrogen-bridged 2-electron, 3-centre bonding arrangement, supplying two additional electrons to increase the count to an 18-electron configuration, accounting for the stability of this and analogous systems.[59] It is worth noting that this agostic interaction can only be achieved due to the geometry of the coordination 'boat' (**Fig. 1.1.7**).

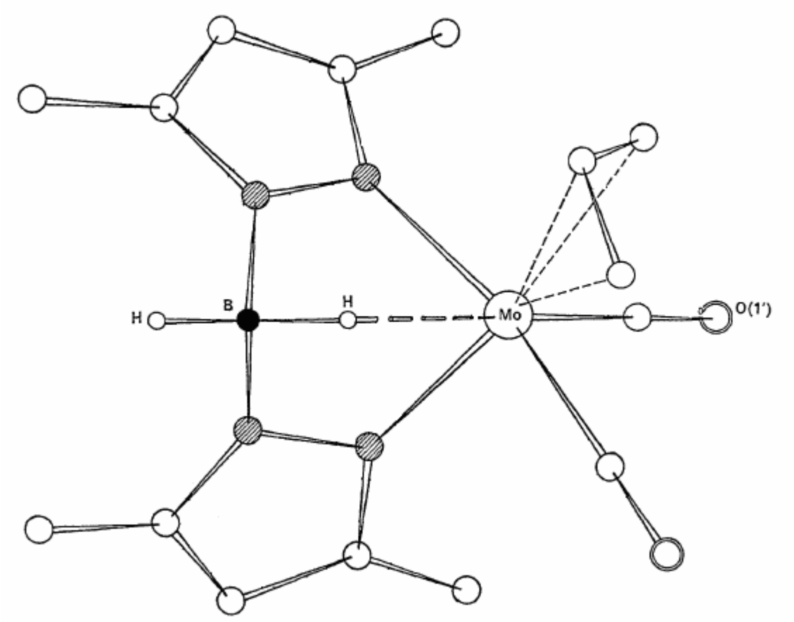

Fig. 1.1.27 – Crystal structure of [$Bp^*Mo(CO)_2(\eta^3$-allyl)]

Such interaction is not limited to 16-electron configurations; the complex of [$(Bp^{t\text{-}Bu,i\text{-}Pr})_2Co$], for example, contains two very short (1.95 Å) agostic B-H-Co bonds.[60] The geometry of the structure is initially viewed as square planar, however when the agostic bonds are considered, the geometry becomes octahedral (**Fig. 1.1.28a**). The same effect is observed in the complex of [$(Bp)_3Y$] which achieves 9-coordinate geometry through these bonds (**Fig. 1.1.28b**).[61]

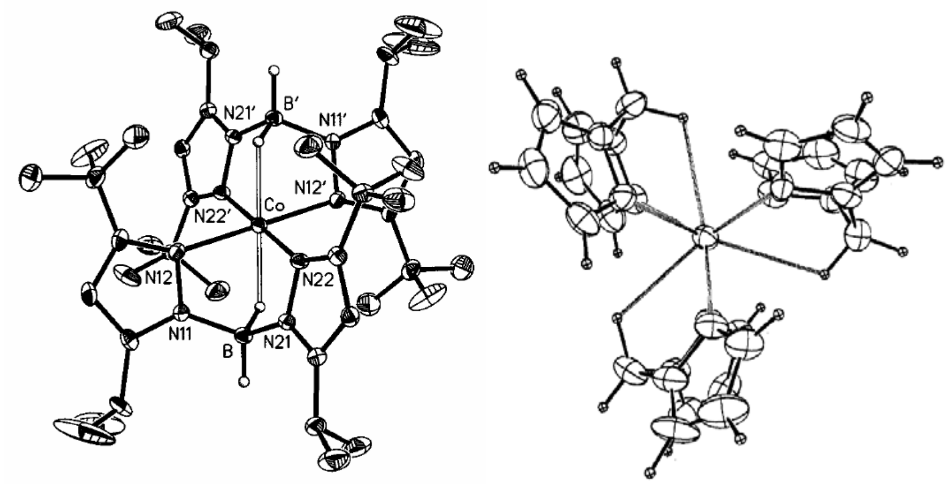

(a) **(b)**

Fig. 1.1.28 – (a) Crystal structure of $[(\mathrm{Bp}^{t\text{-Bu},i\text{-Pr}})_2\mathrm{Co}]$ and (b) Crystal structure of $[(\mathrm{Bp})_3\mathrm{Y}]$

The presence of the BH_2 group makes this type of ligand more hydrolytically labile than the Tp analogues, and consequently, complexes with easily reducible cations such as Pd(II) and Ag(I) are very unstable.[4] This reducing ability can however be harnessed, and some $[\mathrm{Bp}_2\mathrm{M}]$ complexes have been used as reducing agents of cyclohexanone and cyclohex-3-enone with moderate success[62]. The complexes of $[\mathrm{Bp}_2\mathrm{Fe}]$ and $[\mathrm{Bp}_2\mathrm{Mn}]$ were also noted as being air-sensitive,[53] yet this sensitivity was removed in the same complexes of Bp^*, presumably due to the screening effect of the 3-Me groups.[13]

The most impressive results with the Bp^x ligands come from the multidentate systems of $\mathrm{Bp}^{\mathrm{Py}}$ and dihydrobis[3-{6’-(2,2’-bipyridyl)}pyrazol-1-yl]borate ($\mathrm{Bp}^{\mathrm{Bipy}}$). The potentially tetradentate $\mathrm{Bp}^{\mathrm{Py}}$ shows a variety of coordination modes, varying from complete κ^4-coordination in $[(\mathrm{Bp}^{\mathrm{Py}})_2\mathrm{Pb}]$, to κ^2-coordination in $[(\mathrm{Bp}^{\mathrm{Py}})\mathrm{Tl}]$ (**Fig. 1.1.29**).[63]

Lanthanide complexes of the general formula $[(\mathrm{Bp}^{\mathrm{Py}})_2\mathrm{LnX}]$ were readily synthesised, including $[(\mathrm{Bp}^{\mathrm{Py}})_2\mathrm{Ln(NO_3)}]$ and $[(\mathrm{Bp}^{\mathrm{Py}})_2\mathrm{Ln(DMF)}]^+$,[64] and a unique example of anion-templated self-assembly was shown upon the reaction of $\mathrm{Bp}^{\mathrm{Py}}$ with Co^{2+} and sodium perchlorate (**Fig. 1.1.30**).[65]

The mass spectrum of this product mixture showed a fragment of formula $[Co_8(Bp^{Py})_{12}(ClO_4)]^{3+}$, which was confirmed by X-ray crystallography to be an M_8L_{12} wheel with a perchlorate anion residing in its centre.

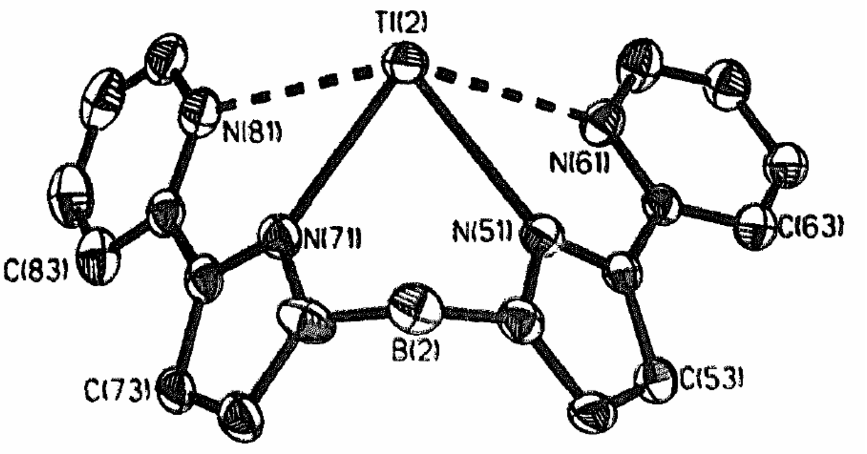

Fig. 1.1.29 – Crystal structure of $[Bp^{Py}Tl]$

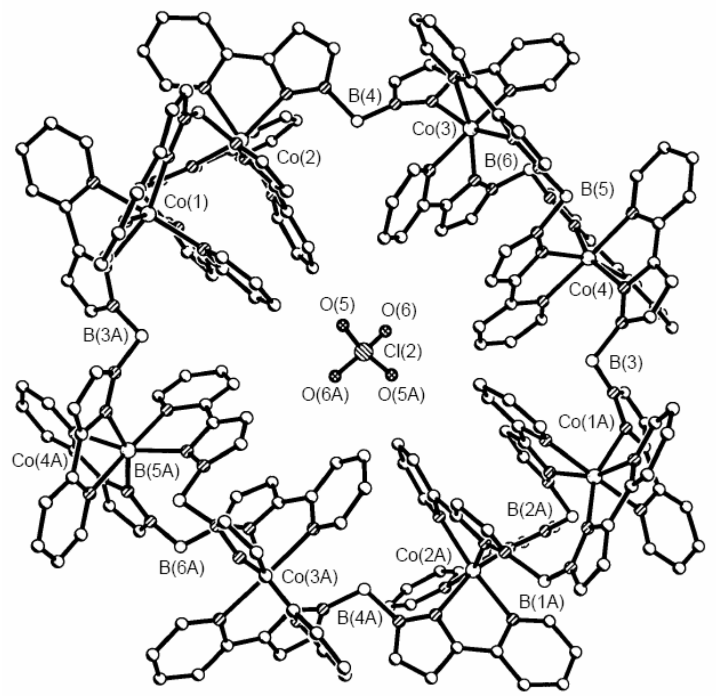

Fig. 1.1.30 – Crystal structure of the cation of $[Co_8(Bp^{Py})_{12}(ClO_4)][ClO_4]_3$

The hexadentate nature of Bp^{Bipy} was exploited in its coordination with potassium and first-row transition metals.[66,67] Its $[(Bp^{Bipy})_2M_2][BF_4]_2$ complexes showed an octahedral dinuclear array, held in place by two ligands in a rigid double-helical arrangement which also included aromatic stacking between the ligands (**Fig. 1.1.31**).

The lanthanide complex of $[(Bp^{Bipy})Gd(NO_3)_2]$ provides the only example of a monomeric complex with this ligand with Bp^{Bipy} acting as a near-planar hexadentate chelate; apart from $(Bp^{Bipy})Tl$ in which the ligand coordinated in κ^3-fashion.[67]

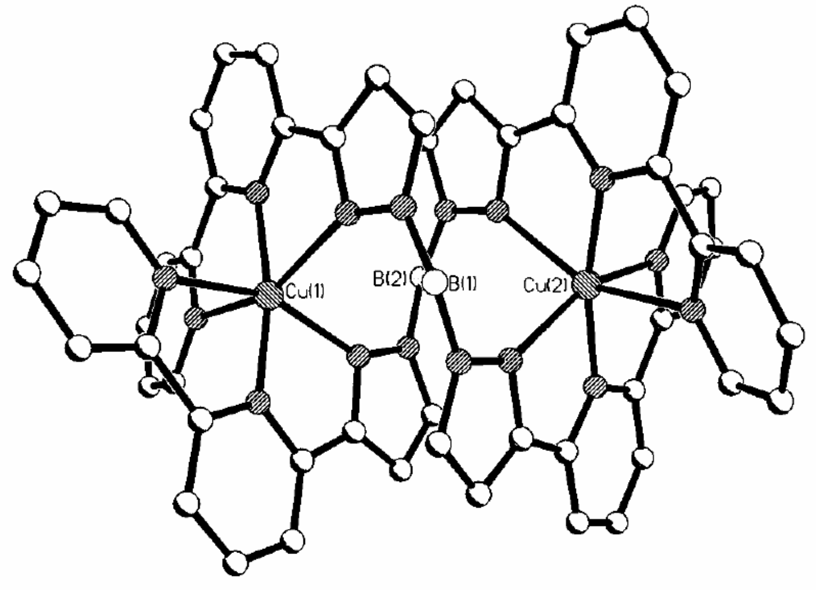

Fig 1.1.31 – Crystal structure of $[(Bp^{Bipy})_2Cu_2][BF_4]_2$

1.1.7.2 $R_2B(pz)_2$

Replacement of the hydrogen atoms of $H_2B(pz)_2$ with either alkyl or aryl groups, removes the reducing power that the BH_2 group possesses. Complexes can then be prepared with reduction-prone metals such as Pd^{2+} and Ag^+. Agostic B-C-H-M interaction is still possible, but these can easily be broken by the approach of external donors.[55]

Suitably sized R-groups can often block both the space above and below the plane of the molecule. This phenomenon explains the behaviour of $[Et_2Bp]_2Ni$, which forms no inner sphere coordination bonds with pyridine, ammonia or amines, in contrast to $[H_2Bp]_2Ni$.[13] An 18-electron configuration is correspondingly achieved in the complex of $[(Et_2Bp)Mo(CO)_2(C_7H_7)]$, but this time through a 2-electron, 3-centre C-H-Mo agostic interaction.[68]

Increasing the length of the R groups serves to heighten the lipophilicity of the scorpionate, drastically changing its physical properties; as is observed with Bu_2Bp, which has no structural characterisations because of the difficulty in obtaining crystalline complexes.[4] The rigidity of the substituents in (BBN)Bp, however, seems to prevent such a physical change, where it forms a rigid cage backbone on the boron atom (BBN = 9-Bora-bicyclo[3,3,1]nonane). This directs a single tertiary hydrogen atom towards the metal ion (**Fig 1.1.32**), which helps to stabilise octahedral $[\{(BBN)Bp\}_2M]$ complexes as well as that of [(BBN)BpTl].[69]

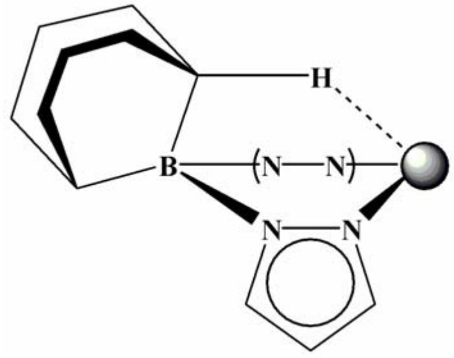

Fig 1.1.32 – Structural diagram of [(BBN)BpM]

Complexes of heteroscorpionates with planar substituents on the boron such as Ph_2Bp have shown great stability, but have never shown any C-H-M agostic interaction. The reason is the relationship between the phenyl rings: one bisects the angle between the pyrazolyl ring planes, whilst the other lies orthogonal to this angle, as in the complex of $[(Ph_2Bp)_2Ni]$ (**Fig 1.1.33**).[70] The absence of any 2-electron, 3-centred bonds also means that complexes such as $[(Ph_2Bp)Mo(CO)_2(\eta^3\text{-}CH_2CMeCH_2)]$ maintain a 16-electron configuration.[71]

It is also worth noting that whilst the complex [(H_2Bp)Ag] is air-sensitive, the analogue [(Ph_2Bp)Ag] is very stable,[72] suggesting that the stability of scorpionate complexes result from a combination of steric effects and not just solely from the 3R, 4R, and 5R substituents.

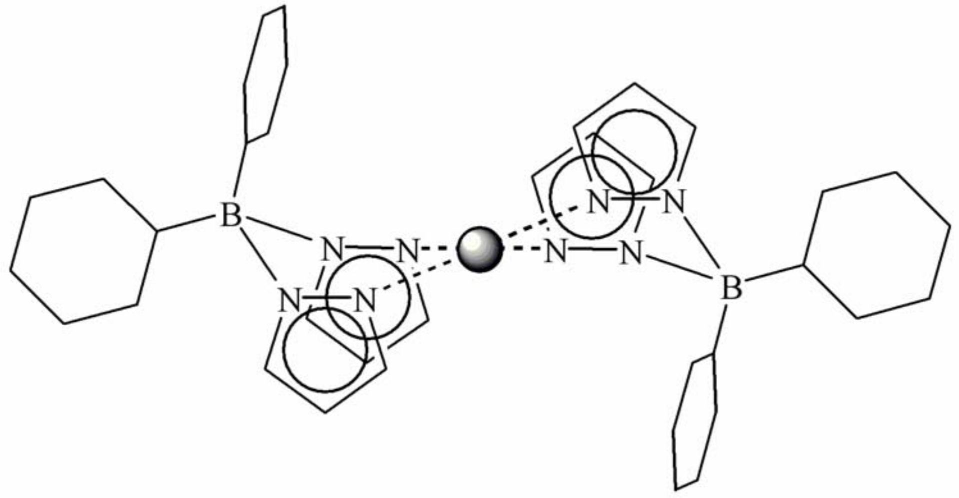

Fig 1.1.33 – Crystal structure of [Ph_2Bp]$_2$Ni

Substituting the boron atom with an alkyl group is also practiced in homoscorpionate chemistry, and an interesting result is observed in the analogue of PhTp$^{t\text{-Bu}}$ - its thallium(I) salt shows the loss of symmetrical tridentate coordination, and one pyrazolyl group rotates by *ca.* 90° to offer its N^1 for coordination to the thallium ion *via* the nitrogen *p*-orbital component of the pyrazole's aromatic π-system (**Fig. 1.1.34**). This is a consequence of the large metal ion widening the face of the cavity on coordination and pushing the pyrazole hydrogen(s) towards the phenyl ring, which subsequently forces the pyrazole to rotate. Needless to say, this behaviour is not observed with the much smaller lithium(I) ion.[73]

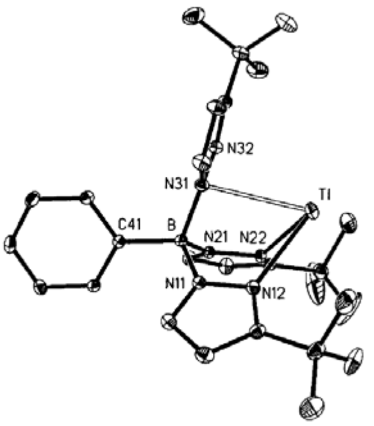

Fig. 1.1.34 – Crystal structure of [(PhTp$^{t\text{-Bu}}$)Tl]

1.1.7.3 R(Z)B(pz)$_2$

Recent activity in heteroscorpionate chemistry has seen the inclusion of a heteroatom (Z) in one of the non pyrazolyl-based boron substituents. This activity is more common in the poly(pyrazolyl)methane scorpionates due to the ease with which ligands can be synthesised, and has been employed in the replication of many enzyme systems.[74] Poly(pyrazolyl)borates, on the other hand, are limited to this application as synthesis needs to start from a boron source already substituted with the appropriate R group, and not a borohydride ion. One exceptional method, however, is the *in situ* reaction of protic reagents with the dihydrobis scorpionate.

Complexes of [(Bp$^{t\text{-Bu}}$)ZnR] and [(Bp$^{t\text{-Bu},i\text{-Pr}}$)ZnR] react with ketones to give functionalised products from insertion of the carbonyl group into the B-H bond, giving a synthetic route to N,N,O ligands (**Fig. 1.1.35**).[75] Carbon dioxide can also undergo insertion into a B-H bond in this manner.[76]

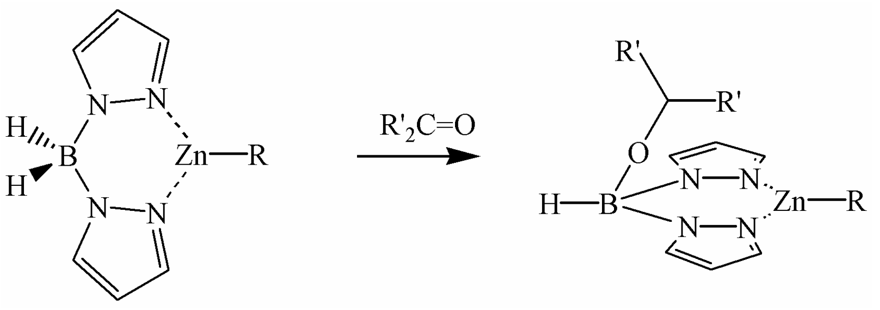

Fig. 1.1.35 – Ketone insertion in BH$_2$ groups

1.1.8 Scorpionates – a Summary

There are many avenues of research which have been explored with the poly(pyrazolyl)borates, and there are still many more to delve into. Whilst it appears the first-generation homoscorpionates are entering retirement, the second generation 'boom' is still very much alive, with the inclusion of additional donor atoms in the 3R substituents being a prime area of research.

The greater versatility offered by heteroscorpionates has seen their chemistry gradually gain interest over the past decade. This is very much a 'fresh' field of research in comparison to the Tp^x ligands and it remains likely that much interest will be focused on this family group, especially for the preparation of enzyme active site models.

In light of the inclusion of extra heteroatoms, for all members of the scorpionate family the most scope lies in attaching substituents that can be deprotonated to form complexes ranging from tridentate to hexadentate with charges of –1 to –4 such as that illustrated in **Fig. 1.1.36.** These ligands, with a higher negative charge and harder donor sets, should make for stronger coordination behaviour between metal ions and donor atoms, depending on the metal ion. Such studies are already underway, once again spearheaded by Trofimenko.[2]

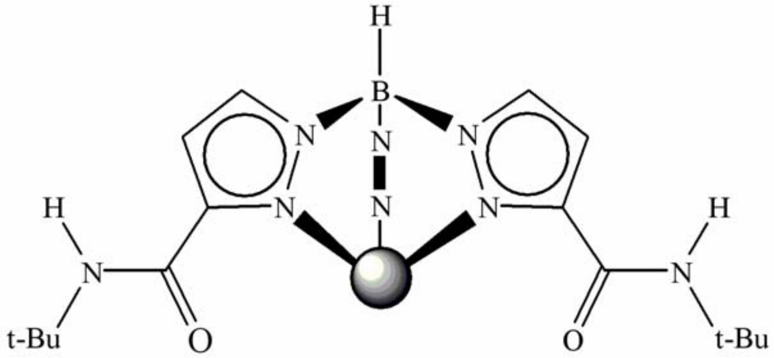

Fig 1.1.36 – [($Tp^{CONHt\text{-}Bu}$)M]

1.2 Lanthanides

1.2.1 Introduction

The term 'lanthanide' is associated with the top half of the elements located in the *f*-block of the periodic table, and encompasses those from lanthanum (La) to lutetium (Lu). Their history dates back to 1794 when a Finnish chemist, J. Gadolin, discovered that a sample of yttrium oxide was impure, and was found to additionally contain various oxides of what we now know as erbium and terbium.[77] The lanthanides all naturally occur as mixtures of oxides and all have the same silvery appearance (**Fig. 1.2.1**). Many more impure oxides were discovered over the years, and because of their similar chemical properties, it took over a century to isolate all of the individual lanthanides.

Fig. 1.2.1 – Erbium (the appearance is typical of the lanthanides)

Whilst the 'actinides' make up the bottom half of the *f*-block elements, with the two halves collectively known as the 'inner transition metals',[78] they bear no relevance to the works in this thesis, and will not be discussed further. Throughout this thesis, unless specified, the term Ln will be used to represent the lanthanides in general.

1.2.2 The Lanthanide Contraction

As we progress across the lanthanide series from lanthanum (Z = 57) to lutetium (Z = 71), gradually filling the nucleus with more protons and neutrons, additional electrons are placed in the 4*f* orbitals. The 4*f* orbitals are a seven-fold degenerate series, and there are two ways to represent them: the *cubic* set, and the *general* set.

The former is the more commonly used as it is readily related to tetrahedral, octahedral and cubic ligand fields, and shall be the preferred method of discussion in this work.

The cubic set comprises of f_{x3}, f_{y3}, f_{z3}, f_{xyz}, $f_{z(x2\text{-}y2)}$, $f_{y(x2\text{-}z2)}$, and $f_{x(y2\text{-}z2)}$ atomic orbitals and **Fig. 1.2.2** illustrates the shapes of the f_{z3} (**a**), f_{xyz} (**b**), and $f_{y(x2\text{-}y2)}$ (**c**) orbitals. A cube is superimposed in **b**, to depict how the lobes of these orbitals relate to a cubic set: the lobes of f_{xyz} point to the corners of the cube, whilst the lobes of f_{x3} and f_{y3} are like f_{z3} but point along their respective x- and y-axes. $f_{z(x2\text{-}y2)}$, $f_{y(x2\text{-}z2)}$, and $f_{x(y2\text{-}z2)}$ look like the f_{xyz} orbital, but are rotated by 45° about the z, y, and x axes respectively.

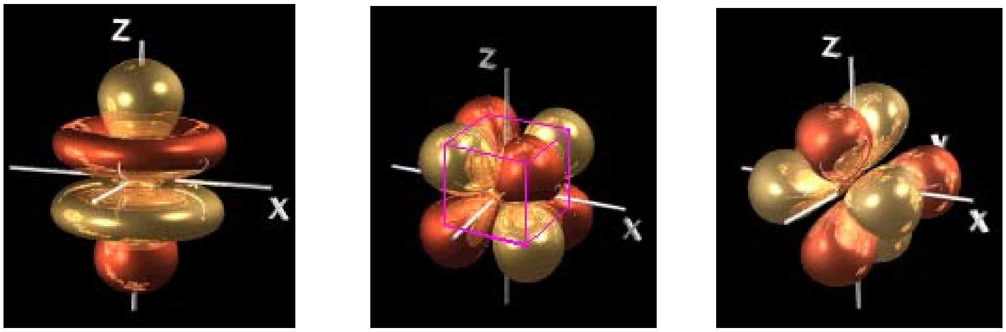

a **b** **c**

Fig. 1.2.2 – Graphical depiction of (a) f_{z3}; (b) f_{xyz}; (c) $f_{y(x2\text{-}y2)}$ orbitals.
Reproduced from the 'Sheffield University Orbitron' with permission from M. J. Winter.

By comparison to the 6*s* and 5*d* orbitals, the 4*f* orbitals are relatively small and are enveloped by the former two, becoming deeply buried within the atom and are therefore unperturbed by surrounding donor atoms (**Fig. 1.2.3**). Consequently, the 4*f* electrons are not available for covalent bonding, causing the coordination geometries of lanthanide complexes to be determined by steric effects of the ligands, rather than crystal field considerations. The 4*f* electrons are also relatively poor at screening the outermost electrons from the nucleus, for as we increase the atomic number of the lanthanides, the positive charge of the nucleus increases and whilst we continue to place electrons in an ineffective 4*f* orbital 'screen', the outermost electrons continually become attracted towards the nucleus. The net effect is a contraction in the radii of the lanthanides as we traverse across the series, more commonly known as the 'lanthanide contraction' (**Table 1.2.1**).

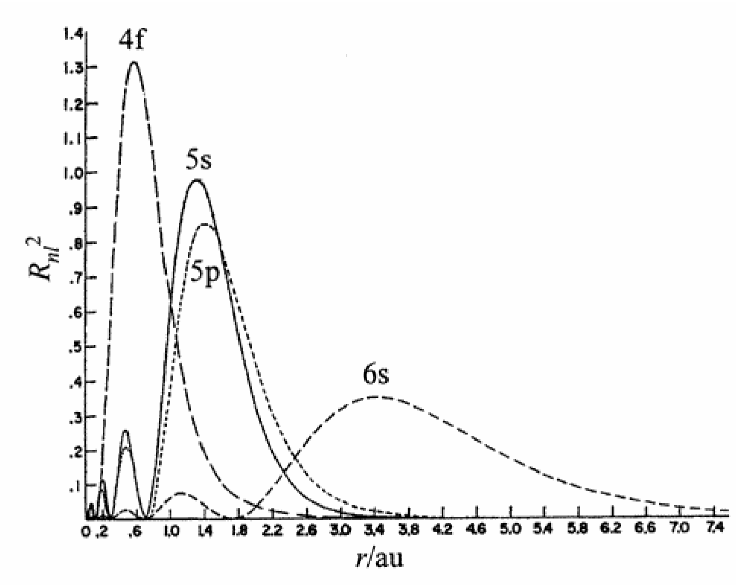

Fig. 1.2.3 - Radial probability functions for the 4*f*, 5*s*, 5*p* and 6*s* orbitals of Gd(I) Reproduced Ref.[79]

			Electronic Configuration[a]			
Atomic No.	Name	Symbol	Atom	Ln(III)	Radius[b] Ln(III) / Å	μ_{eff}[c]
57	Lanthanum	La	$5d^16s^2$	[Xe]	1.17	0
58	Cerium	Ce	$4f^15d^16s^2$	$4f^1$	1.15	2.56
59	Praseodymium	Pr	$4f^36s^2$	$4f^2$	1.13	3.62
60	Neodymium	Nd	$4f^46s^2$	$4f^3$	1.12	3.68
61	Promethium	Pm	$4f^56s^2$	$4f^4$	1.11	2.83
62	Samariam	Sm	$4f^66s^2$	$4f^5$	1.1	1.55 - 1.65
63	Europium	Eu	$4f^76s^2$	$4f^6$	1.09	3.4 - 3.5
64	Gadolinium	Gd	$4f^75d^16s^2$	$4f^7$	1.08	7.94
65	Terbium	Tb	$4f^96s^2$	$4f^8$	1.06	9.7
66	Dysprosium	Dy	$4f^{10}6s^2$	$4f^9$	1.05	10.6
67	Holmium	Ho	$4f^{11}6s^2$	$4f^{10}$	1.04	10.6
68	Erbium	Er	$4f^{12}6s^2$	$4f^{11}$	1.03	9.6
69	Thulium	Tm	$4f^{13}6s^2$	$4f^{12}$	1.02	7.6
70	Ytterbium	Yb	$4f^{14}6s^2$	$4f^{13}$	1.01	4.54
71	Lutetium	Lu	$4f^{14}5d^16s^2$	$4f^{14}$	1	0

Table 1.2.1 – Selected properties of the lanthanides and their ions.

[a]Only the valence shell electrons are stated - [b]values taken from Ref.[80]

[c]Magnetic moments determined by Van Vleck method - values taken from Ref. [81]

The effect is so pronounced, that the radius of Lu(III) (100.1 pm) is comparable to that of yttrium(III) (104 pm) despite their atomic numbers differing by over 50 %. This similarity in size causes these two ions to have similar properties, and yttrium is generally found to occur in Nature with the lanthanides. Collectively, yttrium and the lanthanides are referred to as the *rare earth metals*, despite La, Ce and Nd all being more abundant than lead.[82]

1.2.3 The State of Energy

The first three ionisation energies for the lanthanides are comparatively low, making the elements highly electropositive. However, the energy required to remove a fourth electron is much greater than the sum to remove the first three, and this extra energy, in the vast majority of cases, cannot be recovered by bond formation.[77]

Removal of valence electrons from a 6*s*, 5*d* or 4*f* orbital results in the stabilisation of that orbital, but the 4*f* orbitals are stabilised to a greater extent, meaning that once three electrons have been removed, the 6*s* and 5*d* orbitals are both empty. The next removable electrons are held so close to the nucleus that they may almost be deemed chemically inaccessible. Consequently, the chemistry of the lanthanides is largely restricted to the Ln^{3+} ions.

1.2.3.1 Energy Levels and Magnetic Properties

Each individual electron is characterised by its own unique set of four quantum numbers: principal quantum number n, angular momentum l, the spin quantum number s, and the magnetic quantum number m. However, when an electron is not 'free', but is deemed to be part of an atom, the angular momentum associated with its *spin*, couples with the angular momentum generated by its *orbital* motion. This '*spin-orbit*' coupling is a naturally occurring phenomenon in orbitals, and increases along the series $f > d > p$ for a given primary quantum shell. The states produced by the coupling of the electrons' momenta can be classified by the Russell-Saunders[83] scheme.

The scheme considers that the angular momentum of all the individual electrons' spins (m_s) all couple together to give a *total spin angular momentum* (denoted by the quantum number, S). Likewise, their individual orbital angular momenta (m_l) all couple to generate a *total orbital angular momentum* (denoted by the quantum number, L). Both of these values are found by the addition of the individual momenta vectors. The overall *total angular momentum* (J) resulting from the spin-orbit coupling, is found by vectorial addition of both S and L, so that $J = S + L$.

L	0	1	2	3	4	5	6	7
State Symbol	*S*	*P*	*D*	*F*	*G*	*H*	*I*	*K*

Table 1.2.2 – State symbols of total orbital angular momentum, L

The various atomic and ionic *energy levels* available to an electron can be represented by a 'term symbol': $^{(2S+1)}L_J$ where ($2S$+1) is the *spin multiplicity* of the term, and the value of L is determined from the series in **Table 1.2.2** (note that the spin multiplicity term, S, is not to be confused with the state symbol for L = 0). The various *levels* of the term are denoted by J, which may take on any value between [L + S], [L + S - 1], [L + S - 2] … [L - S].

The most important level is the *ground term,* which is the lowest energy term (i.e. where an electron would most like to be). As there are many possible terms arising from the different combinations of L and S, Hund's[84] rules are employed to govern which one is the ground term:

- ☐ The value of ($2S$+1) must be the highest value possible.
- ☐ If there is more than one term with the same value of ($2S$+1), that with the highest value of L is the ground state.
- ☐ For a shell less than half full, J is as low as possible; for a shell more than half full, J is a high as possible.

Nd^{3+} illustrates an example: The electronic configuration of this ion is f^3 and its three unpaired electrons offer a total spin angular momenta of $^3/_2$. Therefore, S = $^3/_2$, and the spin multiplicity of the term will be 4.

For an *f* electron $l = 3$, which implies that m_l can be an integral value between +3 and -3, and so filling the *f* orbitals according to the Aufbau principle gives a total orbital angular momenta of (3 + 2 + 1), which means $L = 6$ which has the symbol *I*. *J* can therefore have any of the values of (6 + $^3/_2$), (6 + $^3/_2$ - 1) … (6 - $^3/_2$), which is $^{15}/_2$, $^{13}/_2$, $^{11}/_2$ or $^9/_2$. This gives us four different term symbols to work with, and using Hund's rules, we can deduce that, as the shell is less than half full, the term symbol for the ground state is $^4I_{9/2}$.

Fig. 1.2.4 shows the energy level schemes for all the Ln^{3+} ions. The magnitude of the separation between adjacent states of a term is an indication of the strength of the spin-orbit coupling and as there is a consistently large spin-orbit coupling observed across the Ln^{3+} series, from the lack of interaction between *f* electrons and ligands, the effective magnetic moment (μ_{eff}) of these elements depends on both L and S and not just S (as is the case with first row transition metals). Magnetic moments of all lanthanide(III) ions are calculated employing the ground states of the ions in **Eq. 1.1** and agree well with those determined from experiment (**Table 1.2.1**), with the exception of Eu^{3+} and Sm^{3+} which see small population of low lying excited states at room temperature.[85] Upon consideration of these, a better correlation is observed.

$$\mu_{eff} = g\ \{J(J+1)\}^{1/2}\ \text{BM} \qquad \textbf{Eq. 1.1}$$

$$\text{where } g = \frac{S(S+1) + 3J(J+1) - L(L+1)}{2J(J+1)} \qquad \textbf{Eq. 1.2}$$

1.2.4 Spectroscopic Properties

Electronic transitions in Ln^{3+} ions involve the redistribution of electrons between the ground state and the various excited states of the *f* orbitals. All these states are housed within the same orbitals, and therefore have the same parity (symmetry properties about an inversion centre), and as such transitions between these states are not permitted to occur in accordance with the electric dipole 'Laporte' selection rules.[86]

However, due to molecular vibration, the *f* orbitals can undergo a temporary change of symmetry. During this new (transient) geometry, one or more of the *f* orbitals temporarily has the same symmetry as a *d* orbital, which relaxes the selection rule to permit transition, because a 'forbidden' *f-f* transition now has some 'allowed' *f-d* character. In order for this molecular vibration to occur however, significant interaction between the orbitals and the surrounding environment must take place, and as the 4*f* orbitals are very much contracted this 'vibronic coupling' is much weaker in Ln^{3+} systems than in the *d* orbitals of transition metal complexes, and so are the corresponding electronic transitions that we observe.

As the *f* orbitals are well shielded and unperturbed by surrounding ligands, their absorption spectra are always characteristically clear, sharp and well-defined regardless of the lanthanide's environment. This means that crystal field effects are almost non-existent in lanthanide compounds compared to spin-orbit coupling effects and typical field splittings reach $\approx$ 100 cm^{-1}, whereas the opposite is true with transition metals, where crystal field splittings can reach tens of thousands cm^{-1}.

In addition to *f-f* transitions, many of the lanthanide(III) ions give rise to the *f-d* transitions of $[Xe]4f^{n} \rightarrow [Xe]4f^{n-1}5d^{1}$, which are formally permitted by Laporte rules, and normally found in the UV region. Ln^{3+} ions vary in their absorption strengths across the spectral regions (UV, visible, IR), giving rise to their characteristic colours, whilst certain ones, such as Eu^{3+}, have no strong absorption in the visible region, and thus appear colourless. **Table 1.2.3** shows some of the spectroscopic properties of the Ln^{3+} ions as hydrated salts.

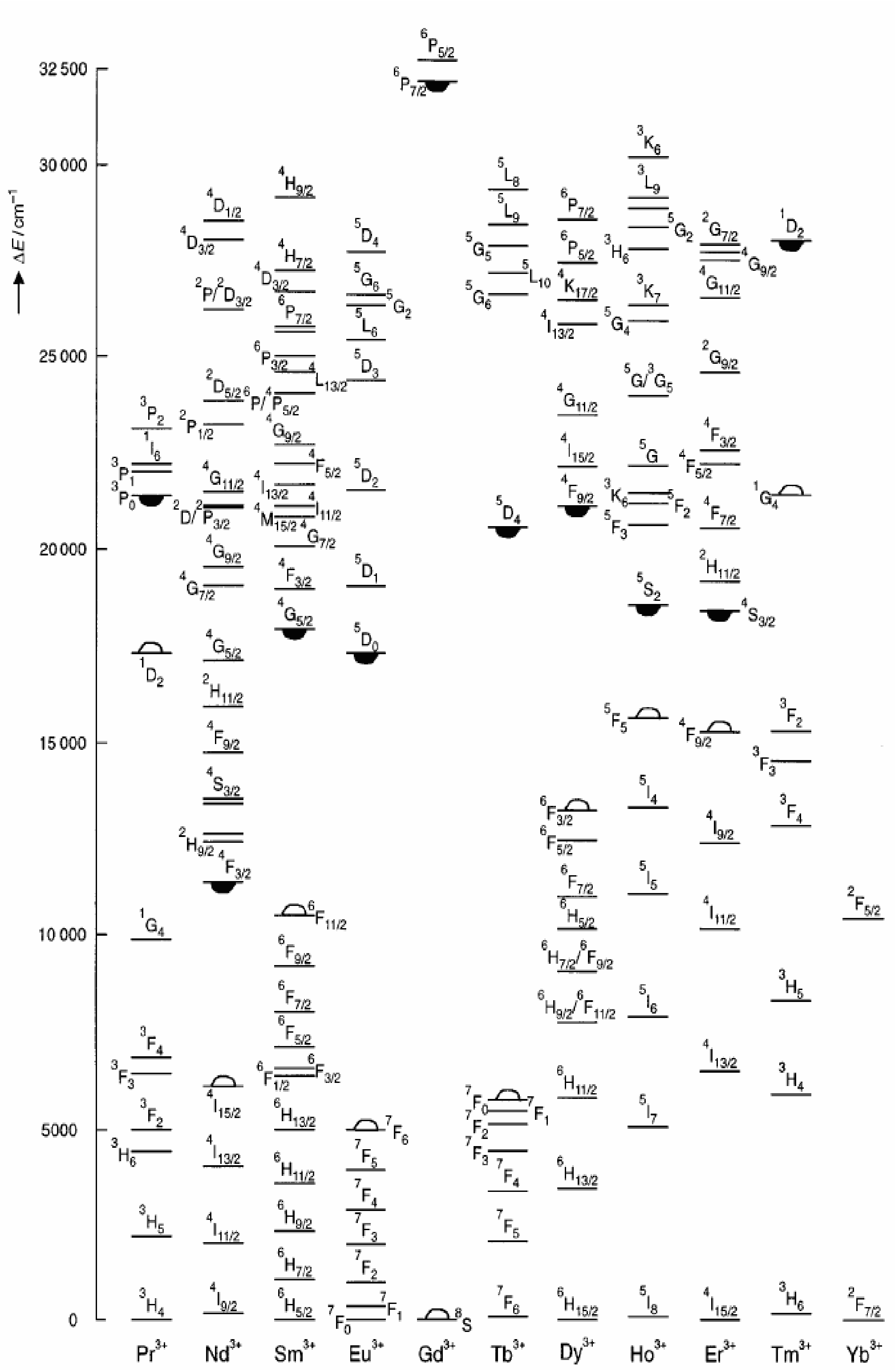

Fig. 1.2.4 – Energy levels for lanthanide(III) ions. The black and white semi-circles represent the lowest fluorescent and highest non-fluorescent levels respectively. Reproduced from Ref .[87]

Ln^{3+}	No. of Unpaired Electrons	Ground State Term Symbol	Colour
La	0	$^{1}S_{0}$	Colourless
Ce	1	$^{2}F_{5/2}$	Colourless
Pr	2	$^{3}H_{4}$	Green
Nd	3	$^{4}I_{9/2}$	Lilac
Pm	4	$^{5}I_{4}$	Pink
Sm	5	$^{6}H_{5/2}$	Yellow
Eu	6	$^{7}F_{0}$	Colourless
Gd	7	$^{8}S_{7/2}$	Colourless
Tb	6	$^{7}F_{6}$	Pale Pink
Dy	5	$^{6}H_{15/2}$	Yellow
Ho	4	$^{5}I_{8}$	Yellow
Er	3	$^{4}I_{15/2}$	Rose Pink
Tm	2	$^{3}H_{6}$	Pale Green
Yb	1	$^{2}F_{7/2}$	Colourless
Lu	0	$^{1}S_{0}$	Colourless

Table 1.2.3 – Selected Spectroscopic Properties of Ln^{3+} ions

1.2.4.1 Lanthanide Luminescence

The term 'luminescence' is used to describe the emission of electromagnetic radiation of a compound, after it has been electronically excited. Emissions usually occurs in the infrared (IR), visible and ultraviolet (UV) regions of the electromagnetic spectrum. Excited states of the lanthanides can be quite high relative to the ground state and population is readily achievable by inter-system crossing (ISC) from the excited state(s) of organic ligands (chromophores) bearing fully allowed $\pi \rightarrow \pi^*$ transitions.[88,89] This process is known as *sensitisation* or the '*antenna effect*' and gets round the problem of the low extinction coefficients of *f-f* transitions which make direct excitation so inefficient. **Fig 1.2.5** illustrates typical lanthanide luminescence *via* this method.

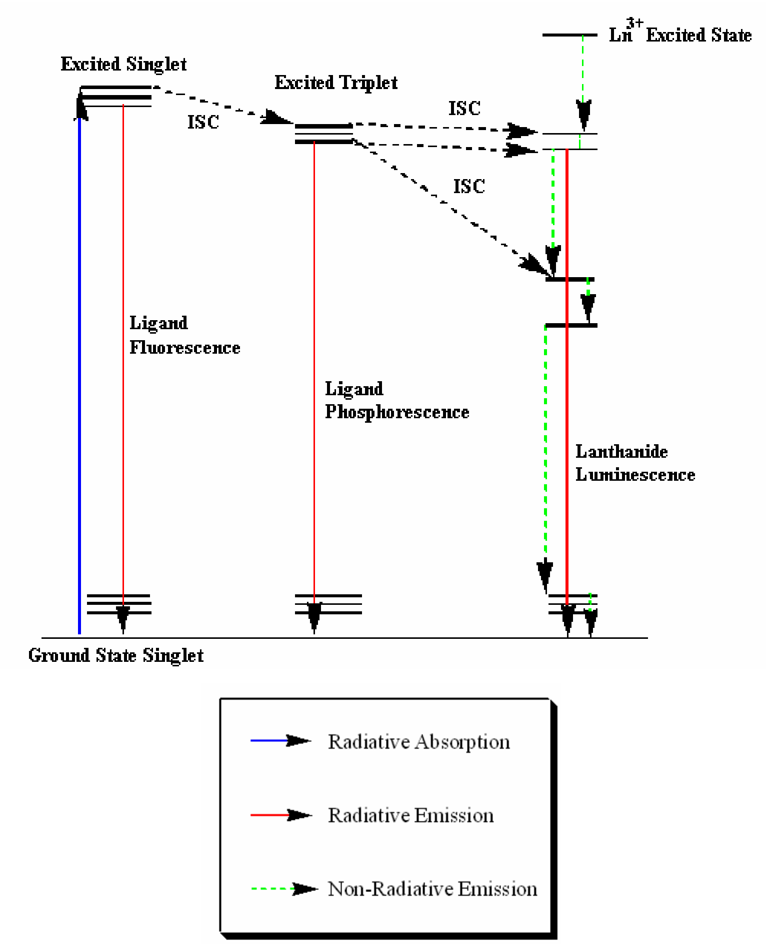

Fig. 1.2.5 – Jablonski diagram for lanthanide(III) luminescence *via* sensitisation with a chromophore.

The electron promoted in the excited ligand singlet state may either return directly to the ground state (ligand fluorescence) or follow a non-radiative path to a ligand triplet state (ISC). From here, the electron can again return to the ground state (ligand phosphorescence), or perform a second successive non-radiative inter-system crossing to populate a nearby excited-state of the Ln^{3+} ion. At this point, the overall energy drop has been too much for the electron to return to the ligand states, and it is now destined to return to the ground state; either by non-radiative emission down a series of successive energy levels, or straight to the ground state causing Ln^{3+} luminescence if the gap is large enough.

Both of these pathways occur to different degrees depending on the metal ion and the majority of Ln(III) ions have excited states that lie lower in energy than the triplet excited states of typical chromophores, giving rise to efficient energy transfer.

Some ions (Eu^{3+}, Tb^{3+}, Yb^{3+} and Dy^{3+}) have few energy levels between their excited states and ground states, resulting in strong metal-ion based luminescence. Others such as La^{3+} (f^0) and Lu^{3+} (f^{14}) have effectively 'filled' *f* orbitals, and so no fluorescence is observed in the visible or IR regions. The rest of the Ln^{3+} ions have a large number of excited levels between their excited states and the ground state, subsequently promoting energy loss *via* the non-radiative path, giving rise to weak luminescence. A special case is observed in Gd^{3+} (f^7), which has its lowest luminescent state located *above* typical ligand triplet states (approx. 32,000 cm^{-1} in the UV region, **Fig. 1.2.3**), making metal-ion luminescence a rarer occurrence.

1.2.4.2 Quenching

Coordinated water molecules and alcohol ligands provide a facile pathway for Ln^{3+} ions to deactivate as the electronic excitation energy of the lanthanide can be effectively transferred to these O-H oscillations.[90] Prior to energy absorption, the OH-bearing molecule is in its lowest vibrational state ($v'' = 0$), and afterwards, is promoted to a higher state (v'). According to the Frank-Condon principle,[91] such a transition occurs without a change in the nuclear framework, and so we can depict the transition as a simple vertical line between two potential energy curves (**Fig. 1.2.6**). There is not just one vibrational state the molecule can reach, but several, and which one is reached depends on how much energy is absorbed in the transition. As the vibrational levels increase ($v' = 1, 2, 3, 4\ldots$), the degree of overlap between these levels and the ground vibrational state ($v = 0$) lessens, and so does the probability of promoting the molecule to that vibrational level.

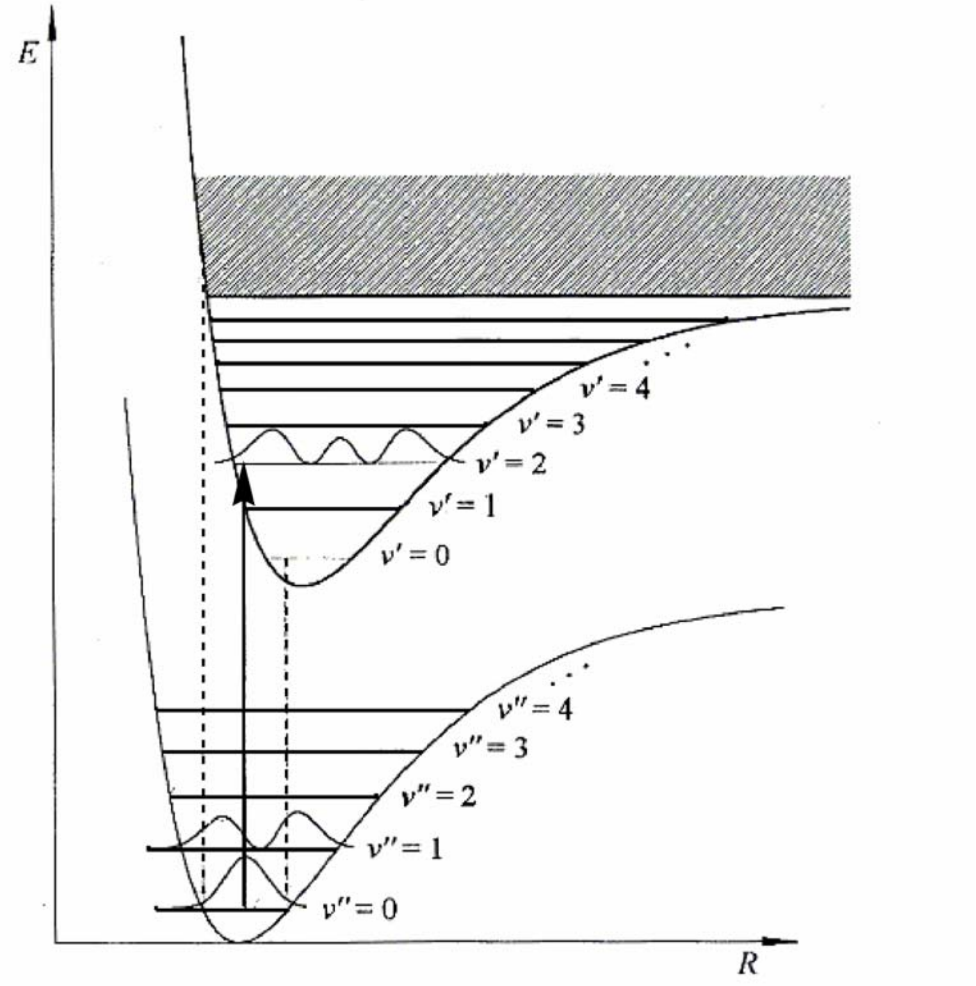

Fig. 1.2.6 –Quantum mechanical version of the Frank-Condon principle
(*R* = internuclear separation, *E* = energy)

The energies of some of the O-H overtones are comparable with the excited-state energy levels of many Ln^{3+} ions, and in such systems a vibronic coupling occurs between the two sets of levels. The presence of these additional OH energy levels between the excited state and ground state of the metal ion makes the non-radiative pathway much more favourable to an excited electron than the direct return to the ground state, thus quenching the lanthanide luminescence.

This effect of luminescence quenching is very pronounced and is more so for O-H groups directly coordinated to the metal ion, than for those from surrounding solvents in the second coordination sphere, although this depends on the coordination environment, the distance, and how many solvent molecules have access to the metal centre.

This pattern is general in all lanthanide ions, and luminescence lifetimes of complexes in the solid state are typically longer,[90] as are lifetimes obtained in dry solvents devoid of O-H oscillators. All O-H oscillators act independently towards this de-excitation, and the rate of quenching is directly proportional to the number of oscillators in the first coordination sphere only.[92] Those in more remote spheres have a much weaker contribution and are often ignored to a first approximation.

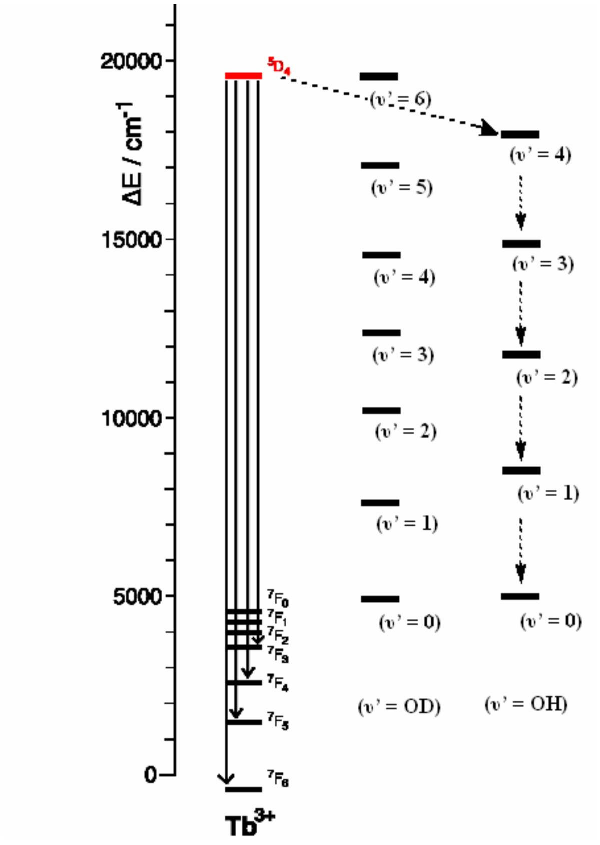

Fig. 1.2.7 – Vibronic coupling between electronic energy levels of Tb(III) and vibrational levels of O-H and O-D oscillations

If the quenching molecule consists of heavier atoms, the energy gaps between the vibrational levels decrease. As shown in **Fig. 1.2.7**, the energy of the $(\nu_{OH} = 4)$ vibrational level of O-H (approx. 19,000 cm^{-1}) is just below the $^5D_4$ energy level of Tb^{3+} (approx. 20,000 cm^{-1}), and this comparability in energy favours ISC by the excited electron to the $(\nu_{OH} = 4)$ level, reducing the fluorescence to the $^7F_5$ level of the lanthanide.

By contrast, a similar degree of vibration with O-D is reached at its sixth vibrational level ($v_{OD} = 6$). However, this higher vibrational level has a much smaller overlap with the ($v_{OD} = 0$) level, making it less likely to be populated in D_2O solutions.[93] Consequently, when OH is replaced with OD-based solvents, the $^5D_4 \rightarrow {}^7F_5$ fluorescence remains strongly observed, with a drastic reduction in energy transfer to the solvent vibrations. Luminescence lifetimes of Ln(III) ions in solution are always optimised by use of deuterated solvents.[94]

Following excitation, the decrease of luminescence usually follows an exponential path. The corresponding experimental reciprocal excited-state lifetime is also the exponential rate constant (τ^{-1}_{obs}) and consists of several terms (**Eq. 1.3**)

$$\tau^{-1}_{obs} = (\tau^{-1}_{nat}) + (\tau^{-1}_{nr}) + (\tau^{-1}_{OH}) \qquad \textbf{Eq. 1.3}$$

Where (τ^{-1}_{nat}) is the natural rate constant for the emission of photons; (τ^{-1}_{nr}) is the rate constant for non-radiative de-excitation which does not involve O-H oscillators; and (τ^{-1}_{OH}) is the rate constant for non-radiative energy transfer resulting from vibronic coupling with O-H oscillators in the first coordination sphere.

τ^{-1}_{OH} is always quite significant. For example, for Eu^{3+}(aq) ion, (τ^{-1}_{nat}) is 0.19, (τ^{-1}_{nr}) is 0.25, and (τ^{-1}_{OH}) is 9.5 ms^{-1}.[90] This quenching efficiency increases as the gap between the excited state and the highest component of the ground state of the metal-ion decreases (**Fig. 1.2.4**). The difference in this gap for Tb^{3+} is 14,800 cm^{-1} and 12,200 cm^{-1} for Eu^{3+}, and explains why the value of (τ^{-1}_{OH}) is less for Tb^{3+} (2.15 ms^{-1}).

1.2.4.3 Working out the Waters

It is possible to deduce the number of O-H oscillators in the first coordination sphere of an Ln^{3+} complex, by measuring the independent luminescence lifetimes in both H_2O and D_2O solutions. The rate constant for the de-excitation in H_2O is:

$$K_{H2O} = K_{nat} + \Sigma K_{nr} + K_{OH} \qquad \textbf{Eq. 1.4}$$

Where K_{H2O} is the observed decay rate in H_2O, K_{nat} is the natural radiative rate constant, ΣK_{nr} is the sum of the rate constants for all other non-radiative de-excitation processes, and K_{OH} is the rate constant for non-radiative de-excitation by O-H oscillations.

In D_2O, the K_{OH} term disappears to give:

$$K_{D2O} = K_{nat} + \Sigma K_{nr} \qquad \textbf{Eq. 1.5}$$

Where ΣK_{nr} also includes any de-excitation by O-D oscillators. The difference between the two rate constants in H_2O and D_2O, is K_{OH}.

$$K_{H2O} - K_{D2O} = K_{OH} \qquad \textbf{Eq. 1.6}$$

The values of K_{H2O} and K_{D2O} are equal to the respective values of ($\tau^{-1}{}_{H2O}$) and ($\tau^{-1}{}_{D2O}$) – i.e. the rate constant for depopulation of the excited state. These can then be used in **Eq. 1.7** (Horrocks equation) to determine how many water molecules (*q*) are coordinated to the lanthanide ion.

$$q = \mathrm{A}\ [K_{OH}] \qquad \textbf{Eq. 1.7}$$

Where A is a proportionality constant for a given Ln^{3+} ion, determined by comparisons of calculated values in the solid state, and actual values determined by crystal structures. The estimated uncertainty in *q* is typically ± 0.5.[92] N-H, C-H, and C=O oscillators also have a quenching effect on the luminescence, but not to the extent of O-H harmonics.[95]

1.2.5 Applications of Lanthanides

1.2.5.1 Magnetic Resonance Imaging (MRI)

MRI is one of the most important tools in diagnostic medicine because of its non-invasive nature, and has featured in the assessment of abnormalities in the blood-brain barrier, kidney clearance and tumour targeting.[96] The technique makes use of ^{1}H NMR imaging in the detection of the protons of water molecules.

The water content of human tissue does not vary much through our bodies: we consist of at least 60 % water in which approximately 57 % is intra cellular and 43 % is extra cellular, and so tissue differentiation is not permitted on this value. A two-dimensional image can be obtained however, by spatially encoding the protons in the water molecules that reside about a specific tissue. This is achieved by placing the subject in a magnetic field gradient to induce resonance amongst all the protons, whose frequency depends on their spatial location.

The protons resonate and return to their equilibrium along the Z-axis with time T_1 (the longitudinal relaxation time) and along an orthogonal axis with time T_2 (the transverse relaxation time), both of which differ between tissue types.[97] Tissues in which the protons have a short relaxation time will generally show up as clearer images, and it is beneficial to try to enhance the image contrast in order to distinguish between healthy and diseased tissues (**Fig. 1.2.8**).[98]

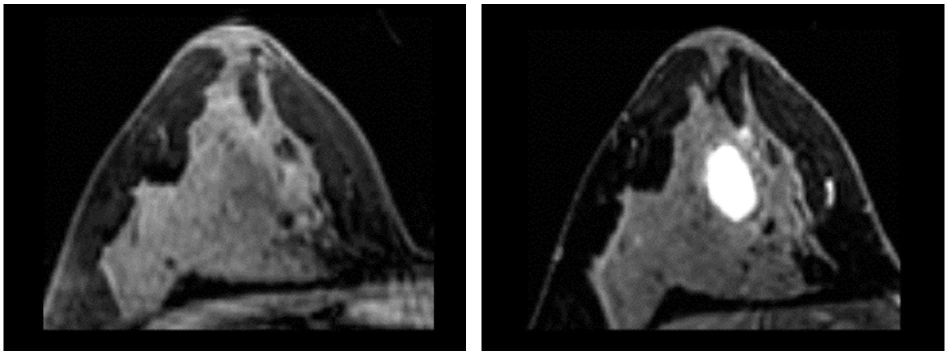

Fig. 1.2.8 – MRI of breast before (a) and after (b) injection of $[Gd(DPTA)]^{2-}$
The second image clearly shows a fiboadenoma not detected with mammography.[99]

The relaxation times of water protons decrease substantially when the molecule is in close proximity to a highly paramagnetic complex – a process known as ‘relaxivity’, and the Gd^{3+} ion is a prime candidate for an MRI contrast agent, possessing seven unpaired electrons, a large magnetic moment and a long electron spin relaxation time ($10^{-9.5}$ s). The relaxation time of water protons decreases by a factor of 10^{6} when coordinated to a Gd^{3+} ion[100] which would lead to a huge enhancement in the intensity of the image associated with the molecules. However the free Gd^{3+} ion itself is toxic, and so must be held in a suitable complex that is kinetically stable and unlikely to dissociate during its time in the body.[101] Such complexes should also be carefully designed so that they successfully hold the metal ion, whilst allowing one or two water molecules to enter the first coordination sphere in order to provide the necessary relaxivity. One commonly used complex is gadolinium-tetraazacyclododecanetetraacetic acid [Gd(DOTA)$^{-}$] (**Fig. 1.2.9**).

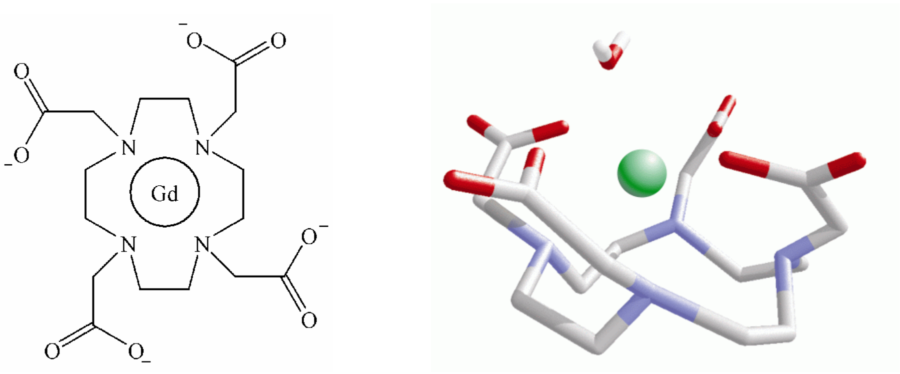

Fig. 1.2.9 – (a) Schematic diagram of Gd(DOTA)$^{-}$

(b) Crystal structure showing the Gd^{3+} held by the carboxylic acid groups with one water molecule coordinated on the exposed face of the metal ion

1.2.5.2 Lanthanide Shift Reagents (LSRs)

Ln^{3+} ions are Lewis acids, and as such are very susceptible to association with Lewis bases. Lanthanide tris(β-diketonates) are a good example of this, readily forming labile adducts of the form [Ln(diket)$_3$L] with bases such as alcohols.[85]

Upon formation of these adducts, a pseudocontact occurs between the coordinated base (L) and the lanthanide ion, and because of the high paramagnetism of the metal ion, this induces a dipolar shift in the protons of the bound Lewis base, with the greatest shifts occurring on those closest to the lanthanide ion.[102] This results in the spreading out and 'simplification' of NMR spectra that is otherwise complicated by overlapping resonance signals.

LSRs are also used to shift the resonances of other nuclei. In high resolution NMR spectra, resonance signals of $^{7}Li^{+}$, $^{23}Na^{+}$ and $^{39}K^{+}$ ions are shifted by paramagnetic complexes such as thulium(III) and dysprosium(III) salts of 1,4,7,10-tetraazacyclododecane-1,4,7,10-tetrakis(methylene phosphonate) $(DOTP)^{8-}$ (**Fig. 1.2.10**)[103,104] These alkali metal ions are also readily found in cellular compartments and living tissue, maintaining trans-membrane electrical potentials.[85]

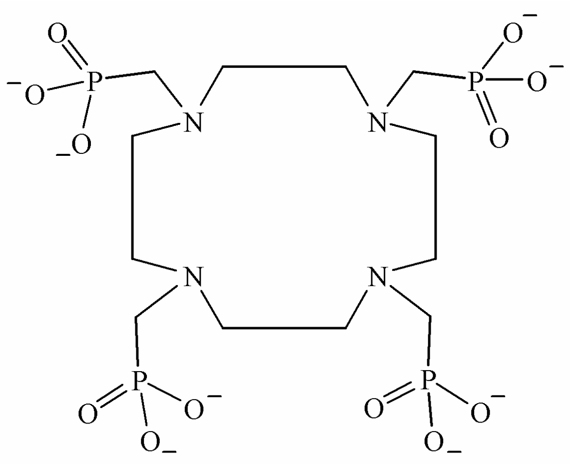

Fig. 1.2.10 – Schematic diagram of $(DOTP)^{8-}$

However, the cations are found on the intra- and extra-cellular compartments, both existing as aquo ions from which it is impossible to distinguish between the two as their identical environments produce identical chemical shifts. The problem is overcome in using anionic LSRs that weakly bind to the alkali metal ions.

Suitable LSRs must obviously be stable under physiological pH, and posses a large magnetic moment to induce the shift in resonance for the nucleus being observed.

A high negative charge on the ligand is also desirable to bind the lanthanide ion, and the overall negative charge of the complex prevents it from crossing the phospholipidic membrane, keeping its distribution about the extra-cellular space where those alkali metal ions reside. The shifts are then applied only to those of one side of the membrane, making it possible to distinguish between the two types of alkali metal ion. $[Dy(DOTP)]^{5-}$ for example, has been used to study $^{23}Na^{+}$ in rat liver.[103, 105]

The negative charge on the ligand arms needs to be concentrated as close to the Dy^{3+} ion as possible, in order to bring the Na^{+} ion towards it and ensure a good pseudocontact.[96] In addition to this, the monitored cations of LSRs do not enter the first coordination sphere of the lanthanide ion, unlike MRI agents, and so it is acceptable for all the lanthanide's coordination sites to be occupied by donor atoms on the ligand.

LSRs are much less used nowadays due to the development and wide availability of high field NMR spectroscopy and two-dimensional correlation spectroscopy (COSY), but are still consistently used in resolving the NMR of chiral molecules. The most commonly used chiral LSR reagent is $[Eu(facam)_3]$, where facam is tris(3-(trifluoromethylhydroxymethylene)-(+)-camphorate) (**Fig. 1.2.11**).

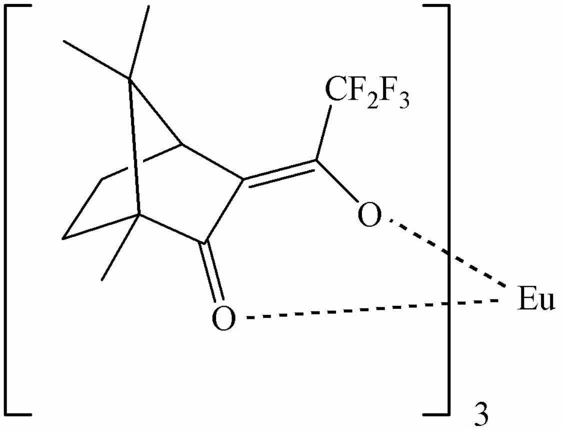

Fig. 1.2.11 – Schematic diagram of $[Eu(facam)_3]$

Like the tris(β-diketonate) complexes, Eu(facam)$_3$ still forms adducts with Lewis bases, yet in a racemic mixture of base (L'), the adducts [Eu(facam)$_3$(*R*-L')] and [Eu(facam)$_3$(*S*-L')] will be formed. Whilst the initial *R*- and *S*-L enantiomers cannot be distinguished in NMR, these new diastereoisomer adducts can, enabling enantiomeric excess to be determined by integration of the resolved resonances.[85]

1.2.6 Near Infrared Luminescence

The near infra-red (NIR) region is the part of the electromagnetic spectrum located between the visible and the infra-red regions (*ca.* 700 – 1500 nm). In recent years, there has been a marked increase in the activity of NIR luminescence generated from *f-f* transitions in Pr^{3+}, Nd^{3+}, Er^{3+}, Yb^{3+} ions. This is attributed to developments in the detection of NIR emission spectra as their lifetimes are much shorter than those of Eu^{3+} and Tb^{3+} (nanoseconds to microseconds). This is generally a weak emission compared to those of Eu^{3+} and Tb^{3+} due to the reduced separation between excited and emissive states which provides non-radiative quenching by molecular vibrations (**Fig. 1.2.4**). [106]

The practical applications of NIR luminescence rest largely in two areas: telecommunications and biological imaging.

1.2.6.1 Telecommunications

Optical fibres have a central core made out of silica glass along which light travels from one end of the fibre to the other *via* total internal reflection. This is only possible due to the mirror-like cladding that encases the silica core, which in turn is coated in a buffer (**Fig. 1.2.12**).

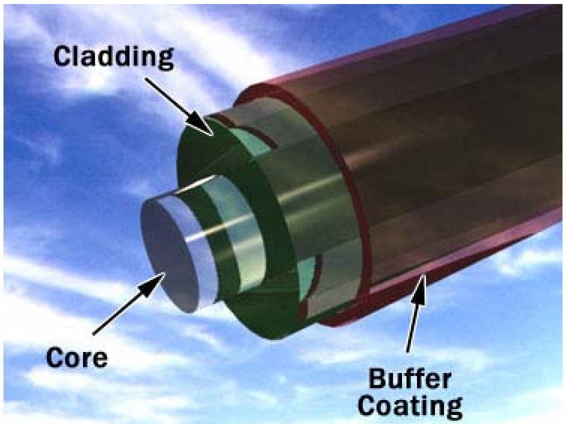

Fig. 1.2.12 – Composition of an optical fibre
Reproduced from Ref.[107]

In order for the fibre to work, the wavelength of light being transmitted must be within the region that corresponds to the window of transparency in the silica, so that it can reach the mirrored cladding and be reflected back into the core. Because the cladding does not absorb any of the light, it is able to travel a sizable distance along the fibre; however silica glass contains a large amount of impurities, particularly hydroxide ions, which cause the signal strength to ebb away over long distances. This extent of signal degradation (attenuation) depends on the quality of the silica glass and the wavelength of light used, (850 and 1550 nm light degrades at 70 and 10 percent/km respectively),[107] but can be overcome by applying a special coating of doping molecules at regular intervals along the fibre, which is then regularly pumped by a laser.

When the degraded light signal hits the coating, this gives rise to a series of ‘doped’ molecules along the coating, which in turn use the energy of the pumping laser to effectively become lasers themselves. The molecules then proceed to emit light at the same wavelength as the incident light, but at a much stronger emission, thus amplifying the original signal.

As **Fig. 1.2.13** shows, narrow windows of transparency exist in the silica glass at *ca*. 1300 and 1550 nm.

These energies are closely matched by the wavelengths of luminescence from Pr^{3+} and Er^{3+} (1330 and 1550 nm respectively, highlighted on **Fig. 1.2.13** as green and pink circles),[106] making them particularly attractive for potential doping molecules.

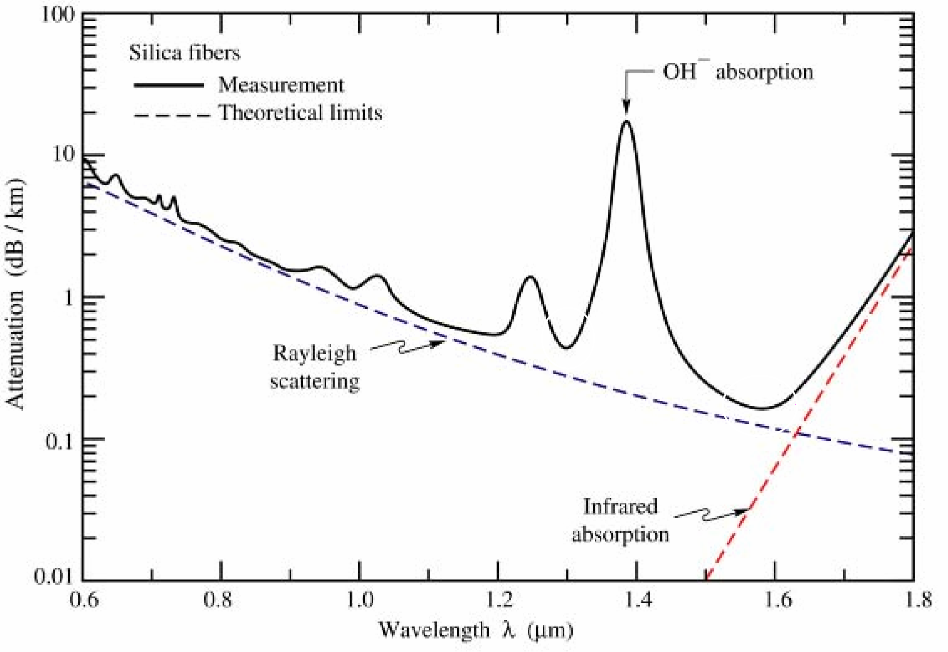

Fig. 1.2.13 – Windows of transparency in silica fibres
Reproduced from Ref.[108]

Awareness in this area has risen drastically since the development of the Internet, which puts a huge demand for high transmission speeds between network portals. Erbium(III) doped fibre amplifiers (EDFA) are very popular in this context and are used to boost 1550 nm light along the lengths of such fibres.[109] More recently, Nd^{3+} has been exploited within polymeric wave-guides to amplify light signals at 1060 nm.[110]

1.2.6.2 Biological Imaging

Biological imaging makes use of NIR luminescence as these photons can penetrate deep into tissue without causing damage to the tissue itself, and there is little loss in signal intensity as photons are not readily absorbed by this medium.[111]

Both human tissue and water vary in the amount of radiation they absorb and let through depending on the wavelength of energy used, and these trends are plotted in **Fig. 1.2.14.** Whilst water lets the most radiation through at *ca*. 550 nm, the absorption coefficient of tissue is still quite high at this wavelength (approx. 10 cm^{-1}) due to the presence of porphyrins in the tissue (e.g. haemoglobin).

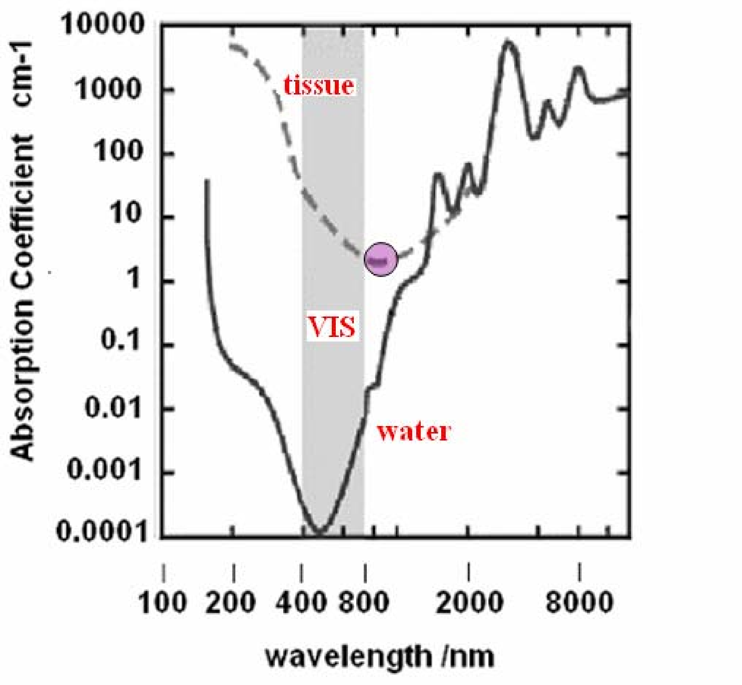

Fig. 1.2.14 – Absorption of energy by tissue and water
Reproduced from Ref.[112]

The optimum region for radiation transparency in tissue-water systems appears at 800-1000 nm (indicated by a purple circle on **Fig. 1.2.14**), where the coefficient of tissue is at a minimum *ca.* 3 cm^{-1} and that of water is still relatively minuscule at 0.03 cm^{-1}.[112] This enables efficient detection of the radiation from outside the tissue, whilst causing minimal biological interference.

Although NIR luminescent organic dyes are currently used for this technique, they undergo rapid decomposition upon photoexcitation which prevents their use over long exposures.

In contrast, lanthanide complexes are much more stable, and their well-defined and long-lived emission bands enable the removal of background fluorescence through time-gating (**Section 1.2.7**), giving rise to better resolved images.[111] Both Nd^{3+} and Yb^{3+} luminesce strongly in the transparency window region at 880 and 980 nm respectively and are the subjects of much research for this very reason.[106]

1.2.7 Time-Gating Measurements

The lifetimes of lanthanide luminescence are quantified by using a technique known as *time gating*, which was first reported back in 1997 when the luminescence lifetime of aqueous Nd^{3+} was recorded.[113]

The technique makes use of the antenna effect explained in **Section 1.2.4.1**. A fast light pulse is used to excite a chromophore which itself has a very short excited state lifetime decay, (typically in the order of nanoseconds) compared to that of the metal-ion (**Fig. 1.2.15**, pink curve). As this excited state decays, the energy transfer to the metal ion begins and reaches a maximum at point β, before luminescence from this metal ion begins (red curve).

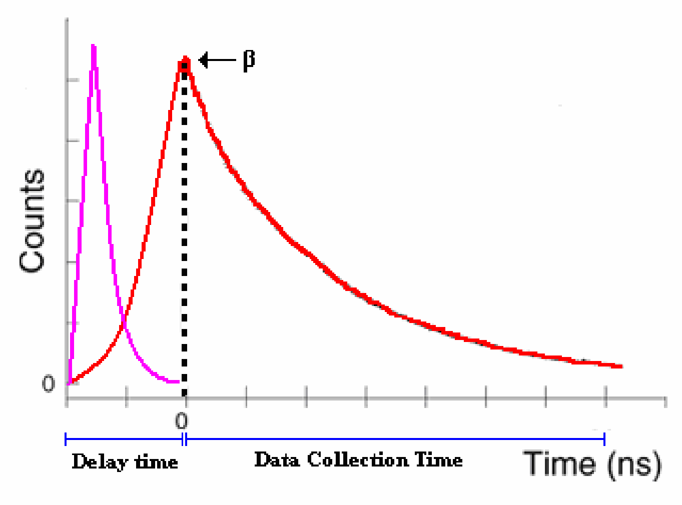

Fig 1.2.15 – Time-resolved fluormetric measurements

By commencing data collection a certain amount of time after excitation of the probe (delay time), the background light provided by a chromophore's own fluorescence (or the short-lived fluorescence from tissue in biological media) is almost reduced to zero, and this has two distinct benefits:

i) the contrast in images will be improved enabling us to observe much more intricate details[114] (**Fig. 1.2.16**); and

ii) we can measure the lifetime of the decay solely from the metal ion (latter half of the red curve). Because the metal ion based luminescence decay is always of an exponential nature, the half life ($t_{1/2}$) of the decay lifetime can always be calculated from commencing data collection after time t = 0.

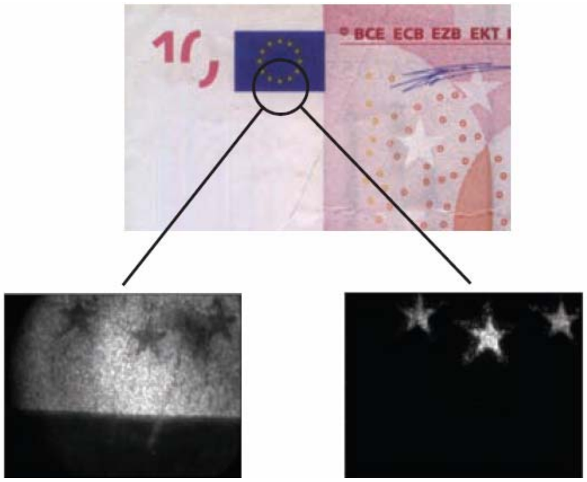

(a) **(b)**

Fig. 1.2.16 – Luminescence image of a 10 EURO note with a delay time of (a) 0 sec, and (b) 1µs. The latter shows the removal of the fluorescence from the blue background, and just that of the Eu^{3+} on the stars

1.3 Coordination Polymers Based on Cyanide Bridges

1.3.1 The Field

The term 'coordination polymer' refers to the infinite extension of molecules, in a given direction, through the aid of linkages formed by coordinate bonds. In its own right, this occupies a large percentage of today's research in inorganic chemistry and relies exclusively on the use of X-Ray crystallography (see Chapter 5) to help determine the intricate details of the structures. Complexes therefore need to be available as single crystals, during the formation of which the components assemble and the dimensionality is determined.

Dimensionality is dependent on two things: i) the geometry of the metal ion, and ii) the orientation (and type) of donor atoms. In principle, it should be easy to predict the geometry of architectures where metal ions have the tendency to adopt definite coordination geometries, but as we shall see in chapters 2 and 4, this is not always the case. By judicious choice of a ligand to remove one or more donor sites from the metal ion(s), control over the topology and geometry of the network can be gained.[115] One of the most common choice of such ligands in today's research is based on the diimine chelate.

Whilst such control allows the design of some diverse architectures, it also gives rise to a vast range of functional materials, particularly when the metal centres retain their original electronic and spectroscopic characteristics. Current research on coordination polymers finds their use in molecular absorption,[116] and electrical conductivity,[117] and catalysis.[117]

1.3.2 The Cyanide $(CN)^-$ Bridging Ligand

The cyanide group is a small, versatile ligand with uninegative charge residing over its atoms, and is often employed in synthesis initially as the anion to an alkali metal (KCN) or as a complementary base to a proton (HCN).

Its preference in coordinating to metal ions stems from its characteristics of being a strong σ-donor and a good π-acceptor. Because of the negative charge, the cyanide anion bonds strongly with metals in high oxidation states, but as a weak acceptor of electron density, it is unable to stabilise complexes with lower oxidation states to the same extent.[118] It is also extremely poisonous as the CN^- group can coordinate more strongly than oxygen to the iron(III) metal ion in cells, removing their means of getting energy from adenosine triphosphate ATP, causing the cell to starve. In this context, cyanide can function as a ligand, available to bond either in a monodentate fashion, or a bidentate one in which it bridges between metal centres. This helps to maintain a conjugated network between metal centres which can then, for example, be used to synthesise conductive materials.[119]

IR stretches of cyanide bonds in metal complexes fall in the region of 2000-2250 cm^{-1} with the lower values diagnostic of a terminal-bonded CN, and higher values diagnostic of a linear bridging CN.[120] The energy of the CN vibration acts as a direct probe of the electron denisty on a coordinated metal ion and can be monitored using time-resolved infra red spectroscopy, making it possible to follow internal energy-transfer in multinuclear complexes if they contain CN ligands.[121] Transition metal-cyanide complexes are often solvatochromic as well, interacting with the surrounding solvent molecules *via* the externally directed lone pair on the N atom. This alters the σ-donor / π-acceptor ability of the other end of the ligand and hence its ligand field strength. This often gives metal-cyanide complexes different coloured appearances in different solvents as their UV-VIS absorption bands vary with the degree of interaction of the solvent with the cyanides.[122]

1.3.3 Cyanide-Based Coordination Polymers

1.3.3.1 Prussian Blue

The most celebrated metal-cyanide complex is Prussian blue, also known as ferrous hexacyanoferrate ($Fe_4[Fe(CN_6]_3.xH_2O$). Ironically, in 1704, its creator Driesbach was actually looking to synthesise a red pigment for use on the military uniforms of German officers, but instead succeeded on arranging Fe^{3+} and Fe^{2+} ions in a unique way that caused them to absorb light at the other end of the visible spectrum.

Prussian blue has widely become regarded as the first example of a synthetic coordination compound and whilst there had been several postulations as to the structure of the complex, its crystal structure was not determined until 1977, in which it was determined as face centred cubic.[123]

There are many analogous structures to that of Prussian blue involving different combinations of metal ions, but all have the same fundamental principle of six cyanide bonds surrounding the octahedral metals. Communication between metal ions can also give long-range magnetic ordering to these complexes.[124] The general formula of these types of compounds is $A_n[B(CN)_6].(H_2O)_m$ where A is a high spin metal ion and B is a low spin metal ion with the linkage order of A-N≡C-B extending along the x ,y, and z-axes (**Fig. 1.3.1**).

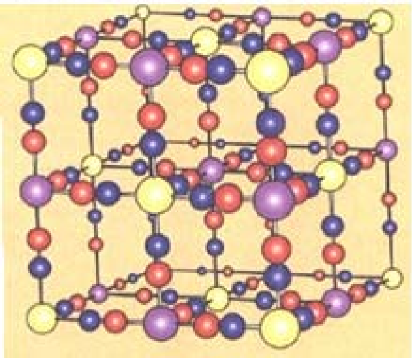

Fig. 1.3.1 – General Prussian blue face-centred cubic structure carbon = red, nitrogen = blue, metal B = purple, metal A = yellow

The magnetic interaction between A and B may be either antiferro- or ferromagnetic, with spin alignment in antiparallel or parallel fashions respectively. This magnetic behaviour is eradicated should the complex be subjected to temperatures beyond a value known as the 'critical value' T_c.[125]

1.3.3.2 Hoffman Clathrates

Square planar d^8-metal ions have also featured heavily in cyano-group coordination polymers, again in the typified form of $A[B(CN)_4]$. Structural studies have been performed on complexes where B = Ni^{2+}, Pt^{2+}, Pd^{2+} and Au^{3+}, and all show the flat cyano-anion acting as a bridge between two A metals through two *trans*-cyanide groups.[126] This results in one-dimensional polymer chains which are then cross-linked by the remaining cyanide groups hydrogen bonding to guest molecules sandwiched between the layers (**Fig. 1.3.2**). A more familiar term for these complexes is 'Hoffman Clathrates'.

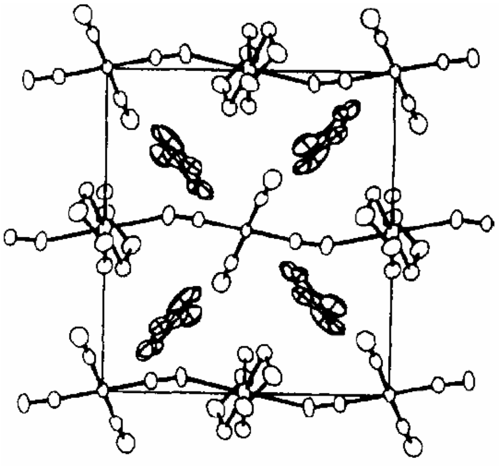

Fig. 1.3.2 – Crystal structure of $[Cd(en)_2Ni(CN)_4].2PhNH_2$

A clathrate itself is a compound which consists of a cage-structure in which one type of molecule is trapped inside the cage of other molecules. Obviously in these d^8-based cyanide compounds there is no cage structure, but Hoffman clathrates realise the inclusion of guest molecules in these complexes is possible. The general form of a Hoffmann clathrate is $[A(en)_2B(CN)_4].2G$ where G represents the guest molecule and *en* is ethylenediamine.

Hoffman-type analogues exist with different ligands about A, but the principle is the same with the replacement ligand blocking two donor sites on the A metal ion. In some cases, two-dimensional polymer sheets are formed between the B(CN)$_4$ unit and the A metal, with guest molecules sandwiched between these layers.[127]

Steric repulsion from the inorganic frameworks restricts the size and shape of guest molecules, which have included biphenyl,[127] water,[128] phenol, and aniline,[129] and in some cases gaseous guests can be removed and exchanged in the solid state network without it losing its crystallinity.[126d] Whilst molecular porosity appears useful in this respect, analytical data of such complexes are often misleading due to their abilities to undergo surface absorption and zeolitic bonding to organic substrates.[123]

1.3.3.3 Cyanide-Bridged Lanthanide-Transition Metal Hybrids

In replacing the A metal in the A-N≡C-B bond with a lanthanide ion, the predictable topology of the complex is removed, as the lanthanide ions have highly variable coordination geometries. Few complexes have been reported with combinations of octahedral hexacyanometallates with lanthanides, but each show formation of a 1-D chain with the lanthanide ions bridged on opposite sides by the cyanide anions.[130]

Shore has done extensive work on M-CN-Ln coordination networks, prepared by the simple metatheses of lanthanide chlorides and K$_2$[M(CN)$_4$] in DMF.[131] In this context, the chemistry of Ln(II) ions is limited to Yb(II), Sm(II) and Eu(II), and reaction products of this series are isostructural in forming 1-D ladders in which three of the four cyanide groups bond to three separate Ln(II) ions (**Fig. 1.3.3**)

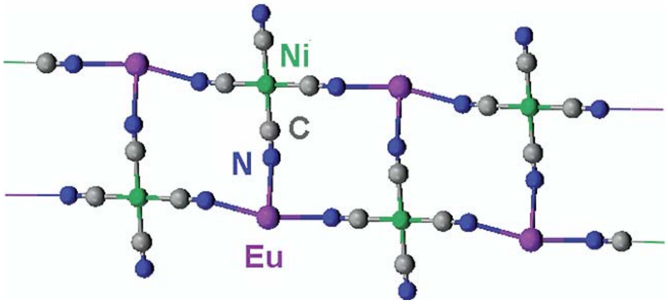

Fig. 1.3.3 – Crystal structure of {(DMF)$_4$Eu[Ni(CN)$_4$]}

The trivalent lanthanide ions generate a wide range of structural types depending on the proportions of cyanometallate and lanthanide used. **Scheme 1.3.1** shows those obtained with a 3:2 addition, whilst **Figures 1.3.4** and **1.3.5** show those obtained on 1:1 and 1:2 additions respectively. In the case of the latter, both structures have their charges neutralised by the inclusion of K^+ or NH_4^+ ions in the crystal lattice.

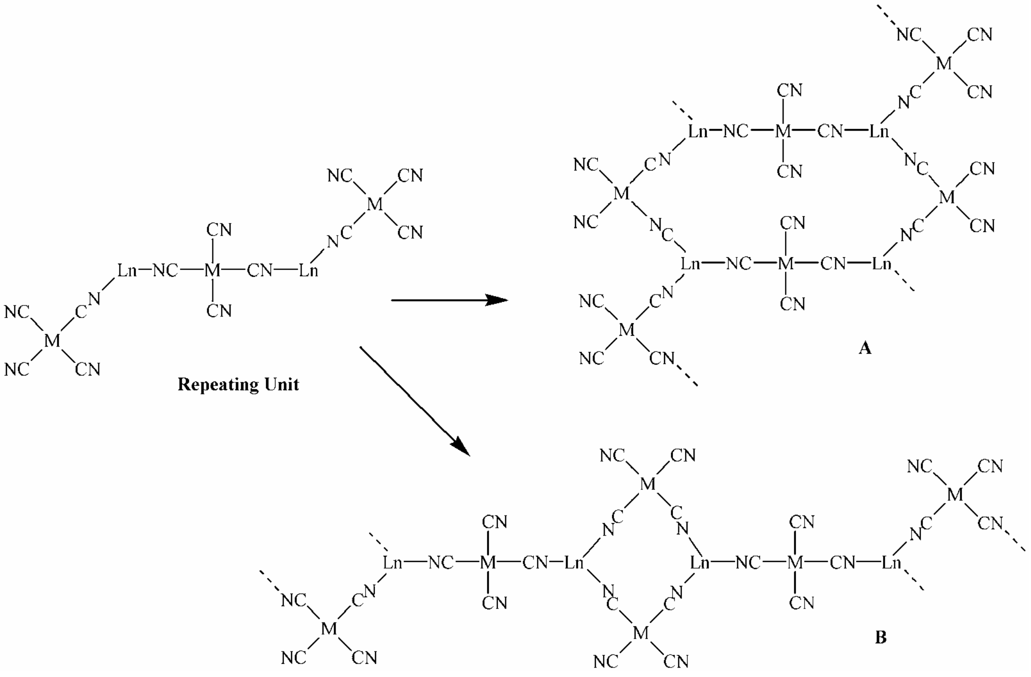

Scheme 1.3.1 – Repeating unit combines to give 1-D chains as either (a) double strand or (b) single strand

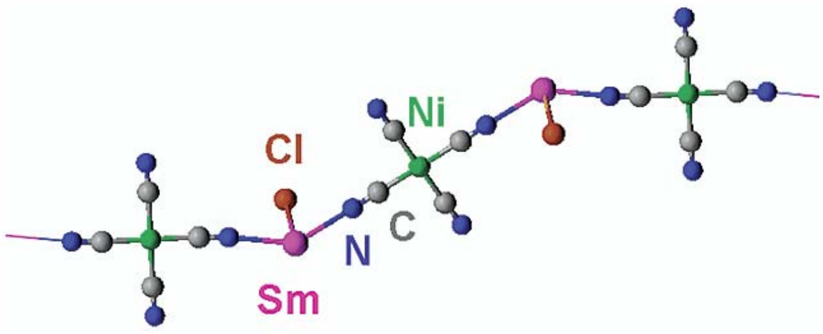

Fig. 1.3.4 – 1-D chain-like array formed on equimolar addition of reagents

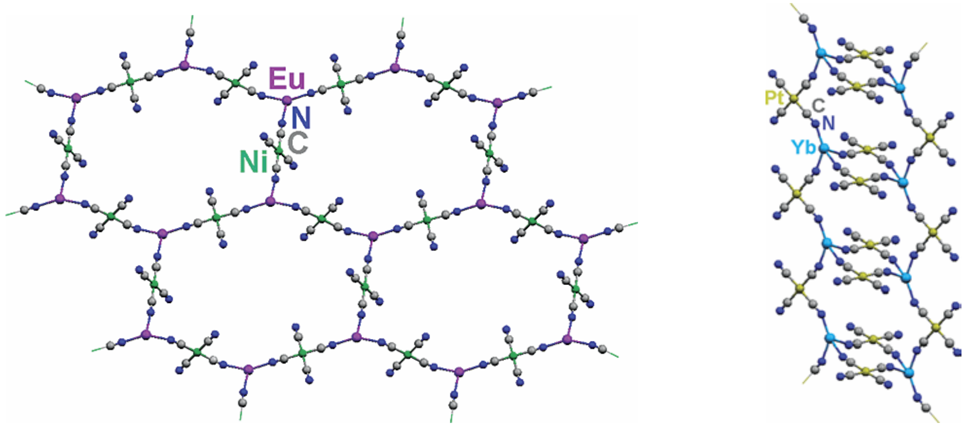

(a) (b)

Fig. 1.3.5 – Different topologies formed on 1:2 additions of Ln(III) and $[M(CN)_4]^{2-}$ ions: (a) 2-D puckered sheets of 12-membered rings and (b) 1-D negatively charged columns by pure *cis* binding cyanide bonds.

Of course, these complexes do not have to be formed just by the addition of two components, and it is perfectly possible to obtain novel topologies by the separate addition of lanthanide ions, transition metal ions and cyanide salts in a three component metathesis. On doing this with Gd^{3+}, Cu^{+} and KCN in a 1:6:3 ratio in DMF, Shore produced an anionic 3-D network of $[Cu_6(CN)_9]$ units which played host to several $[Gd(DMF)_8]$ cluster cations (**Fig. 1.3.6a**). Surprisingly though, upon repeating the synthesis with $K[Cu(CN)_2]$ and Gd^{3+} (i.e. pre-combined Cu^{+} and KCN), a 2-D extended sheet was formed comprising both metal ions (**Fig. 1.3.6b**).[132]

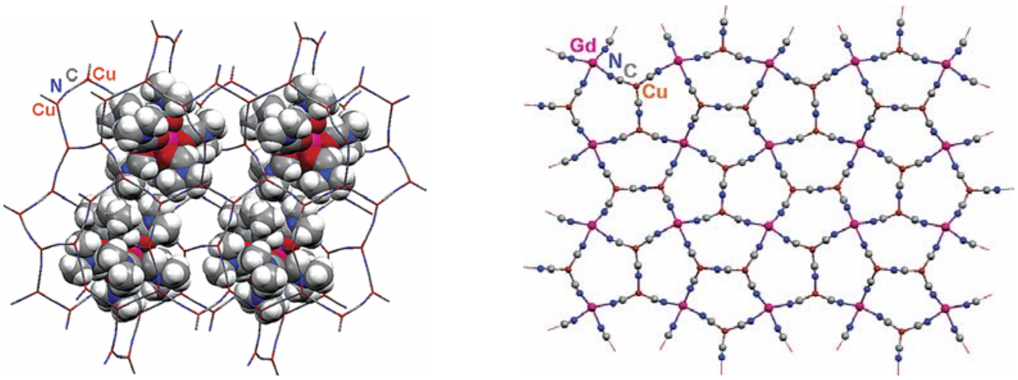

(a) (b)

Fig. 1.3.6 – Crystal structures of (a) $\{[Gd(DMF)_8][Cu_6(CN)_9.2DMF]\}$ showing the trapped cations and (b) 2-D extended layer of $\{Gd_2(DMF)_8Cu_4(CN)_{10}\}$

1.4 Summary & Overview

This section has provided an introduction to the three areas explored in this thesis: Section one provided an overview of poly(pyrazolyl)borate chemistry, with a focus on those with additional donor atoms on the 3-subsitutents of the pyrazolyl ring; section two illustrated the physical properties of the lanthanide(III) ions, with a particular focus on their spectroscopic characteristics; and section three gave a brief review of some current research in coordination polymers that incorporate cyanide as bridging ligands.

The aims of this thesis fall in several categories: In chapter 2 we continue to explore the chemistry of the scorpionates where the 3-pyrazole substituent is replaced with a 3N- or 4N-pyridyl group; chapter 3 examines the structural and photophysical behaviour of lanthanides with the anionic tetradentate ligand $[Bp^{2py}]^-$ and 1,3-diketonate molecules; chapter 4 describes the synthesis, structural characterisation and luminescence properties of coordination networks based on a combination of tetracyanoruthenate(II) or hexacyanochromate(III) units with lanthanide(III) ions; whilst chapter 5 offers a detailed review of the practice of X-ray crystallography including the history of the technique, the theory, and the current technology employed; as well as a few independent crystal structures solved by the author.

An experimental section can be found at the end of each chapter, and the thesis concludes with a summary of the findings within each chapter, and suggestions for future work.

1.5 References

1. S. Trofimenko, *J. Am. Chem. Soc.*, 1966, **88**, 1842.
2. S. Trofimenko, *Polyhedron*, 2004, **23**, 197.
3. T. Kitano, Y. Sohrin, Y. Hata, H. Kawakami, T. Hori, K. Ueda, *J. Chem. Soc., Dalton Trans.*, 2001, 3564.
4. S. Trofimenko, '*Scorpionates – The Coordination Chemistry of Polypyrazolylborate Ligands.*', Imperial Colledge Press, 1999.
5. S. Trofimenko, *Inorg. Syn.*, 1970, **12**, 99.
6. S.Trofimenko, J. C. Calabrese, P. J. Domaille, J. S. Thompson, *Inorg. Chem.*, 1989, **28**, 1091.
7. C. A. Tolman, *Chem. Rev.*, 1977, **77**, 313.
8. A. L. Rheingold, R. L. Ostrander, B. S. Haggerty, S. Trofimenko, *Inorg. Chem.*, 1994, **33**, 3666.
9. A. L. Rheingold, B. S. Haggerty, S. Trofimenko, *J. Chem. Soc., Chem. Commun.*, 1994, 1973.
10. S. Trofimenko, *Chem. Rev.*, 1993, **93**, 943.
11. S. Trofimenko, J. C. Calabrese, J. S. Thompson, *Inorg. Chem.*, 1987, **26**, 1507.
12. J. C. Calabrese, S. Trofimenko, J. S. Thompson, *J. Chem. Soc., Chem. Commun.*, 1986, 1122.
13. S. Trofimenko, *J. Am. Chem. Soc.*, 1967, **89**, 6288.
14. M. I. Bruce, A. P. P. Ostazewski, *J. Chem. Soc., Dalton Trans.*, 1973, 2433.
15. S. G. Roundhill, D. M. Roundhill, D. R. Bloomquist, C. Landee, R. D. Willett, D. M. Dooley, H. A. Gray, *Inorg. Chem.*, 1979, **18**, 831.
16. A. J. Canty, N. J. Minchin, L. M. Engelhardt, B. W. Skelton, A. H. White., *J. Chem. Soc., Dalton Trans.*, 1986, 645.
17. M. D. Curtis, K, -B, Shiu, W. M. Butler, J. C. Hauffman, *J. Am. Chem. Soc.*, 1986, **108**, 3335.
18. M. D. Curtis, K. –B. Shiu, *Inorg. Chem.*, 1985, **24**, 1213.
19. S. A. Roberts, C. G. Young, C. A. Kipke, W. E. Cleland Jr, K. Yamanouchi, M. D. Carducci, J. H. Enemark, *Inorg. Chem.*, 1990, **29**, 3650.
20. M. Onishi, K. Ikemoto, K. Hiraki, *Inorg. Chim. Acta.*, 1991, **190**, 157.

21. C. Vicente, G. B. Shul'pin, B. Moreno, S. Sabo-Etienne, B. Chaudret, *J. Mol. Cat. A Chem.,* 1995, **98**, L5.
22. C. Slugovc, R. Schmid, K. Kirchner, *Coord. Chem. Rev*., 1999, **185**, 109.
23. K. Niedenzu, P. M. Niendenzu, K. R. Warner, *Inorg. Chem*., 1985, **24**, 1604.
24. (a) L. Hasinoff, J. Takats, X. W. Zhang, A. H. Bond, R. D. Rogers, *J. Am. Chem. Soc*., 1994, **116**, 8833. (b) G. H. Maunder, A. Sella, D. A. Tocher, *J. Chem. Soc., Chem. Commun*., 1994, 2689.
25. J. C. Calabrese, S. Trofimenko, *Inorg. Chem*., 1992, **31**, 4810.
26. A. L. Rheingold, L. M. Liable-Sands, G. P. A. Yap, S. Trofimenko, *J. Chem. Soc., Chem. Commun*., 1996, 1233.
27. D. M. Eichhorn, W. H. Armstring, *Inorg. Chem*., 1990, **29**, 3607
28. S. Trofimenko, J. C. Calabrese, J. K. Kochi, S. Wolowiec, F. B. Hulsbergen, J. Reedijk, *Inorg. Chem*., 1992, **31**, 3943.
29. G. Ferguson, M. C. Jennings, F. J. Lalor, C. Shanahan, *Acta. Cryst*., **C47**, 1991, 2079.
30. A. L. Rheingold, C. B. White, S. Trofiemnko, *Inorg. Chem*., 1993, **32**, 3471.
31. R. Han, G. Parkin, S. Trofimenko, *Polyhedron*, 1995, **14**, 387.
32. C. Lopez, D. Sanz, R. M. Claramunt, S. Trofimenko, J. Elguero, *J. Organomet. Chem*., 1995, **503**, 265.
33. A. L. Rheingold, G. P. A. Yap, L. M. Liable-Sands, I. A. Guzei, S. Trofimenko, *Inorg. Chem*., 1997, **36**, 6261.
34. A. L. Rheingold, G. P. A. Yap, L. N. Zakharov, S. Trofimenko, *Eur. J. Inorg. Chem.,* 2002, 2355.
35. S. Trofimenko, A. L. Rheingold, L. M. Liable-Sands, *Inorg. Chem*., 2002, **41**, 1889.
36. M. A. Halcrow, C. A. Kilner, M. Thornton-Pett, *Acta Cryst*. 2001, C**57**, 711.
37. A. L. Rheingold, L. M. Liable-Sands, S. Trofimenko, *J. Chem. Soc., Chem. Commun*., 1997, 1691.
38. J. C. Calabrese, P. J. Domaille, S. Trofimenko, G. J. Long, *Inorg. Chem*., 1991, **30**, 2795.
39. A. J. Amoroso, A. M. Cargill-Thompson, J. C. Jeffery, P. L.Jones, J. A. McCleverty, M. D. Ward, *J. Chem. Soc., Chem. Commun*., 1994, 2751.

40. A. J. Amoroso, J. C. Jeffery, P. L.Jones, J. A. McCleverty, L. H. Rees, A. L. Rheingold, Y. Sun, J. Takats, S. Trofimenko, M. D. Ward, G. P. A. Yap, *J. Chem. Soc., Chem. Commun*., 1995, 1881.
41. A. J. Amoroso, J. C. Jeffery, P. L. Jones, J. A. McCleverty, P. Thornton, M. D. Ward, *Angew. Chem. Int. Ed. Engl*., 1995, **34**, 1443.
42. P. L. Jones, J. C. Jeffery, J. P. Maher, J. A. McCleverty, P. H. Rieger, M. D. Ward, *Inorg. Chem*., 1997, **36**, 3088.
43. D. A. Bardwell, J. C. Jeffery, P. L. Jones, J. A. McCleverty, M. D. Ward, *J. Chem. Soc., Dalton Trans.*, 1995, 2921.
44. R. L. Paul, A. J. Amoroso, P. L. Jones, S. M. Couchman, Z. R. Reeves, L. H. Rees, J. C. Jeffery, J. A. McCleverty, M. D. Ward, *J. Chem. Soc., Dalton Trans*., 1999, 1563.
45. P. L. Jones, K. L. V. Mann, J. C. Jeffery, J. A. McCleverty, M. D. Ward, *Polyhedron*, 1997, **16**, 2435.
46. A. J. Amoroso, J. C. Jeffery, P. L. Jones, J. A. McCleverty, E. Psillakis, M. D. Ward, *J. Chem. Soc., Chem. Commun*., 1995, 1175.
47. E. R. Humphrey, N. C. Harden, L. H. Rees, J. C. Jeffery, J. A. McCleverty, M. D. Ward, *J. Chem. Soc., Dalton Trans*., 1998, 3353.
48. E. R. Humphrey, K. L. V. Mann, Z. R. Reeves, A. Behrendt, J. C. Jeffery, J. P. Maher, J. A. McCleverty, M. D. Ward, *New. J. Chem*. 1999, **23**, 417.
49. A. L. Rheingold, C. D. Incarvito, S. Trofimenko, *J. Chem. Soc., Dalton Trans*., 2000, 1233.
50. B. S. Hammes, M. W. Carrano, C. J. Carrano, *J. Chem. Soc., Dalton Trans*., 2001, 1448.
51. B. S. Hammes, X. Luo, B. S. Chohan, M. W. Carrano, C. J. Carrano, *J. Chem. Soc., Dalton Trans*., 2002, 3374.
52. R. N. Armstrong, *Biochem*., 2000, **39**, 13625.
53. S. Trofimenko, *J. Am. Chem. Soc*., 1967, **89**, 3170.
54. (a) S. Trofimenko, *J. Am. Chem. Soc*., 1970, **92**, 5118. (b) A. Otero, J. Fernandez-Baeza, A. Antinolo, J. Tejeda, A. Lara-Sanchez, *Dalton Trans*., 2004, 1499.
55. S. Trofimenko, *Inorg Chem*., 1970, **9**, 2493.
56. D. L. Reger, P, -T. Chou, S. L. Studer, S. J. Knox, M. L. Martinez, W. E. Brewer, *Inorg. Chem*., 1991, **30**, 2397.

57. C. A. Kosky, P. Ganis, G. Avitable, *Acta. Cryst*. 1971, **B27**, 1859.
58. S. J. Lippard, K. M. Melmed, *Inorg. Chem*., 1967, **6**, 2223.
59. F. A. Cotton, M. Jeremic, A. Shaver, *Inorg. Chim. Acta*., 1972, **6**, 543.
60. P. Ghosh, J. Bonanno, G. Parkin, *J. Chem. Soc., Dalton Trans*., 1998, 2779.
61. D. L. Reger, J. A. Lindeman, L. Lebioda, *Inorg. Chem*., 1988, **27**, 1890.
62. G. Paolucci, S. Cacchi, L. Cagliotti, *J. Chem. Soc., Perkin Trans*., 1979, 1129.
63. D. A. Bardwell, J. C. Jeffery, J. A. McCleverty, M. D. Ward, *Inorg. Chim. Acta*., 1998, **267**, 323.
64. D. A. Bardwell, J. C. Jeffery, P. L. Jones, J. A. McCleverty, E. Psillakis, M. D. Ward, *J. Chem. Soc., Dalton Trans*., 1997, 2079.
65. P. L. Jones, K. J. Byron, J. C. Jeffery, J. A. McCleverty, M. D. Ward, *J. Chem. Soc., Chem. Commun*., 1997, 1361.
66. E. Psillakis, J. C. Jeffery, J. A. McCleverty, M. D. Ward, *J. Chem. Soc., Chem. Commun*., 1997, 479.
67. J. S. Fleming, E. Psillakis, S. M. Couchman, J. C. Jeffery, J. A. McCleverty, M. D. Ward, *J. Chem. Soc., Dalton Trans*., 1998, 537.
68. F. A. Cotton, V. W. Day, *J. Chem. Soc., Chem. Commun*., 1974, 415.
69. S. Trofimenko, J. C. Calabrese, J. S. Thompson, *Angew. Chem. Int. Ed. Engl*., 1989, **28**, 205.
70. F. A. Cotton, C. A. Murillo, *Inorg. Chim. Acta*., 1976, **17**, 121.
71. F. A. Cotton, B. A. Frenz, C. A. Murillo, *J. Am. Chem. Soc*., 1975, **97**, 2118.
72. M. I. Bruce, J. D. Walsh, *Aust. J. Chem*., 1979, **32**, 2753.
73. J. L. Kisko, T. Hascall, C. Kimblin, G. Parkin, *J. Chem. Soc., Dalton Trans*., 1999, 1929.
74. B. S. Hammes, M. T. Kieber-Emmons, J. A. Letizia, Z. Shirin, C. J. Carrano, L. N. Zakharov, A. L. Rheingold, *Inorg. Chim. Acta*., 2003, **346**, 227.
75. (a) A. Looney, R. Hau, I. B. Gorrell, M. Cornebise, K. Yoon, G. Parkin, *Organomet*., 1995, **14**, 274. (b) I. B. Gorrell, A. Looney, G. Parkin, A. L. Rheingold, *J. Am. Chem. Soc*., 1990, **112**, 4068.
76. P. Ghosh, G. Parkin, *J. Chem. Soc., Dalton Trans*., 1998, 2281.
77. N. Kaltsoyannis, P Scott, *The f-elements*, Oxford University Press, Oxford, 1999.
78. http://library.thinkquest.org/3659/pertable/intmetal.html

79. J. –C. G. Bünzli, C. Piguet, *Chem. Rev.*, **102**, 2002, 1897.

80. R. D. Shannon, *Acta Cryst.*, 1979, A**32**, 751.

81. S. Cotton, *Lanthanides and Actinides*, McMillan Education London, 1991.

82. F. A. Cotton, G. Wilkinson, *Advanced Inorganic Chemistry, 5th Ed.* Wiley-Interscience, 1988.

83. http://hyperphysics.phy-astr.gsu.edu/hbase/atomic/lcoup.html#c1

84. http://hyperphysics.phy-astr.gsu.edu/hbase/atomic/hund.html

85. H. C. Aspinall, *Chemistry of the f-block Elements*, Gordon and Breach Science, 2001.

86. http://scienceworld.wolfram.com/chemistry/LaporteRule.html

87. G. Stein, E. Würzberg, *J. Chem. Phys.*, 1975, **62**, 208.

88. M. H. V. Werts, J. W. Verhoeven, J. W. Hofstraat, *J. Chem. Soc., Perkin Trans. 2*, 2000, **3**, 433.

89. G. A. Hebbink, S. I. Klink, L. Grave, P. G. B. Oude Alink, F. C. J. M. van Veggel, *Chem. Phys. Chem.*, 2002, **3**, 1014

90. W. D. Horrocks, D. R. Sudnick, *Acc. Chem. Res.*, 1981, **14**, 384.

91. P. Atkins, *Physical Chemistry 6th Ed*, Oxford University Press, 1998.

92. W. D. Horrocks, D. R. Sudnick, *J. Am. Chem. Soc.*, 1979, **101**, 334.

93. Y. Haas, G. Stein, *J. Phys. Chem.*, 1972, **76**, 1093.

94. J. L. Kropp, M. W. Windsor, *J. Chem. Phys.*, 1965, **42**, 1599.

95. A. Beeby, I. M. Clarkson, R. S. Dickins, S. Faulkner, D. Parker, L. Royle, A. S. de Sousa, J. A. G. Williams, M. Woods, *J. Chem. Soc. Perkin Trans. 2*, 1999, 493.

96. S. Aime, M. Botta, M. Fasano, E. Terreno, *Chem. Soc. Revs.*, 1998, **27**, 19 and references therein.

97. G. R. Choppin, K. M. Schaab, *Inorg. Chim. Acta*, 1996, **252**, 299.

98. R. B. Lauffer, *Chem. Rev.*, 1987, **87**, 901.

99. http://int.ch.liv.ac.uk/Lanthanide/Ln_Chemistry_folder/MRI%20folder/MRImages.html

100. Z. R. Bell, *PhD Thesis*. University of Bristol. 2001.

101. D. Parker, J. A. G. Williams, *J. Chem. Soc., Dalton Trans.,* 1996, 3613.

102. D. Parker, *Chem. Soc. Rev.*, 2004, **33**, 156.

103. N. Bansal, M. J. Germann, V. Seshan, G. T. Shires, C. R. Malloy, A. D. Sherry, *Biochem.*, 1993, **32**, 5638.

104. P. M. Winter, N. Bansal, *Magn. Reson. Med.*, 2001, **45**, 436.
105. J. –M. Colet, N. Bansal, C. R. Malloy, A. D. Sherry, *Magn. Reson. Med.*, 1999, **41**, 1127.
106. S. Faulkner, S. J. A. Pope, B. P. Burton-Pye, *App. Spec. Revs.*, 2004, **39**, 1.
107. http://electronics.howstuffworks.com/fiber-optic1.htm
108. http://www.theorphys.science.ru.nl/people/fasolino/sub_teaching/leraren/img028.gif
109. http://www.meos.com/PDF/ENP14.pdf
110. D. An, Z. Yue, R. T. Chen, *App. Phys. Lett.*, 1998, **72**, 2806.
111. J. Zhang, P. D. Badger, S. J. Geib, S. Petoud, *Angew. Chem. Int. Ed.*, 2005, **44**, 2508. and references therein.
112. http://www.nibib1.nih.gov/events/Jackson/ppt/Session1/Gore.pdf
113. A. Beeby, S. Faulkner, *Chem. Phys. Lett.*, 1997, **266**, 116.
114. http://www.internationallabmate.com/pdf/ilm/2005/02/ilm200502_020_021_ILM_FEB_05.pdf
115. S. R. Batten, Curr. Opin. *Solid State Mater. Sci.,* 2001, **5**, 107.
116. (a) J. L. C. Rowsell, A. R. Millward, K. S. Park, O. M. Yaghi, *J. Am. Chem. Soc.*, 2004, **126**, 5666; (b) S. Kitagawa, R. Kiaura, S. –I. Noro, *Angew. Chem. Int. Ed.*, 2004, **43**, 2334.
117. C. Janiak, *Dalton Trans.*, 2003, 2781.
118. G. O. Spessard, G. L. Miessler, '*Organometallic Chemistry*', Prentice-Hall, NJ, 1996.
119. M. Hanack, S. Deger, A. Lange, T. Zipplies, *Syn. Met.*, 1986, **15**, 207.
120. M. Zhou, B. W. Pfennig, J. Steiger, D. van Engen, A. B. Bocarsly, *Inorg. Chem.*, 1990, **29**, 2456.
121. (a) M. K. Kuimova, M. Y. Mel'nikov, J. A. Weinstein, M. W. George, *J. Chem. Soc., Dalton Trans.*, 2002, 2857; (b) S. Encinas, A. F. Morales, F. Barlgelletti, A. M. Barthram, C. M. White, S. M. Couchman, J. C. Jeffery, M. D. Ward, D. C. Grills, M. W. George, *J. Chem. Soc., Dalton Trans.*, 2001, 3312.
122. C. J. Timpson, C. A. Bignozzi, B. P. Sullivan, E. M. Kober, T. S. Meyer, *J. Phys. Chem.*, 1996, **100**, 2915.
123. H. J. Buser, D. Schwarzenbach, W. Petter, A. Ludi, *Inorg. Chem.*, 1977, **16**, 2704.

124. S. –I. Ohkoshi, K. Hashimoto, *J. Electrochem. Soc., Interface*, 2002, **11**, 34.

125. O. Kahn, J. Larionova, L. Ouahab, *Chem. Commun*., 1999, 945.

126. (a) M. Munakata, J. C. Zhong, I. Ino, T. Kuroda-Sowa, M. Maekawa, Y. Suenaga, N. Oiji, *Inorg. Chim. Acta*., 2001, **317**, 268; (b) P. S. Mukherjee, T. K. Maji, T. Mallah, E. Zangrando, L. Randaccio, N. R. Chaudhuri, *Inorg. Chim. Acta*., 2001, **315**, 249; (c) C. J. Shorrock, H. Jong, R. J. Batchelor, D. B. Leznoff, *Inorg. Chem*., 2003, **42**, 3917; (d) T. K. Maji, P. S. Mukherjee, N. R. Chaudhuri, G. Mostafa, E. Zangrando, *Chem. Commun*., 2001, 1368; (e) R. W. Gable, B. F. Hoskins, R. Robson, *J. Chem. Soc., Chem. Commun*., 1990, 762.

127. T. Iwamoto, T. Miyoshi, Y. Sasaki, *Acta Crys*t. B**30**, 1974, 292.

128. J. Cernák, J. Chomic, P. Domaino, O. Ori, G. D. Andreetti, *Acta Cryst*. C**46**, 1990, 2103.

129. H. Yuge, T. Iwamoto, *J. Chem. Soc., Dalton Trans*., 1994, 1237.

130. (a) G. Li, T. Akitsu, O. Sato, Y. Einaga, *J. Coord. Chem*., 2004, **57**, 189; (b) D. F. Mullica, J. M. Farmer, B. P. Cunningham, J. A. Kautz, *J. Coord. Chem*., 2000, **49**, 239; (c) A. Figuerola, C. Diaz, J. Ribas, V. Tangoulis, C. Sangregorio, D. Gatteschi, M. Maestro, J. Mahia, *Inorg. Chem*., 2003, **42**, 5274; (d) R. A. Combs, J. M. Farmer, J. A. Kautz, *Acta Cryst.,* C**56**, 1420.

131. C. E. Plečnik, S. Liu, S. G. Shore, *Acc. Chem. Res*., 2003, **36**, 499.

132. S. Liu, E. A. Meyers, S. G. Shore, *Angew. Chem. Int. Ed*., 2002, **41**, 3609.

Chapter Two

New Scorpionates

2.1 Introduction

As we saw in the previous chapter, the addition of substituents in the 3-position of pyrazole rings has completely revolutionised the coordination chemistry of the scorpionates; and the inclusion of donor atoms in these substituents allows the ligands to successfully bind to metals with a high number of coordination sites, such as lanthanides. No ligands have demonstrated this better than those based on the Tp^{2py} and Bp^{2py} cores (whose chemistry we continue to explore in chapter 3).[1]

These scorpionates are formed by the attachment of pyridyl substituents to the pyrazole rings at their 2-position, thus giving the pyridyl-pyrazole arm the ability to chelate to metal atoms (**Fig. 2.1.1a**). On coordination to a scorpionate, the metal ion will always be held in the pocket of pyrazole nitrogens (N_{pz}), and we can see that by attaching the pyrazole ring (N_{py}) to the 3-position of the pyridyl unit (**Fig. 2.1.1b**) it becomes obvious that the chelating ability is removed. If a distant association with the metal ion is not possible for the pyridyl donor in this situation, electronic repulsion between N_{py} and N_{pz} will subsequently force the arm into a transoid arrangement. Any possible association of N_{py} with the same N_{pz}-held metal ion is negated when the pyrazole substituent is shifted further round to the 4-position (**Fig. 2.1.1c**).

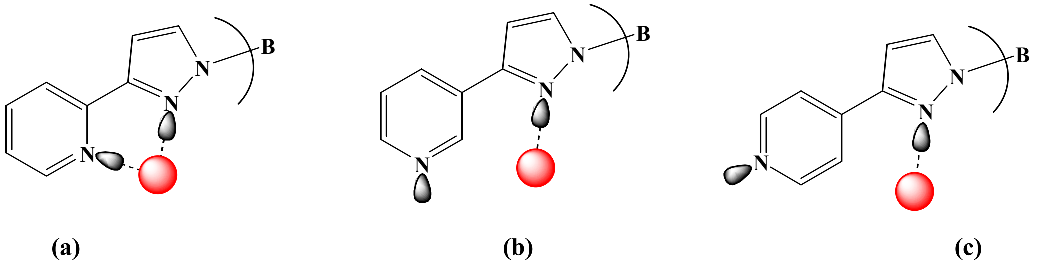

Fig. 2.1.1 – Varying the position of the pyrazole ring

In this chapter, we describe the synthesis of several new scorpionate ligands based on the above pyridyl-pyrazole arms, and their complexes with various metal ions. By shifting the location of the pyridyl nitrogen away from the central cavity of the scorpionate, it was hoped that it would coordinate to an external metal ion, which could give rise to polymeric coordination behaviour.

We were encouraged by the results observed with dihydrobis-[3-(2-pyrazinyl)-pyrazol-1-yl]borate[2] in which an externally orientated nitrogen donor of a [L_2Pb] complex coordinated to the metal ion of a second identical complex (**Fig. 2.1.2**).

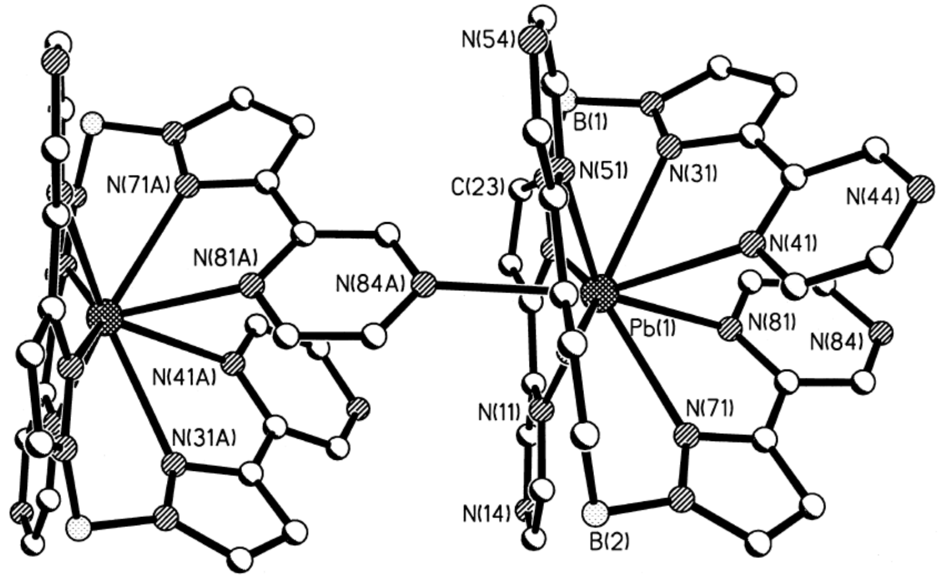

Fig. 2.1.2 – Crystal structure of lead(II) dihydrobis-[3-(2-pyrazinyl)-pyrazol-1-yl]borate

The new scorpionates we discuss here are: dihydro-bis[3-(4-pyridyl)pyrazol-1-yl]borate (Bp^{4py}); dihydro-bis[3-(3-pyridyl)pyrazol-1-yl]borate (Bp^{3py}); hydro-tris[3-(4-pyridyl)pyrazol-1-yl]borate (Tp^{4py}) and hydro-tris[3-(3-pyridyl)pyrazol-1-yl]borate (Tp^{3py}) (**Fig. 2.1.3**). These ligands and their complexes were synthesised and characterised by the author whilst at the Universities of Sheffield and Bristol.

The related ligands tetrakis[3-(4-pyridyl)pyrazol-1-yl]borate (Tkp^{4py}) and tetrakis[3-(3-pyridyl)pyrazol-1-yl]borate (Tkp^{3py}) and their complexes were synthesised and characterised by Martin Duriska and Dr. Stuart Batten at Monash University, Australia, and will be included in discussions for comparison, as these ligands are directly related to the previous four and thus complete the series. A joint paper on this work has recently been published, and contains a more detailed review of these two ligands.[3] From here onwards, we refer to the scorpionates by their shorthand notation (given in parenthesis).

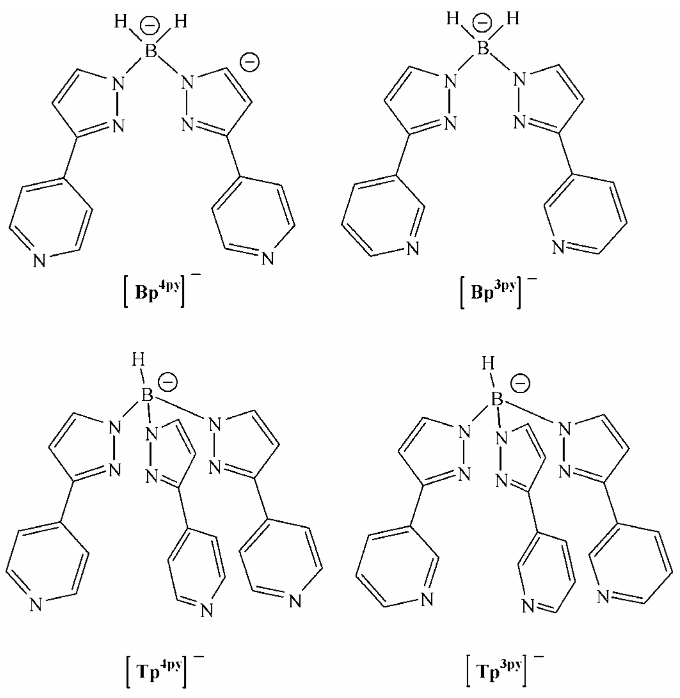

Fig. 2.1.3 – Structural diagrams of $[Bp^{4py}]^-$, $[Bp^{3py}]^-$, $[Tp^{4py}]^-$ and $[Tp^{3py}]^-$

2.2 Results and Discussion

2.2.1 Synthesis of the Scorpionates

2.2.1.1 Pyridyl-pyrazoles (pypz)

In synthesising the pyridyl-pyrazole arm, we replicate Lin and Lang's[4] facile conversion of acetyl groups to pyrazole groups that was employed in the synthesis of 3-(*2*-pyridyl)pyrazole (*2*pypz).[1j] The synthesis is outlined in **Scheme 2.2.1** using 4-acetylpyridine as the reagent.

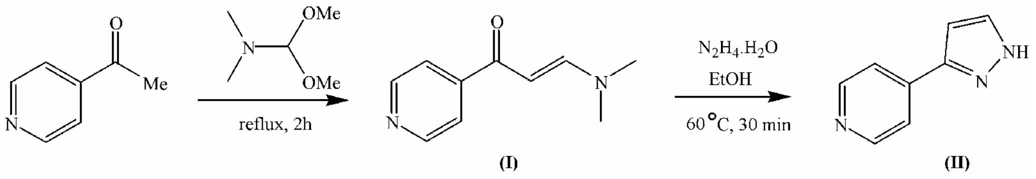

Scheme 2.2.1 – The synthesis of 4-pyridylpyazole

Reaction of 4-acetylpyridine with an excess of dimethylformamide-dimethylacetal (DMF-DMA) afforded the intermediate 3-dimethylamino-1-pyridin-4-yl-propenone (**I**) in excellent yield. Subsequent reaction with hydrazine converts this into the pyrazole (**II**). Further recrystallisation of the product improved its purity, but in turn depleted their yields.

2.2.1.2 The Scorpionates

In accordance with the methods published by Trofimenko,[5-7] a suitable excess of pypz was heated with KBH_4 to promote bis- or tris-substitution of the boron atom and form the Bp or Tp scorpionates respectively. The reaction conditions were varied accordingly, with higher temperatures and longer reaction times employed to achieve the higher degrees of substitution. Despite the rather liquid texture of 3pypz and the solid texture of 4pypz, this common 'melt' method was suitable for the synthesis of all our scorpionates. Reaction details are summarised in **Table 2.2.1**. Unless stated, for each scorpionate and subsequent complex, satisfactory elemental analysis, mass spectra and NMR data were obtained (see **Section 2.3**).

Scorpionate	pypz:KBH_4	Temp / °C	Duration / h
Bp^{4py}	2.5:1	175	0.5
Bp^{3py}	2.5:1	140	2
Tp^{4py}	3.5:1	230	3.5
Tp^{3py}	3.6:1	215	2

Table 2.2.1 – Reaction conditions for the new scorpionates
(See Section 2.3 for further details)

2.2.2 Crystallographic Studies of 3pypz and 4pypz

2.2.2.1 4pypz

Single crystals of both 3pypz and 4pypz were grown by diffusion of pentane into a concentrated CH_2Cl_2 solution of the ligand. 4pypz crystallises in the monoclinic space group $P2_1/c$, with one independent molecule in the asymmetric unit.

Within the crystal, the ligand forms a one-dimensional chain in a direction that bisects both the **a** and **c** axes of the unit cell. The chain propagates *via* H-bonding between the pyridyl nitrogen and a pyrazole hydrogen [NH(2)···N(9) (2.034 Å), N(2)···N(9) = 2.899(1) Å] as the ligands lie head (pz) to tail (py) along the chain, with alternate chains extending in the opposite direction (i.e. T → H → T → H *vs* T ← H ← T ← H). Bonding through the lone pyrazole nitrogen and a pyridyl hydrogen [CH(7)···N(1) = 2.716 Å, C(7)···N(1) = 3.528(2) Å] connects adjacent chains, giving rise to a two-dimensional sheet. **Fig. 2.2.1** shows the ligands pack themselves in a herringbone-type arrangement, the torsion angle between the pyrazole and pyridyl rings of the ligand being 29.5°.

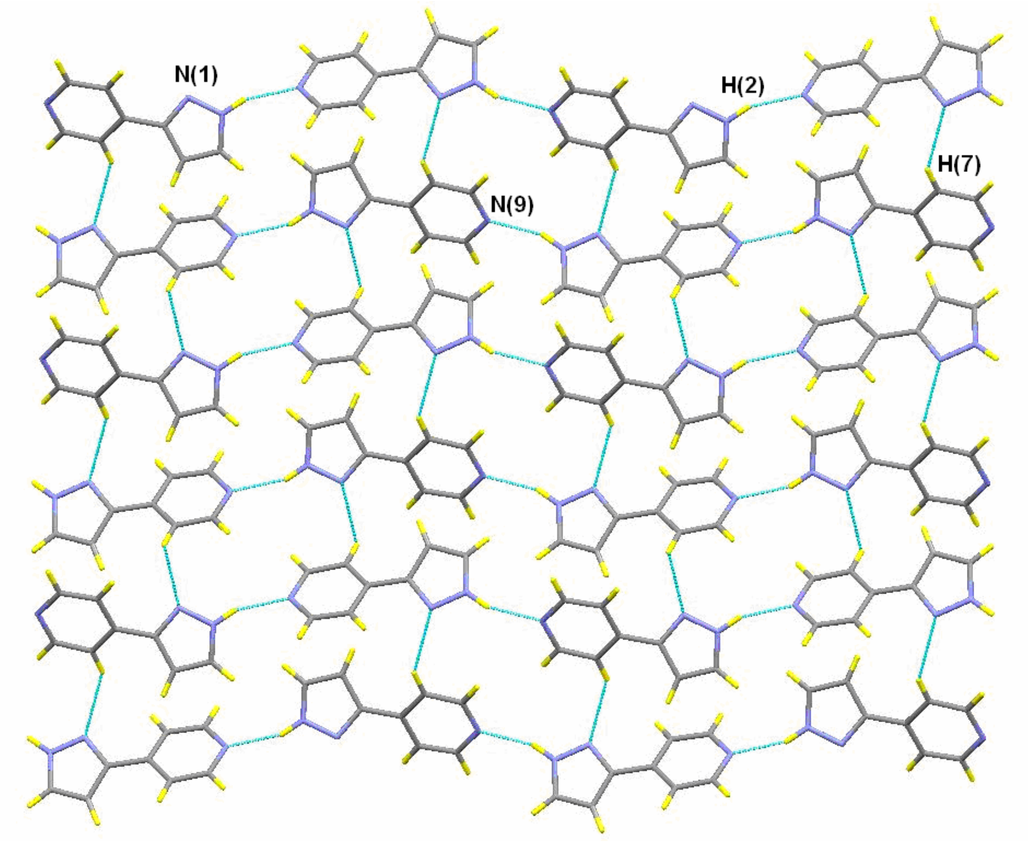

Fig. 2.2.1 – Packing diagram showing the arrangement of 4pypz in the crystal

2.2.2.2 3pypz

The main difference in the crystal of 3pypz is the presence of two independent molecules in the asymmetric unit. The same one-dimensional chain propagation occurs through $N_{py}\cdots H\text{-}N_{pz}$ hydrogen bonding [NH(102)···N(8) = 1.857(23) Å, and NH(2)···N(108) = 1.963 Å where N(2)···N(108) = 2.892(3) Å] with the chains bisecting the **a** and **b** axes of the unit cell. Torsion angles between the pyrazole-pyridyl rings are 11.9° and 23.7° for the N(1)-N(8) and N(101)-N(108) ligands respectively.

An adjacent chain follows the opposite head to tail arrangement and the two are held together by hydrogen bonding through CH(103)···N(1) (2.665 Å) [C(103)···N(1) = 3.564(3) Å] to form a wave-like pairing (**Fig. 2.2.2**). This interaction is also helped by π-stacking between the overlapping N(8) pyridyl rings (3.363 Å separation, offset by 1.197 Å with a centroid-centroid distance of 3.544 Å). These pairings are then held by H-bonding through the CH(9)···N(101) bond (2.692 Å) [C(9)···N(101) = 3.336(3) Å] to give the overall herringbone appearance as observed with 4pypz.

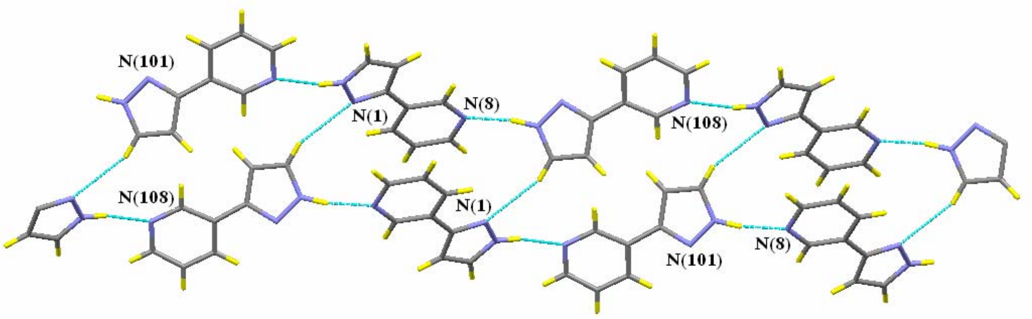

Fig. 2.2.2 – Cross linking of 1D chains in the crystal structure of 3pypz

This ligand has also been shown to crystallise as a polymorph in the orthorhombic space group $Pna2_1$, where perfectly flat chains of the same head to tail alignment connect themselves in a zig-zag fashion *via* H-bonds between the lone pyrazolyl nitrogen and a pyridyl hydrogen.[3]

2.2.2.3 [Co(4pypz)Cl_2]·4MeCN

Whilst the coordination chemistry of 2pypz with transition metals has featured in the literature, such studies arose from *in situ* decomposition of the Tp^{2py} ligand – an occurrence not uncommon among the scorpionates.[8,9]

Resultant structures have included both neutral[10,11] and deprotonated[11-13] 2pypz species, with the former generating mononuclear complexes, and the latter (having terdentate character) giving rise to more complex polynuclear architectures. In addition to having a bidentate chelating site, the terdentate ligand can use its third donor to bridge to a second metal ion, although no evidence suggests this favours the generation of infinite regular arrays. Relocation of the pyridyl nitrogen in 4pypz gives the ligand an appearance reminiscent of 4,4'-bipyridine,[14] with its two donors at opposing ends of the bridging ligand. Lindoy and Kepert recently described the coordination chemistry of 4-(4-pyridyl)pyrazole, in which the pyridyl donor lies equidistant of both pyrazole nitrogens.[15] In our 4pypz system, the pyrazole nitrogens lie to the same side of the pyrazole ring and the ligand does not have twofold symmetry.

Reaction of 4pypz with anhydrous $CoCl_2$ in MeCN gave a deep blue solution from which purple crystals readily appear after a few moments. The crystal structure was solved in the tetrahedral space group I_4 and is shown in **Fig. 2.2.3**.

In their studies, Lindoy and co-workers noted that there are three possible modes of coordination that pyridyl-pyrazole ligands can take: (i) *Neutral* - where the pyrazole NH is maintained; (ii) *Anionic* – where the pyrazole NH is deprotonated; and (iii) *Cationic* – where the pyridyl N becomes protonated. Whilst he observed both *anionic* and *cationic* forms [using Co(II) nitrate], our structure illustrates the *neutral* binding mode: The cobalt(II) metal centre retains both chloride ions [average Co···Cl = 2.487 Å] and has four 4pypz ligands about its equatorial plane.

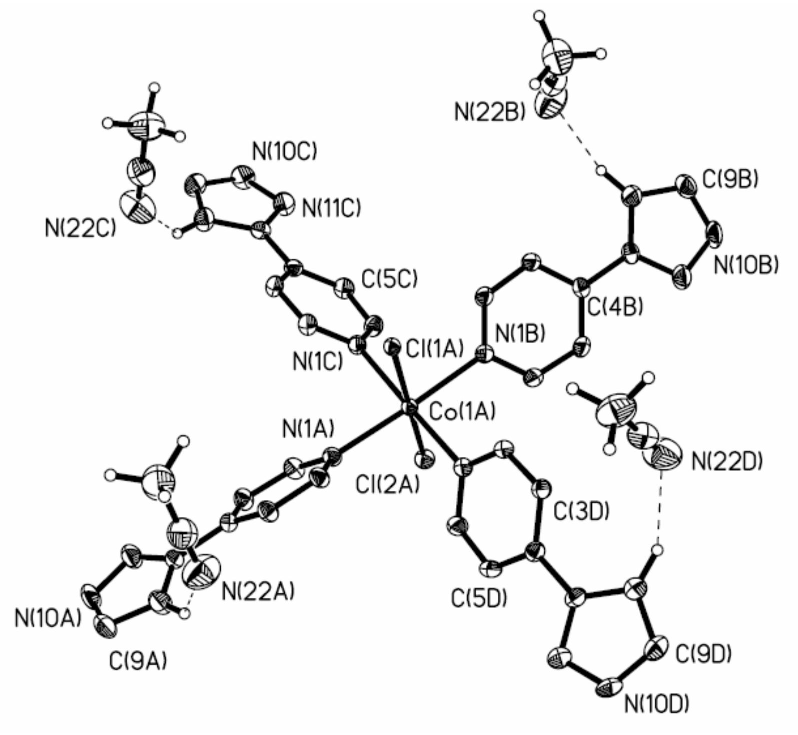

Fig. 2.2.3 – Crystal structure of [Co(4pypz)$_4$Cl$_2$]·4(MeCN)

Flack parameter = 0(10)

Metal ion coordination occurs through the pyridyl donors with a Co(1)···N(1) bond length of 2.166(16) Å and only one 4pypz arm is located in the asymmetric unit, with the Co(II) ion residing in the centre of the unit cell - the cobalt(II) displays near perfect octahedral geometry.

In relation to the mean plane of the four pyridyl nitrogens, the pyridyl and pyrazole rings are twisted 46.3° and 26.6° respectively, and 20.0° with respect to each other. The pyrrolic nitrogen atoms form the vertices of a perfect square with a N(10)-N(10)-N(10) angle of 90.00° and N(10)-N(10) side length of 11.935(3) Å, offset 7° to the square outline of the unit cell. The mean plane of the four N(10) donors lies 0.273 Å below that of the four pyridyl donors.

In the absence of an inversion centre, each pyrazole ring is orientated to face the same side of the four N_{py} donor plane, and the pyrrolic hydrogen atoms bond to the chloride ions of separate [Co(4pypz)Cl$_2$] units [NH(10)···Cl(1) = 2.409Å; N(10)···Cl(1) = 3.261(2) Å].

The chloride ion has four of these bonds about it arranged in a perfect square (**Fig. 2.2.4**), and as the Cl-Co-Cl line lies parallel to the **c**-axis, the network extends along both **a**- and **b**-axes of the unit cell. In addition to this, the network also extends along the **c**-axis because of the orientation of the pyrazole rings, giving an overall three-dimensional coordination network. Selected bond lengths and angles are given in **Table 2.2.2**.

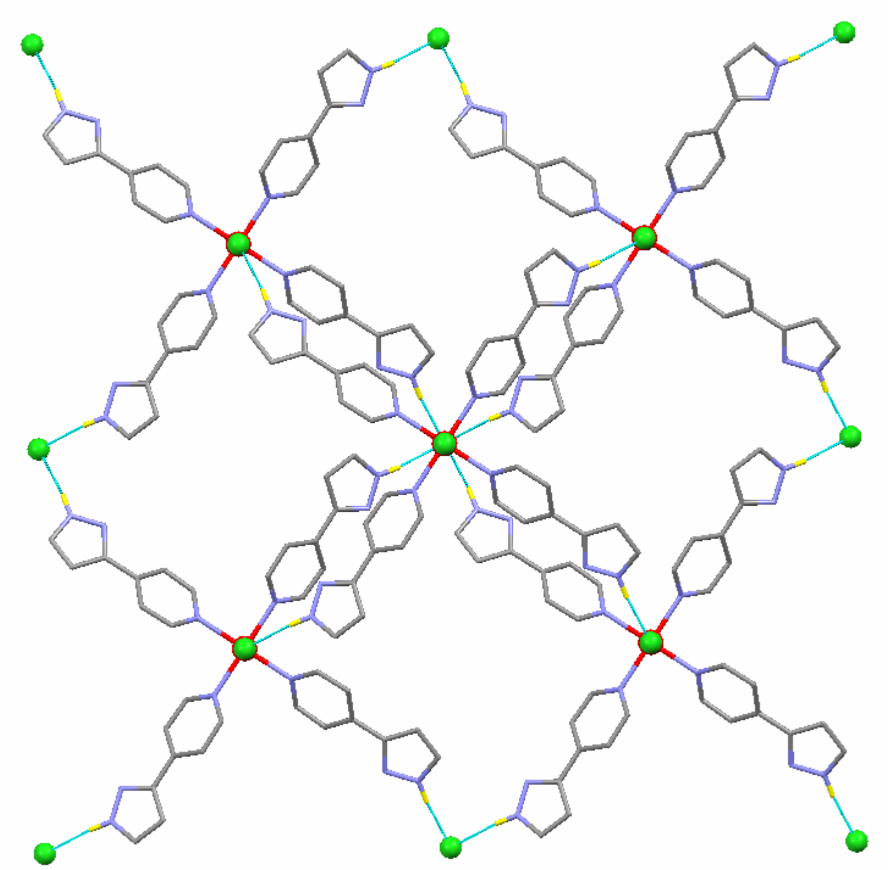

Fig. 2.2.4 – Packing diagram of [Co(4pypz)$_4$Cl$_2$]·4MeCN
Viewing down the c-axis

Co(1)-N(1A)	2.1658(16)
Co(1)-Cl(2)	2.3976(14)
Co(1)-Cl(1)	2.5759(13)
N(1A)-Co(1)-N(1B)	174.78(12)
N(1A)-Co(1)-N(1C)	89.881(6)
N(1A)-Co(1)-Cl(2)	92.61(6)
N(1A)-Co(1)-Cl(1)	87.39(6)
Cl(2)-Co(1)-Cl(1)	180

Table 2.2.2 – Selected bond lengths (Å) and angles (°) for [Co(4pypz)$_4$Cl$_2$]·4MeCN

Hydrogen bonding also occurs between a pyrazole hydrogen and the nitrogen atom of a lone MeCN solvent molecule [CH(8)···N(22) = 2.607 Å, C(8)···N(22) = 3.363(4) Å]. Four such interactions occur in the unit cell, all orientated in the same direction (**Fig. 2.2.3**).

These solvent molecules reside in the channels created in the coordination network and are arranged in a spiral manner as we progress through the channel with a separation of 5.0 Å between the N(22) atoms (**Fig. 2.2.5**). During elemental analyses, samples continued to lose weight and measurements were taken on samples that had remained on the balance for 30 min. Results show that in this time, MeCN had evaporated which was confirmed by the absence of C≡N stretches in the IR spectrum.

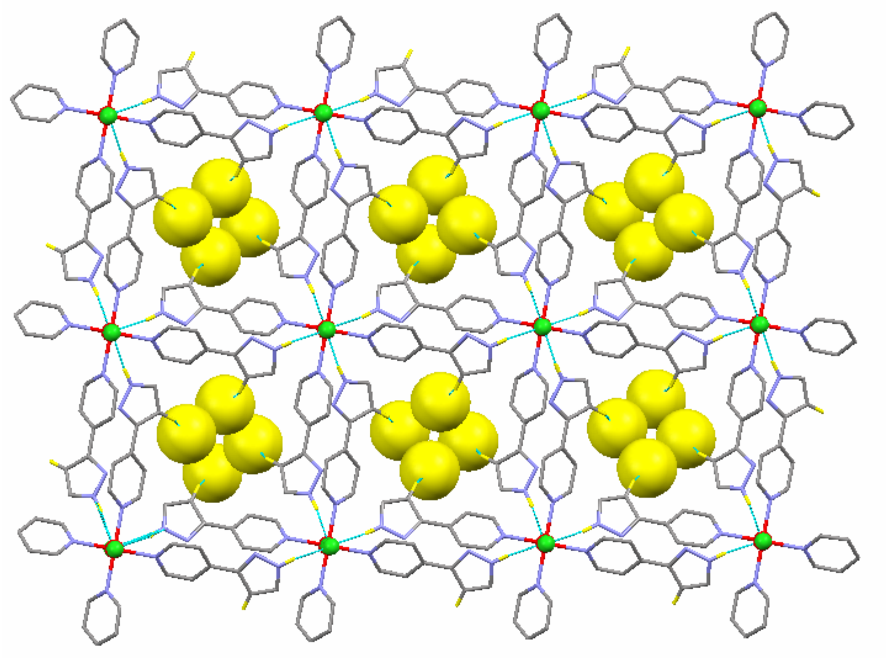

Fig. 2.2.5 – Packing diagram of [Co(4pypz)$_4$Cl$_2$]·4MeCN showing the solvent molecules. Viewing down the c-axis

2.2.3 Thallium(I) Salts of Scorpionates based on the 4pypz Motif

All scorpionates were initially synthesised as the potassium salts and successfully purified. For the purposes of structural characterisation these were then converted to the Tl(I) salts as TlTp complexes tend to crystallise more easily than KTp complexes, and Tl(I) is also taken to be the default reference metal in such discussions of scorpionates.[7]

Reaction of the potassium-scorpionate salt with one equivalent of Tl(OAc) in methanol afforded the desired products as white precipitates, and X-Ray quality crystals were grown from diffusion of ether vapour into a concentrated DMF solution [$\mathrm{Tl(Bp^{4py})}$] or by slow evaporation of a concentrated CH_2Cl_2-MeOH solution of the complex [$\mathrm{Tl(Tp^{4py})}$].

2.2.3.1 $\mathrm{Tl(Bp^{4py})}$

Fig. 2.2.6 shows that this complex does display the coordination polymer behaviour that we were hoping for in the solid state. The metal ion, whilst being chelated by the two pyrazole nitrogens (average $N_{pz}\cdots$Tl distance = 2.696 Å), is also coordinated to the pendant 4-pyridyl group of a second $\mathrm{Tl(Bp^{4py})}$ unit [N(109)···Tl(1) = 2.678(7) Å]. Only one of the ligand's two 4-pyridyl units coordinates to the Tl(1) metal ion, giving rise to the formation of a one dimensional polymeric chain along the b-axis, and as the $\mathrm{Bp^{4py}}$ is bent at 110.48° (due to the hybridisation of the boron atom), this chain is helical (**Fig. 2.2.7**).

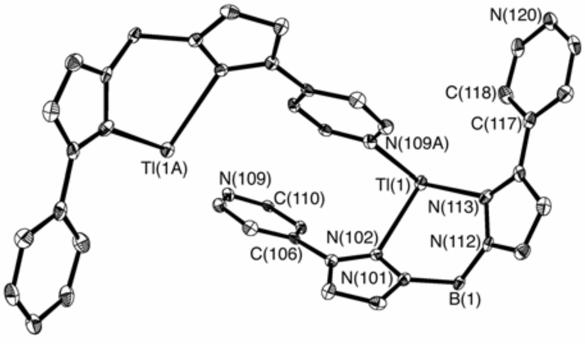

Fig. 2.2.6 – Crystal structure of $\mathrm{Tl(Bp^{4py})}$ showing the labelling system

Flack parameter = -0.020(14)

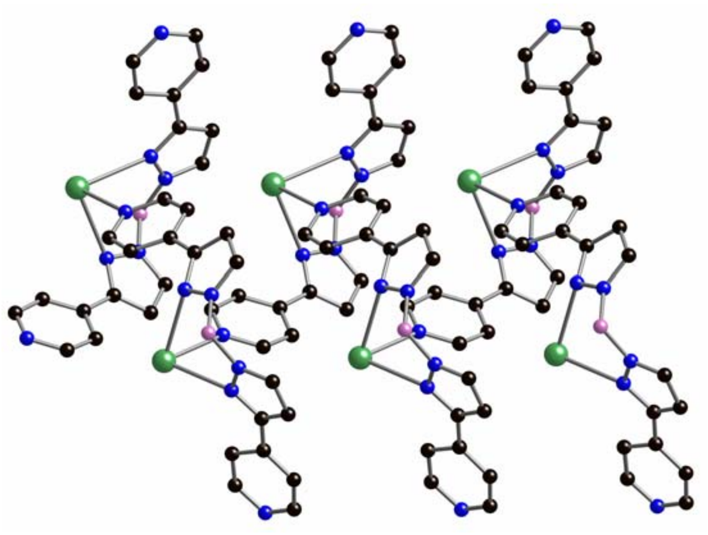

Fig. 2.2.7 – One-dimensional helical polymer of Tl(Bp^{4py}) viewing down the c-axis [Tl, green; B, purple; N, blue; C, black]

With three nitrogen donors about it (two pyrazole and one pyridyl), the metal ion resides in a pyramidal three-coordinate environment. This environment is common in Tl-scorpionate complexes,[16-18] but mainly with Tp-based ligands as Bp-based scorpionates appear to favour coordination through the two pyrazole nitrogens and an agostic Tl···H interaction from a B-H bond on the same ligand.[19,20] The pyramidal arrangement suggests that the thallium's lone pair is stereochemically active in completing the tetrahedral array of electron pairs about the metal ion,[21] yet the N-Tl-N angles are considerably compressed compared to the tetrahedral ideal (**Table 2.2.3**) (attributed to the steric requirements of the ligand).

Tl(1)-N(102)	2.641(6)
Tl(1)-N(109)	2.678(7)
Tl(1)-N(113)	2.751(7)
N(102)-Tl(1)-N(109)	77.4(2)
N(102)-Tl(1)-N(113)	84.5(2)
N(109)-Tl(1)-N(113)	82.1(2)

Table 2.2.3 – Selected bond lengths (Å) and angles (°) for Tl(Bp^{4py})

To assist packing, the pyridyl groups are twisted with respect to the pyrazole rings at angles of 4° and 26° for the units containing N(109) and N(120) respectively, with the former unit assisting in building up the polymer chain. Whilst the 4-pyridyl group containing N(120) does not coordinate to a metal ion, N(120) does form a hydrogen bond with a pyridyl hydrogen of a separate Tl(Bp^{4py}) unit [CH(107)···N(120) = 2.515 Å, C(107)···N(120) = 3.359(13) Å]. This holds the helical chains in a 'sheet' (**Fig. 2.2.8**) with the stacking of these sheets forming the complete structure of the crystal.

It is worth noting that these one-dimensional chains are also chiral, and that the chiral space group ($P2_1$) of the crystal system indicates that it comprises only chains of the same chirality, rather than a racemic mixture. The solubility of the complex in DMF implies that the polymer breaks up into its monomer units in solution, with loss of the N(109)···Tl(1) bond. This was confirmed when ^{1}H NMR studies showed only the one set of protons at low-temperature, indicating that all pyridyl groups were in the same environment when in solution.

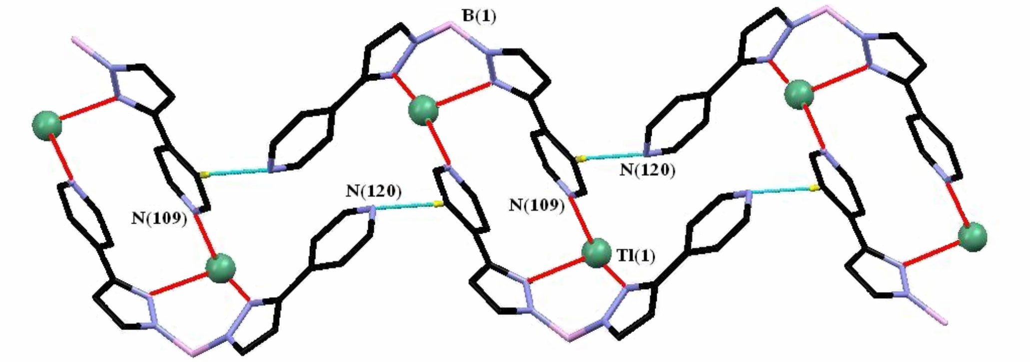

Fig. 2.2.8 – Sheet of one-dimensional chains
Viewing down the b-axis

2.2.3.2 Tl(Tp^{4py})

As a monomer, the complex Tl(Tp^{4py}) is reminiscent of the functionalised bowl-shaped ligands synthesised by Fujita and co-workers to template the formation of capsules.[22]

Whilst the base of their bowl was made of a mesitylene unit, and ours a boron atom, the sides of the bowl and the functionalised 'rim' comprise the same 4-pyridyl units and their nitrogen atoms respectively. However, the crystal structure of Tl(Tp^{4py}) shows that capsule formation is not possible when the metal ion in the cavity has a vacant coordination site (**Fig. 2.2.9**).

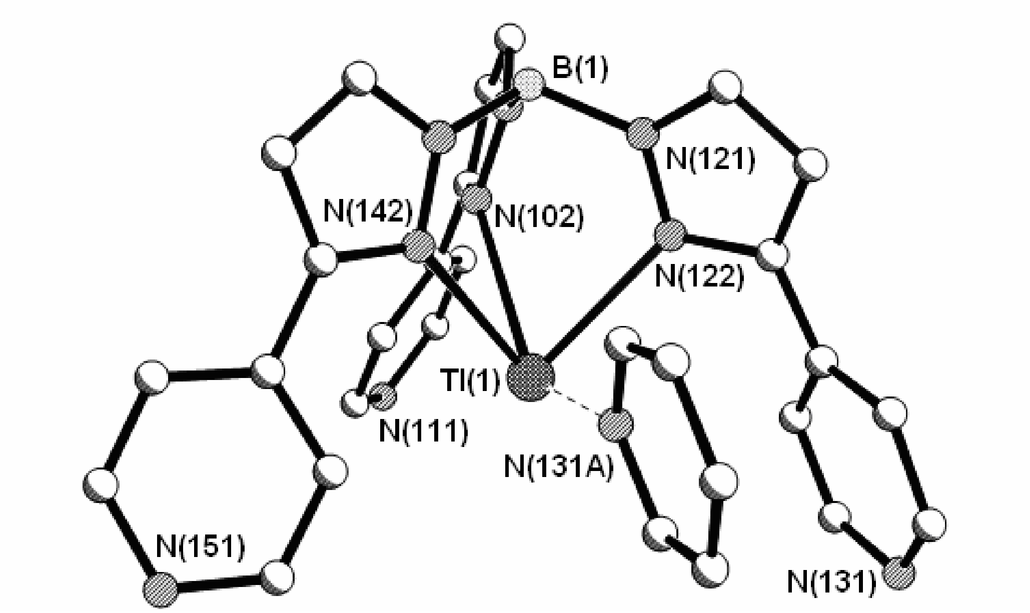

Fig. 2.2.9 – Crystal structure of Tl(Tp^{4py}) showing approach of an external unit
Flack parameter = 0.031(10)

Even though there are now three pyridyl-pyrazole arms surrounding the metal ion, the large wedge angle of the complex (average N_{pz}-B-N_{pz} value = 75.4°, where N_{pz} is the non-boron bound nitrogen) still permits the 4-pyridyl group of a separate monomer unit to coordinate and again build up a one dimensional chain, this time along the **c**-axis [**Fig. 2.2.10**, N(131)···Tl(1) = 2.978(8) Å]. This is also reminiscent of the Tl(Tp^{tol}) complex synthesised by Ferguson (**Fig. 1.1.16**), where the cavity was still sufficiently large for the toluene group on a separate complex unit to fill it, even though it did not contain any donor atoms.[17]

The bridging N_{py}···Tl bond is quite long compared to the average N_{pz}···Tl values (2.98 Å *vs.* 2.66 Å respectively) forming through the two ligating arms with the largest wedge angle (those arms containing N(121) and N(141), at 78.53°).

As with the Tl(Tp^{tol}) complex,[17] the metal ion here is held in a pyramidal geometry by the three pyrazole donors and the N$_{py}$···Tl bond is very much a side-on coordination, occurring directly opposite the N(102)···Tl bond - the longest of the N$_{pz}$···Tl bonds at 2.791(7) Å. With the Tl(I) lone pair, the geometry about the metal centre becomes a distorted square-based pyramid.

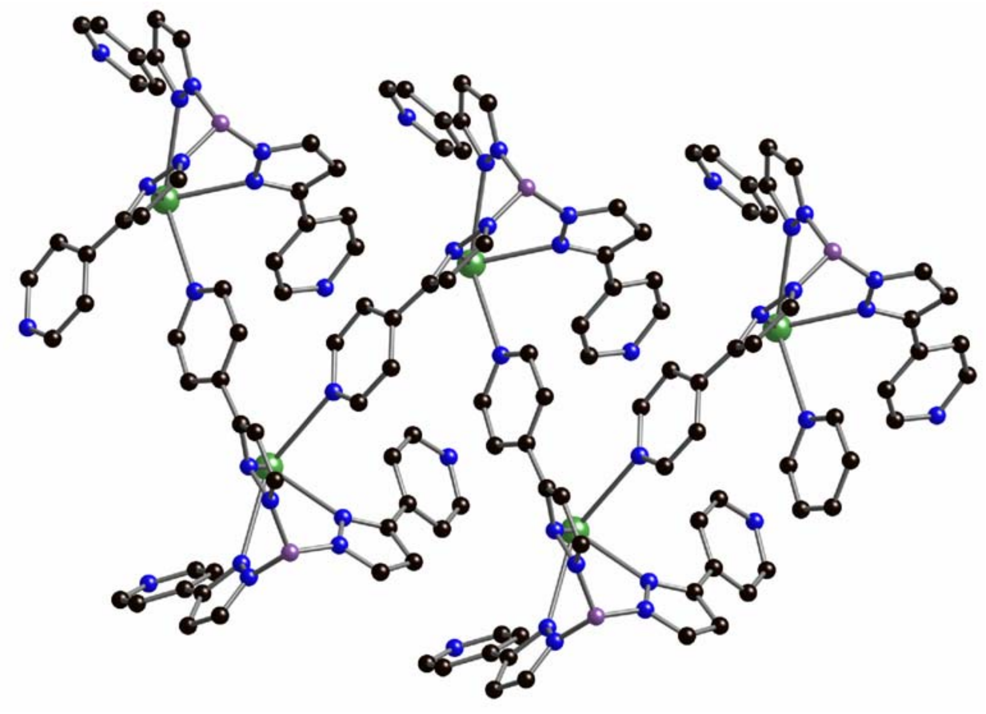

Fig. 2.2.10 – One-dimensional polymeric chain formation in Tl(Tp^{4py})
View along the a-axis

All three pyridyl groups are twisted from their neighbouring pyrazole rings by 29, 27 and 35° for the rings containing N(151), N(111) and N(131) respectively, with the largest twist present on the one coordinating to Tl(1) [N(131)]. No helical formation is apparent in the chain, as the steric bulk of the Tp^{4py} ligands do not favour such behaviour; instead the chain has a side-to-side 'rocking' appearance as it extends parallel to the **c**-axis (**Fig. 2.2.11**).

As we found with Tl(Bp^{4py}) only one pyridyl group coordinates to a metal ion, and there seems to be no second- nor third-dimension polymeric behaviour induced by having two additional 4-pyridyl groups.

However, as **Fig. 2.2.11** shows, both N(151) and N(111) pyridyl groups participate in CH···N hydrogen bonding to atoms in adjacent chains [CH(135)···N(151), CH(145)···N(111), CH(105)···N(111) at 2.455, 2.398 and 2.732 Å respectively; with C(135)···N(151), C(145)···N(111), C(105)···N(111) at 3.242(15), 3.319(15) and 3.648(15) Å respectively] giving rise to a stacking of sheets in the crystal motif. Selected bond lengths and angles are given in **Table 2.2.4**.

Tl(1)-N(122)	2.577(8)
Tl(1)-N(142)	2.609(9)
Tl(1)-N(102)	2.791(7)
N(122)-Tl(1)-N(142)	77.9(3)
N(122)-Tl(1)-N(102)	72.3(2)
N(142)-Tl(1)-N(102)	67.3(2)

Table 2.2.4 – Selected bond lengths (Å) and angles (°) for Tl(Tp^{4py})

The chiral space group P*c* indicates again that the crystal comprises only chains of the same chirality, as was the case with Tl(Bp^{4py}), and it is worth noting that both complexes form these chiral chains whilst the units themselves are achiral. Chiral coordination polymers have found use in enantiomeric selection of small organic molecules[23] and catalysis[24] and can be formed through non-covalent interactions of chiral ligands,[25] or through the spontaneous self-assembly (as in our case) of achiral ligands.[26,27] Such non-centrosymmetric, polymeric crystal systems, may also meet the criteria for displaying second-order nonlinear optical properties.[28,29]

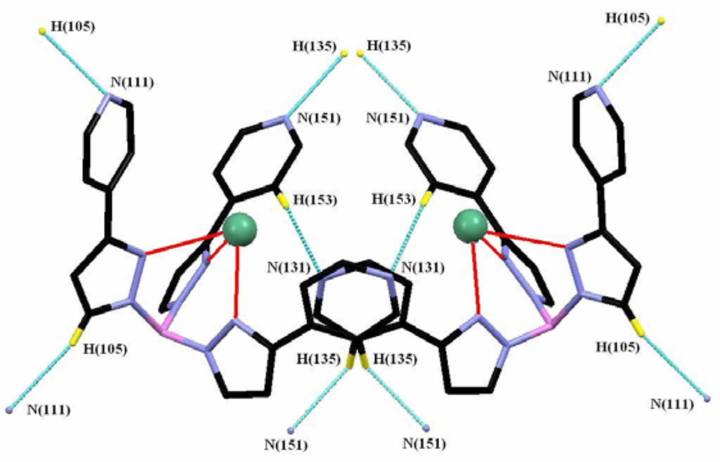

Fig. 2.2.11 – View of the one-dimensional chain along the c-axis

2.2.3.3 Tl(Tkp^{4py})

Batten and Duriska[3] achieved tetra-substitution of the boron atom by using a 4:1 excess of pyridyl-pyrazole and heating the reaction mixture to 250 °C. Whilst the Tl(I) ions sits in the usual N_{pz} pocket, a fourth $N_{pz}\cdots$Tl bond is not possible because the sp^3-hybridisation of the boron atom directs the nitrogen [N(171)] away from the metal ion (**Fig. 2.2.12a**). Only two pyridyl nitrogens [N(111) and N(131)] interact with adjacent metal ions, making the Tl(I) centres five coordinate, although the geometry about the metal ions is in fact distorted octahedral with the inclusion of the lone pair (**Fig. 2.2.12b**).

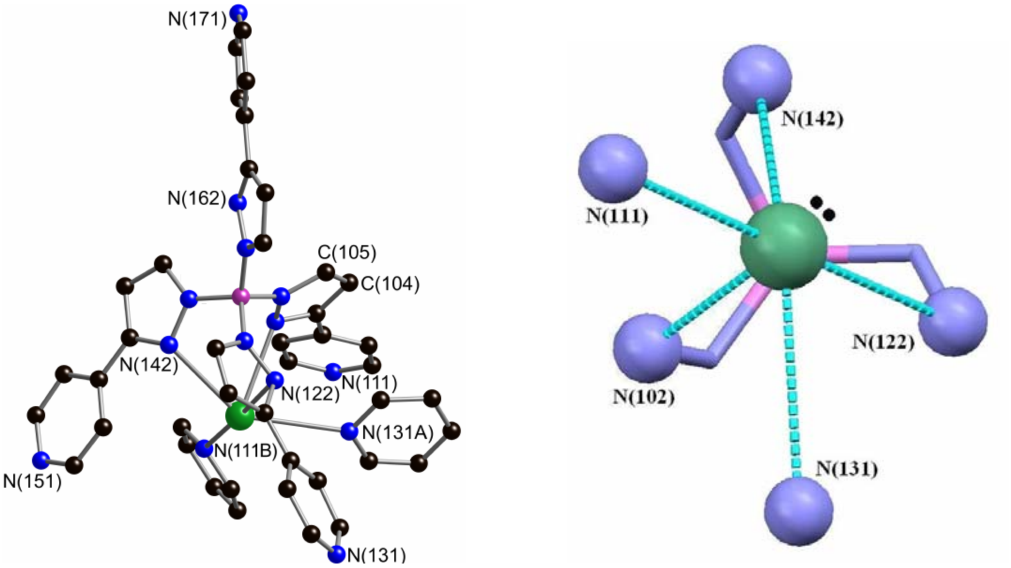

(a) **(b)**

Fig. 2.2.12 – (a) Crystal structure of Tl(Tkp^{4py})
(b) Geometry about the Tl(I) ion [viewing down the Tl(1)-B(1)-N(161) bond]

N(111) and N(131) bridge the metal ions of adjacent [Tl(Tkp^{4py})] units in perpendicular directions to produce a chiral two-dimensional sheet. This can be seen in **Fig. 2.2.13** in which the non Tl(I)-coordinating pyridyl-pyrazole arms have been removed for clarity.

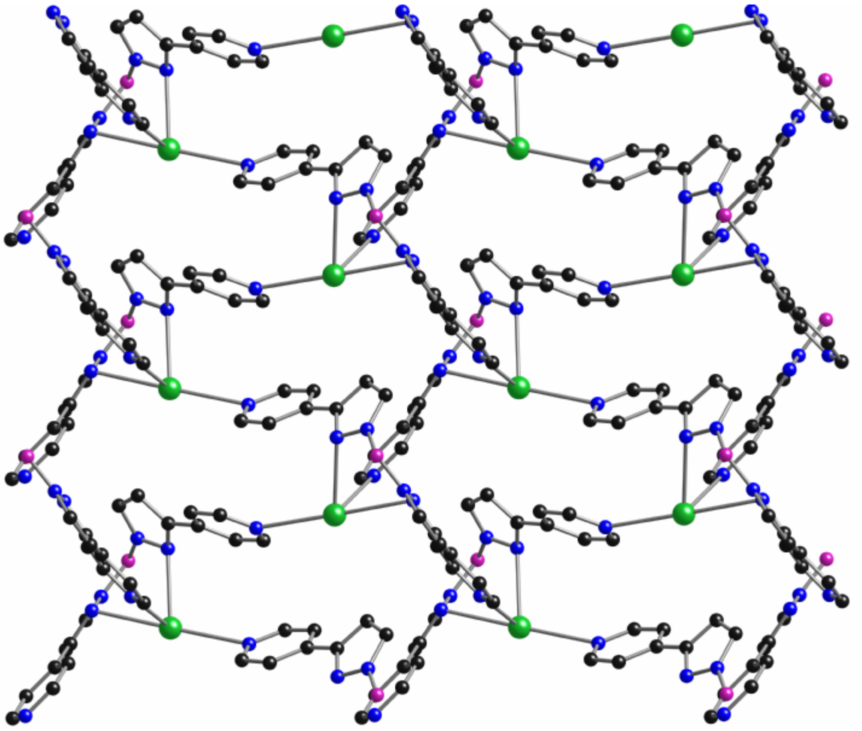

Fig. 2.2.13 – Two dimensional sheet formed by N(131) and N(111) bridging Tl(1) in perpendicular directions

Reaction of [KTkp^{4py}] with Ag(I) sees two pyridyl donors bond to the metal ion, but this time at the expense of a $N_{pz}\cdots M$ bond, leaving a distorted tetrahedral geometry about the metal centre. A more detailed description of this and the Tl(I) structure can be found in our joint publication.[3]

2.2.4 Other Metal Salts of Scorpionates based on 4pypz

2.2.4.1 Re(Tp^{4py})(CO)$_3$

Given the likeness of our Tp^{4py} system to that of the Fujita bowl,[22] we hoped to find a suitable metal that would allow us to isolate a 1:1 metal:ligand complex devoid of polymeric behaviour. The uncoordinated pyridyl nitrogens would then give the complex the potential to act as a 'functionalised' bowl.

Following a similar method to the preparation of [(Tp)Re(CO)$_3$] by McCleverty *et al*,[30] the title complex was produced in good yield by the reaction of KTp^{4py} and one equivalent of Re(CO)$_5$Cl in thf.

The carbonyl stretches in the IR spectrum were similar to those obtained for [(Tp*)Re(CO)$_3$][30] and [(Tp)Re(CO)$_3$],[31] indicating a *fac*-tricarbonyl arrangement, which was to be expected given the geometry of the pyrazole donors.[7] X-Ray quality crystals were grown by the slow evaporation of a concentrated acetone solution of the complex.

Data for the crystal structure (**Fig. 2.2.14**) were collected and the structure solved by Professor Michael Hurthouse and Dr Simon Coles at the University of Southampton.

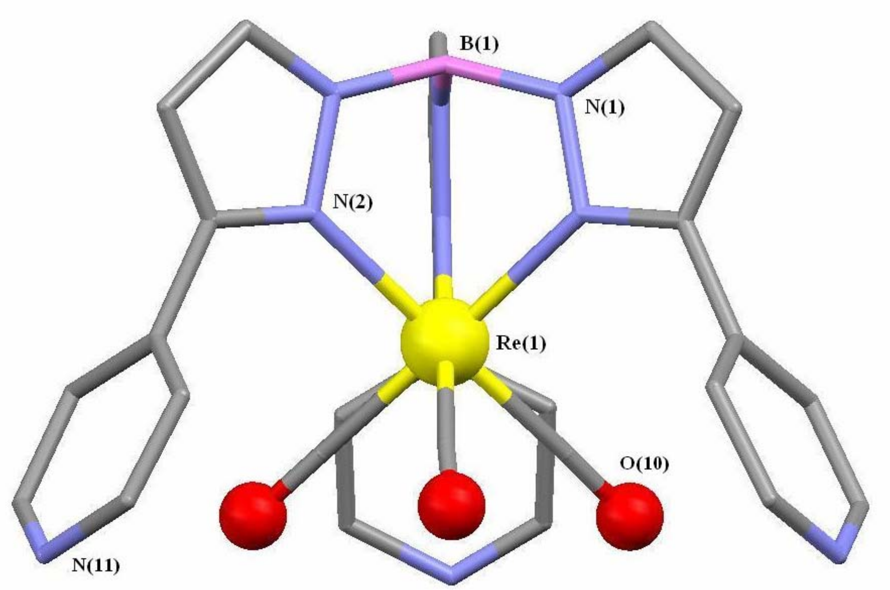

Fig. 2.2.14 – Crystal structure of [Re(Tp^{4py})(CO)$_3$], viewing down the b-axis

The reaction is accompanied by formation of KCl and the displacement of two CO molecules by the scorpionate to give a *fac*-N$_3$(CO)$_3$ coordination environment about the rhenium(I) centre (selected bond lengths and angles given in **Table 2.2.5**).

The complex has 3-fold symmetry (crystallising in the hexagonal space group $P6_3$), with the carbonyl groups pointing between the pyridyl-pyrazole arms to minimise steric and electronic repulsions. The pyridyl substituents reside almost at right angles to the pyrazole rings (91.7°) and the Re(I) atom sits 1.7 Å out of the plane of the three N_{pz} donors [N(2)···Re(I) = 2.229(12) Å].

Re(1)-C(10)	1.980(16)
Re(1)-N(2)	2.229(12)
C(10)-Re(1)-C(10A)	86.9(6)
C(10)-Re(1)-N(2)	94.8(5)
C(10)-Re(1)-N(2B)	178.0(5)
N(2)-Re(1)-N(2A)	84.0(5)

Table 2.2.5 – Selected bond lengths (Å) and angles (°) for $[Re(Tp^{4py})(CO)_3]$

Graham Motson (in the McCleverty/Ward group) had previously synthesised the analogous Tp^{2py} complex without the displacement of additional carbonyl groups, even though the pyridyl donors point towards the metal centre in the perfect orientation for coordination.[3] This suggests that the $\{Re(CO)_3\}^+$ unit has a high stability and explains why none of the 4-pyridyl groups in the Tp^{4py} complex undergo coordination to a second metal centre - unlike the cases we have previously seen with +1 metal ions. However, they do undergo hydrogen bonding to neighbouring complexes, which are stacked directly above and below each other, with a separation of 1.24 Å, and held partly in place by the CH(5)···N(11) interaction (2.763 Å).

The hydrogen bond N(11)···H(15) at 2.766 Å [N(11)···C(5) = 3.367(22) Å] connects the chains together and gives rise to the packing motif illustrated in **Fig. 2.2.15**, where it can be seen that a network of N(11)···H(15) bonds outline the shape and define the walls of hexagonal channels with an approximate diameter of 9 Å. The network occurs between neighbouring complexes on progressive planes rather than the same plane, and the hexagonal periphery is formed by viewing down the **c**-axis of a one-dimensional helical array of six $[Re(Tp^{4py})(CO)_3]$ units (illustrative of the crystal's chiral space group, **Fig. 2.2.16**).

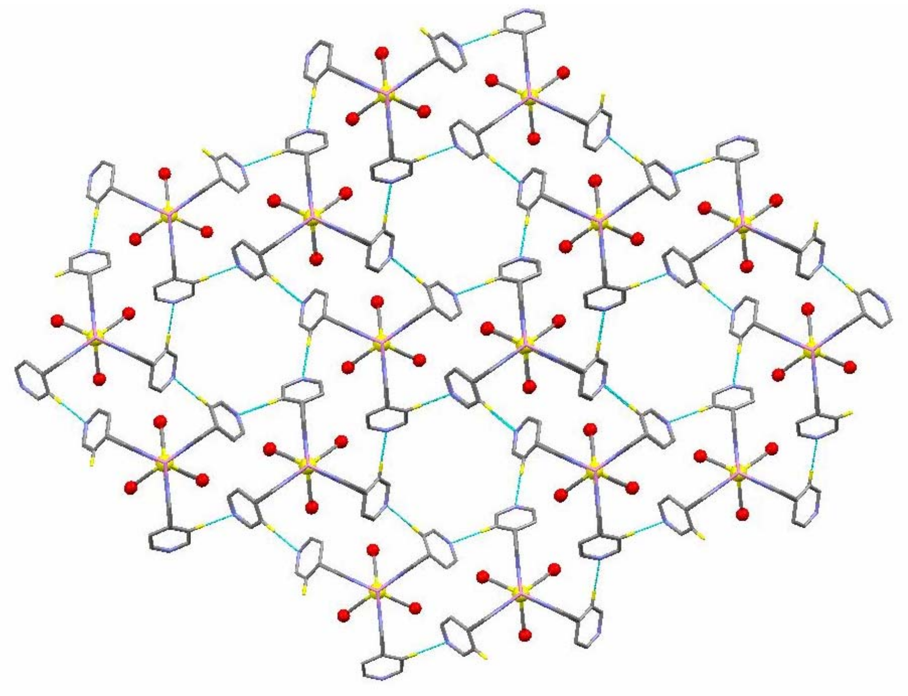

Fig. 2.2.15 – Packing diagram of [Re(Tp^{4py})(CO)$_3$], viewing down the c-axis
Spurious electron density and all hydrogen atoms bar H(15) have been removed for clarity

The hexagonal channels may contain disordered solvent molecules as residual electron density peaks in the lattice which could not be modelled, and presumably correspond to disordered solvent molecules, were removed from the data set using the SQUEEZE function from PLATON.[32]

2.2.4.2 Cu$_2$(Tp^{4py})

Reaction of KTp^{4py} with one equivalent of [Cu(MeCN)$_4$]PF$_6$ in methanol produced a green precipitate which was found to be insoluble in most common solvents. Heavy sonication in DMF encouraged partial solubility however, and slow diffusion of diethyl ether into this solution produced X-ray quality crystals.

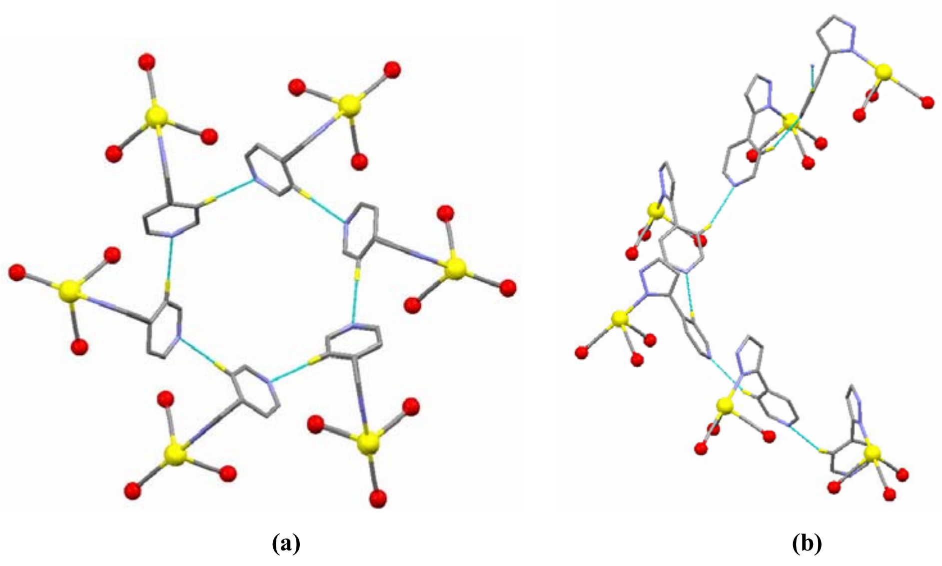

Fig. 2.2.16 – [Re(Tp^{4py})(CO)$_3$]: (a) viewing down the c-axis
(b) side on view of the same six molecules.
Selected pyridyl-pyrazole arms and hydrogen atoms have been removed for clarity.

Elemental analysis of the green powder was inconsistent with any foreseeable 'simple' formulation, whilst FAB mass spectra indicated peaks at *m/z* 508 and also at 1016, indicative of 1:1 and 2:2 Cu:Tp^{4py} complexes respectively. A UV/VIS spectrum of the complex in DMF showed a weak transition at 641 nm, indicative of a metal-centred Cu(II) *d-d* transition, with a characteristically small molar extinction coefficient ($\varepsilon \approx 30$ M^{-1} cm^{-1})[33] suggesting that the reaction mixture contained either $\{Cu(Tp^{4py})\}^+$ or $\{Cu_2(Tp^{4py})_2\}^{2+}$ cations. It is well known however that mixtures of Cu(I) and Cu(II) can exist in solution,[34] and upon single crystal formation the complexes crystallises in the form of a 2:2 complex, but in the Cu(I) oxidation state (**Fig. 2.2.17**).

In the crystal, the pyridyl nitrogen N(151) of one Cu(Tp^{4py}) unit coordinates to an adjacent metal ion to complete a pseudo-tetrahedral N_4 donor array about the Cu(1) metal, which is already held by the three N_{pz} donors, resulting in a centrosymmetric dimer.

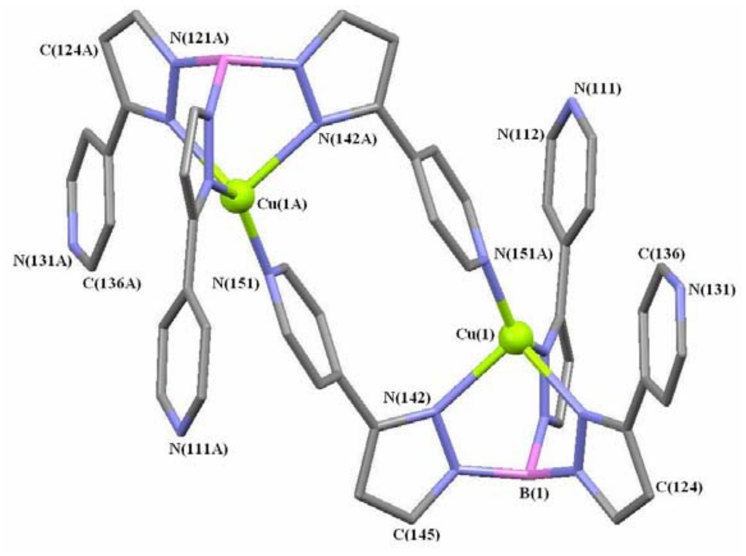

Fig. 2.2.17 – Crystal structure of [$Cu_2(Tp^{4py})_2$]

The average N_{pz}···Cu(1) distance is 2.120 Å, and the metal ion sits 1.204 Å above the mean plane of these donors whilst bonding to the N(151) atom at a distance of 1.965(3) Å to form the dimer. The resultant 'box' formed between Cu(1)-N(142)-Cu(1A)-N(142A) has an approximate area of 21 Å^2. Selected bond lengths and angles are given in **Table 2.2.6**.

Cu(1)-N(151A)	1.965(3)	Cu(1)-N(122)	2.110(3)
Cu(1)-N(102)	2.062(2)	Cu(1)-N(142)	2.187(3)
N(151A)-Cu(1)-N(102)	134.27(10)	N(151A)-Cu(1)-N(142)	110.20(10)
N(151A)-Cu(1)-N(122)	127.36(11)	N(102)-Cu(1)-N(142)	91.36(10)
N(102)-Cu(1)-N(122)	90.54(10)	N(122)-Cu(1)-N(142)	90.68(10)

Table 2.2.6 – Selected bond lengths (Å) and angles (°) for [$Cu(Tp^{4py})$]$_2$

Torsion angles vary depending on the arm concerned, with the N(151) pyridyl ring twisted 57° from the mean plane of the N(141) pyrazolyl ring, and 34° [N(111)] and 27° [N(131)] torsion angles for the other two substituents. There is also a 3.466 Å separation between the bridging N(151) pyridyl rings with an offset overlap of 1.164 Å (centroid-centroid distance = 3.716 Å), suggesting that the structure is formed with the help of π-π stacking.

N(111) bonds with H(156) from the pyridyl ring of a neighbouring dimer unit [CH(156)···N(111) = 2.586 Å, C(156)···N(111) = 3.225(45) Å] to form a channel of stacked dimer units along the **b**-axis. Cross linkage of these channels is then performed by bonding between N(131) and H(125) at 2.550 Å [N(131)···C(125) = 3.466(34) Å] connecting the channels across the **ac** face of the unit cell (**Fig. 2.2.18**).

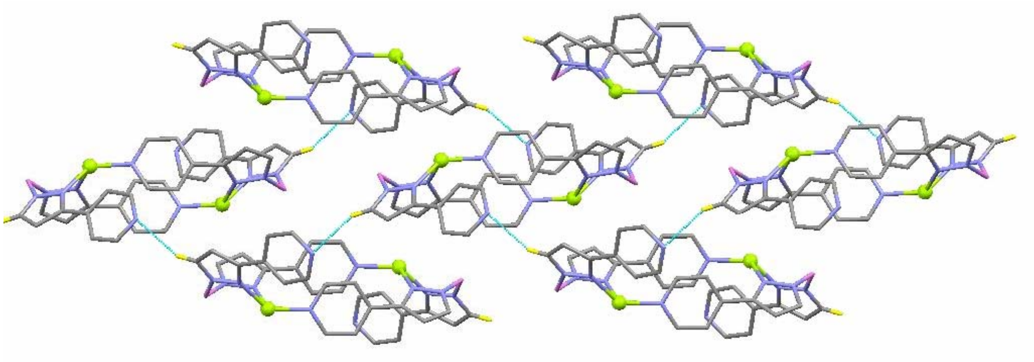

Fig. 2.2.18 – Packing diagram of [$Cu_2(Tp^{4py})_2$] viewing down the b-axis
Selected H atoms and the N(111)-containing pypz arm have been removed for clarity

Such 2:2 dinuclear complexes are a familiar occurrence in supramolecular chemistry, resulting from the complementary interaction of two identical components whose units contain a pendant donor atom and a metal ion with a vacant coordination site. Both Hannon[35] and Champness[36] observed this in their researches, with Hannon's ligand designed specifically to eliminate polymeric formation, and Champness' dimer resulting from an absence of suitable anions to template cage formation. In both cases, the external donor was a pyridyl unit (2- or 4-pyridyl respectively).

Batten and co-workers discovered that this bridging behaviour of Tp^{4py} can lead to remarkable cage–type architectures.[37] What is remarkable about their structure (**Fig. 2.2.19**) is it contains eight Tp^{4py} ligands with fourteen copper metal centres – eight Cu(I) ions and six Cu(II) ions (shown in pink and blue respectively) – with neutrality achieved by perchlorate counter anions. A Cu(I) ion resides in each Tp^{4py} cavity whilst the pyridyl donors occupy one corner of the d_{x2-y2} orbital of the Cu(II) square plane, giving a cubic structure with a {Cu(I)Tp^{4py}} unit at each corner and a Cu(II) ion in the centre of each face, with a perchlorate ion occupying the central cavity.

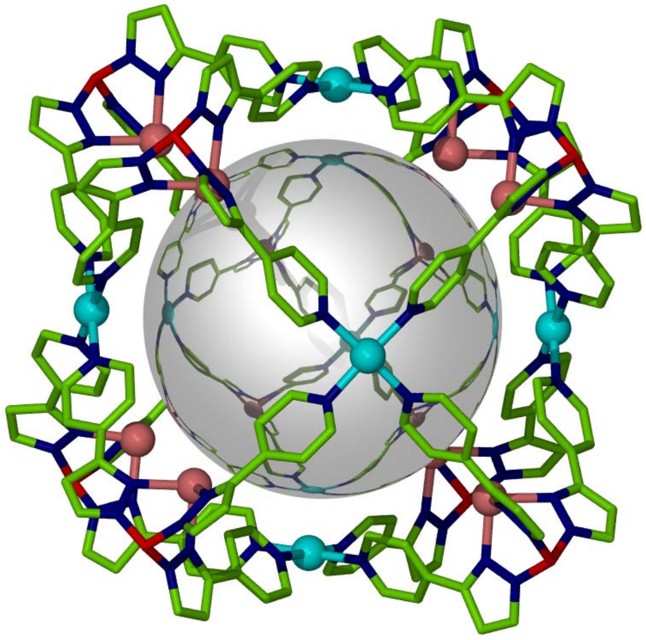

Fig. 2.2.19 – Crystal Structure of $[Cu_{14}(Tp^{4py})_8][ClO_4]_{12}$
Reproduced with permission from Dr Stuart R. Batten

2.2.5 Thallium(I) Salts of Scorpionates based on the 3pypz Motif

Tl(I) complexes of Bp^{3py} and Tp^{3py} were prepared from the K^+ salts of the ligands in a similar manner to those of the 4pypz scorpionates (**Section 2.2.3**). X-Ray quality crystals were grown from the layering of isopropyl ether onto a concentrated CH_2Cl_2 $[Tl(Bp^{3py})]$ or CH_2Cl_2-MeOH $[Tl(Tp^{3py})]$ solution of the complex.

2.2.5.1 $Tl(Bp^{3py})$

Shifting the pyrazole ring to the 3-position on the pyridyl group removes the C_2 rotation axis of the latter, relative to the pyrazole group, with the consequence that there are now two conformations the pyridyl-pyrazole arm can now adopt – *cisoid* or *transoid* (**Fig. 2.2.20**).

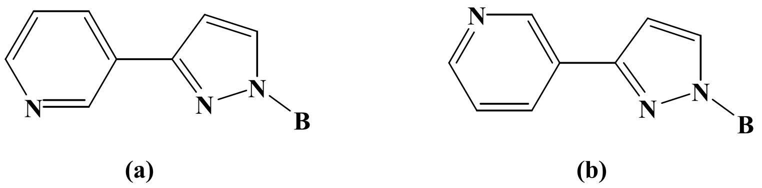

Fig. 2.2.20 – Cisoid (a) and transoid (b) arrangements in 3pypz

Tl(Bp^{3py}) crystallises with two independent molecules in the asymmetric unit; each Bp^{3py} unit has one arm in a transoid arrangement and the other in a cisoid arrangement (**Fig. 2.2.21**). The pyridyl ring containing N(31) was found to be disordered over two closely spaced sites, and has been modelled as such with 51 % : 49 % site occupancies.

All four of the pyridyl donors in the asymmetric unit coordinate to the Tl(I) of an adjacent complex unit, and as the N(11)···Tl(1)···N(111) and N(31)···Tl(2)···N(131) bonds both extend along parallel paths, this results in a helical one-dimensional polymer along the **a**-axis (**Fig. 2.2.22**).

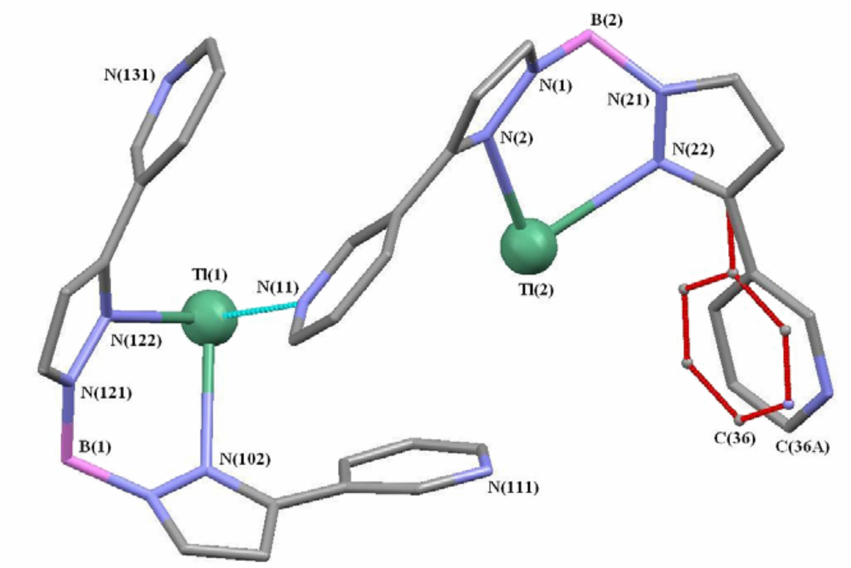

Fig. 2.2.21 – Crystal structure of Tl(Bp^{3py})·0.5CH$_2$Cl$_2$ showing the two crystallographically independent monomer units (the disordered component is shown in red)

The metal ion is 'pinched' by the two N$_{pz}$ donors - average N$_{pz}$···Tl distance = 2.653 Å, Tl(1) and 2.613 Å, Tl(2) – and forms a third bond with the pyridyl nitrogen of the second crystallographically independent monomer [Tl(1)···N(11) = 2.758(9) Å or Tl(2)···N(131) = 2.709(10) Å]. As it stands, the metal ion appears to be held by a pyramidal array of donors, with the Tl(1) lone pair completing a tetrahedron geometry.

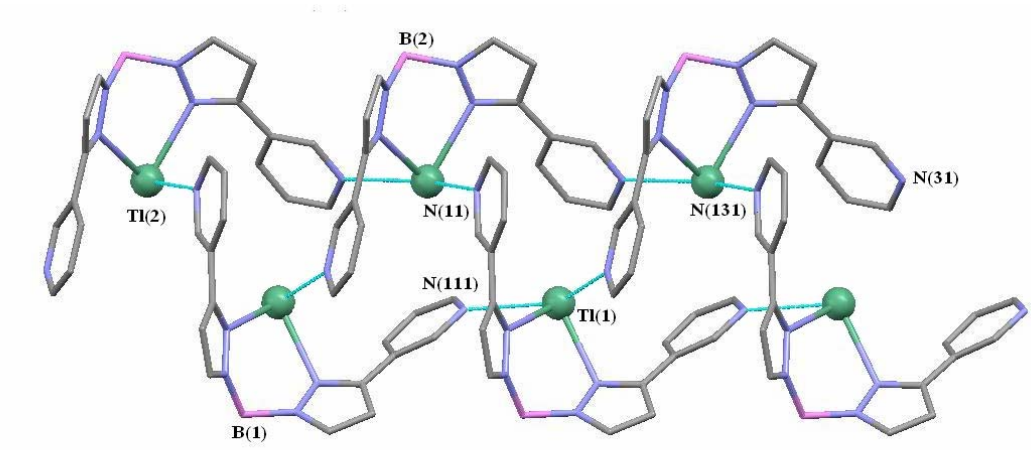

Fig. 2.2.22 – One-dimensional polymer of Tl(Bp^{3py})·0.5CH$_2$Cl$_2$ viewing down the b-axis (only one of the disordered components is shown)

However, a fourth (rather long) bond is formed to the pyridyl nitrogen of the *same* crystallographically independent unit [Tl(1)···N(111) = 2.985(10) Å, Tl(2)···N(31A) = 2.900(28) Å], giving rise to a distorted trigonal bipyramidal geometry, with the axial positions occupied by both pyridyl donors and the lone pair in an equatorial position with the pyrazole donor atoms (**Fig. 2.2.23**). Selected bond lengths and angles are given in **Table 2.2.7**.

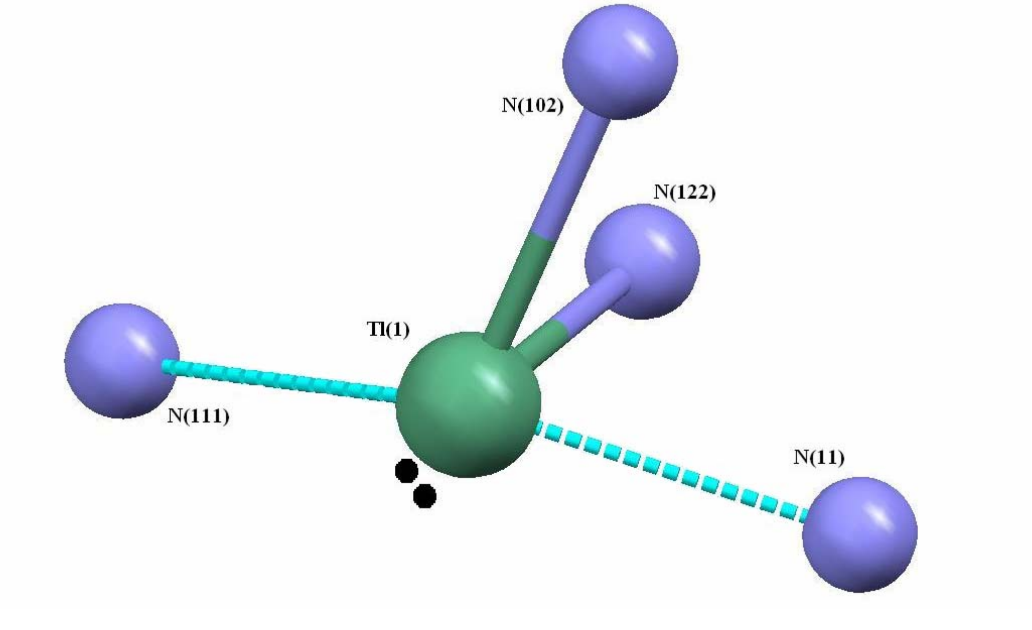

Fig. 2.2.23 – Distorted Trigonal bipyramidal geometry about the metal centre in Tl(Bp^{3py})·0.5CH$_2$Cl$_2$

N(2)-Tl(2)	2.601(8)	Tl(1)-N(102)	2.650(9)
N(22)-Tl(2)	2.624(8)	Tl(1)-N(122)	2.654(8)
Tl(2)-N(131)	2.709(10)	Tl(1)-N(11)	2.758(9)
N(2)-Tl(2)-N(22)	81.5(3)	N(102)-Tl(1)-N(122)	78.5(3)
N(2)-Tl(2)-N(131)	76.9(3)	N(102)-Tl(1)-N(11)	83.4(3)
N(22)-Tl(2)-N(131)	81.5(3)	N(122)-Tl(1)-N(11)	76.0(3)

Table 2.2.7 – Selected bond lengths (Å) and angles (°) for [Tl(Bp^{3py})].0.5CH$_2$Cl

Neighbouring chains reside approximately 3 Å from each other in the crystal and have the same internal helical arrangement of monomer units, albeit in opposite directions. The complex crystallises in the centrosymmetric space group $P2_1/c$ showing that the crystal contains an equal number of chains of both helical orientations (unlike the Bp^{4py} complex). As with all the Tl(I) complexes we have seen so far, the crystal's solubility in strong donor solvents such as DMF suggests that the polymer breaks up in solution.

2.2.5.2 Tl(Tp^{3py})

The monomer unit of Tl(Tp^{3py}) appears basically identical to the Tl(I) salts of Tp^{tol} and Tp^{4py}, and indeed Tp^{2py} (bar the relocation of the pyridyl nitrogens).[17,38] Whilst the average N$_{pz}$···Tl bond lengths of these complexes were 2.578, 2.659 and 2.691 Å respectively, that of Tl(Tp^{3py}) is larger at 2.828 Å. Also, in Tl(Tp^{4py}) the metal ion sat 1.924 Å out of the N$_{pz}$ mean plane, and this value again increases in Tl(Tp^{3py}) to 2.039 Å.

These changes in Tl-N$_{pz}$ bond length are related to the presence of bridging pyridyl groups from other monomers. For example, in Tl(Tp^{tol}), the average N$_{pz}$···Tl bond length was 2.585 Å; in Tl(Tp^{2py}), the pyridyl nitrogens also (albeit weakly) bond to the metal ion which results in lengthening of the N$_{pz}$···Tl bonds for electroneutrality reasons; whilst in Tl(Tp^{4py}), coordination of a pendant pyridyl unit from an adjacent monomer again results in long Tl···N$_{pz}$ bonds.

In Tl(Tp^{3py}), an extra *three* external pyridyl units are able to approach the metal ion from three different monomer units: N(111), N(131) and N(151) (**Fig. 2.2.24**). Although the average N_{py}···Tl bond length is 3.140 Å, the combined effect of three of these Tl···N_{py} bonds lengthens the N_{pz}···Tl bonds to an average of 2.828 Å – an adjustment necessary to maintain electroneutrality within the complex.

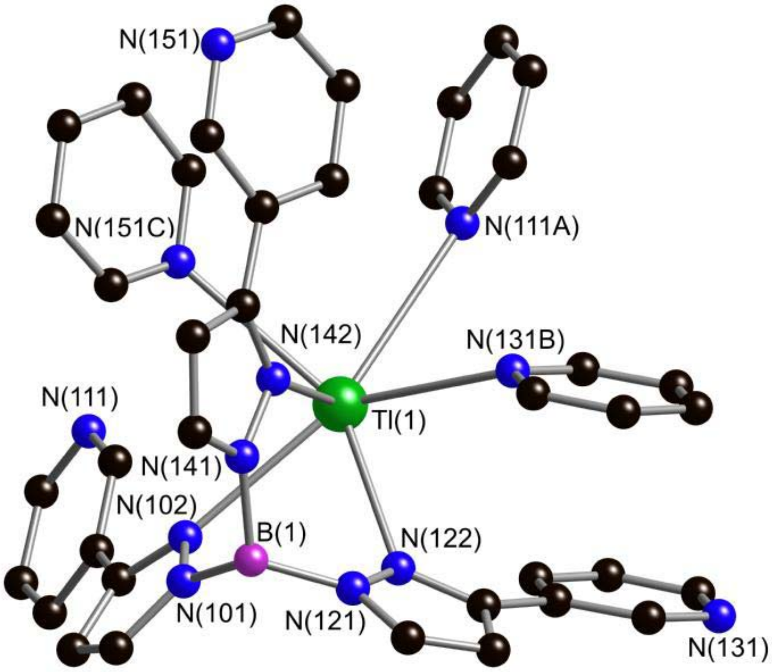

Fig. 2.2.24 – Crystal structure of Tl(Tp^{3py}) showing the labelling scheme

Only one Tl(Tp^{3py}) monomer resides in the asymmetric unit, with two of its arms in a transoid conformation and the third in a cisoid conformation. The cisoid arm displays a higher torsion angle between the pyridyl-pyrazole planes (24°, compared to 17° and 19° for the N(131) and N(151) pyridyl rings respectively).

These two bridging pyridyl donors result in formation of a polymer chain in a direction parallel to the **ab** face of the unit cell. Pairs of N(151) pyridyl rings are situated 3.400 Å apart by additional π-stacking forces (offset by 1.398 Å with a centroid-centroid separation of 3.470 Å, **Fig. 2.2.25**).

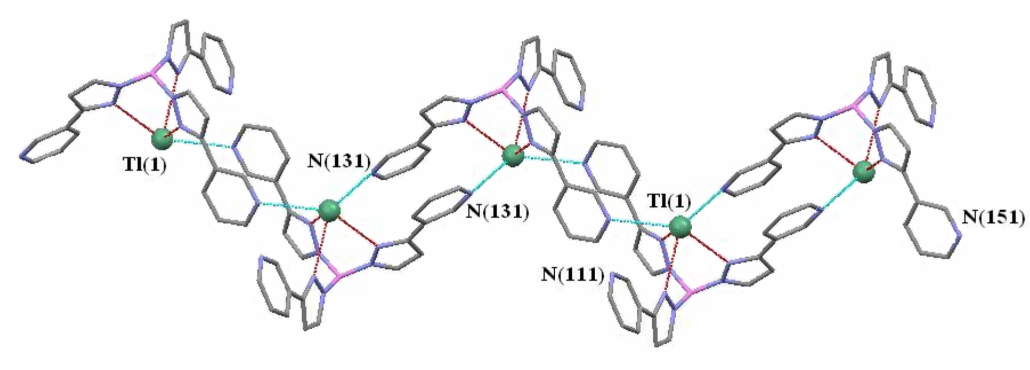

Fig. 2.2.25 – Extension of Tl(Tp^{3py}) *via* N(131)-Tl(1)-N(151) bridging

These one-dimensional chains are held together by the N(111)···Tl(1) bond which runs parallel to the **c**-axis at 3.368(3) Å, to give a two-dimensional sheet arrangement of chains which are then stacked in close proximity within the crystal (**Fig. 2.2.26**).

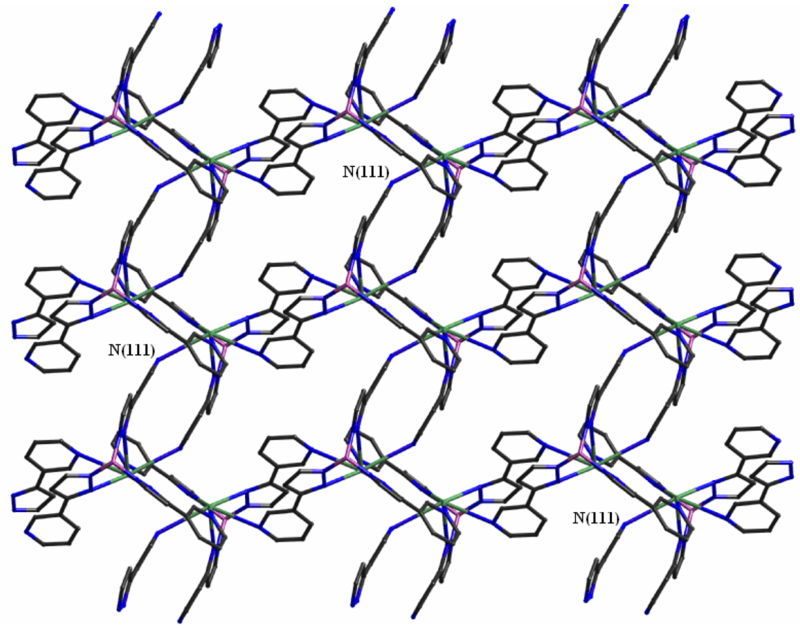

Fig. 2.2.26 – Two-dimensional sheet in Tl(Tp^{3py})
Viewing down the c-axis

The three N_{pz} and N_{py} donors about the metal ion do not represent any immediately obvious octahedral geometry, but there is a noticeably large vacant space on one side of the metal ion which is presumably filled by the lone pair of the metal ion, although no simple geometry can be determined for this arrangement. Selected bond lengths and angles are given in **Table 2.2.8**.

Tl(1)-N(142)	2.756(3)		
Tl(1)-N(122)	2.783(3)	N(142)-Tl(1)-N(122)	78.4(1)
Tl(1)-N(102)	2.937(3)	N(102)-Tl(1)-N(122)	67.8(1)
Tl(1)-N(131A)	2.950(3)	N(142)-Tl(1)-N(102)	73.0(1)
Tl(1)-N(151B)	3.111(3)		

Table 2.2.8 – Selected bond lengths (Å) and angles (°) for [Tl(Tp^{3py})]

It should be noted that Vahrenkamp previously synthesised a pair of Tp^{3py} analogues with methyl substituents residing on either the pyridyl and/or pyrazolyl rings, and obtained crystal structures of their potassium salts.[39] Due to the smaller size of the K$^+$ ion compared to Tl(I), only one external pyridyl donor coordinates to the metal ion, acting in the same manner as N(131) in Tl(Tp^{3py}), giving rise to 2:2 dimers as in **Fig. 2.2.17**, or 1:1 coordination polymers similar to that illustrated in **Fig. 2.2.25**. In the case of the 2:2 dimer, a single water molecule also occupies the coordination sphere of the K$^+$ ions, linking the units together *via* hydrogen bonding to nearby pyridyl donors. Similar structures were also observed in the analogous Zn^{2+} complex but with a halide ion in place of the water molecule, removing cross linking of the coordination polymers.[40]

2.2.5.3 Tl(Tkp^{3py})

In a similar way to Tl(Tp^{3py}), Tkp^{3py} wraps three of its pypz arms around the Tl(I) ion with two having a transoid conformation and the other a cisoid conformation. Batten and Duriska found the usual Tl···N$_{pz}$ coordination is adopted by two of the arms whilst one coordinates in an unusual η^2 side-on manner through both N$_{pz}$ atoms. Such coordination behaviour has been seen before in poly(pyrazolyl)borate complexes where the B-N$_{pz}$-N$_{pz}$-M torsion angle lies between 75 to 92° (i.e. the pyrazolyl ring is 'face-on' to the metal ion, **Fig. 2.2.27**).[41] In this example, the torsion is 95°.

The metal ion further coordinates to three external pyridyl donors from three independent Tl(Tkp^{3py}) units, effectively making the metal ion 7-coordinate.

The fourth 3pypz arm extends away from the cavity but this time, unlike in Tl(Tkp^{4py}), the pyridyl donor, N(171), coordinates to a metal ion - the longest of the three N_{py}···Tl bonds.

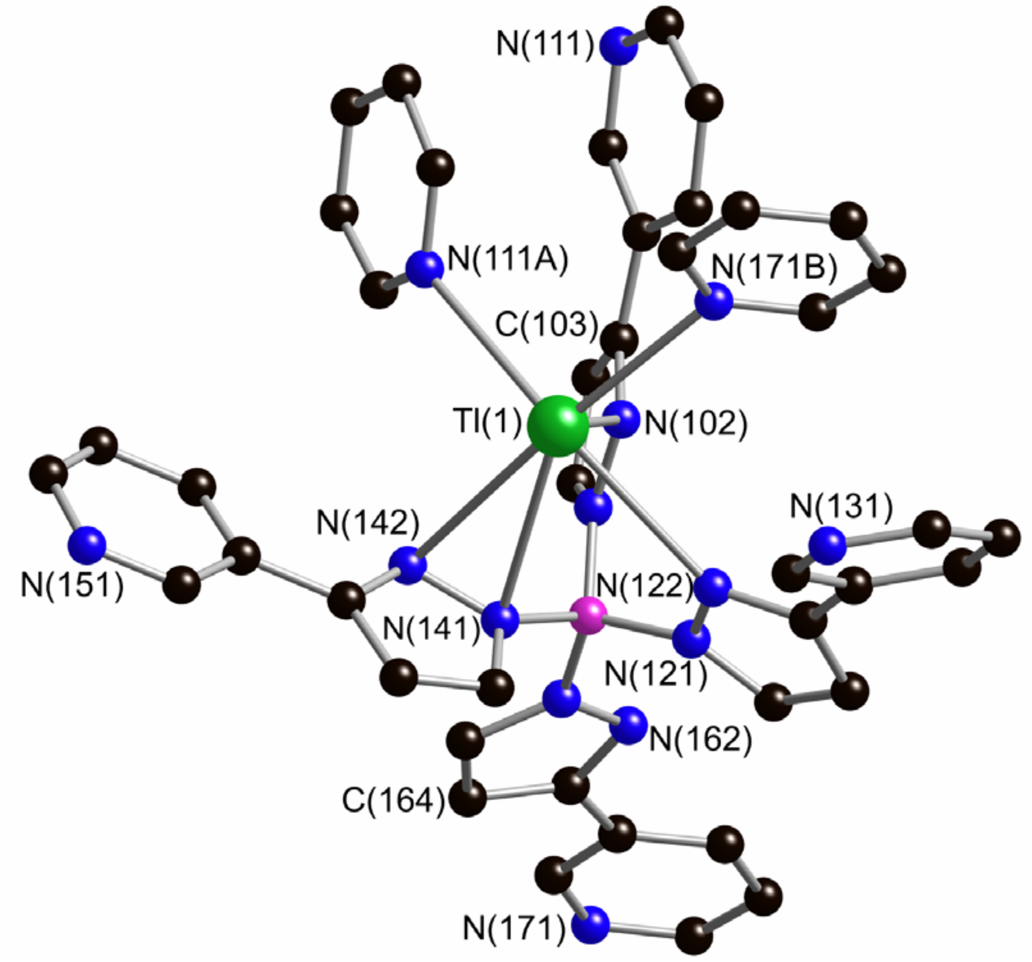

Fig. 2.2.27 – Crystal structure of Tl(Tkp^{3py}) showing the labelling scheme

Tl(Tkp^{3py}) units pair up by the complementary pairing of N(131) atoms and another such pairing of N(111) donor atoms. The former pairing has its pyridyl rings arranged parallel to each other in the same plane, whilst the latter dimer is assisted by a π-stacking interaction at 3.5 Å separations (**Fig. 2.2.28**). The N_{py} donor of the longest N_{py}···Tl bond then connects these chains forming a two-dimensional sheet [N(171)···Tl(1) = 2.885(5) Å]. A more detailed analysis of the structure can be found in our joint publication.[3]

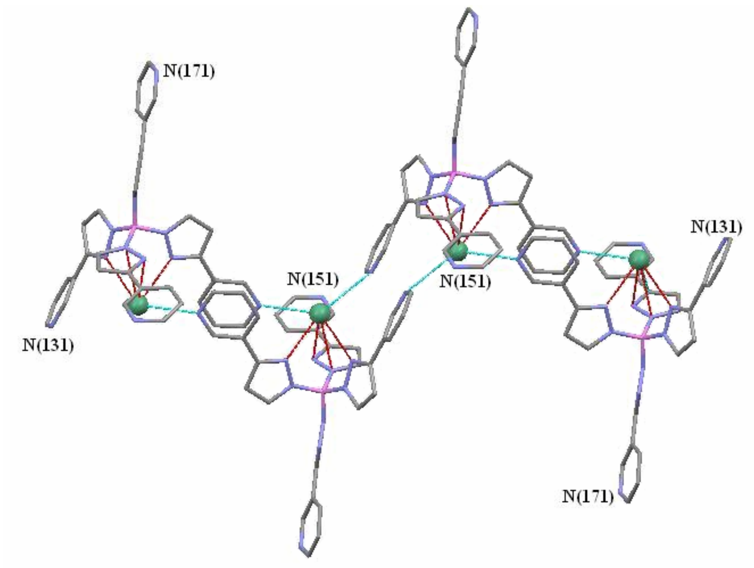

Fig. 2.2.28 – One dimensional chain of Tl(Tkp^{3py}) viewing down the b-axis

2.2.6 Other Metal Salts of Scorpionates based on 3pypz

2.2.6.1 [Cd(Tp^{3py})(OAc)]$_2$·1.5(DMF)

In all the previous examples so far the metal ions employed in the scorpionate complexes have been unipositive and, in the case of Tl(1), have been quite variable in the geometry adopted about the metal centre. If external pyridyl donors can approach the central cavity, then octahedral metal ions should offer a more defined arrangement of donors about themselves, and a higher oxidation state should see a move away from the 1:1 complexes we have already seen so many of.

In [Re(Tp^{4py})(CO)$_3$], we saw that the pyrazolyl pocket is a perfect fit for one face (*fac*-arrangement) of a pseudo octahedral geometry, yet Batten and Duriska discovered that a second pyrazolyl pocket could just as easily cap the other face when they reacted Ni(ClO$_4$)$_2$ with a slight excess of K(Tp^{3py}), giving rise to a conventional 2:1 sandwich complex (**Fig. 2.2.29**).[3]

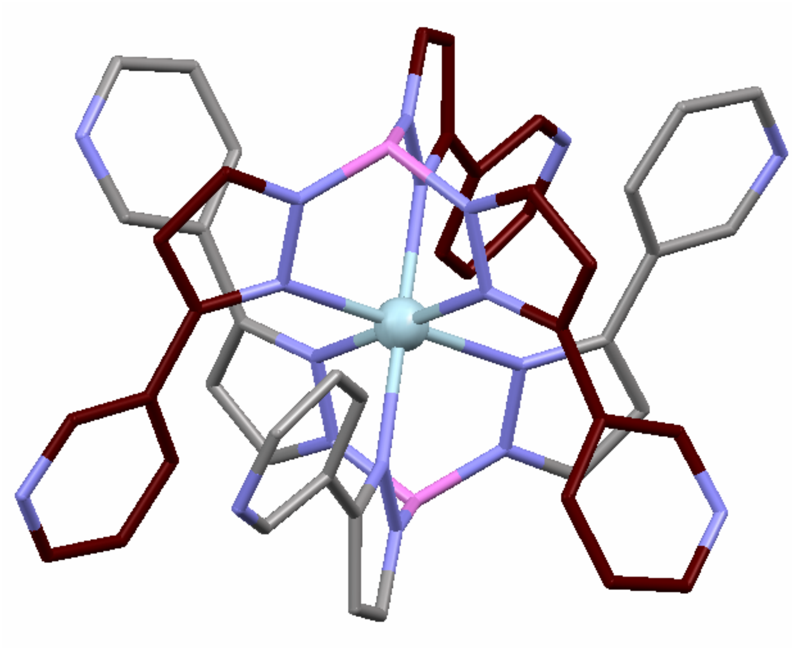

Fig. 2.2.29 – Crystal structure of Ni(Tp^{3py})$_2$

Indeed this sandwich behaviour has been observed in many octahedral complexes of simple Tp-based ligands,[40,42] but in this case we are defeating the objective of fixing peripheral donor atoms to the pyrazolyl rings to build up multinuclear assemblies. Such sandwich coordination allows the metal ion's geometry requirements to be satisfied with near-perfect octahedral geometry, and it seems likely that other octahedral metals will form these complexes if reacted with a suitable excess of tris-based scorpionate. The answer to avoiding this, and generating polynuclear species, appears to lie in blocking one or more of the metal ions coordination sites.

In lowering the ratio of reagents to 1:1 in the reaction of Cd(OAc)$_2$ with K(Tp^{3py}), we observe a different behaviour (**Fig. 2.2.30**). Whilst one Tp^{3py} ligand does coordinate to the Cd(II) ion in its cavity, one of the acetate anions remains in the cavity as a bidentate ligand to the metal ion, creating a neutral complex. With five of its six donor sites satisfied, the coordination sphere about the ion is completed with the pyridyl donor of a separate [Cd(OAc)(Tp^{3py})] unit, whose own Cd(II) ion is satisfied by a complementary pyridyl donation from the initial unit, effectively mirroring the dimer behaviour we observed with Cu$_2$(Tp^{4py})$_2$ [N(151)···Cd(1) = 2.386(4) Å].

The geometry about the metal is pseudo-octahedral with two oxygen donors from the acetate, one nitrogen from the external pyridyl ring and a *fac*-arrangement from the three N_{pz} donors. The two units in the dimer are related by an inversion centre associated with the triclinic space group P-1, and the separation between the bridging pyridyl rings is 3.317 Å (offset by 1.173 Å with a centroid-centroid distance of 3.645 Å) - indicating a slight π-stacking interaction.

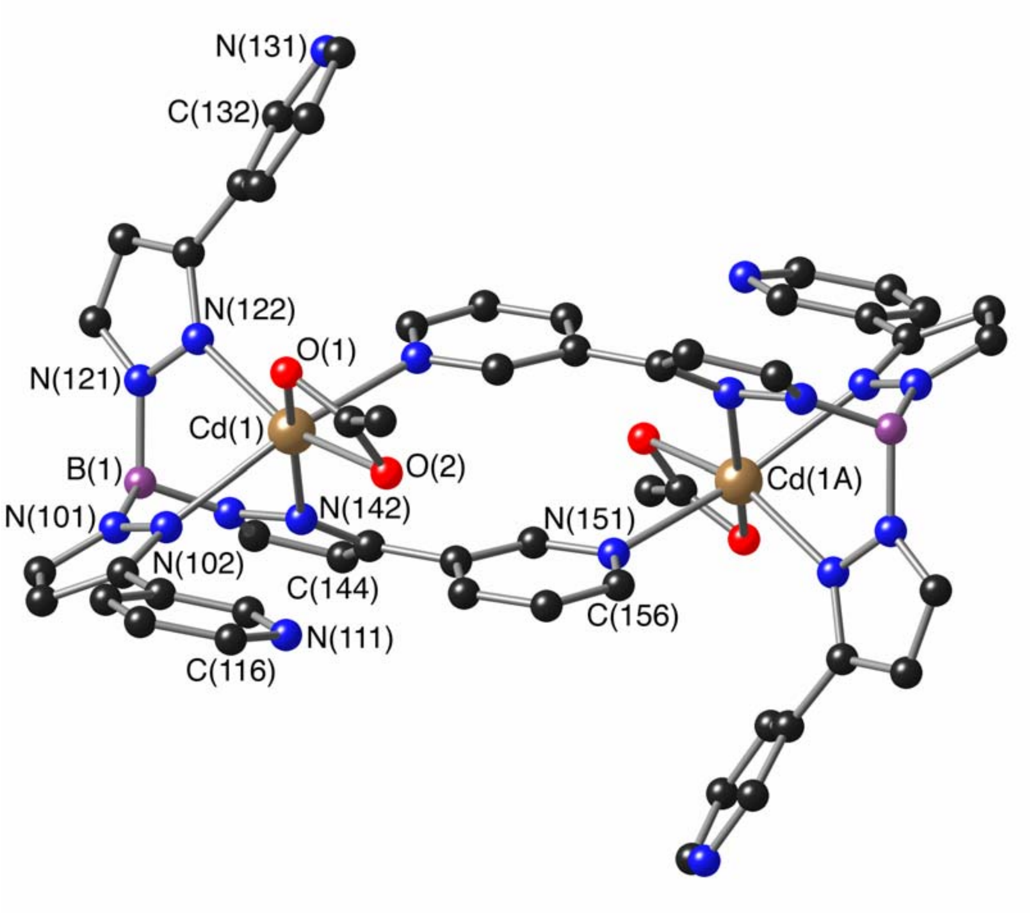

Fig. 2.2.30 – Crystal structure of $[Cd(Tp^{3py})(OAc)]_2 \cdot 1.5(DMF)$

Both N(131) and N(111) participate in hydrogen bonding – the former to a pyridyl hydrogen, H(116), and the latter to the methyl group of a disordered DMF molecule to give the overall packing structure: neighbouring dimer units regularly interspersed by DMF molecules. Selected bond lengths and angles are given in **Table 2.2.9.**

Cd(1)-N(142)	2.315(4)	Cd(1)-O(1)	2.351(4)
Cd(1)-O(2)	2.325(4)	Cd(1)-N(151A)	2.386(4)
Cd(1)-N(122)	2.340(4)	Cd(1)-N(102)	2.411(4)

N(142)-Cd(1)-O(2)	113.75(13)	N(122)-Cd(1)-N(151A)	90.31(13)
N(142)-Cd(1)-N(122)	87.30(13)	O(1)-Cd(1)-N(151A)	102.39(13)
O(2)-Cd(1)-N(122)	157.91(14)	N(142)-Cd(1)-N(102)	76.78(13)
N(142)-Cd(1)-O(1)	166.79(13)	O(2)-Cd(1)-N(102)	105.06(13)
O(2)-Cd(1)-O(1)	56.18(13)	N(122)-Cd(1)-N(102)	85.57(14)
N(122)-Cd(1)-O(1)	103.95(13)	O(1)-Cd(1)-N(102)	96.93(13)
N(142)-Cd(1)-N(151A)	84.18(13)	N(151A)-Cd(1)-N(102)	160.67(13)
O(2)-Cd(1)-N(151A)	85.51(13)		

Table 2.2.9 – Selected bond lengths (Å) and angles (°) for $[Cd(Tp^{3py})(OAc)]_2 \cdot 1.5(DMF)$

2.3 Experimental

2.3.1 Synthesis of Ligands

3-(4-pyridyl)pyrazole

This was prepared in two steps from 4-acetylpyridine as shown in **Fig. 2.2.1**. In the first step, a mixture of 4-acetylpyridine (24.2 g, 0.2 mol) and *N,N*-dimethylformamide-dimethylacetal (40 cm^3) was heated to reflux for 2 h. After concentration *in vacuo*, recrystallisation of the orange residue from $CHCl_3$/hexane afforded an orange/yellow powder (intermediate **A**) in 58% yield. Chemical ionization MS: *m/z* 177 (M + H)$^+$. ^{1}H NMR ($CDCl_3$): δ 8.64 (2H, d, *J* 5.9; pyridyl H^2/H^6), 7.79 (1H, d, *J* 12.5; alkene CH), 7.63 (2H, d, *J* 5.9; pyridyl H^3/H^5), 5.60 (1H, d, *J* 12.5 Hz; alkene CH), 3.12 (3H, s, Me), 2.89 (3H, s, Me). ^{13}C NMR ($CDCl_3$): δ 186.31 (1C, carbonyl), 155.09 (1C, alkene CH), 150.08 (2C, pyridyl CH), 147.07 (1C, pyridyl C), 121.07 (2C, pyridyl CH), 91.52 (1C, alkene CH), 45.19 (1C, CH_3), 37.30 (1C, CH_3). Found: C, 64.5; H, 6.8; N, 15.2. Required for [$C_{10}H_{12}N_2O\bullet0.5H_2O$]: C, 64.8; H, 7.0; N, 15.1%. A mixture of **A** (20.3 g, 0.115 mmol), ethanol (30 cm^3) and hydrazine hydrate (30 cm^3) was then heated to 60°C with stirring for 30 min. After addition to cold water (130 cm^3) and overnight refrigeration, the resulting off-white precipitate was filtered off, washed with copious amounts of water, and dried to give 3-(4-pyridyl)pyrazole in 77% yield. Although characterisation data were satisfactory at this stage, the material could be further purified by vigorous washing with toluene (ultrasound cleaning bath) followed by recrystallisation from water. X-Ray quality crystals were grown by diffusion of pentane into a concentrated DCM solution of the sample. EI-MS: 145 (M^+). ^{1}H NMR ($CDCl_3$): δ 11.68 (1H, br s, N*H*), 8.65 (2H, d, *J* 6.2, pyridyl H^2/H^6), 7.72 (2H, d, *J* 5.9, pyridyl H^3/H^5), 7.68 (1H, d, *J* 2.6; pyrazolyl), 6.76 (1H, d, *J* 2.2 Hz; pyrazolyl). ^{13}C NMR (MeOD): δ 150.5, 149.8, 143.4, 131.6, 121.6, 104.4. Found: C, 66.3; H, 5.1; N, 29.2. Required for $C_8H_7N_3$: C, 66.2; H, 4.9; N, 29.0%.

3-(3-pyridyl)pyrazole

This was prepared in a similar manner to 3-(4-pyridyl)pyrazole (above), except using 3-acetylpyridine as starting material. A mixture of 3-acetylpyridine (24.2 g, 0.20 mol) and *N,N*-dimethylformamide-dimethylacetal (40 cm^3) was heated to reflux for 2 h. Removal of the solvent *in vacuo* delivered a brown sludgy residue, which was recrystallised, from CH_3Cl/hexane to afford intermediate **B** as a yellow powder in 94% yield. Chemical ionization MS: *m/z* 177 $(M + H)^+$, 159 $(M^+ - H_2O)$. ^1H NMR ($CDCl_3$): δ 8.95 (1H, s; pyridyl H^2), 8.52 (1H, d, *J* 4.8; pyridyl H^6), 8.05 (1H, d, *J* 8.1; pyridyl H^4), 7.70 (1H, d, *J* 12.5; alkene CH), 7.22 (1H, dd, *J* 4.8, 8.1; pyridyl H^5), 5.54 (1H, d, *J* 12.5; alkene CH), 3.02 (3H, s; Me), 2.82 (3H, s; Me). ^{13}C NMR ($CDCl_3$): δ 186.21 (1C, carbonyl), 154.68 (1C, alkene, CH), 151.31 (1C, pyridyl, CH), 148.79 (1C, pyridyl, CH), 135.57 (1C, pyridyl, C), 134.98 (1C, pyridyl, CH), 123.22 (1C, alkene, CH), 45.16 (1C, CH_3), 37.32 (1C, CH_3). Found: C, 68.6; H, 7.2; N, 16.0. Required for $C_{10}H_{12}N_2O$: C, 68.2; H, 6.9; N, 15.9%. Compound **B** (33.5 g, 0.19 mol), ethanol (60 cm^3) and hydrazine hydrate (60 cm^3) was then heated to 65°C with stirring for 40 min. Removal of the solvent *in vacuo* afforded a dark orange oil. This was heated overnight whilst under vacuum and upon cooling formed either a beige hard solid of 3-(3-pyridyl)pyrazole in 85% yield. X-Ray quality crystals were grown by diffusion of pentane into a concentrated DCM solution of the sample. Characterisation data were satisfactory at this stage, although the material could be purified further by recrystallisation from CH_2Cl_2/hexane. EI-MS: 145 (M^+). ^1H NMR ($CDCl_3$): δ 9.06 (1H, s; pyridyl H^2), 8.54 (1H, d, *J* 4.7; pyridyl H^6), 8.08 (1H, d, *J* 8.1; pyridyl H^4), 7.61 (1H, d, *J* 2.3; pyrazolyl), 7.30 (1H, dd, *J* 5.0, 7.9; pyridyl H^5), 6.62 (1H, d, *J* 2.0; pyrazolyl). ^{13}C NMR ($CDCl_3$): δ 148.3, 147.0, 146.8, 133.3, 131.9, 129.1, 123.8, 102.7. Found: C, 66.4; H, 5.3; N, 29.1. Required for $C_8H_7N_3$: C, 66.2; H, 4.9; N, 29.0%.

$K(Bp^{4py})$

3-(4-Pyridyl)pyrazole (1.44 g, 9.9 mmol) and KBH_4 (0.215 g, 4 mmol) were ground together thoroughly in a pestle and mortar and heated for 30 min in a Schlenk tube at 175-180 °C under N_2. The mixture was stirred throughout, although this was hindered once melting occurred at 150 °C.

After cooling to r.t., toluene (30 cm^3) were added and the mixture was agitated in an ultrasound cleaning bath for 20 min. The suspension was filtered, and the solid was washed with hot toluene and hot hexane and then dried gave KBp^{4py} as a white powder in 80% yield. Negative-ion electrospray MS: *m/z* 301 $[C_{16}H_{14}N_6B]^-$. ^{1}H NMR (MeOD): δ 8.43 (4H, d, *J* 6.2; pyridyl H^2/H^6), 7.82 (4H, d, *J* 6.6; pyridyl H^3/H^5), 7.61 (2H, d, *J* 2.2; pyrazolyl), 6.64 (2H, d, *J* 1.9; pyrazolyl). ^{13}C NMR (MeOD): δ 150.5, 150.0, 144.9, 137.9, 121.6, 103.8. ^{11}B NMR (MeOD): δ –7.59. Found: C, 53.9; H, 4.9; N, 23.7. Required for $[C_{16}H_{14}N_6BK{\bullet}H_2O]$: C, 53.6; H, 4.5; N, 23.5%. IR (cm^{-1}): 2380m, 2263m, 1650w, 1604s, 1555w, 1483m, 1457m, 1420m, 1357m, 1304w, 1247w, 1216w, 1175s, 1142s, 1093m, 1105m, 1050s, 996s, 956w, 925w, 882w, 830s, 775s.

K(Bp^{3py})

A mixture of 3-(3-pyridyl)pyrazole (3.6 g, 24.7 mmol) and dried, freshly ground KBH_4 (554 mg, 10.3 mmol) was heated in a Schlenk tube at 140 °C for 2 h under N_2. The mixture was stirred throughout, although this was hindered once melting had occurred. After cooling to r.t., toluene (30 cm^3) and chloroform (25 cm^3) were added and the mixture was agitated in an ultrasound cleaning bath for 20 min. Eventually a white suspension was produced. The mixture was filtered and the white solid was washed with warm toluene. The white powder was then washed with several portions of hexane (total 50 cm^3) before final washing with ether and overnight drying. This gave KBp^{3py} in 52 % yield. Negative-ion electrospray MS: *m/z* 301 $[C_{16}H_{14}N_6B]^-$. ^{1}H NMR (MeOD): δ 8.94 (2H, d, *J* 2.4; pyridyl H^2), 8.35 (2H, dd, *J* 1.2, 4.8; pyridyl H^6), 8.21 (2H, ddd, *J* 8.1, 3.4, 1.8; pyridyl H^4), 7.61 (2H, d, *J* 2.1; pyrazolyl), 7.40 (2H, dd, *J* 4.9, 7.9; pyridyl H^5), 6.53 (2H, d, *J* 1.8; pyrazolyl). ^{13}C NMR (MeOD): δ 149.1, 147.6, 147.3, 137.8, 134.8, 133.1, 125.2, 102.8. ^{11}B NMR (MeOD): δ –7.02. Found: C, 54.7; H, 4.4; N, 23.7. Required for $[(C_{16}H_{14}N_6BK)(H_2O)_{0.5}]$: C, 55.0; H, 4.3; N, 24.1%. IR (cm^{-1}): 2373m, 2340m, 2256m, 1599w, 1579w, 1486m, 1466w, 1424m, 1358m, 1309m, 1247w, 1174s, 1139s, 1094m, 1050s, 1028m, 1006m, 950m, 898m, 853w, 810m, 756s, 723s, 709s.

K(Tp^{4py})

3-(4-Pyridyl)pyrazole (0.96 g, 6.6 mmol) and KBH_4 (0.108 g, 2 mmol) were ground together thoroughly in a pestle and mortar, and heated under N_2 in a Schlenk tube, with stirring, at 230 °C for 3.5 h. After cooling to r.t., 30 cm^3 of toluene were added and the mixture was agitated in an ultrasound cleaning bath for 20 min. The suspension was filtered, and the solid was washed with hot toluene and hot hexane and then dried gave KTp^{4py} as a white powder in 25% yield. Negative-ion ES MS: *m/z* 444 [$C_{24}H_{19}N_9B$]$^-$. ^{1}H NMR (MeOD): δ 8.50 (6H, d, *J* 6.2, pyridyl H^2/H^6), 7.88 (6H, d, *J* 6.2, pyridyl H^3/H^5), 7.41 (3H, d, *J* 2.2, pyrazolyl), 6.80 (3H, d, *J* 2.4 Hz, pyrazolyl). ^{13}C NMR (MeOD): δ 151.0, 150.1, 144.5, 136.7, 121.7, 104.3. ^{11}B NMR (MeOD): δ 0.37. Found: C, 57.8; H, 4.0; N, 25.0. Required for [$C_{24}H_{19}N_9BK{\bullet}H_2O$]: C, 57.5; H, 4.2; N, 25.1%. IR (cm^{-1}): 2418m, 1606s, 1487m, 1455m, 1420m, 1357m, 1306w, 1252w, 1200s, 1175s, 1127w, 1107w, 1081s, 1053s, 996s, 958w, 831s, 763s.

K(Tp^{3py})

3-(3-Pyridyl)pyrazole (12.68 g, 87 mmol) and dried, freshly ground KBH_4 (1.27 g, 24 mmol) were heated in a Schlenk tube at 215 °C for 2 h under N_2. The mixture was stirred throughout, although this became more difficult once melting had occurred. After cooling to r.t., toluene (40 cm^3) and chloroform (40 cm^3) were added and the mixture was agitated in an ultrasound cleaning bath for 20 min. The mixture was periodically agitated with a glass rod, and sonicated for a further 20 mins, to produce a white suspension. The mixture was filtered and the white solid washed with several portions of warm toluene and several portions of hexane before finally washing with ether, and overnight drying. This gave K(Tp^{3py}) in 73% yield. Negative-ion ES MS: *m/z* 444 [$C_{24}H_{19}N_9B$]$^-$. ^{1}H NMR (MeOD): δ 8.97 (3H, d, *J* 2.1; pyridyl H^2), 8.39 (3H, dd, *J* 1.5, 4.9; pyridyl H^6), 8.25 (3H, ddd, *J* 1.8, 3.9, 8.1; pyridyl H^4), 7.42 (3H, dd, *J* 5.2, 7.9; pyridyl H^5), 7.34 (3H, d, *J* 2.1; pyrazolyl), 6.66 (3H, d, *J* 2.1; pyrazolyl). ^{13}C NMR (MeOD): δ 150.5, 148.1, 147.6, 136.6, 135.1, 132.6, 125.3, 103.2. ^{11}B NMR (MeOD): δ 1.21. Found: C, 56.9; H, 4.1; N, 24.7. Required for [$(C_{24}H_{19}N_9BK)(H_2O)_{1.5}$]: C, 56.5; H, 4.3; N, 24.7%. IR (cm^{-1}): 2460w, 1572w, 1488w, 1462w, 1418m, 1359w, 1310w, 1238w, 1201m, 1177s, 1119m, 1093m, 1046m, 1009m, 948m, 926w, 811m, 765s, 730s.

2.3.2 Synthesis of Complexes

$[Co(4pypz)_4Cl_2]\cdot 4MeCN$

A solution of 3-(4-pyridyl)pyrazole (100 mg, 0.69 mmol) in MeCN (10 ml) was added to a solution of $CoCl_2$ (22.4 mg, 0.17 mmol) in MeCN (10 ml) and the reaction mixture stirred once and filtered through celite. Upon leaving to stand for a few moments, purple X-Ray quality crystals were seen to crash out of the filtrate. After a few hours the crystals were filtered off and dried, to give 37 mg of opaque pink crystals (30% yield). Found: C, 53.4; H, 4.2; N, 23.4. Required for $[C_{32}H_{28}N_{12}CoCl_2]\cdot 0.5H_2O$: C, 53.4; H, 4.1; N, 23.4%. IR: 3287 (m); 1614 (s); 1556 (w); 1496 (w); 1456 (m); 1424 (m); 1356 (w); 1290 (w); 1216 (m); 1178 (m); 1122 (w); 1079 (w); 1039 (m); 1014 (m); 947 (m); 843 (s); 758 (s); 740 (s); 701 (s); 663 (w); 622 (m) cm^{-1}.

$Tl(Bp^{4py})$

Methanolic solutions of thallium(I) acetate (0.18 mmol) and KBp^{4py} (0.18 mmol), both in 5 cm^3 MeOH, were combined and stirred at r.t. for 40 min, during which time a white precipitate formed. The solution was concentrated *in vacuo* and refrigerated for several hours before being filtered off and washed with MeOH to give a white powder. Recrystallisation by diffusion of Et_2O vapour into a solution of the complex in DMF afforded colourless crystals suitable for X-ray diffraction studies. These were filtered off and washed with Et_2O to give pure $Tl[Bp^{4py}]$ in 42 % yield. FAB-MS: *m/z* 507 [M^+]; 358 [M^+ - pyridylpyrazole unit]. Found: C, 37.8; H, 2.5; N, 16.5. Required for $[C_{16}H_{14}N_6BTl]$: C, 38.0; H, 2.8; N, 16.6%. IR: $\upsilon_{B\text{-}H}$ 2412, 2389, 2264 cm^{-1}. ^1H NMR (DMSO-d_6): δ 8.46 (4 H, m; pyridyl H^2/H^6); 7.68 (4 H, m; pyridyl H^3/H^5); 7.52 (2 H, d, *J* 2.1; pyrazolyl); 6.61 (2 H, d, *J* 2.1; pyrazolyl).

Tl(Bp^{3py})

Methanolic solutions of K(Bp^{3py}) (100 mg, 0.29 mmol) and thallium(I) acetate (78 mg, 0.29 mmol) were combined and stirred at room temperature; no precipitate appeared. Complete removal of the solvent left an off-white precipitate. This was dissolved in CH_2Cl_2 (approx. 3 cm^3) using ultrasound treatment to assist dissolution, and ether (10 cm^3) was slowly added whilst the solution was stirring.

The resultant white precipitate was filtered, and washed with ether to give Tl(Bp^{3py}) in 65 % yield (96 mg). X-Ray quality crystals were grown by layering of isopropyl ether onto a concentrated solution of the complex in DCM and allowing the layers to mix. FAB MS: *m/z* 711 [*M* + Tl]$^+$, 506 [*M*]$^+$. Found: C, 37.6; H, 2.6; N, 16.5. Required for $C_{16}H_{14}N_6BTl$: C, 38.0; H, 2.8; N, 16.6%}. IR: $\upsilon_{B\text{-}H}$ 2372, 2252 cm^{-1}. ^{1}H NMR (DMSO-d$_6$): δ 8.93 (2 H, dd, *J* 0.9, 2.1; pyridyl H^2); 8.36 (2 H, dd, *J* 1.5, 4.9; pyridyl H^6); 8.07 (2 H, ddd, *J* 2.0, 4.0, 8.0; pyridyl H^4); 7.49 (2 H, d, *J* 2.1; pyrazolyl); 7.32 (2 H, ddd, *J* 0.8, 4.7, 7.9; pyridyl H^5); 6.52 (2 H, d, *J* 2.1; pyrazolyl).

Tl(Tp^{4py})

Methanolic solutions of thallium(I) acetate (0.346 g, 1.33 mmol) and KTp^{4py} (0.59g, 1.33 mmol), were combined and stirred at r.t. After 30 min. a white precipitate had started to evolve. Diethyl ether (20 cm^3) was added and stirring continued for an additional 15 min; this procedure was repeated once more. The reaction mixture was refrigerated (5 ˚C) for several hours before filtration of the precipitate which was washed with ether to give Tl(Tp^{4py}) as a white powder in 51% yield. Colourless crystals, suitable for X-ray diffraction studies, were grown from slow evaporation of a CH_2Cl_2/MeOH solution of the complex. FAB-MS: *m/z* 650 [*M* + H]$^+$; 505 [MH$^+$ - pyridylpyrazole unit]. Found: C, 44.3; H, 2.7; N, 19.4. Required for $C_{24}H_{19}N_9BTl$: C, 44.4; H, 3.0; N, 19.4%. IR: $\upsilon_{B\text{-}H}$ 2441 cm^{-1}. ^{1}H NMR (DMSO-d$_6$): δ 8.48 (6 H, dd, *J* 1.5, 4.5; pyridyl H^2/H^6); 7.72 (6 H, dd, *J* 1.7, 4.4; pyridyl H^3/H^5); 7.59 (3 H, d, *J* 2.1; pyrazolyl); 6.71 (3 H, d, *J* 2.1; pyrazolyl).

Tl(Tp^{3py})

Methanolic solutions of K(Tp^{3py}) (150 mg, 0.31 mmol) and thallium(I) acetate (82 mg, 0.31 mmol) were combined and stirred at room temperature for 20 mins. A white precipitate appeared quickly. Ether (10 cm^3) was added and the mixture was refrigerated to ensure that precipitation was complete. The white precipitate was filtered, washed with a little methanol and ether, and then dried to give Tl(Tp^{3py}) in 61% yield. X-Ray quality crystals were grown by layering of isopropyl ether onto a concentrated solution of the complex in 50:50 DCM:MeOH and allowing the layers to mix. FAB MS: *m/z* 650 [*M* + H]$^+$. Found: C, 44.6; H, 2.8; N, 19.3. Required for $C_{24}H_{19}N_9BTl$: C, 44.4; H, 3.0; N, 19.4%. IR: υ_{B-H} 2440 cm^{-1}. ^{1}H NMR (DMSO-d$_6$): δ 8.97 (3 H, dd, *J* 0.8, 2.3; pyridyl H^2); 8.41 (3 H, dd, *J* 1.7, 4.7; pyridyl H^6); 8.12 (3 H, ddd, *J* 1.9, 3.8, 7.9; pyridyl H^4); 7.59 (3 H, d, *J* 2.1; pyrazolyl); 7.36 (3 H, ddd, *J* 0.8, 4.7, 7.9; pyridyl H^5); 6.64 (3 H, d, *J* 2.1; pyrazolyl).

[Re(CO)$_3$(Tp^{4py})]

A mixture of K(Tp^{4py}) (200 mg, 0.41 mmol) and Re(CO)$_5$Cl (150 mg, 0.42 mmol) in THF (10 cm^3) was stirred at room temperature for 72 hours. The mixture was filtered through celite to remove the precipitate (KCl) and the solvent was then removed *in vacuo* to leave an oil. CH_2Cl_2 (40 cm^3) was added and the mixture was agitated for 10 mins in an ultrasound cleaning bath to generate a solid precipitate, which was filtered, washed with ether and dried to give [Re(CO)$_3$(Tp^{4py})] in 67% yield. X-Ray quality crystals were grown by slow evaporation of a concentrated acetone solution of the complex. FAB MS: *m/z* 716 [*M*$^+$]. Found: C, 45.7; H, 3.1; N, 17.4. Required for $C_{27}H_{19}N_9O_3BRe$: C, 45.4; H, 2.7; N, 17.6%. IR: υ_{B-H} 2442 cm^{-1}, υ_{CO} 2019, 1881 cm^{-1}.

$[Cu_2(Tp^{4py})_2]$

Solutions of $K(Tp^{4py})$ (67 mg, 0.14 mmol) and $[Cu(MeCN)_4][PF_6]$ (52 mg, 0.14 mmol) in MeOH (10 cm^3 each) were combined and stirred at room temperature. After 30 min, a green precipitate was evident. Ether (10 cm^3) was added and stirring continued for 5 min, before the precipitate was filtered off and washed with methanol and ether. The complex is essentially insoluble in all common solvents apart from dmf in which it is sparingly soluble; yellow X-ray quality crystals were grown by ether diffusion into a DMF solution of the complex. FAB MS: *m/z* 1016 [M^+], IR: υ_{B-H} 2444 cm^{-1}.

$[(Tp^{3py})Cd(OAc)]_2$

$K(Tp^{3py})$ (0.31 mmol) and cadmium(II) acetate hydrate (0.31 mmol) were combined in dmf (5 cm^3) and stirred at room temp for 20 min. The reaction mixture was then filtered through celite and transferred to a Young's tube where it was layered with diethyl ether. After several days, this gave a generous crop of colourless X-ray quality crystals. Found: C, 48.9; H, 4.3; N, 19.5. Required for $[(C_{24}H_{19}N_9B)Cd(CH_3CO_2)_2(DMF)_2(H_2O)_3]$: C, 48.7; H, 4.4; N, 19.6%. IR: υ_{B-H} 2450cm^{-1}.

Complex	**3-(4-pyridyl)pyrazole**	**3-(3-pyridyl)pyrazole**	**[Tl(Bp^{4py})]**
Empirical formula	$C_8H_7N_3$	$C_8H_7N_3$	$C_{16}H_{14}BN_6Tl$
Formula weight	145.17	145.17	505.51
Temperature	150(2)K	150(2) K	100(2) K
Crystal system	Monoclinic	Monoclinic	Monoclinic
Space group	$P2_1/c$	$P2_1/n$	$P2_1$
a /Å	6.9317(6)	15.009(2)	10.454(2)
b /Å	9.0964(8)	5.8998(9)	6.3740(13)
c /Å	11.0059(10)	16.526(3)	12.338(3)
α /°	90	90	90
β /°	92.2630(10)	91.308(3)	98.96(3)
γ /°	90	90	90
Volume /Å^3	693.42(11)	1463.0(4)	812.1(3)
Z	4	8	2
Density (calculated) / Mg/m^3	1.391	1.318	2.067
Absorption coefficient / mm^{-1}	0.090	0.085	9.954
F(000)	304	608	476
Crystal size / mm	0.61 x 0.55 x 0.21	0.40 x 0.35 x 0.50	0.18 x 0.10 x 0.09
θ range for data collection	2.91 to 27.55°	1.81 to 27.53°	1.67 to 27.48°
Reflections collected	7586	16023	9464
Independent reflections	1590 [R(int) = 0.0213]	3347 [R(int) = 0.0931]	3693 [R(int) = 0.0455]
Completeness to θ	99.1 %	99.2 %	100.0 %
Data / restraints / parameters	1590 / 0 / 104	3347 / 0 / 207	3693 / 1 / 1225
Goodness-of-fit on F^2	S = 1.072	0.902	0.999
R indices [for reflections with I>2σ(I)]	$R_1 = 0.0414$, $wR_2 = 0.1061$	$R_1 = 0.0468$, $wR_2 = 0.0994$	$R_1 = 0.0370$, $wR_2 = 0.0773$
R indices (for all data)	$R_1 = 0.0440$, $wR_2 = 0.1086$	$R_1 = 0.1082$, $wR_2 = 0.1200$	$R_1 = 0.0407$, $wR_2 = 0.0785$
Absolute Structure Parameter	n/a	n/a	-0.020(14)
Largest diff. peak and hole	0.187 and -0.381 eÅ^{-3}	0.161 and -0.233 e.Å^{-3}	1.466 and -0.653 e.Å^{-3}

Table 2A Crystallographic Data for the Complexes of Chapter 2

.

Complex	**[Tl(Tp^{4py})]**	**[Re(Tp^{4py})(CO)$_3$]**	**[Cu$_2$(Tp^{4py})$_2$]**
Empirical formula	$C_{24}H_{19}BN_9Tl$	$C_{27}H_{19}BN_9O_3Re$	$C_{24}H_{19}BN_9Cu$
Formula weight	648.66	714.52	507.83
Temperature	150(2)K	120(2) K	150(2) K
Crystal system	Monoclinic	Hexagonal	Monoclinic
Space group	Pc	$P6_3$	$P2_1/n$
a /Å	8.7477(9)	14.468(2)	14.470(3)
b /Å	16.5928(17)	14.468(2)	9.7387(17)
c /Å	8.3841(9)	8.0751(16)	17.593(3)
α /°	90	90	90
β /°	96.281(2)	90	112.583(3)
γ /°	90	120	90
Volume /Å^3	1209.6(2)	1463.9(4)	2289.1(7)
Z	2	2	4
Density (calculated) / Mg/m^3	1.781	1.621	1.474
Absorption coefficient / mm^{-1}	6.708	4.195	0.987
F(000)	624	696	1040
Crystal size / mm	0.28 x 0.13 x 0.05	0.36 x 0.02 x 0.02	0.50 x 0.20 x 0.04
θ range for data collection	1.23 to 27.47°	3.00 to 27.20°	1.56 to 27.52°
Reflections collected	12713	10655	15501
Independent reflections	5428 [R(int) = 0.0636]	2173 [R(int) = 0.1957]	5172 [R(int) = 0.0751]
Completeness to θ	99.9 %	99.8 %	98.0 %
Data / restraints / parameters	5428 / 2 / 316	2173 / 64 / 124	5172 / 0 / 317
Goodness-of-fit on F^2	S = 0.763	1.059	0.999
R indices [for reflections with I>2σ(I)]	R_1 = 0.0337, wR_2 = 0.621	R_1 = 0.0734, wR_2 = 0.1715	R_1 = 0.0488, wR_2 = 0.1029
R indices (for all data)	R_1 = 0.0503, wR_2 = 0.0837	R_1 = 0.1034, wR_2 = 0.1852	R_1 = 0.0995, wR_2 = 0.1220
Absolute Structure Parameter	0.031(10)	0.06(4)	n/a
Largest diff. peak and hole	0.761 and -0.794 eÅ^{-3}	1.284 and -0.907 e.Å^{-3}	0.521 and -0.368 e.Å^{-3}

Table 2B Crystallographic Data for the Complexes of Chapter 2

.

Complex	**$[\mathrm{Tl(Bp^{3py})}]\cdot 0.5\mathrm{CH_2Cl_2}$**	**$[\mathrm{Tl(Tp^{3py})}]$**	**$[\mathrm{Cd(Tp^{3py})(CH_3CO_2)}]\cdot 1.5\mathrm{DMF}$**
Empirical formula	$\mathrm{C_{16.5}H_{15}BN_6ClTl}$	$\mathrm{C_{24}H_{19}BN_9Tl}$	$\mathrm{C_{30.5}H_{32.50}BN_{10.50}O_{3.50}Cd}$
Formula weight	547.98	648.66	725.38
Temperature	150(2)K	150(2) K	150(2) K
Crystal system	Monoclinic	Monoclinic	Triclinic
Space group	$P2_1/c$	P2(1)/n	P -1
a /Å	8.1673(13)	9.2506(13)	9.5334(13)
b /Å	16.983(3)	12.3819(17)	13.7358(18)
c /Å	27.131(4)	19.887(3)	13.8959(19)
α /°	90	90	70.983(2)
β /°	92.016(3)	94.968(2)	84.410(2)
γ /°	90	90	70.248(2)
Volume /$Å^3$	3760.8(10)	2269.3(5)	1619.0(4)
Z	8	4	2
Density (calculated) / Mg/m^3	1.936	1.899	1.488
Absorption coefficient / mm^{-1}	8.743	7.151	0.726
F(000)	2072	1248	740
Crystal size / mm	0.46 x 0.16 x 0.08	0.48 x 0.25 x 0.13	0.30 x 0.20 x 0.20
θ range for data collection	1.41 to 27.54°	1.94 to 27.55°	1.55 to 27.59°
Reflections collected	41391	23976	18642
Independent reflections	8548 [R(int) = 0.1369]	5118 [R(int) = 0.0488]	7263 [R(int) = 0.0579]
Completeness to θ	98.4 %	97.8 %	97.0 %
Data / restraints / parameters	8548 / 2 / 426	5118 / 0 / 320	7263 / 1 / 422
Goodness-of-fit on F^2	S = 1.019	1.027	0.975
R indices [for reflections with I>2σ(I)]	$R_1 = 0.0567$, $wR_2 = 0.1187$	$R_1 = 0.0263$, $wR_2 = 0.0631$	$R_1 = 0.0524$, $wR_2 = 0.1198$
R indices (for all data)	$R_1 = 0.1261$, $wR_2 = 0.1451$	$R_1 = 0.0322$, $wR_2 = 0.0659$	$R_1 = 0.0864$, $wR_2 = 0.1326$
Largest diff. peak and hole	2.821 and -1.547 e$Å^{-3}$	1.891 and -0.920 e.$Å^{-3}$	2.232 and -0.743 e.$Å^{-3}$

Table 2C Crystallographic Data for the Complexes of Chapter 2

Complex	**[Co(4pypz)$_4$Cl$_2$]·4MeCN**
Empirical formula	$C_{40}H_{40}N_{16}Cl_2Co$
Formula weight	874.71
Temperature	150(2)
Crystal system	Tetragonal
Space group	I_4
a /Å	15.649(2)
b /Å	15.649(2)
c /Å	8.653(2)
α /°	90
β /°	90
γ /°	90
Volume /Å^3	2119.2(7)
Z	2
Density (calculated) / Mg/m^3	1.371
Absorption coefficient / mm^{-1}	0.582
F(000)	906
Crystal size / mm	0.31 x 0.31 x 0.19
θ range for data collection	1.84 to 27.52°
Reflections collected	11871
Independent reflections	2407 [R(int) = 0.0319]
Completeness to θ	99.2 %
Data / restraints / parameters	2407 / 1 / 138
Goodness-of-fit on F^2	0.969
R indices [for reflections with I>2σ(I)]	$R_1 = 0.0290$, $wR_2 = 0.0672$
R indices (for all data)	$R_1 = 0.0341$, $wR_2 = 0.0692$
Absolute Structure Parameter	0(10)
Largest diff. peak and hole	0.271 and -0.164 eÅ^{-3}

Table 2C **Crystallographic Data for the Complexes of Chapter 2**

2.4 References

1. (a) For a comprehensive review on scorpionates with 3-(2-pyridyl)pyrazole arms prior to 2001 - M. D. Ward, J. A. McCleverty, J. C. Jeffery, *Coord. Chem. Rev.*, 2001, **222**, 251; (b) D. A. Bardwell, J. C. Jeffery, P. L. Jones, J. A. McCleverty, E. Psillakis, Z. Reeves, M. D. Ward, *J. Chem. Soc., Dalton Trans.*, 1997, 2079; (c) N. Armaroli, G. Accorsi, F. Barigelletti, S. M. Couchman, J. S. Fleming, N. C. Harden, J. C. Jeffery, K. L. V. Mann, J. A. McCleverty, L. H. Rees, S. R. Starling, M. D. Ward, *Inorg. Chem.*, 1999, **38**, 5769; (d) Z. R. Reeves, K. L. V. Mann, J. C. Jeffery, J. A. McCleverty, M. D. Ward, F. Barigelletti, N. Armaroli, *J. Chem. Soc., Dalton Trans.*, 1999, 349; (e) A. J. Amoroso, A. M. Cargill Thompson, J. C. Jeffery, P. L. Jones, J. A. McCleverty, M. D. Ward, *J. Chem. Soc., Chem. Commun.*, 1994, 2751; (f) A. Beeby, B. P. Burton-Pye, S. Faulkner, G. R. Motson, J. C. Jeffery, J. A. McCleverty, M. D. Ward, *J. Chem. Soc., Dalton Trans.*, 2002, 1923; (g) A. J. Amoroso, J. C. Jeffery, P. L. Jones, J. A. McCleverty, L. Rees, A. L. Rheingold, V. Sun, J. Takats, S. Trofimenko, M. D. Ward, G. P. A. Vap, *J. Chem. Soc., Chem. Commun.*, 1995, 1881; (h) D. A. Bardwell, J. C. Jeffery, J. A. McCleverty, M. D. Ward, *Inorg. Chim. Acta*. 1998, **267**, 323; (i) N. Armaroli, V. Balzani, F. Barigelletti, M. D. Ward, J. A. McCleverty, *Chem. Phys. Lett.*, 1997, **276**, 435; (j) P. L. Jones, K. J. Byrom, J. C. Jeffery, J. A. McCleverty, M. D. Ward, *Chem. Commun.*, 1997, 1361; (k) A. J. Amoroso, J. C. Jeffery, P. L. Jones, J. A. McCleverty, M. D. Ward, *Polyhedron*, 1996, **15**, 2023; (l) P. L. Jones, A. J. Amoroso, J. C. Jeffery, J. A. McCleverty, E. Psillakis, L. H. Rees, and M. D. Ward, *Inorg. Chem.*, 1997, **36**, 10; (m) D. A. Bardwell, J. C. Jeffery, P. L. Jones, J. A. McCleverty, M. D. Ward, *J. Chem. Soc.*, *Dalton Trans.*, 1995, 2921; (n) Z. R. Bell, G. R. Motson, J. C. Jeffery, J. A. McCleverty, M. D. Ward, *Polyhedron*, 2001, **20**, 2045
2. K. L. V. Mann, J. C. Jeffery, J. A. McCleverty, M. D. Ward, *Polyhedron*, 1999, **18**, 721.
3. H. Adams, S. R. Batten, G. M. Davies, M. B. Duriska, J. C. Jeffery, P. Jensen, J. Lu, G. R. Motson, S. J. Coles, M. B. Hursthouse, M. D. Ward, *Dalton Trans*, 2005, 1910.

4. Y. Lin, S. A. Lang, *J. Heterocycl. Chem.*, 1977, **14**, 345.
5. S. Trofimenko, *Chem. Rev.*, 1993, **93**, 943.
6. S. Trofimenko, *Inorg. Synth.*, 1970, **12**, 99.
7. S. Trofimenko, *Scorpionates – The Coordination Chemistry of Polypyrazolylborate Ligands*, Imperial College Press, 1999.
8. D. J. Harding, H. Adams, T. Tuntulani, *Acta Cryst*. 2005, C**61**, 301.
9. L. M. L. Chia, S. Radojevic, I. J. Scowen, M. McPartlin, M. A. Halcrow, *J. Chem. Soc., Dalton Trans.*, 2000, 133.
10. G. R. Motosn, *PhD Thesis*, University of Bristol, 2001.
11. M. D. Ward, J. S. Fleming, E. Psillakis, J. C. Jeffery, J. A. McCleverty, *Acta Cryst*. 1998, C**54**, 609.
12. M. D. Ward, K. L. V. Mann, J. C. Jeffery, J. A. McCleverty, *Acta Cryst*. 1998, C**54**, 601.
13. P. L. Jones, J. C. Jeffery, J. A. McCleverty, M. D. Ward, *Polyhedron*, 1997, **16**, 1567.
14. M. Fujita, O. Sasaki, T. Mitsuhoshi, T. Fujita, J. Yazahi, K. Yamaguchi, K. Ogura, *Chem. Commun*., 1996, 1535.
15. Y. Mulyana, C. J. Kepert, L. F. Lindoy, A. Parkin, P. Turner, *Dalton Trans*., 2005, 1598.
16. E. Craven, E. Mutlu, D. Lundberg, S. Temizdemir, S. Dechert, H. Brombacher, C. Janiak, *Polyhedron*, 2002, **21**, 553.
17. G. Ferguson, M. C. Jennings, *Acta Cryst*. 1991, **C47**, 2079.
18. A. H. Cowley, R. L. Geerts, C. M. Nunn, S. Trofimenko, *J. Organamet. Chem*., 1989, **365**, 19.
19. P. Ghosh, T. Hascall, C. Dowling, G. Parkin, *J. Chem. Soc., Dalton Trans*., 1998, 3355.
20. T. Fillebeen, T. Hascall, G. Parkin, *Inorg. Chem*., 1997, **36**, 3787.
21. O. Kristiansson, *Eur. J. Inorg. Chem*., 2002, 2355.
22. S. Hiraoka, Y. Kubota, M. Fujita, *Chem. Commun*, 2000, 1509.
23. R. –G. Xiong, X. –Z. You, B. F. Abrahams, Z. Xue, C. –M. Che, *Angew. Chem,. Int. Ed*., 2001, **40**, 4422.
24. J. S. Seo, D. Whang, H. Lee, S. I. Jun, J. Oh, Y. J. Jeon, K. Kim, *Nature*, 2000, **404**, 982.
25. E. V. Anokhina, A. J. Jacobson, *J. Am. Chem. Soc*., 2004, **126**, 3044.

26. E. –Q. Gao, S. –Q. Bai, Z. –M. Wang, C. –H. Yan, *J. Am. Chem. Soc*., 2003, **125**, 4984.
27. V. Balamurugan, R. Mukkerjee, *CrystEngComm*., 2005, **7**, 337.
28. C. Janiak, *Dalton Trans*., 2003, 2781.
29. O.R. Evans, Z. Y. Wang, W. B. Lin, *Chem. Commun*., 1999, 1903.
30. J. A. McCleverty, I. Wolochowiez, *J. Organomet. Chem*., 1979, **169**, 289.
31. M. Angaroni, G. A. Ardizzoia, G. D'Alfonso, G. La Monica, N. Masciocchi, M. Moret, *J. Chem. Soc., Dalton Trans*., 1990, 1895.
32. 'PLATON: A Multipurpose Crystallographic Tool' A. L. Spek, *J. Appl. Cryst*., 2003, **36**, 7-13.
33. F. Rafat, M. Y. Siddiqi, K. S. Siddiqi, *J. Serb. Chem. Soc*., 2004, **69**, 641
34. F. A. Cotton, G. Wilkinson, *Advanced Inorganic Chemistry*, *5th Ed*., Wiley-Interscience, 1988.
35. M. J. Hannon, C. L. Painting , W. Errington, *Chem. Commun*, 1997, 307.
36. O. V. Dolomanov, A. L. Blake, N. R. Champness, M. Schröder, C. Wilson, *Chem. Commun*, 2003, 682.
37. M. B. Duriska, S. R. Batten, J. Lu, P. Turner, *Manuscript in Preparation.*
38. A. J. Amoroso, J. C. Jeffery, P. L. Jones, J. A. McCleverty, E. Psillakis, M. D. Ward, *J. Chem. Soc., Chem. Commun*., 1995, 1175.
39. K. Weis, H. Vahrenkamp, *Inorg. Chem*., 1997, **36**, 5589.
40. K. Weis, H. Vahrenkamp, *Inorg. Chem*., 1997, **36**, 5592.
41. (a) Y. Sun, R. McDonald, J. Takats, V. W. Day, T. A. Eberspacher, *Inorg. Chem*., 1994, **33**, 4433; (b) G. M. Ferrence, R. McDonald, M. Morissette, J. Takats, *J. Organomet. Chem*., 2000, **596**, 95; (c) A. C. Hiller, S. –Y. Liu, A. Sella, M. R. J. Elsegood, *Inorg. Chem*., 2000, **39**, 2635.
42. (a) S. Trofimenko, J. C. Calabrese, P. J. Domaille, J. S. Thompson, *Inorg. Chem*., 1989, **28**, 1091; (b) S. G. Roundhill, D. M. Roundhill, D. R. Bloomquist, C. Landee, R. D. Willett, D. M. Dooley, H. A. Gray, *Inorg. Chem*., 1979, **18**, 831; (c) A. J. Canty, N. J. Minchin, L. M. Engelhardt, B. W. Skelton, A. H. White., *J. Chem. Soc., Dalton Trans*., 1986, 645; (d) K. Niedenzu, P. M. Niendenzu, K. R. Warner, *Inorg. Chem*., 1985, **24**, 1604 (e) J. C. Calabrese, P. J. Domaille, S. Trofimenko, G. J. Long, *Inorg. Chem*., 1991, **30**, 2795; (f) A. L. Rheingold, C. D. Incarvito, S. Trofimenko, *J. Chem. Soc., Dalton Trans*., 2000, 1233.

Chapter Three

Lanthanides & Scorpionates

3.1 Introduction

As mentioned in chapter one, the multidentate ligands bis[3-(2-pyridyl)pyrazol-1-yl]dihydroborate (Bp^{2py}) and tris[3-(2-pyridyl)pyrazol-1-yl]dihydroborate (Tp^{2py}) (**Fig. 3.1.1**) have proven extremely popular in the studies of lanthanide ions.[1] Their large cavity sizes are well suited to these metal ions, and they provide it with a set of hard-donor *N* atoms making their complexes both stable and easy to isolate. Their highly encapsulating nature, particularly that of Tp^{2py} which offers six *N* donors, often promotes the exclusion of solvent molecules from the metal ion's coordination sphere[2,3], and the ligands themselves have relatively few C-H oscillators in close proximity to the metal centre. Both these phenomena help to optimise the lifetimes of the lanthanide luminescence by removing undesirable non-radiative pathways (**Section 1.2.4.2**).[4,5]

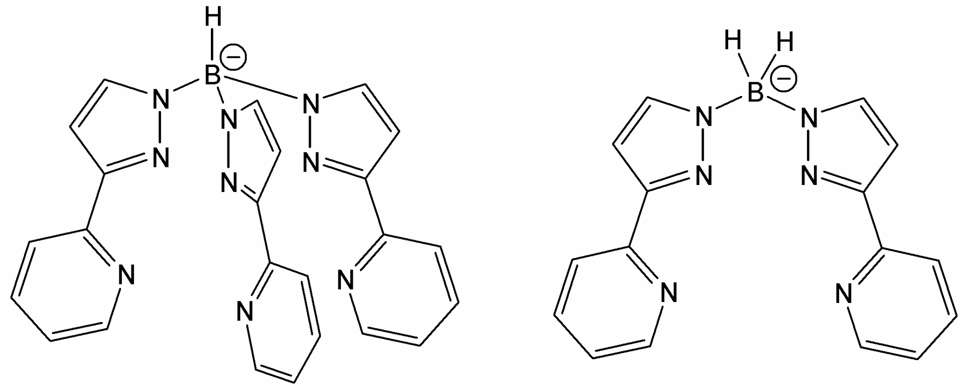

$[Tp^{2py}]^-$ $[Bp^{2py}]^-$

Fig. 3.1.1 – Scorpionates of Tp^{2py} and Bp^{2py}

In this chapter we continue to expand on this aspect of the ligands' chemistry by studying their behaviour in a range of ternary lanthanide (III) complexes with (i) the 1,3-diketonate ligand of the dibenzoylmethane anion (dbm^-) (**Fig. 3.1.2**) and (ii) the nitrate anion (NO_3^-). The structural and chelating natures of these co-ligands respectively favour the exclusion of both C-H oscillators and solvent molecules from the metal centre,[6] giving rise to mixed-ligand complexes whose luminescence lifetimes are maximised as far as possible.

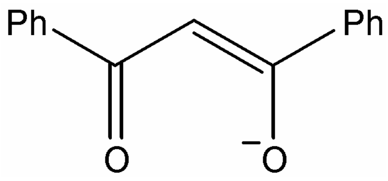

Fig. 3.1.2 – Monoanion of dibenzoylmethane

3.2 Results and Discussion

3.2.1 Structural Studies of Tp^{2py} Complexes

Earlier studies by Graham Motson on the complexes of [Ln(Tp^{2py})(dbm)$_2$] (where Ln = Nd, Tb, Yb), produced some questions on the behaviour of these systems when an inconsistency in the photophysical measurements was noticed.[7] In the Nd complex, Motson observed an unusual rearrangement in the reaction mixture to afford a crystalline complex of 12-coordinate [Nd(Tp^{2py})$_2$]$^+$ cations and 8-coordinate [Nd(dbm)$_4$]$^-$ anions, with the latter being a near-perfect example of cubic O$_8$ coordination geometry. The 12-coordinate [Nd(Tp^{2py})$_2$]$^+$ species had already been observed with Nd(III),[8] as well as Sm(III) and U(III),[9] and whilst initial FAB results indicated formation of the [Nd(Tp^{2py})(dbm)$_2$] species in solution, the rearrangement upon crystal growth was deemed to be driven by the potential coordinating ability of the pendant arm. This prompted us to have a closer look at the series by synthesising the europium and praseodymium analogues.

3.2.1.1 Synthesis of Complexes

Reaction of the appropriate lanthanide(III) chloride with KTp^{2py} and Hdbm (1:1:2) in MeOH and several drops of Et$_3$N, gave rise to a coloured solution from which a precipitate was isolated after the addition of water. Both elemental analysis and FAB mass spectrometry showed the complexes to be of the form [Ln(Tp^{2py})(dbm)$_2$] (**Table 3A**). Crystals suitable for X-Ray diffraction studies were grown over several days after the layering of hexanes onto a concentrated solution of the complex in CH$_2$Cl$_2$.

3.2.1.2 $[Eu(Tp^{2py})(dbm)_2]$

As in the Tb complex,[10] the environment about the Eu(III) centre comprises an 8-coordinate N_4O_4 donor set made up from the two dbm ligands and two arms of the now tetradentate Tp^{2py} ligand, whose third arm is uncoordinated and pendant (**Fig. 3.2.1**).

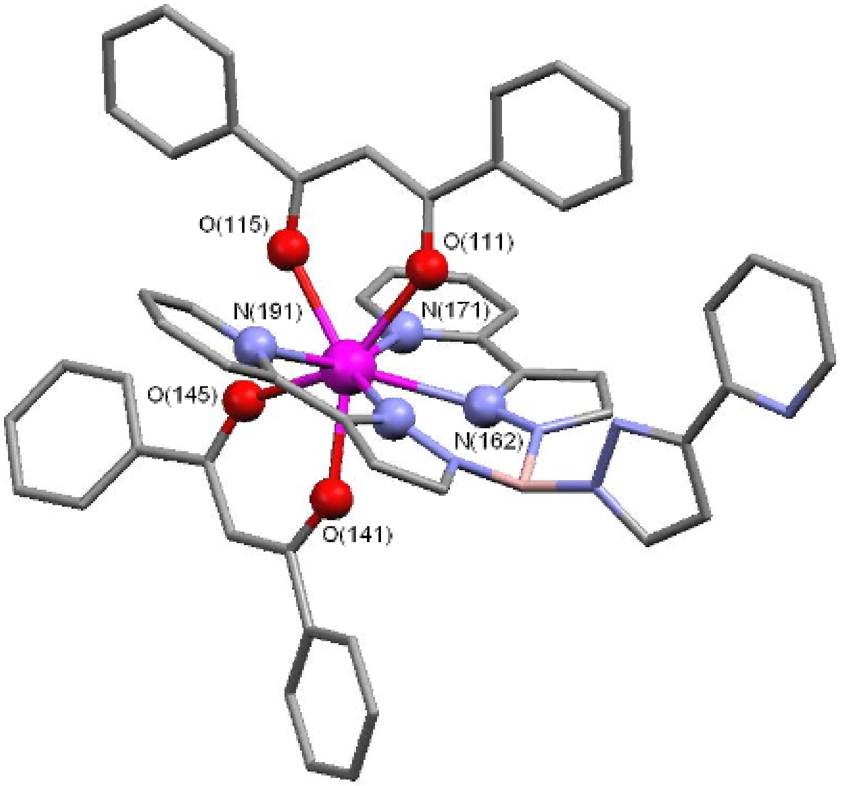

Fig. 3.2.1 – Crystal structure of $[Eu(Tp^{2py})(dbm)_2]$

Given the geometric constraints on the ligands and their bite angles, the geometry about the metal centre can be described as approximately square antiprismatic, with one square face defined by O(111)/O(115)/N(182)/N(191) and the other by O(141)/O(145)/N(162)/N(171), with mean deviations from the plane of 0.32 and 0.17 Å respectively (**Fig. 3.2.2a**). The former plane has an average edge length and corner angle of 2.89 Å and 87.15°, whilst the latter's are 2.95 Å and 89.22°. The angle between these two planes is 9.0°.

Alternatively, the structure can be viewed as a near-perfect equatorial belt of four nitrogen atoms N(162)/N(171)/N(182)/N(191) with axial 'capping' on both sides by the dbm oxygen pairs of O(111)/O(115) and O(141)/O(145) (**Fig. 3.2.2b**). The N_4 and O_4 planes deviate from the mean plane by 0.016 and 0.16 Å respectively, and the Eu metal ion sits 0.24 Å out of the N_4 plane.

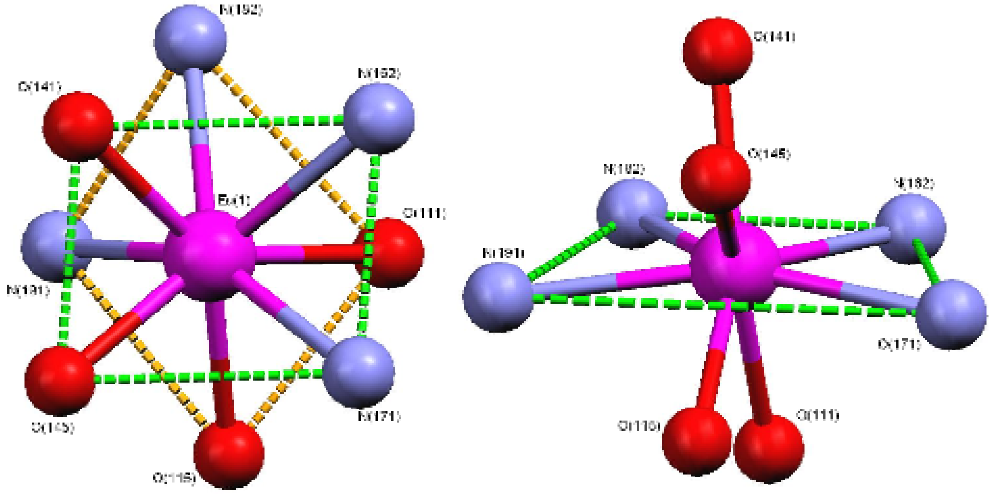

(a) **(b)**

Fig. 3.2.2 – Geometry about the metal centre of [Eu(Tp^{2py})($dbm)_2$]

The large steric bulk of both types of ligand favour the dbm units coordinating on opposite sides of the N_4 plane and is no doubt a partial cause in forcing the third pyridyl-pyrazole arm away from the metal, which now resides in a trans-coplanar arrangement to minimise electrostatic repulsions between the nitrogen atoms (the torsion angle between pyrazolyl and pyridyl rings is 14.4°). Selected bond lengths are given in **Table 3.2.1**, whilst bond angles can be found in **Appendix 3**.

This 'hypodentate' behaviour of Tp^{2py} has been seen before in many situations in its coordination chemistry to the *f*-block elements,[10-12] and indeed the transition metals.[13]

As the *f*-block +3 metal cations have no directional influence on the arrangements of surrounding ligands (**Section 1.2.2**), coordination behaviour in such complexes is only affected by the aspects of (i) the size of the ligand(s), and (ii) the size of the metal ion. Earlier works by Kanellakopulos and Takats showed that complexes of [Ln(Tp)$_3$] were 9-coordinate in cases of Pr and Nd,[14] but 8-coordinate when the smaller Yb metal was used,[15] proving that the ionic radius of the lanthanide ion plays a decisive role in controlling the ligand coordination mode.

Eu(1)-O(141)	2.328(4)	Eu(1)-N(162)	2.527(5)
Eu(1)-O(111)	2.336(4)	Eu(1)-N(182)	2.535(5)
Eu(1)-O(145)	2.348(4)	Eu(1)-N(171)	2.551(5)
Eu(1)-O(115)	2.357(4)	Eu(1)-N(191)	2.570(5)

Table 3.2.1 - Selected bond lengths (Å) for [Eu(Tp^{2py})(dbm)$_2$]

3.2.1.3 [Pr(Tp^{2py})(dbm)$_2$]

In synthesising the analogous Pr complex, we found that by using a larger metal ion, this 'hypodentate' ligand behaviour can be eradicated to leave us with the initially desired complex in which all three arms of Tp^{2py} chelate to the metal centre.

Elemental analysis confirmed the formation of [Pr(Tp^{2py})(dbm)$_2$] and FAB mass spectrometry of the bulk sample gave a strong peak at 808 corresponding to the loss of one dbm unit to give the fragment {Pr(Tp^{2py})(dbm)}$^+$ and a weaker signal at 1029 suggested the presence of the {Pr(Tp^{2py})(dbm)$_2$} unit, minus two hydrogen ions. Unit cell comparisons of several crystals suggested the structure (**Fig. 3.2.3**) was representative of the bulk sample.

The five chelating groups all lie along the same axis as the B-H bond, and as all five are now coordinating, the metal centre is in a 10-coordinate N$_6$O$_4$ coordination environment, making this only the third example of such an environment about a Pr metal.[2,16] The average bond lengths of Pr-N$_{pz}$ (2.652 Å), Pr-N$_{py}$ (2.738 Å) and Pr-O (2.469 Å) remain unremarkable, but are each understandably larger than those of the Eu (2.531; 2.562; 2.343 Å) and Tb (2.506; 2.532; 2.321 Å) analogues.

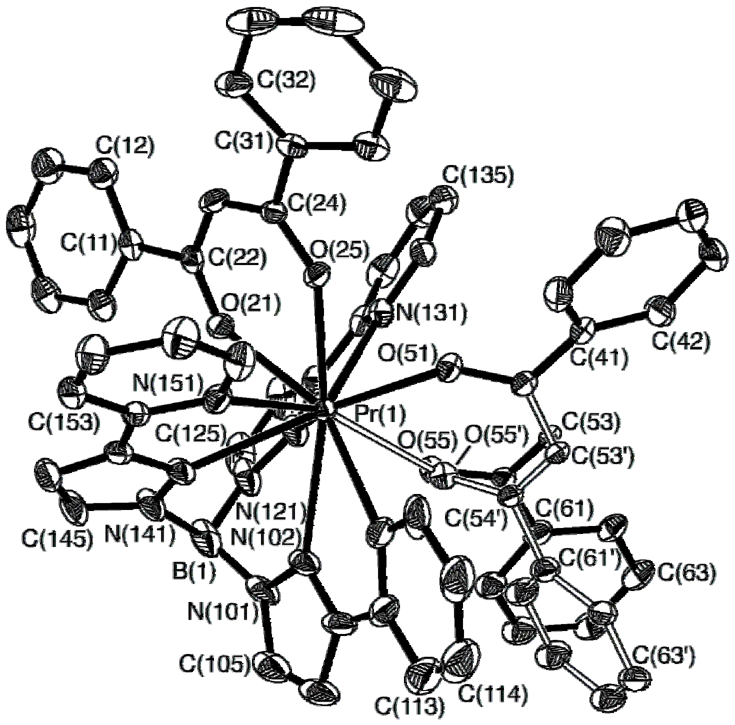

Fig. 3.2.3 – Crystal structure of $[\mathrm{Pr(Tp^{2py})(dbm)_2}]$

- The disordered component is shown with white bonds.

There is also a degree of disorder about the C(52) atom on one of the dbm units, as illustrated on **Fig. 3.2.3**. Here, both the phenyl and diketonate rings have been constrained to the ideal geometries and the disorder modelled over two independent sites at 0.486 % and 0.514 % site occupancies.

The geometry about the metal centre does not fit any of the previously suggested ‘ideal’ 10-coordination arrangements,[17] but the best visual description is illustrated in **Fig. 3.2.4** by viewing down the N(122)-Pr(1) bond. With the pyrazolyl nitrogen N(122) in the centre of the picture at the ‘apex’, the two other pyrazole nitrogens, N(102) and N(142) form a pentagon with a pyridyl nitrogen, N(131), and an oxygen atom from each dbm unit, O(55) and O(21).

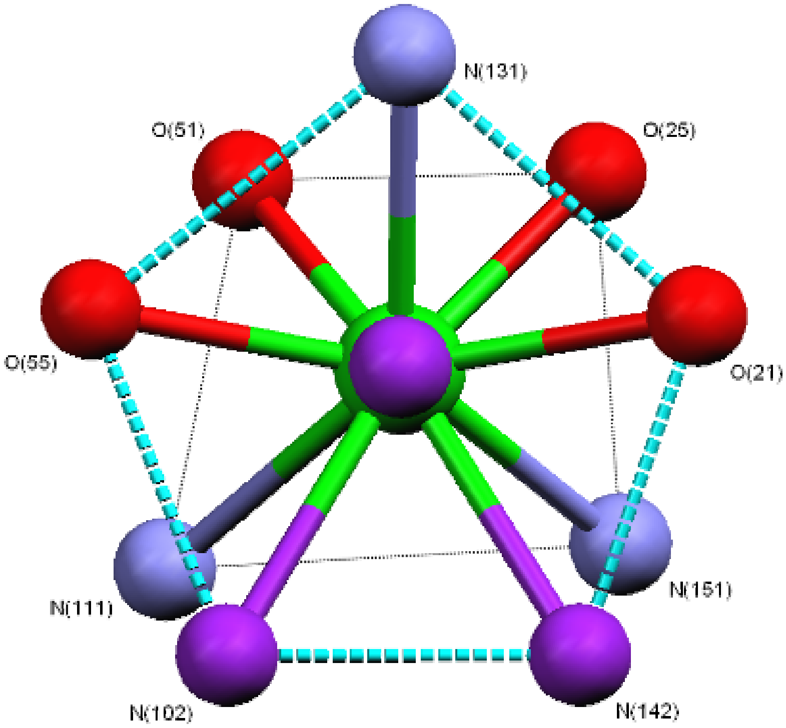

Fig. 3.2.4– Geometry about the metal centre of [Pr(Tp^{2py})(dbm)$_2$] viewing down the N(122)-Pr bond (only one disordered component is shown)

The average edge length and vertex angle for this pentagon are 2.818 Å and 107.6° respectively, using O(55); if O(55’) is used instead these figures become 2.871 Å and 106.9°.

The five atoms display an average deviation from the mean plane of 0.095 Å [using O(55)] or 0.180 Å [using O(55’)]. The pentagon is capped with the N(122) atom 1.595 Å [O(55)] or 1.663 Å [O(55’)] above it, whilst on its other side resides a distorted square defined by atoms O(25)/N(151)/N(111)/O(51).

Pr(1)-N(122)	2.595(3)	Pr(1)-O(55)	2.448(17)
Pr(1)-N(142)	2.656(3)	Pr(1)-O(25)	2.454(2)
Pr(1)-N(131)	2.656(3)	Pr(1)-O(51)	2.464(2)
Pr(1)-N(102)	2.704(3)	Pr(1)-O(55')	2.492(17)
Pr(1)-N(151)	2.754(3)	Pr(1)-O(21)	2.496(2)
Pr(1)-N(111)	2.804(3)		

Table 3.2.2 - Selected bond lengths (Å) for [Pr(Tp^{2py})(dbm)$_2$]

This 'square' has an average length of 2.983 Å along its edges and an average angle of 89.5° at its corners, but is rather irregular with its corner angles varying from 75.50° to 102.31°. The mean deviation from this plane of four atoms is 0.135 Å. Selected bond lengths about the metal centre are given in **Tables 3.2.2**.

3.2.2 *Structural Studies of Bp^{2py} Complexes*

Due to the varying coordination behaviour of the Tp^{2py} ligand in the $[Ln(Tp^{2py})(dbm)_2]$ complexes, it is apparent that any photophysical studies on the series are complicated, with the behaviour of the complexes even more unpredictable in solution. It is for these reasons that we have now replaced Tp^{2py} with the tetradentate analogue Bp^{2py}, in the hope that the absence of the third pyridyl-pyrazole arm will provide stable 8-coordinate species with no structural ambiguity, suitable for subsequent photophysical studies.

In addition to this, such luminescence studies have seldom been performed on complexes containing Er and Pr metals, which are also luminescent in the near-IR region. In order to expand this field we have synthesised the complexes of $[Ln(Bp^{2py})_2(NO_3)]$ and $[Ln(Tp^{2py})(NO_3)_2]$ (where Ln = Pr or Er).

3.2.2.1 Synthesis of Complexes

All complexes of the type $[Ln(Bp^{2py})(dbm)_2]$ were prepared in an identical manner to those of $[Ln(Tp^{2py})(dbm)_2]$ (**Section 3.2.1.1**), whilst those of $[Ln(Bp^{2py})_2(NO_3)]$ and $[Ln(Tp^{2py})(NO_3)_2]$ were prepared by the published methods *via* mixing methanolic solutions of the appropriate lanthanide(III) nitrate salt and KBp^{2py} or KTp^{2py} respectively.[2,18,19] All complexes were subjected to subsequent precipitation and recrystallisation procedures. Elemental analyses and FAB mass spectrometry indicated the above compositions (**Tables 3A-3B**), and X-Ray quality crystals were again grown by the layering of hexanes onto a concentrated CH_2Cl_2 solution of the complex.

3.2.2.2 [Ln(Bp^{2py})(dbm)$_2$] (Ln = Pr, Nd, Eu, Gd, Tb, Er, Yb)

All seven members of this series were shown to be both isomorphous and isostructural in sharing near identical unit cell dimensions and crystallising in the same space group (P2$_1$/c). The geometries observed about the coordination spheres of the metal centres are identical to that observed in 8-coordinate [Eu(Tp^{2py})(dbm)$_2$] (**Fig. 3.2.5**).

In each case, there are two crystallographically independent molecules residing in the asymmetric unit, only one of which is shown in **Fig. 3.2.5**. Whilst selected bond lengths and angles of both these molecules are given for all members in the series in **Appendix 3**, the two independent molecules are very similar to the extent that there is no need to describe them both. Therefore, only one molecule is used in the following structural discussions. In addition to this, we also limit these discussions to the extreme members of the series, Pr and Yb, with selected bond lengths for these complexes shown in **Table 3.2.3**.

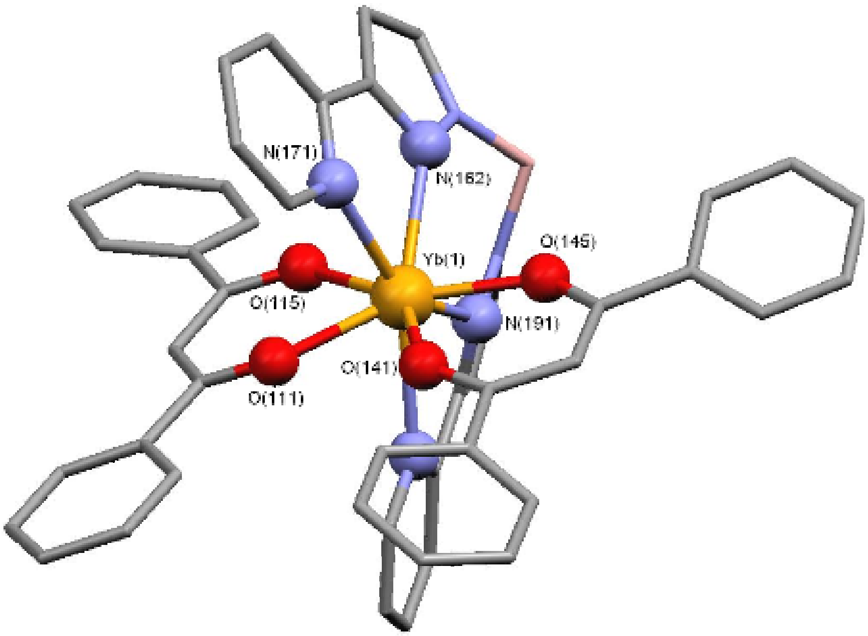

Fig. 3.2.5– Crystal structure of [Yb(Bp^{2py})(dbm)$_2$]

In its previous chemistry with lanthanides,[3,8,20] Bp^{2py} has always coordinated all four of its nitrogen donors to the metal ion, and the $[Ln(Bp^{2py})(dbm)_2]$ system here is no exception. As expected, the metal centres reside in an 8-coordinate N_4O_4 geometry which again can be viewed either as a square antiprismatic geometry, or as a N_4 equatorial belt capped either side by a pair of chelating oxygens with the four nitrogen atoms forming a near-perfect plane (**Fig. 3.2.6**).

The mean deviation of the constituent atoms from the N_4 plane is 0.0012 Å for the Yb structure and 0.0093 Å for that of Pr, with the metal ions sitting out of this plane by 0.197 and 0.279 ° respectively. The Bp^{2py} ligand itself cannot remain perfectly flat due to the *sp*^{3}-hybridisation at the boron atom (also the case in the Tp^{2py} systems). Consequently the pyridyl rings are inclined at an angle of 33.8° to one another for the Yb complex, and 34.9° for the Pr complex.

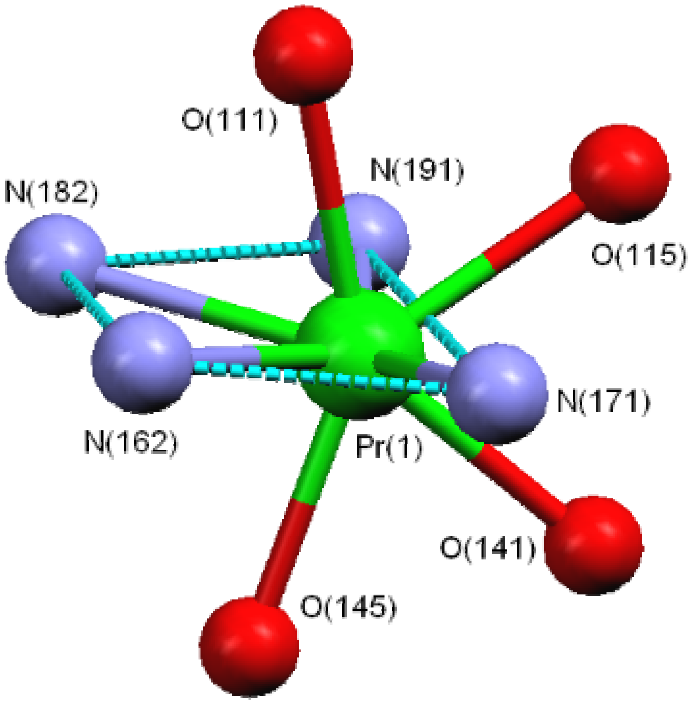

Fig. 3.2.6 – Equatorial N_4 belt about the Pr metal centre

Pr(1)-O(145)	2.390(2)	Yb(1)-O(145)	2.247(2)
Pr(1)-O(111)	2.391(2)	Yb(1)-O(115)	2.256(2)
Pr(1)-O(115)	2.397(2)	Yb(1)-O(111)	2.2743(18)
Pr(1)-O(141)	2.403(2)	Yb(1)-O(141)	2.2879(19)
Pr(1)-N(182)	2.589(3)	Yb(1)-N(182)	2.452(2)
Pr(1)-N(162)	2.603(3)	Yb(1)-N(162)	2.466(2)
Pr(1)-N(171)	2.627(3)	Yb(1)-N(171)	2.478(2)
Pr(1)-N(191)	2.656(3)	Yb(1)-N(191)	2.509(2)

Table 3.2.3 - Selected bond lengths (Å) for the complexes of [Pr(Bp^{2py})(dbm)$_2$] and [Yb(Bp^{2py})(dbm)$_2$] (data for only one of the two independent molecules is shown)

In the case of Yb, the square antiprismatic geometry consists of two square planes comprising O(141)/O(145)/N(182)/N(191) [average edge (2.865 Å) and corner (87.6°)] and O(111)/O(115)/N(162)/N(171) [average edge (2.764 Å) and corner (86.9°)], which again, are far from perfectly square due to the bite constraints imposed by the ligands.

As expected, there are slightly larger dimensions on the comparable square planes of the Pr structure [(2.878 Å / 87.5°) and (3.056 Å / 87.6°) respectively] although the corner angles of these square planes remain relatively similar. The two square planes are near parallel with an angle of 6.1° (Yb) or 7.5° (Pr) between them (**Fig. 3.2.7**).

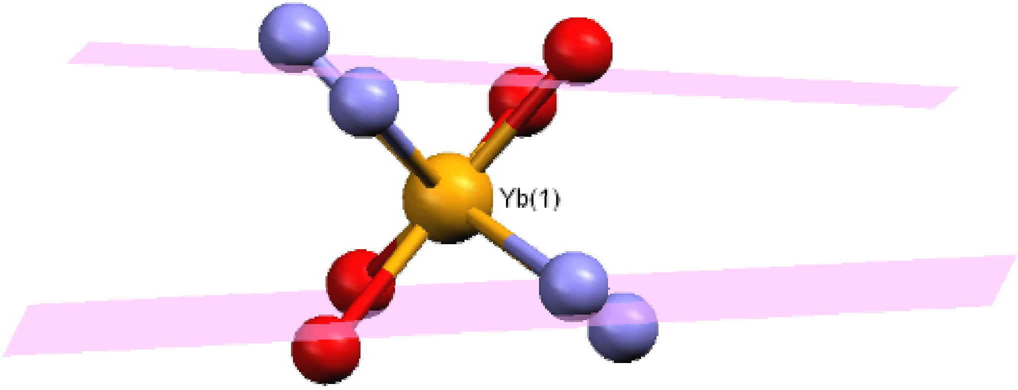

Fig. 3.2.7 – Near parallel planes of square antiprismatic geometry

As the lanthanide series is traversed, the data show a progressive decrease in bond length and an increase in bite angle, consistent with the contraction of the ionic radius of the metal. From the above discussions on changes in geometry, it is clear that ligand conformation in the $[Ln(Bp^{2py})(dbm)_2]$ systems, varies only slightly with the ionic radius of the lanthanide ion.

Another common aspect of this series is the presence of a CH_2Cl_2 molecule, which lies astride a C_2 axis and has been modelled with the appropriate disorder. From a first glance, the purpose of this molecule appears to be assisting the packing arrangement of the complexes in the crystalline form through various Cl···H hydrogen bonds.

However, the hydrogen atom(s) the chlorines choose to bond with vary throughout the series; ranging from bridging $H_{pz}\cdots Cl\cdots H_{py}$ bonds in the Pr complex (**Fig. 3.2.8**, average Cl···H = 2.961 Å) to single $H_{py}\cdots Cl$ bonds in that of Yb (**Fig. 3.2.9**, average Cl···H = 2.927 Å).

3.2.2.3 $[Ln(Bp^{2py})_2(NO_3)]$ (Ln = Pr, Er)

Both Er and Pr form isostructual complexes to the Tb, Nd and Yb analogues already published,[8,18] with the displacement of two nitrate anions from hydrated $[Ln(NO_3)_3]$ by two fully coordinating Bp^{2py} units to give a 10-coordinate N_8O_2 donor environment about the metal centre (**Fig. 3.2.10**). Two molecules of CH_2Cl_2 are present in the asymmetric units and absent from the first coordination spheres of the metal ions.

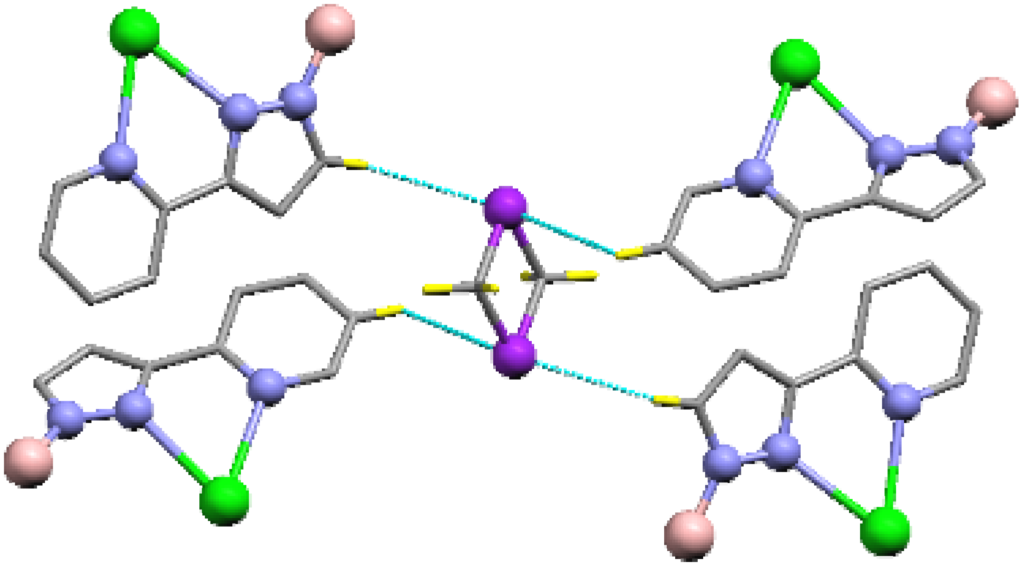

Fig. 3.2.8 – Disordered CH_2Cl_2 in the lattice of [Pr(Bp^{2py}(dbm)$_2$]

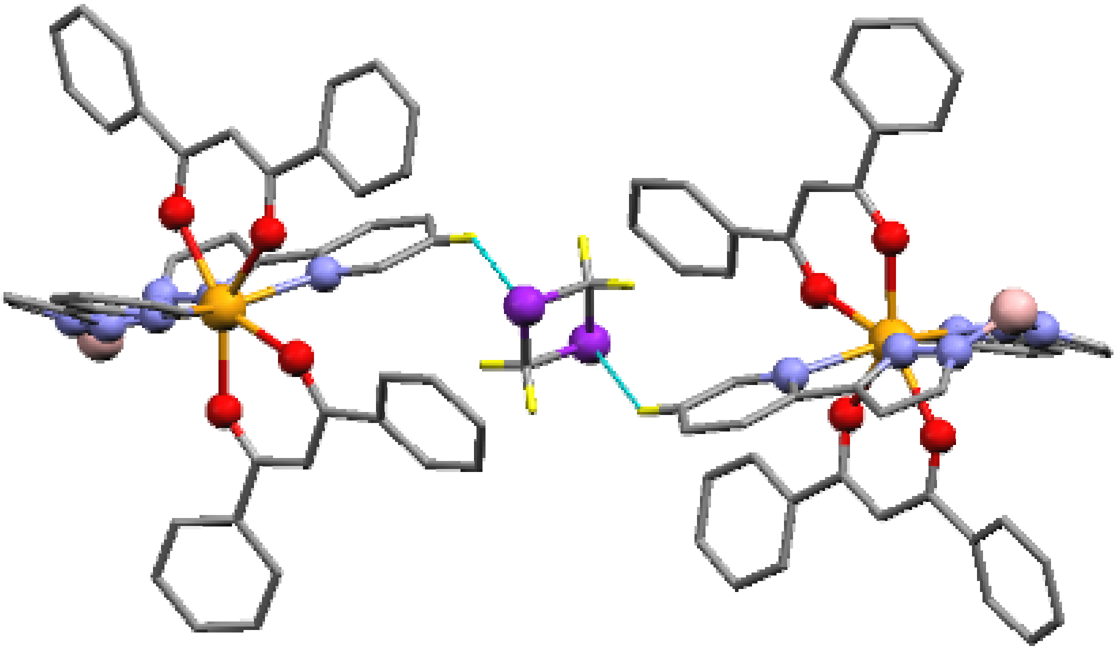

Fig. 3.2.9 – Disordered CH_2Cl_2 in the lattice of [Yb(Bp^{2py}(dbm)$_2$]

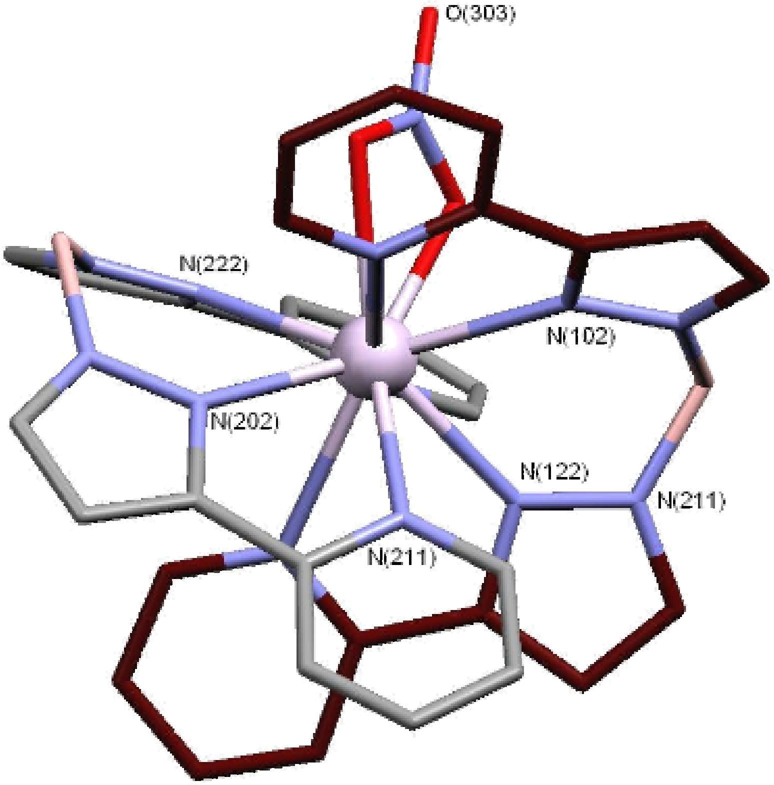

Fig. 3.2.10 – Crystal structure of $[Er(Bp^{2py})_2(NO_3)]$

Such similarities to the already published analogues do not warrant significant further discussions about their geometries, it is noticeable that these two complexes adopt the same coordination geometry about the metal centre as the $[Pr(Tp^{2py})(dbm)_2]$ complex described earlier. This is shown in **Fig. 3.2.11** with the erbium complex, viewing down the N(131)···Er(1) bond.

The distorted five-sided pentagon comprises N(211)/N(202)/N(222)/N(231)/N(122) with an average side length and vertex corner of 2.864 Å and 107.6° respectively, with a mean deviation from this plane of 0.103 Å. The Er atom resides 0.8931 Å below this plane and towards the approximate square base made up of the set N(102)/N(111)/O(301)/O(302), which itself has an average side length and vertex angle of 2.643 Å and 88.8° respectively.

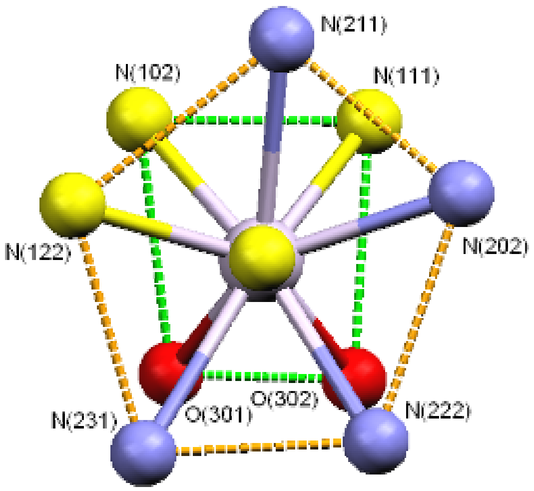

Fig. 3.2.11 – Geometry about the metal centre in $[Er(Bp^{2py})_2(NO_3)]$ viewing down the N(131)···Er(1) bond. The N_4 donor set of one Bp^{2py} is coloured yellow, the other blue.

From **Fig. 3.2.12** it appears the Pr and Er complexes have opposite chirality from the arrangement of the ligands about the metal centres. However, as neither these (nor the analogous complexes[8,18]) crystallise in chiral space groups, the complexes are likely to have crystallised in racemic mixtures, with the enantiomer solved in the asymmetric unit chosen at random.

The expected decrease in metal-donor bond lengths between the Pr and Er analogues is observed (selected bond lengths are given in **Tables 3.2.4**), but here the contraction of the relative ionic radii has a distinctly marked effect on the structure.

Er(1)-N(102)	2.5067(19)	Er(1)-N(211)	2.593(2)
Er(1)-N(111)	2.840(2)	Er(1)-N(222)	2.525(2)
Er(1)-N(122)	2.452(2)	Er(1)-N(231)	2.929(2)
Er(1)-N(131)	2.5840(19)	Er(1)-O(301)	2.4612(18)
Er(1)-N(202)	2.4509(19)	Er(1)-O(302)	2.4923(18)

Pr(1)-N(122)	2.589(5)	Pr(1)-N(222)	2.656(5)
Pr(1)-N(102)	2.655(5)	Pr(1)-N(211)	2.732(5)
Pr(1)-N(131)	2.720(5)	Pr(1)-N(231)	2.808(5)
Pr(1)-N(111)	2.765(5)	Pr(1)-O(301)	2.577(5)
Pr(1)-N(202)	2.587(5)	Pr(1)-O(302)	2.606(5)
Pr(1)-N(300)	3.005(5)		

Table 3.2.4 - Selected bond lengths (Å) for the complexes of $[Er(Bp^{2py})_2(NO_3)]$ and $[Pr(Bp^{2py})_2(NO_3)]$

Whilst the M···N_{pz} bonds remain shorter on average to those of M···N_{py}, two of the Er···N_{py} bonds are especially long at 2.840(2) and 2.929(2) Å [to N(111) and N(231) respectively]. This is unlike the environment in the $[Pr(Bp^{2py})_2(NO_3)]$ complex where Pr···N_{py} distances lay between 2.720(5) and 2.808(5) Å, and remarkably larger than the average Er···N_{pz} bond length (2.484 Å).

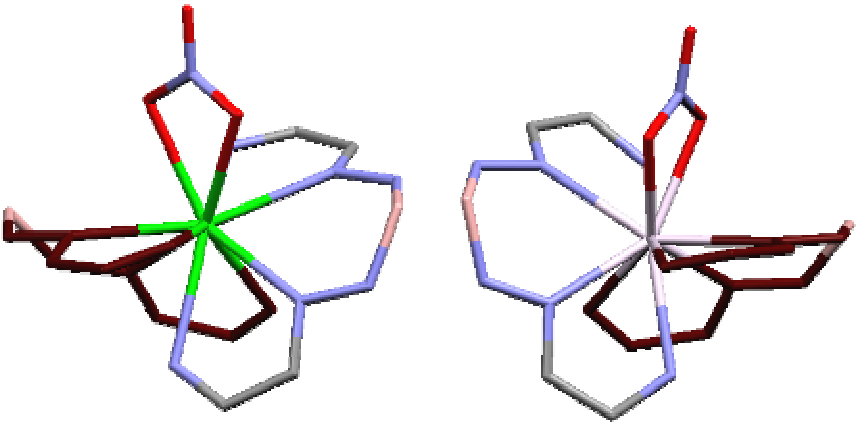

Fig. 3.2.12 – Optical isomers of $[Pr(Bp^{2py})_2(NO_3)]$ (GREEN) **and $[Er(Bp^{2py})_2(NO_3)]$** (LILAC)

Therefore, the expected contraction of the coordination environment resulting from the smaller ionic radius of Er(III,) results in steric congestion which is relieved by pushing two of the pyridyl ligands on the erbium complex further out of the coordination sphere. Such a significant structural rearrangement could have repercussions on subsequent photophysical measurements.

Crystal structures of the complexes $[Ln(Tp^{2py})(NO_3)_2]$ (where Ln = Pr or Er) have already been described in detail,[2] yet it is worth recalling that all three arms of the scorpionate ligand and both nitrate anions are chelating here to the metal centres, thus completing another example of a 10-fold N_6O_4 coordination geometry about the lanthanide ions. No unusual bond distances were observed in this erbium complex.

3.2.3 *Photophysical Studies of [Ln(Bp^{2py})($dbm)_2$] Complexes*

The electronic absorption spectrum of [Yb(Bp^{2py})($dbm)_2$] in CH_2Cl_2 is shown in **Fig. 3.2.13**. This spectrum is representative of the other six members of the [Ln(Bp^{2py})($dbm)_2$] series in that it shows three strong transitions in the UV/Visible region of the electromagnetic spectrum at: *ca*. 250, 297 ± 4, and 359 ± 3 nm. The first two transitions can be attributed to ligand-centred $\pi \rightarrow \pi^*$ transitions of the pyrazolyl and pyridyl rings,[18] whilst the third at longer wavelength is attributed to a similar transition localised on the dbm molecule.[21]

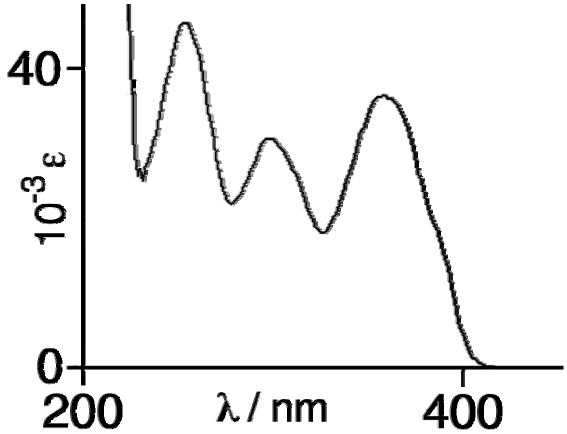

Fig. 3.2.13 – Electronic absorption spectrum of [Yb(Bp^{2py})($dbm)_2$] in CH_2Cl_2 solution.

Due to their characteristic near-IR luminescence and subsequent practical applications (**Sections 1.2.5-6**), the luminescence spectra for those members of the series where Ln = Pr, Nd, Gd, Er, and Yb were recorded.

As a consequence of their insolubility in H_2O, measurements were performed in the anhydrous protic solvents of CH_2Cl_2, CH_3OH and CD_3OD, as well as in the solid state. By using an excitation wavelength of 337 nm into the dbm-based transition, an electron should be promoted to an excited ligand *singlet* state ($\pi \rightarrow \pi^*$, **Section 1.2.4**). Those that collapse to the ligand *triplet* state and subsequently undergo intersystem crossing to the adjacent Ln(III) excited state, should then collapse to the *ground* state of the Ln(III) ion, giving rise to *metal-ion based luminescence*.

This emission can then be monitored (the results for the series [Ln(Bp^{2py})$(dbm)_2$] are summarised in **Table 3.2.5**).

	Emission lifetime τ / μs			
Complex	solid state	CH_2Cl_2	CH_3OH	CD_3OD
Yb	9.33	11.2	1.27, 8.95	12.5
Er	1.39	1.88	0.85 (weak)	1.23
Nd	0.74	0.69	0.18	0.59
Pr	0.064	0.058	0.013	0.11

Table 3.2.5 – Luminescence data for [Ln(Bp^{2py})$(dbm)_2$] using 337 nm excitation

3.2.3.1 [Yb(Bp^{2py})$(dbm)_2$]

The characteristic emission band[22] of the only possible transition $^2F_{5/2} \rightarrow {}^2F_{7/2}$ is observed at 980 nm in all solvents with very long lived luminescence lifetimes – the longest of the series. The lifetime of 11.2 μs achieved in CH_2Cl_2 is typical of such ytterbium-scorpionate complexes.[8,18]

In CH_3OH however, the emission is clearly resolved into two separate components with lifetimes of 1.3 and 9.0 μs (70 and 30 % weightings respectively). This suggests the presence of two distinct species in methanolic solution, which are interconverting slowly on the luminescence timescale.

It is likely that the shorter-lived luminescence arises from [Ln(Bp^{2py})$(dbm)_2(CH_3OH)_q$], in which the presence of one or more coordinated O-H oscillators drastically reduces the luminescence lifetime by providing a non-radiative decay path for the energy in the Ln(III) excited state. The relatively small ionic radius of Yb(III) (the smallest of all in the series), may be inducing the same behaviour observed by Takats[13] in that the decrease in bond length between donor atoms and metal ion causes fluxional dissociation of a ligand's donor atom.

Whilst this behaviour is not observed in the solid state (hence the observation of one long lived lifetime decay at 9.3 μs), it may be promoted in good donor solvents.

The longer lived component at 9.0 μs is indicative of the originally unsolvated 'intact' complex, with the small reduction in lifetime (compared to that in CH_2Cl_2) attributed to surrounding O-H oscillators in the second coordination sphere, whose deactivating effects are not as dramatic as those in the first coordination sphere.[23] Both lifetimes are independently observed here because the species' luminescence decays faster than the time it takes for the two species (solvated and unsolvated) to interconvert.

The presence of such clearly resolved 'dual species' has been seen before in similar Yb complexes,[8] but whilst the luminescence lifetimes of Nd and Pr in CH_3OH are also short-lived, we only see single species in these solutions. This result is consistent with the rate of solvent exchange at the Yb centre being much slower in comparison to the earlier metals (**Fig. 3.2.14**) due to its smaller ionic radius,[24,25] and thus the presence of two species in solution for the Pr and Nd complexes is not detectable by luminescence methods.

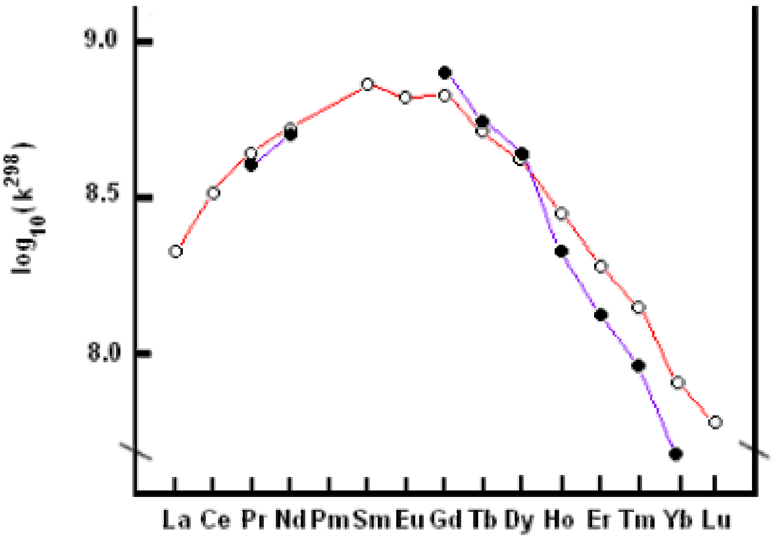

Fig. 3.2.14 – Rates of solvent exchange of SO_4^{2-} (o) and H_2O (•) on $Ln(H_2O)_n^{3+}$ (Reproduced from Ref 24)

O-D oscillators have a poorer overlap with intermediate energy levels of Ln(III) ions than O-H (**Section 1.2.4.2**), and so changing the surrounding solvent to CD_3OD restores the luminescence lifetimes by removing O-H oscillators from both the first and subsequent coordination spheres. As CD_3OD has equal dimensions to its non-deuterated cousin, we can presume that both the species $[Yb(Bp^{2py})(dbm)_2]$ and $[Yb(Bp^{2py})(dbm)_2(CD_3OD)_q]$ exist in solution, but both now have similar lifetimes. Consequently, the two lifetimes are not sufficiently different to resolve into two separate components, and we observe a single luminescence decay in CD_3OD solution with a luminescence lifetime of 12.5 μs.

The value of 'q' in the formula $[Yb(Bp^{2py})(dbm)_2(CH_3OH)_q]$ can be calculated by comparing the luminescence lifetimes in the standard and deuterated solvents with **Equation 3.1**

$$q = \mathrm{A}(K) - \mathrm{B} \qquad \textbf{Eq. 3.1}$$

A is a statistically pre-determined coefficient (characteristic of an individual lanthanide ion), and K is the change in luminescence decay rates in methanol-H_4 and methanol-D_4. B is another pre-determined correction factor that considers decay effects from outer sphere contributors. For Yb(III) in methanolic solutions,[26] A is 2.0 μs^{-1} and B is 0.1 μs^{-1} giving us

$$q = 2(\tau_{\mathrm{MeOH}}^{-1} - \tau_{\mathrm{MeOD}}^{-1}) - 0.1 \qquad \textbf{Eq. 3.2}$$

As we cannot resolve the separate luminescence decays of $[Yb(Bp^{2py})(dbm)_2]$ and $[Yb(Bp^{2py})(dbm)_2(CD_3OD)_q]$, we have to assume that they both have the same lifetime decay of 12.5 μs. By using the corresponding values for $[Yb(Bp^{2py})(dbm)_2]$ and $[Yb(Bp^{2py})(dbm)_2(CH_3OH)_q]$ in methanol-H_4 (9.0 and 1.3 μs respectively) we can calculate that the values of q (and the approximate number of methanol molecules in the first coordination sphere) are 0 for $[Yb(Bp^{2py})(dbm)_2]$ and 1.3 for $[Yb(Bp^{2py})(dbm)_2(CH_3OH)_q]$, which sensibly approximates to 1.

3.2.3.2 [Nd(Bp^{2py})(dbm)$_2$] and [Er(Bp^{2py})(dbm)$_2$]

Luminescence in both the solid state and in solution was observed for both of these complexes. The Nd(III) complex showed the characteristic emission bands of 880, 1055, and 1340 nm which correspond to transitions from the excited state of $^4F_{3/2}$, to the emissive states of $^4I_{9/2}$, $^4I_{11/2}$, and $^4I_{13/2}$ respectively.[27] Emission at 1530 nm was seen for the Er(III) analogue, indicative of the $^4I_{13/2} \rightarrow {}^4I_{15/2}$ transition.[28] Each decay fitted well to a single exponential curve, indicating the presence of a single luminescent species.

Compared to the Yb(III) analogue, the luminescence lifetimes of these two complexes are remarkably small, being less than 1 μs for Nd(III) in both solution and the solid state. This is to be expected as both Nd(III) and Er(III) have a greater manifold of intermediate excited states in their network of energy levels (**Fig. 3.2.15**) which increases the chance of energy deactivation to the ground state *via* radiationaless additional emissive states.

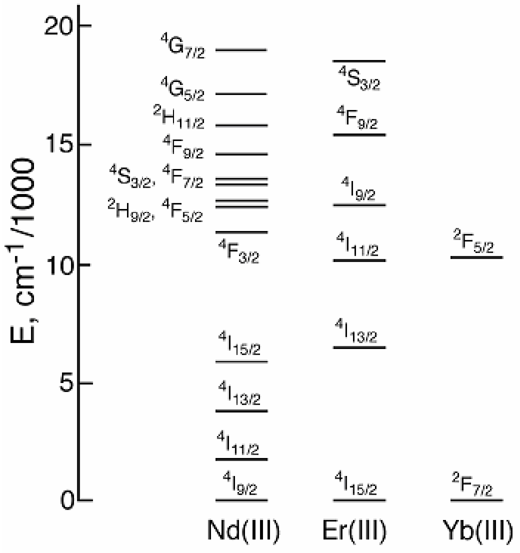

Fig. 3.2.15 – Energy levels within selected lanthanide(III) ions

In addition to this, and especially in Nd(III), the energy gaps between these extra levels closely match the vibrational energies of C-H oscillators, providing another energy quenching pathway.[29] As C-H bonds are readily present in both our scorpionate and dbm ligands, as well as in conventional solvents, Nd(III) luminescence lifetimes are more sensitive to their surroundings than the other Ln(III) ions, and they become highly dependent on the structure and environments of the coordinating ligand(s) in their complexes. Consequently, values of A and B for **Equation 3.2** have limited use, and we need to reconsider the factors in the equation.

The 'revised' equation is **Equation 3.3**, in which the values of A and B are adjusted to account not only for the effect of replacing the solvents' O-H groups with O-D oscillators, but CH_3 with CD_3 as well – something not considered in **Equation 3.2**.[8]

$$q = 0.29(\tau_{\mathrm{MeOH}}^{-1} - \tau_{\mathrm{MeOD}}^{-1}) - 0.4 \qquad \textbf{Eq. 3.3}$$

Taking the values of 0.59 and 0.18 μs for the deuterated and non-deuterated species respectively, the value of *q* for $[\mathrm{Nd(Bp^{2py})(dbm)_2}]$ is 0.7, which is right in between the values of 0 and 1.3 we achieved for the two Yb(III) species, suggesting that there is a partial degree of solvent coordination. There are two separate theories to explain this:

(i) If there are two species in solution (i.e. $[\mathrm{Nd(Bp^{2py})(dbm)_2}]$ and $[\mathrm{Nd(Bp^{2py})(dbm)_2(CH_3OH)}_q]$) then their luminescence lifetimes are sufficiently similar to prevent them being resolved into two separate species;

(ii) The rate of solvent exchange is occurring much faster than the timescale of the experiment, so a single averaged luminescence lifetime is observed.

Given the vast quenching effect we have seen between the coordinated and uncoordinated Yb(III) species, the first theory is hard to justify in not seeing such species with Nd(III).

It is more likely that the exchange rate of solvent (much faster compared to that of Yb, **Fig. 3.2.14**) is sufficiently fast enough to warrant the observation of an 'averaged out' species in solution. This behaviour has already been seen in similar studies of other lanthanide(III) ions.[8]

At the time of writing, no relationship between inner sphere solvation number (*q*) and luminescence lifetimes has been proposed for Er(III) complexes, and as these are derived purely on statistical examples, it would be unwise to attempt a relation based on this single example.

3.2.3.3 [Pr(Bp^{2py})(dbm)$_2$]

To date, there have been very few studies on the luminescence from Pr(III) complexes, with those already reported concentrating on the measurement and assignment of steady-state emission spectra.[30-33]

Assignment of emission bands from Pr(III) is more complicated due to its plethora of energy levels, enabling transitions to occur from several excited levels ($^3P_0$, $^1D_2$, and $^1G_4$, **Fig. 3.2.16a**) which emit in both the visible and near-IR regions. In our system, luminescence was observed at 600, 1030 and 1440 nm. The first of these values was recorded in CH_2Cl_2 only, and is shown to comprise several individual components (**Fig. 3.2.16b**). These consist of two emission maxima at 603 and 610 nm, as well as some definite shoulders on both the high (594 nm) and low energy sides (620 and 628 nm).

Voloshin and co-workers also observed similar closely overlapping maxima at *ca.* 605 and 610 nm in numerous β–diketonate-Pr(III) complexes, crediting them to the transitions of $^1D_2 \rightarrow {}^3H_4$ and $^3P_0 \rightarrow {}^3H_6$ respectively.[30] In reference to our observations; this implies successful population of the $^3P_0$ energy level by the triplet excited state of the dbm ligand.

But Voloshin also observed $^3P_0$-based emissions from transitions to the $^3H_4$ and $^3F_2$ levels (490 and 645 nm respectively) which we do not see in our system; signifying that the triplet state of the dbm ligand lies beneath the $^3P_0$ excited state at approximately 20,000 cm^{-1}, and is thus unable to populate the $^3P_0$ level. In this instance, the composite structure of the visible emission must arise from crystal field effects rather than from two overlapping transitions.

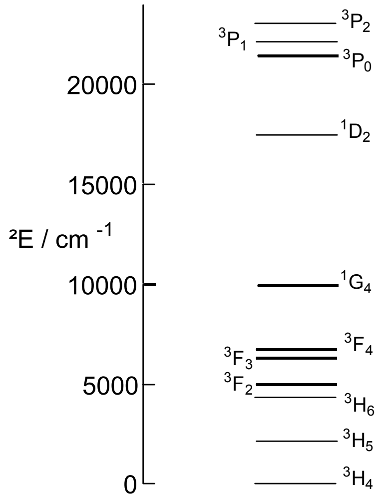

Fig. 3.2.16a
– Energy level diagram for Pr(III)

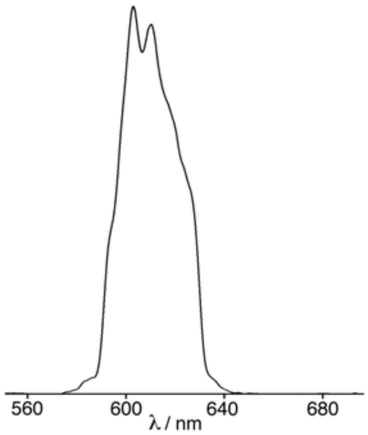

Fig. 3.2.16b
- Emission spectrum of [Pr(Bp^{2py})(dbm)$_2$] in CH$_2$Cl$_2$

As *f*-orbitals are so well shielded by the 5*s* and 5*p* orbitals, they are often deemed not to be perturbed by the approach and subsequent coordination of ligand molecules. This means that crystal field effects for Ln(III) ions are negligible when compared to those of early *d*-metals (between 1-10 % of those experienced by *d*-block metals) and are often ignored. However, such effects have been noted before in Pr(III) systems with the $^3H_4$ ground state level splitting into several closely spaced states. In the presence of weak-field splitting ligands such as acetates, the separation between the new levels approximates to 100 cm^{-1}.[34] With our stronger-field ligand system this splitting is increased to almost 200 cm^{-1}, as shown by the gap between the main components of the 600 nm emission band.

Fig. 3.2.17 shows a 3-dimensional image of the emission peaks in the near-IR region taken in the solid state (the results are identical for those in solution). In collecting these time-resolved data, a cut-off filter was employed to remove signals below 850 nm as our main focus is on near-IR luminescence; however, residual scattering from the visible emission peak gives rise to a weak component at ≈ 1210 nm (marked with * in the diagram) which subsequently passed through the filter. Regardless of which near-IR transition was observed, the luminescence lifetimes were found to be the same, suggesting both emissions stem from a common excited state.

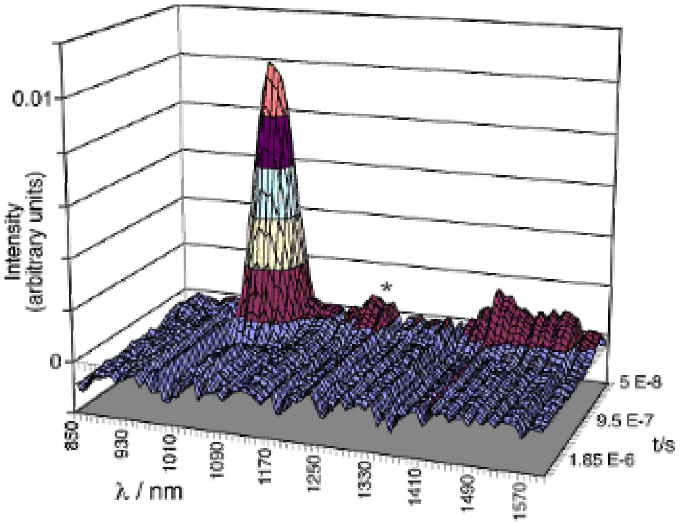

Fig. 3.2.17 – Solid state time-resolved emission spectra in the near-IR region of $[Pr(Bp^{2py})(dbm)_2]$

The emission at *ca.* 1030 nm has already been reported in the related compounds of $[Pr(TTA)_3.2H_2O]$[30], $[Pr(FOD)_3]$[31], and $[La_{(1-x)}Pr_xP_5O_{14}]$[35] varying slightly with the surrounding solvents, and is ascribed to the $^1D_2 \rightarrow {}^3F_4$ transition. No one however, has reported any emissions at lower energies.

On the basis of the energy scheme in **Fig. 3.2.16a**, and assuming emission stems from the $^1D_2$ excited state as well, the emission at 1440 nm (albeit weak) is assigned to $^1D_2 \rightarrow {}^1G_4$. This is also the only available level that energy from $^1D_2$ can pass too with a lower energy transition.

The luminescence lifetimes in the various media show the expected quenching also observed in the other Ln(III) complexes, with the O-H oscillators in methanol-H_4 (13 ns) showing very efficient degrees of quenching compared to methanol-d_4 (110 ns). Such a marked quenching effect on Pr(III) has been noted by Güdel and co workers,[34] and understandably, the lifetimes in methanol-d_4 are superior to the other media. The degrees of quenching observed in the solid state stem from non-radiative pathways *via* vibrational dissipation throughout the lattice.

3.2.4 *Photophysical Studies of $[Ln(Bp^{2py})_2(NO_3)]$ and $[Ln(Tp^{2py})_2(NO_3)]$ Complexes*

With the exception of the absorption band at 359 nm, the UV spectra for these complexes mirror that shown in **Fig. 3.2.13**, with ligand centred $\pi \rightarrow \pi^*$ transition pairings of *ca.* 254 and 295 nm; and 245 and 288 nm for the Bp^{2py} and Tp^{2py} complexes respectively.[2,18] The ligand-centred triplet excited state level was again populated by excitation of the molecule at 337 nm into the tail of the UV absorption bands.

3.2.4.1 Ln = Pr(III)

Visible region steady-state luminescence spectra for $[Pr(Bp^{2py})_2(NO_3)]$ is shown in **Fig. 3.2.18**, recorded in CH_2Cl_2 solution. From previous studies with the Gd(III) analogue of the Tp^{2py} complex,[36] the energy of the ligand-centred triplet level of our pyridyl-pyrazole based ligand was found to reside at 23900 cm^{-1}, higher than both the $^1D_2$ (*ca*. 17000 cm^{-1}) and $^3P_0$ (*ca*. 21000 cm^{-1}) excited states (see **Fig. 3.2.16a**).

In these systems, this results in several additional transitions from the $^3P_0$ level which the dbm-based triplet state could not populate. Again, we assign these in comparison to the work by Voloshin and co-workers.[30]

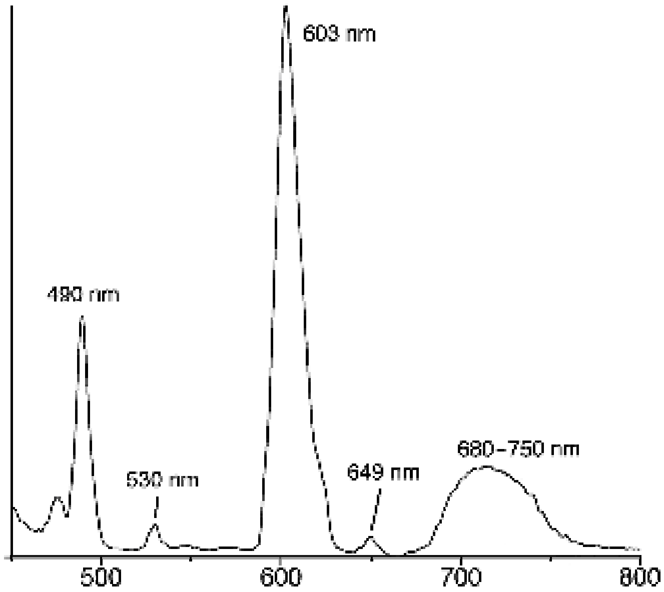

Fig. 3.2.18 – Steady state luminescence from [Pr(Bp^{2py})$_2$(NO$_3$)]

The dominant emission at 603 nm arises from the combination of overlapping $^3P_0 \rightarrow {}^3H_6$ and $^1D_2 \rightarrow {}^3H_4$ transitions, whilst the smaller peak at 649 nm is attributed to $^3P_0 \rightarrow {}^3F_2$. Emissions at 490 and 530 nm stem from the $^3P_0$ level as well, with transitions to $^3H_4$ and $^3H_5$, respectively. The broad peak between 680 and 750 nm cannot be resolved completely because there are several energy transitions that fall into this range. These include $^3P_0 \rightarrow {}^3F_3$, $^3P_0 \rightarrow {}^3F_4$, and $^1D_2 \rightarrow {}^3H_5$ at least, with the overlap accounting for the broadness of the signal.

Moving into the near-IR region, we again see $^1D_2$-based luminescence occurring at 1020 ($^3F_4$) and 1440 ($^1G_4$) nm energy. Whilst both have already been assigned, further evidence that the 1440 nm transition originates from the $^1D_2$ state as well is provided by both these emissions having lifetimes that are the same within experimental error. Emission peaks arising from different excited states of Pr(III) have shown to have significantly different lifetimes.[37,38]

In the [Pr(Tp^{2py})(NO$_3$)$_2$] complex, the dominant transitions of $^3P_0 \rightarrow {}^3H_4$ (489 nm); $^3P_0 \rightarrow {}^3H_6$ and $^1D_2 \rightarrow {}^3H_4$ (602 nm) are still evident, with the noticeable differences being the splitting of the weaker signals at *ca.* 530 and 649 nm (**Fig. 3.2.19**).

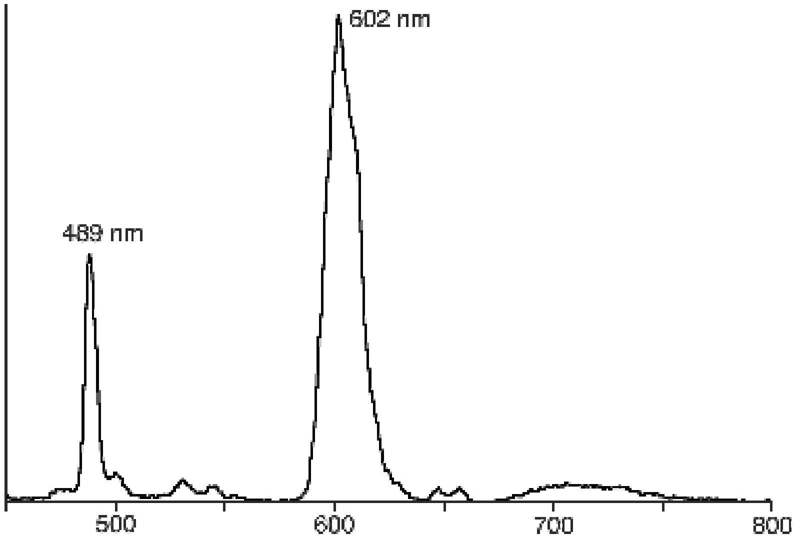

Fig. 3.2.19 – Steady state luminescence from [Pr(Tp^{2py})(NO$_3$)$_2$]

As the $^3P_0$ state is impervious to crystal field effects, the change in symmetry of the Pr(III) coordination environment in the Tp^{2py} structure must induce a splitting in the $^3H_5$ and $^3F_2$ states. The separation between the new pairs of peaks is typically a few hundred cm^{-1}, consistent with those induced by such effects.[34] The near-IR transitions at 1020 and 1440 nm are again present.

Even though both 1020 and 1440 nm transitions have identical half lives, we used the more intense (former) signal to estimate the luminescence lifetime of the complexes (**Table 3.2.6**) which, due to solubility restrictions, were performed in the solid state, and CH_2Cl_2 only. The short lifetimes are in good agreement with those observed for [Pr(Bp^{2py})(dbm)$_2$] earlier, and are reflective of the degree of quenching by C-H oscillators in solution, and vibrational effects in the lattice structure of the solid. The presence of additional C-H oscillators on the dbm ligand explains this complex's slightly smaller luminescence lifetimes. Decays were indicative of a single species present for both complexes.

It is worth noting in these Pr(III) complexes, that the solid state lifetimes are shorter than in solution, whereas the opposite is true with [Pr(Bp^{2py})(dbm)$_2$]. This indicates that the vibrational manifolds of the nitrate complexes arising from their structures in the solid state, have a better overlap with the energy levels of Pr(III) than in the dbm complex.

	Emission Lifetime τ /µs	
Complex	CH_2Cl_2 solution	solid state
$[Pr(Bp^{2py})_2(NO_3)]$	0.11	0.073
$[Er(Bp^{2py})_2(NO_3)]$	0.52, 1.64	1.20
$[Pr(Tp^{2py})(NO_3)_2]$	0.056	0.054
$[Er(Tp^{2py})(NO_3)_2]$	0.19, 1.49	1.59

Table 3.2.6 – Luminescence lifetimes of the complexes $[Ln(Bp^{2py})_2(NO_3)]$ and $[Ln(Tp^{2py})(NO_3)_2]$ (Ln = Pr and Er)

At this stage it is hard to say whether the main contribution comes from vibrations of the local environment, or those of the crystal's global structure.

3.2.4.2 Ln = Er

The only expected emission at 1530 nm was observed in both Er(III) complexes ($^4I_{13/2} \rightarrow {}^4I_{15/2}$) with luminescence lifetimes in solution (for both complexes) fitting best to a dual exponential decay. These were 0.52 and 1.64 µs for the Bp^{2py} complex and 0.19 and 1.49 µs for that of Tp^{2py}, with the latter species in each case likely to be an unsolvated one. Direct approach of a quenching CH_2Cl_2 molecule would at first appear difficult as both sets of complexes are 10-coordinate; however in **Section 3.2.2.3** it was noted that some $Er\cdots N_{py}$ distances were abnormally long suggesting that partial detachment of a pyridyl-pyrazole arm is likely, exposing a coordination site for interaction with solvent molecule(s). This complication is not present in the solid state where all Er(III) ions are coordinatively saturated.

The absence of dual exponential decay from both Pr(III) complexes in solution, suggests that there is less steric congestion about the metal centres, as they retain their 10-coordinate environments. However, we must also consider the possibility that any transmutation between intact and solvated forms could occur on a time scale much faster than that of the instrument, and that we are only seeing an average decay for the two.

Indeed, this is true for all of the complexes reviewed in this chapter which have showed the presence of single emitting species in their respective media. Any shorter-lived Pr(III)-based emission that may have arisen from partial solvation would be at the limits of our detection system and may not be detectable.

3.3 Experimental

3.3.1 Synthesis of Complexes

Potassium bis[3-(2-pyridyl)pyrazol-1-yl]dihydroborate (KBp^{2py}),[39] and Potassium tris[3-(2-pyridyl)pyrazol-1-yl]dihydroborate (KTp^{2py}),[40] were prepared according to the previously published methods.

$[Ln(Bp^{2py})(dbm)_2]$ (Ln = Pr, Nd, Eu, Gd, Tb, Er, Yb)

These complexes were all prepared in the same way. Solutions of KBp^{2py} (0.204 g, 0.6 mmol) in CH_3OH (5 ml) and the corresponding lanthanide trichloride hydrate (0.6 mmol) in CH_3OH (5 ml) were combined at room temperature and stirred. After several minutes, a solution of Hdbm (0.270 g, 1.2 mmol) in CH_3OH (5 ml) was added to the mixture followed by 1 ml of Et_3N. The mixture was stirred for a further 10 mins, after which the addition of 10-20 ml of H_2O afforded off-white precipitates.

These were isolated by filtration and washed with copious amounts of H_2O and ether. Drying *in vacuo* gave the desired products in 70-90% yield. Crystals suitable for X-Ray studies were grown by layering hexanes onto a concentrated CH_2Cl_2 solution of the bulk products. This slow recrystallisation technique also helped to increase the purity of the complexes, although with a reduction in their yields (53–65%). Characterisation data for these complexes are displayed in **Table 3B**.

$[Ln(Bp^{2py})_2(NO_3)]$ and **$[Ln(Tp^{2py})(NO_3)_2]$ (Ln = Pr, Er)**

These complexes were prepared in accordance with the previously described methods.[2,10,18] Characterisation data are given in **Table 3A**.

$[Ln(Tp^{2py})(dbm)_2]$ (Ln = Pr, Eu)

These complexes were prepared in accordance with the previously described methods.[10] Characterisation data are given in **Table 3A**

3.3.2 Physical Data for Complexes

Complex	Colour	Yield (%)[b]	Elemental analysis (%)[a] C	H	N	IR[c] ν(BH)/cm^{-1}	FAB MS[d] M$^+$ /(m/z)
[Eu(Tp^{2py})(dbm)$_2$]	Yellow	49	62.3 (62.2)	4.0 (4.0)	11.9 (12.1)	2444	1043, 820 (M$^+$ - dbm)
[Pr(Tp^{2py})(dbm)$_2$]	Green	67	62.2 (61.8)	4.0 (4.1)	12.0 (12.0)[e]	2444	1029, 808 (M$^+$ - dbm)
[Er(Bp^{2py})$_2$(NO$_3$)]	Pink	34	45.7 (45.4)	3.4 (3.4)	21.1 (21.4)[f]	2401, 2288	769 (M$^+$ - NO$_3$)
[Pr(Bp^{2py})$_2$(NO$_3$)]	Green	37	45.1 (44.5)	3.2 (3.4)	20.7 (20.5)[g]	2403, 2276	743 (M$^+$ - NO$_3$)

[a] Calculated values in parentheses. [b] Final yields after slow recrystallisation from CH_2Cl_2/hexane. [c] Solid-state, as diamond ATR.

[d] Recorded with 3-nitrobenzyl alcohol as matrix; the molecular ions have the appropriate isotopic pattern in every case.

[e] These values are based on the presence of 1 molecule of H_2O per complex molecule.

[f] These values are based on the presence of 0.25 molecules of CH_2Cl_2 per complex molecule.

[g] These are based on the presence of one molecule of CH_2Cl_2 per complex molecule.

Table 3A Analytical and Physical Data for the Complexes of Chapter 3

Complex	Colour	Yield (%)[b]	Elemental analysis (%)[a] C	H	N	IR[c] ν(BH)/cm^{-1}	FAB MS[d] M$^+$ /(m/z)
[Pr(Bp^{2py})(dbm)$_2$]	Green	58	61.0 (61.1)	4.1 (4.0)	9.2 (9.2)[f]	2390, 2270	887
[Nd(Bp^{2py})(dbm)$_2$]	Lilac	58	60.3 (60.8)	3.9 (4.0)	9.2 (9.2)[f]	2389, 2270	891
[Eu(Bp^{2py})(dbm)$_2$]	Yellow	64	60.1 (60.3)	4.0 (4.0)	9.0 (9.1)[f]	2390, 2270	900
[Gd(Bp^{2py})(dbm)$_2$]	Yellow	65	59.7 (59.9)	3.8 (3.9)	9.0 (9.1)	2390, 2271	905
[Tb(Bp^{2py})(dbm)$_2$]	Yellow	64	60.0 (59.8)	4.0 (3.9)	8.7 (9.1)[f]	2389, 2270	906
[Er(Bp^{2py})(dbm)$_2$]	Peach	54	59.6 (59.3)	3.9 (3.9)	8.8 (9.0)[f]	2389, 2271	914
[Yb(Bp^{2py})(dbm)$_2$]	Yellow	53	59.4 (58.9)	3.8 (3.9)	8.7 (8.9)[f]	2389, 2270	921

--- See page 159 for key---

Table 3B **Analytical and Physical Data for the Complexes of Chapter 3**

Complex	**[Eu(Tp^{2py})(dbm)$_2$]**	**[Pr(Tp^{2py})(dbm)$_2$]**	**[Pr(Bp^{2py})(dbm)$_2$]**
Empirical formula	$C_{54}H_{41}BN_9O_4Eu$	$C_{54}H_{41}BN_9O_4Pr$	$C_{46.25}H_{36.50}BC_{10.50}N_6O_4Pr$
Formula weight	1042.73	1031.68	909.76
Temperature	100(2)K	150(2) K	150(2) K
Crystal system	Triclinic	Triclinic	Monoclinic
Space group	P-1	P-1	P2(1)/c
a /Å	11.4041(14)	11.6308(15)	19.2028(12)
b /Å	14.1965(17)	11.9248(16)	26.5714(17)
c /Å	16.391(2)	18.569(2)	18.1524(12)
α /°	108.379(2)	96.558(2)	90
β /°	91.613(2)	106.782(2)	117.7670(10)
γ /°	110.797(2)	105.669(2)	90
Volume /Å^3	2324.7(5)	2321.9(5)	8195.6(9)
Z	2	2	8
Density (calculated) / Mg/m^3	1.490	1.476	1.475
Absorption coefficient / mm^{-1}	1.407	1.108	1.274
F(000)	1056	1048	3684
Crystal size	0.125 x 0.225 x 0.05 mm	0.34 x 0.25 x 0.18 mm^3	0.38 x 0.21 x 0.20 mm^3
θ range for data collection	1.64 to 27.49°	1.17 to 25.00°	1.20 to 27.53°
Reflections collected	17759	22669	91231
Independent reflections	9989 [R$_{int}$ = 0.0676]	8143 [R(int) = 0.0320]	18617 [R(int) = 0.0753]
Completeness to θ	93.5 %	99.8 %	98.6 %
Data / restraints / parameters	9989 / 0 / 625	8143 / 230 / 680	18617 / 0 / 1087
Goodness-of-fit on F^2	S = 0.965	1.049	0.880
R indices [for reflections with I>2σ(I)]	R$_1$ = 0.0509, wR$_2$ = 0.0922	R$_1$ = 0.0334, wR$_2$ = 0.0706	R$_1$ = 0.0385, wR$_2$ = 0.0667
R indices (for all data)	R$_1$ = 0.1063, wR$_2$ = 0.1267	R$_1$ = 0.0428, wR$_2$ = 0.0744	R$_1$ = 0.0743, wR$_2$ = 0.0733
Largest diff. peak and hole	0.764 and -1.422 eÅ^{-3}	0.725 and -0.717 e.Å^{-3}	1.007 and -0.865 e.Å^{-3}

Table 3C Crystallographic Data for the Complexes of Chapter 3

Complex	**[Nd(Bp^{2py})(dbm)$_2$]**	**[Eu(Bp^{2py})(dbm)$_2$]***	**[Gd(Bp^{2py})(dbm)$_2$]**
Empirical formula	$C_{46.25}H_{36.50}BCl_{0.50}N_6O_4Nd$	$C_{46.25}H_{36.50}BCl_{0.50}N_6O_4NEu$	$C_{46}H_{36}BN_6O_4Gd$
Formula weight	913.09	920.81	904.87
Temperature	100(2)K	100(2) K	100(2) K
Crystal system	Monoclinic	Monoclinic	Monoclinic
Space group	P2(1)/c	P2(1)/c	P2(1)/c
a /Å	19.194(4)	19.21303(10)	19.2403(18)
b /Å	26.548(5)	26.6410(2)	26.613(2)
c /Å	17.996(4)	17.80700(10)	17.8124(16)
α /°	90	90	90
β /°	117.64(3)	117.45	117.1740(10)
γ /°	90	90	90
Volume /Å^3	8123(3)	8087.48(9)	8114.1(13)
Z	8	8	8
Density (calculated) / Mg/m^3	1.493	1.513	1.481
Absorption coefficient / mm^{-1}	1.364	11.830	1.687
F(000)	3692	3716	3640
Crystal size / mm	0.2 x 0.1 x 0.1	0.25 x 0.2 x 0.15	0.18 x 0.13 x 0.13
θ range for data collection	1.42 to 27.49°	2.59 to 70.13°	1.19 to 27.56°
Reflections collected	35906	55578	68424
Independent reflections	18149 [R_{int} = 0.0656]	14537 [R(int) = 0.0379]	18339 [R(int) = 0.0559]
Completeness to θ	97.4 %	94.5 %	97.8 %
Data / restraints / parameters	18149 / 0 / 1075	14537 / 0 / 1069	18339 / 0 / 1045
Goodness-of-fit on F^2	S = 0.947	1.024	0.992
R indices [for reflections with I>2σ(I)]	R_1 = 0.0533, wR_2 = 0.0914	R_1 = 0.0264, wR_2 = 0.0662	R_1 = 0.0377, wR_2 = 0.0737
R indices (for all data)	R_1 = 0.0951, wR_2 = 0.1055	R_1 = 0.0294, wR_2 = 0.0677	R_1 = 0.0655, wR_2 = 0.0812
Largest diff. peak and hole	2.122 and -1.237 eÅ^{-3}	0.513 and -0.654 e.Å^{-3}	1.255 and -1.241 e.Å^{-3}

Table 3D **Crystallographic Data for the Complexes of Chapter 3**

---

*Data Collection performed on Cu-anode Proteum® Diffractometer.

Complex	**[Tb(Bp^{2py})(dbm)$_2$]**	**[Er(Bp^{2py})(dbm)$_2$]**	**[Yb(Bp^{2py})(dbm)$_2$]**
Empirical formula	$C_{46.25}H_{36.50}BCl_{0.50}N_6O_4Tb$	$C_{46.25}H_{36.50}BCl_{0.50}N_6O_4Er$	$C_{46.25}H_{36.50}BCl_{0.50}N_6O_4Yb$
Formula weight	927.77	936.11	941.89
Temperature	100(2)K	150(2) K	100(2) K
Crystal system	Monoclinic	Monoclinic	Monoclinic
Space group	P2(1)/c	P2(1)/c	P2(1)/c
a /Å	17.624(4)	19.232(3)	19.133(4)
b /Å	26.721(5)	26.871(4)	26.895(5)
c /Å	19.177(4)	17.501(2)	17.426(4)
α /°	90	90	90
β /°	116.84(3)	116.158	115.92(3)
γ /°	90	90	90
Volume /Å^3	8058(3)	8117.8(18)	8065(3)
Z	8	8	8
Density (calculated) / Mg/m^3	1.529	1.532	1.551
Absorption coefficient / mm^{-1}	1.841	2.153	2.405
F(000)	3732	3756	3772
Crystal size / mm	0.25 x 0.25 x 0.20	0.43 x 0.15 x 0.10	0.25 x 0.15 x 0.125
θ range for data collection	1.50 to 27.50°	1.40 to 27.59°	1.18 to 27.48°
Reflections collected	87683	65690	57155
Independent reflections	17377 [R_{int} = 0.0361]	18254 [R(int) = 0.1952]	18498 [R(int) = 0.0314]
Completeness to θ	93.9 %	97.0 %	100.0 %
Data / restraints / parameters	17377 / 0 / 1063	18254 / 0 / 1063	18498 / 0 / 1079
Goodness-of-fit on F^2	S = 0.937	0.944	0.962
R indices [for reflections with I>2σ(I)]	$R_1 = 0.0263$, $wR_2 = 0.0573$	$R_1 = 0.0669$, $wR_2 = 0.1324$	$R_1 = 0.0270$, $wR_2 = 0.0583$
R indices (for all data)	$R_1 = 0.0364$, $wR_2 = 0.0596$	$R_1 = 0.1919$, $wR_2 = 0.1852$	$R_1 = 0.0404$, $wR_2 = 0.0642$
Largest diff. peak and hole	1.313 and -0.447 eÅ^{-3}	1.419 and -2.167 e.Å^{-3}	0.915 and -0.699 e.Å^{-3}

Table 3E **Crystallographic Data for the Complexes of Chapter 3**

Complex	**$[Pr(Bp^{2py})_2(NO_3)]$**	**$[Er(Bp^{2py})_2(NO_3)]$**
Empirical formula	$C_{34}H_{32}B_2Cl_4N_{13}O_3Pr$	$C_{34}H_{32}B_2Cl_4N_{13}O_3Er$
Formula weight	975.06	1001.41
Temperature	150(2)K	150(2) K
Crystal system	Monoclinic	Monoclinic
Space group	P2(1)/n	P2(1)/n
a /Å	10.414(3)	10.8892(16)
b /Å	21.894(5)	20.125(3)
c /Å	17.805(4)	18.381(3)
α /°	90	90
β /°	99.730(4)	105.919
γ /°	90	90
Volume /$Å^3$	4001.3(17)	3873.6(10)
Z	4	4
Density (calculated) / Mg/m^3	1.619	1.717
Absorption coefficient / mm^{-1}	1.538	2.498
F(000)	1952	1988
Crystal size	0.29 x 0.18 x 0.13 mm	0.26 x 0.20 x 0.16 mm^3
□ range for data collection	1.49 to 27.57°	1.53 to 27.51°
Reflections collected	41645	43030
Independent reflections	9009 [R_{int} = 0.0985]	8809 [R(int) = 0.0316]
Completeness to θ	97.1 %	98.9 %
Data / restraints / parameters	9009 / 0 / 530	8809 / 0 / 524
Goodness-of-fit on F^2	S = 1.046	1.060
R indices [for reflections with I>2σ(I)]	$R_1 = 0.0677$, $wR_2 = 0.1933$	$R_1 = 0.0239$, $wR_2 = 0.0556$
R indices (for all data)	$R_1 = 0.0985$, $wR_2 = 0.2181$	$R_1 = 0.0310$, $wR_2 = 0.0576$
Largest diff. peak and hole	2.415 and -2.306 $eÅ^{-3}$	0.736 and -0.555 $e.Å^{-3}$

Table 3F **Crystallographic Data for the Complex of Chapter 3**

3.5 References

1. N. Marques, A. Sella, J. Takats, *Chem. Rev*., 2002, 2137
2. P. L. Jones, A. J. Amoroso, J. C. Jeffery, J. A. McCleverty, E. Psillakis, L. H. Rees, M. D. Ward, *Inorg. Chem*., 1997, **36**, 10
3. Z. R. Bell, G. R. Motson, J. C. Jeffery, J. A. McCleverty, M. D. Ward, *Polyhedron* 2001, **20**, 2045
4. S. Faulkner, A. Beeby, M-C. Carrie, A. Dadabhoy, A. M. Kenwright, P. G. Sammes, *Inorg. Chem. Commun*., 2001, **4**, 187
5. G. A. Hebbink, D. N. Reinhoudt, F. C. J. M. van Veggel, *Eur. J. Org. Chem*., 2001, 4101
6. R-G. Xiong, X-Z. You, *Inorg. Chem. Commun*., 2001, **5**, 677
7. Graham Motson. PhD Thesis, 2001, University of Bristol
8. A. Beeby, B. P. Burton-Pye, S. Faulkner, G. R. Motson, J. C. Jeffery, J. A. McCleverty, M. D. Ward, *J. Chem. Soc., Dalton Trans*., 2002, 1923
9. A. J. Amoroso, J. C. Jeffery, P. L. Jones, J. A. McCleverty, L. Rees, A. L. Rheingold, Y. Sun, J. Takats, S. Trofimenko, M. D. Ward, G. P. A. Yap, *J. Chem. Soc., Chem. Commun.*, 1995, 1881
10. M. D. Ward, J. A. McCleverty, K. L. V. Mann, J. C. Jeffery, G. R. Motson, J. Hurst, *Acta Cryst*. 1999, **C55**, 2055
11. Z. R. Reeves, K. L. V. Mann, J. C. Jeffery, J. A. McCleverty, M. D. Ward, F. Barigelletti, N. Armaroli, *J. Chem. Soc., Dalton Trans*., 1999, 349
12. A. J. Amoroso, J. C. Jeffery, P. L. Jones, J. A. McCleverty, M. D. Ward, *Polyhedron 199*6, **15**, 2023
13. D. A. Bardwell, J. C. Jeffery, P. L. Jones, J. A. McCleverty, M. D. Ward, *J. Chem. Soc., Dalton Trans*., 1995, 2921
14. C. Apostolidis, J. rebizant, B. Kanellakopulos, R. von Ammon, E. Dornberger, J. Müller, B. Powietzka, B. Nuber, *Polyhedron* 1997, **16**, 1057
15. M. V. R. Stainer, J. Takats, *Inorg. Chem*., 1982, **21**, 4050
16. F. B. Tamoura, P. M. Haba, M. Gaye, A. S. Sall, A. H. Barry, T. Jouini, *Polyhedron* 2004, **23**, 1191
17. D. L. Kepert, *Comprehensive Coordination Chemistry*, 1987, editoed by G. Wilkinson, R. D. Gillard, J. A. McCleverty, 1st Ed., Vol. 1, 31-107, Oxford, Pergamon Press

18. D. A. Bardwell, J. C. Jeffery, P. L. Jones, J. A. McCleverty, E. Psillakis, Z. Reeves, M. D. Ward, *J. Chem. Soc., Dalton Trans*., 1997, 2079
19. N. Armaroli, G. Accorsi, F. Barigelletti, S. M. Couchman, J. S. Fleming, N. C. Harden, J. C. Jeffery, K. L. V. Mann, J. A. McCleverty, L. H. Rees, S. R. Straling, M. D. Ward, *Inorg. Chem*., 1999, **38**, 5769
20. P. L. Jones, K. J. Byrom, J. C. Jeffery, J. A. McCleverty, M. D. Ward, *Chem. Commun*., 1997, 1361
21. H. Jiu, H. Tang, J. Zhou, J. Xu, Q. Zhang, H. Xing, W. Huang, A. Xia, *Optics Lett.,* 2005, **30**, 774
22. A. Beeby, R. S. Dickins, S. Faulkner, D. Parker, J. A. G. Williams, *Chem. Commun.,* 1997, 1401
23. D. Parker, J. A. G. Williams, *J. Chem. Soc., Dalton Trans*., 1996, 3613
24. L. Helm, A. E. Merbach, *Coord. Chem. Rev*., 1999, **187**, 151
25. A. S. Batsanov, A. Beeby, J. I. Bruce, J. K. Howard, A. M. Kenwright, D, Parker, *Chem. Commun*., 1999, 1011
26. A. Beeby, I. M. Clarkson, R. S. Dickins, S. Faulkner, D. Parker, L. Royle, A. S. de Sousa, J. A. G. Williams, M. Woods, *J. Chem. Soc., Perkin Trans. 2*, 1999, 493
27. A. Beeby, S. Faulkner, *Chem. Phys. Lett*., 1997, **266**, 116
28. K. Masaki, H. Isshiki, T. Kimura, *Optical Materials*, 2005, **27**, 876
29. S.Yanagida, Y. Hasegawa, K. Murakoshi, Y. Wada, N. Nakashima, T. Yamanaka, *Coord. Chem. Rev*., 1998, **171**, 461
30. A. I. Voloshin, N. M. Shavaleev, V. P. Kazakov, *J. Lumin*., 2001, **93**, 199
31. V. P. Kazakov, A. I. Voloshin, N. M. Shavaleev, *J. Photchem. Photobiol. A*, 1998, **119**, 177
32. J. Yu, H. Zhang, L. Fu, R. Deng, L. Zhou, H. Li, F. Liu, H. Fu, *Inorg. Chem. Commun*., 2003, **6**, 852
33. M. P. Oude Wolbers, F. C. J. M. van Veggel, B. H. M. Snellink-Ruël, J. W. Hofstraat, F. A. J. Guerts, D. N. Reinhoudt, *J. Chem. Soc., Perkin Trans. 2*, 1998, 2141
34. M. P. Hehlen, H. Riesen, H. U. Güdel, *Inorg. Chem*., 1991, **30**, 2273
35. H. Dornauf, J. Neber, *J. Lumin*., 1979, **20**, 217
36. N. Armaroli, V. Balzini, F. Barigelletti, M. D. Ward, J. A. McCleverty, *Chem. Phys. Lett*., 1997, **276**, 435
37. A. H. Qusti, J. Chrysochoos, *J. Less -Common Metals,* 1985, **112**, 291

38. J. Chrysochoos, A. H. Qusti, *J. Less-Common Metals*, 1896, **126**, 169
39. D. A. Bardwell, J. C. Jeffery, J. A. McCleverty, M. D. Ward, *Inorg. Chim. Acta*., 1998, 267, 323
40. A. J. Amoroso, A. M. Cargill Thompson, J. C. Jeffery, P. L. Jones, J. A. McCleverty, M. D. Ward, *J. Chem. Soc., Chem. Commun*., 1994, 2751

Chapter Four

Cyanide-Bridged *d-f* Hybrids

4.1 Introduction

4.1.1 Origins of d→f Energy Transfer

Chapter three has shown that the excitation of aromatic ligands in the UV/blue region (dbm-based transition ≈ 360 nm) can be used to stimulate near-IR emission from Ln(III) ions *via* a ligand to metal energy transfer. One of the main reasons for the recent interest in near-IR luminescence is its possible application in medical diagnostics; because the longer emission wavelength (compared to Eu(III) and Tb(III) in the visible region) can penetrate tissue far more effectively than UV or visible light (**Section. 1.2.6.2**).[1] In addition to the longer emission wavelength of near-IR emission, there is the adjoining possibility of using longer excitation wavelengths to sensitise the lanthanide luminescence, which again would be attractive to the application in obtaining the maximum penetration of the tissue and, in turn, an optimised near-IR emission. It is also a lot more energy efficient, as using a 300 nm photon to stimulate 1500 nm emission from Er(III) for example, is clearly wasteful of energy.

In light of this, there has been a surge of work in recent years aimed at designing complexes that display sensitised lanthanide luminescence *via* the absorption of light at longer wavelengths; largely based on the incorporation of transition metal-based chromophores into the complex. The benefits of using a d-block metal to sensitise emission are multiple: (i) they have very strong charge-transfer absorptions over the visible and near-IR regions with variations in the metal ion, ancillary ligand(s) and its substituents being used to help tune the absorption wavelength; (ii) their broad absorption bands maximise the necessary spectral overlap with the necessary energy levels of the lanthanide(III) ions to aid energy transfer; (iii) they promote intersystem crossing after excitation to give the excited triplet states which in turn (iv) are long-lived and thus encourage energy transfer to the lanthanide before the excited state collapses; (v) they do not degrade upon photochemical stimulation; and (vi) they have synthetic convenience. This last quality is very important as the entire crux of the system depends on holding the d-block metal in a close enough proximity to the lanthanide ion in order to facilitate energy transfer.

An early synthetic strategy was to connect the d-block unit to the f-block unit by a bridging ligand, which was employed by van Veggel and co-workers in using ferrocenyl (**Fig. 4.1.1a**) or $[Ru(bipy)_3]^{2+}$ (**Fig. 4.1.1b**) units as the d-block chromophores.[2] However, synthesis was appreciably complicated in such complexes with elaborate ligand designs, and because of the large metal-metal separation and lack of a conjugated pathway between the metal centres, the rate of energy transfer (k_{ET}) was relatively slow ($k_{ET(Ru\rightarrow Nd)} \approx 10^6$ s^{-1} and $k_{ET(Ru\rightarrow Yb)} \approx 10^5$ s^{-1}).

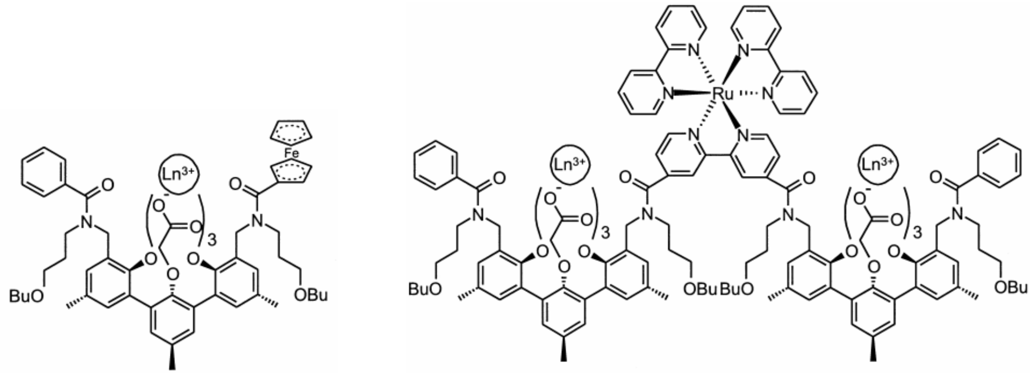

(a) **(b)**

Fig. 4.1.1 – Sensitised near-IR luminescence using (a) ferrocenyl or (b) $[Ru(bipy)_3]^{2+}$ units.

4.1.2 Take the Shorter Bridge

Work by Dr Nail Shavaleev of our group[1,3-5] moved towards connecting both d- and f-block metal ions with a single short bridging ligand such as 2,2'-bipyrimidine (**Fig. 4.1.2a**) or 5,6-dihydroxyphenanthroline (**Fig. 4.1.2b**) in which the ligand contains vacant, externally-directed bidentate sites. This gave rise to shorter metal-metal distances with the centres separated by an unsaturated bridge, making d→f energy transfer faster and more efficient, compared to the earlier systems. Recent work from other groups has used a metal-polypyridyl unit bound to a lanthanide ion, and is now a common strategy when synthesising d-f hybrids with the intention of energy transfer.[6-8]

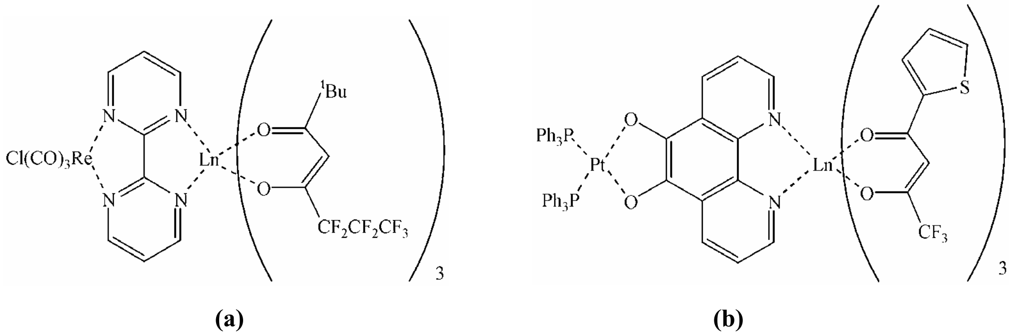

Fig. 4.1.2 – Sensitised near-IR luminescence from d- and f-block units held by a common ligand

Our attention turned to $[Ru(bipy)(CN)_4]^{2-}$ as a suitable d-block chromophore (**Fig. 4.1.3**), the choice of which follows from simple synthetic and photophysical considerations: (i) the negative charge of the unit means Ln^{3+} cations will be attracted towards it - the lone pairs on the cyanide nitrogens providing a sufficient means of promoting coordination; (ii) the resultant Ru-CN-Ln bridges are relatively short in comparison to other *d-f* systems we have already observed, and are also unsaturated; (iii) the ^{3}MLCT lifetime of the $[Ru(bipy)(CN)_4]^{2-}$ unit is relatively long and has a broad emission spectrum favouring overlap with the higher energy levels of near-IR Ln(III) emitters.

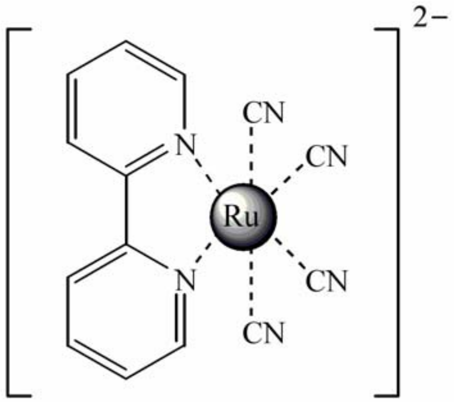

Fig. 4.1.3 – Structural diagram of $[Ru(bipy)(CN)_4]^{2-}$

In this chapter we investigate the different complexes formed by the co-crystallisation of $K_2[Ru(bipy)(CN)_4]$ with Ln(III) cations (where bipy represents 2,2'-bipyridine), with both structural and photophysical studies performed on the series.[9] We also describe the crystal structure of $K_2[Ru(1,10\text{-phenanthroline})(CN)_4]$ for the first time,[10] as well as the near-IR luminescence of Ln(III) ions, sensitised from hexacyanochromate(III) units.[11]

4.2 Results and Discussion

4.2.1 Structural Studies: $[Ru(bipy)(CN)_4]^{2-}$ - Ln(III)

4.2.1.1 Synthesis of Complexes

$K_2[Ru(bipy)(CN)_4]$ unit was first synthesised by Scandola and co-workers[12] *via* the photochemical irradiation of potassium hexacyanoruthenate and 2,2'-bipyridine in aqueous methanol. However, for these studies we adopted the modified method[13] of refluxing the components in an acidic methanol:water solution, with the subsequent work-up identical to that of Scandola's, often producing yields in excess of 70 %.

Over a period of about 4-6 weeks, slow evaporation of the combined D_2O solutions of $K_2[Ru(bipy)(CN)_4]$ and lanthanide(III) chlorides in a 2:1 ratio yielded generous crops of orange/yellow single crystals that were suitable for X-Ray studies. Their solid state IR spectra all showed two cyanide stretching vibrations in the expected region: one in the 2038-2050 cm^{-1} region comprising several overlapping components and a second just above 2100 cm^{-1}. D_2O was employed as the crystallisation solvent to maximise the inherently weak near-IR lanthanide luminescence should the lanthanide centres contain any OH oscillators in their coordination spheres (**Section 1.2.4.2**).

Crystallographic studies and elemental analysis show there to be two distinct structural types adopted across the series (Ln = Pr, Nd, Gd, Er, Yb): (a) $[\{Ru(bipy)(CN)_4\}_2\{Ln(H_2O)_m\}\{K(H_2O)_n\}]\cdot xH_2O$ in which one Ln^{3+} ion and one K^+ ion balance the charge of two $[Ru(bipy)(CN)_4]^{2-}$ units; and (b) $[\{Ru(bipy)(CN)_4\}_3\{Ln(H_2O)_4\}_2]\cdot xH_2O$ in which no K^+ ions are required as three $[Ru(bipy)(CN)_4]^{2-}$ units are charge-balanced by two Ln^{3+} ions. In all cases, numerous water molecules reside in the crystal lattice. Hereafter, the former series is abbreviated as **Ru$_2$LnK**, and the latter series as **Ru$_3$Ln$_2$**.

4.2.1.2 Ru$_2$LnK - (Ln = Pr, Er, Yb)

Reaction of $[Ru(bipy)(CN)_4]^{2-}$ with praseodymium(III) or erbium(III) chloride produced the tetranuclear species **Ru$_2$LnK**, albeit with a few slight differences between the two.

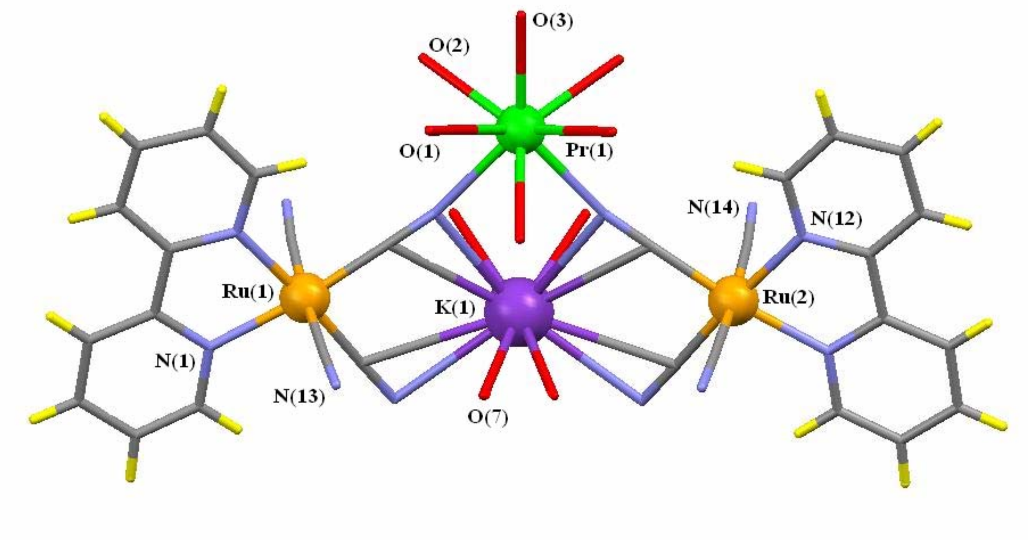

Fig. 4.2.1 – Crystal structure of $[\{Ru(bipy)(CN)_4\}_2\{Pr(H_2O)_7\}\{K(H_2O)_4\}]\cdot 10H_2O$
O(4) lies behind the Pr(1) atom

In **Ru$_2$PrK**, two $[Ru(bipy)(CN)_4]^{2-}$ units are linked to a $\{Pr(H_2O)_7\}^{3+}$ unit *via* one end-on CN···Pr bond from each Ru-based unit [Pr(1)-N(16) = 2.538(6) Å] (**Fig. 4.2.1**). The average Ru···Pr separation is 5.627 Å (remarkably shorter than the M···Ln separations of our group's previous *d-f* hybrids: 6.2-8.5 Å)[1,3-5] with a Ru-Pr-Ru angle of 96.46°.

In addition to the two cyanide groups, seven water molecules are bound to the Pr(III) ion making it 9-coordinate. The geometry about the Pr(III) centre is capped square-antiprismatic with one plane defined by O(1)/N(16)/N(16A)/O(1A) and the other by O(3)/O(2)/O(4)/O(2A) (mean deviation from plane = 0.000 and 0.076 Å respectively). The two planes are separated by a distance of 2.435 Å with the Pr(1) atom 1.505 and 0.930 Å from the O(1)/N(16)/N(16A)/O(1A) and O(3)/O(2)/O(4)/O(2A) planes respectively (**Fig. 4.2.2**). O(5) occupies the capping position, resting 1.633 Å above the O(1)/N(16)/N(16A)/O(1A) plane.

An accompanying K^+ ion is held in a pocket defined by four cyanide groups [two from either $[Ru(bipy)(CN)_4]^{2-}$ unit, including those bound to the praseodymium(III)], preventing the Ru-based units from residing in an *anti* conformation with respect to the Pr(III) ion. The K^+ is effectively 8 coordinate with bonds formed to the C≡N bridges as well as four additional water molecules.

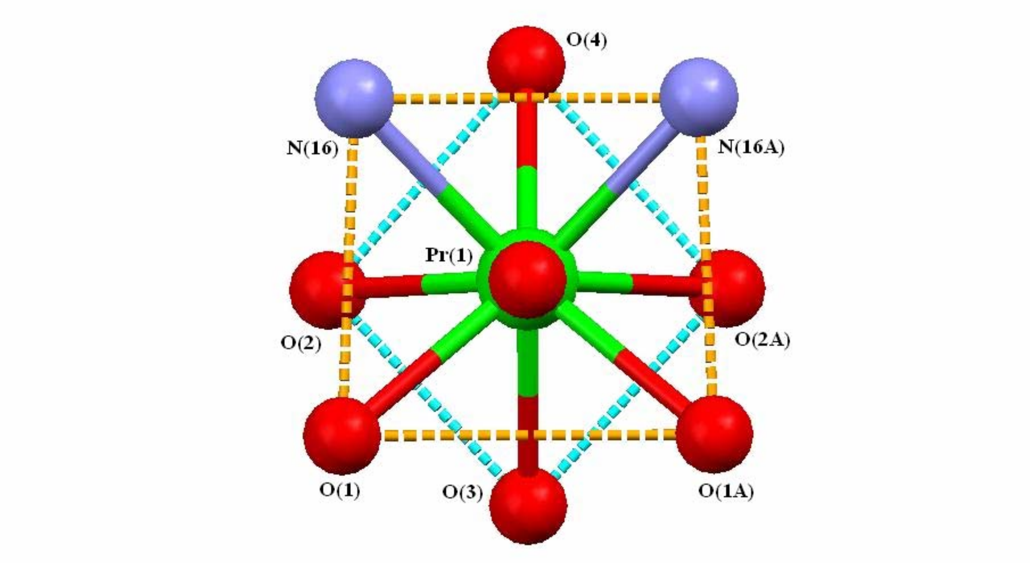

Fig. 4.2.2 – Geometry about the Pr(1) atom of $[\{Ru(bipy)(CN)_4\}_2\{Pr(H_2O)_7\}\{K(H_2O)_4\}]\cdot 10H_2O$ O(5) is projected from the plane of the paper.

This side-on π-mode of cyanide binding with alkali metals has been observed in the works of Rauchfuss and co-workers in employing such interactions in templating the formation of elaborate cyanometallate cages.[14-16]

One example sees the cyanide groups bridge two octahedral metals in forming the perimeter of the cage, whilst side-on binding occurs to an alkali metal ion residing in the centre of the cage (**Fig.4.2.3a**). Analogous bonds were formed in the works of Gokel and co-workers when they observed the interactions of alkene/alkyne groups with alkali metal cations in both solution and the solid state (**Fig.4.2.3b**).[17-19]

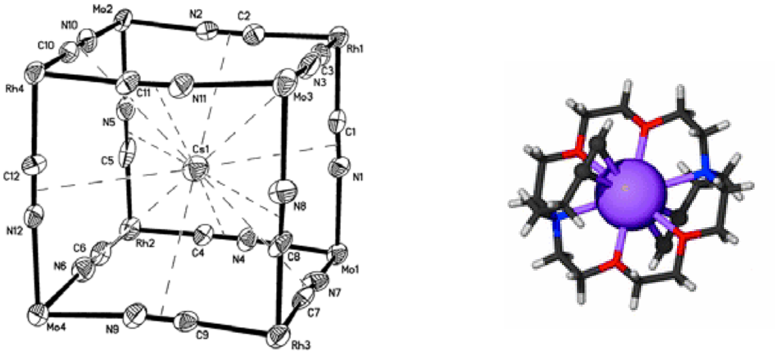

(a) **(b)**

Fig. 4.2.3 – π-bonding to alkali metal ions with (a) cyanides and (b) alkenes

The plane of the four CN groups in **Ru_2PrK** deviates 0.0579 Å from the mean, with K(1) sitting 0.3955 Å above this plane. The C-N bond lengths are typical, and the average K-C bond lengths (3.22 Å) are slightly longer than those of K-N (3.05 Å), but both are comparable to the values found in Rauchfuss'[20] and Gokel's[17] K^+ complexes. Due to the side-on bonding between K^+ and the CN groups, the Ru-CN-Pr bond is kinked slightly away from the 180° ideal, with the C(16)-N(16)-Pr(1) angle now at 166.7°.

The coordination geometry about the K^+ ion is not simple, although it is reminiscent of the metal centre in $[Ln(Bp^{2py})(dbm)_2]$ systems with a central plane capped either side by a pair of oxygen atoms O(6)/O(6A) and O(7)/O(7A) (**Section 3.2.2.1**). Both of these water molecules hydrogen bond to neighbouring ones: O(6) bonds to both O(4) on the adjacent Pr atom, and O(1) on a second complex unit, whilst O(7) bonds to O(4S).

From this, the roles of the hydration spheres about both Pr and K centres becomes obvious: O(2) on the Pr(1) atom forms hydrogen bonds to N(15) and N(15A) on an adjacent complex unit [OH(2A)···N(15) = 1.998 Å, O(2)···N(15) = 2.849(9) Å] to form a regular alignment of **Ru_2PrK** units, with a separation of 2.150 Å between Pr(1)/N(16)/N(16A) planes (**Fig. 4.2.4**); these chains are then held by hydrogen bonds formed between O(6)···O(1), O(7)···O(4S), O(4S)···O(4), whose non-bonded separations are 2.748(17), 2.169(17), 2.915(15) Å respectively. The remaining lattice water molecules are also involved in a H-bonded network between each other; metal-bound water molecules; and cyanide nitrogens, as indicated by numerous non-bonded contacts of < 3 Å, which again associates the **Ru_2PrK** chains.

Ru_2PrK crystallises in the monoclinic space group $P2_1/m$ with Pr(1), K(1), O(3), O(4), and O(5) all lying on the mirror plane. Selected bond lengths are given in **Table 4.2.1**.

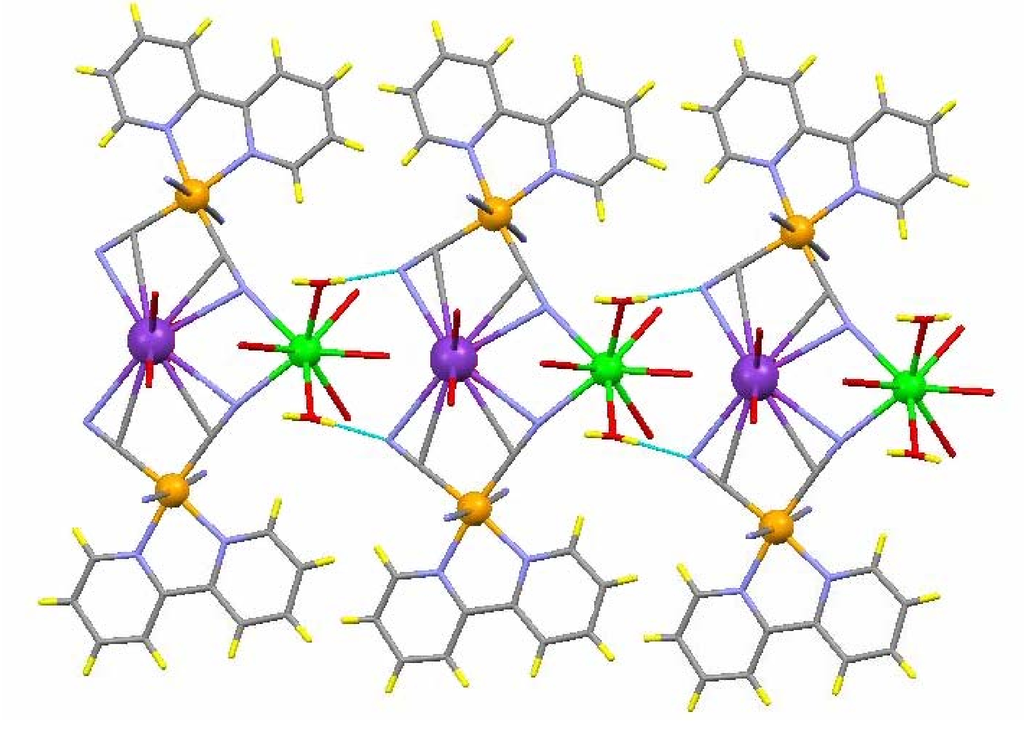

Fig. 4.2.4 – Crystal structure of $[\{Ru(bipy)(CN)_4\}_2\{Pr(H_2O)_7\}\{K(H_2O)_4\}]\cdot10H_2O$ showing the chain propagation through the H(2A)···N(15) bonds

Pr(1)-N(16)	2.538(6)	K(1)-C(15)	3.246(7)
Pr(1)-O(1)	2.542(6)	K(1)-N(15)	3.056(7)
Pr(1)-O(2)	2.483(5)	K(1)-N(16)	3.046(6)
Pr(1)-O(3)	2.499(9)	K(1)-C(16)	3.202(6)
Pr(1)-O(4)	2.620(7)	K(1)-O(7)	2.853(10)
Pr(1)-O(5)	2.572(8)	K(1)-O(6)	2.865(13)

Table 4.2.1 – Selected bond lengths (Å) for Ru_2PrK

Ru_2ErK crystallises in the tetragonal space group P*ca*2_1 with a very similar structure to that of **Ru_2PrK** (**Fig. 4.2.5**). Two independent **Ru_2ErK** units appear in the asymmetric unit, both near identical, and so only one is shown in the following figures. A tetranuclear species is again formed with the lanthanide(III) ion being bridged by two cyanide groups N(116)/N(132) giving an average Ru···Er separation of 5.397 Å, yet in this case the smaller Er(III) ion only accommodates six water molecules about it in addition to the two cyanide nitrogens.

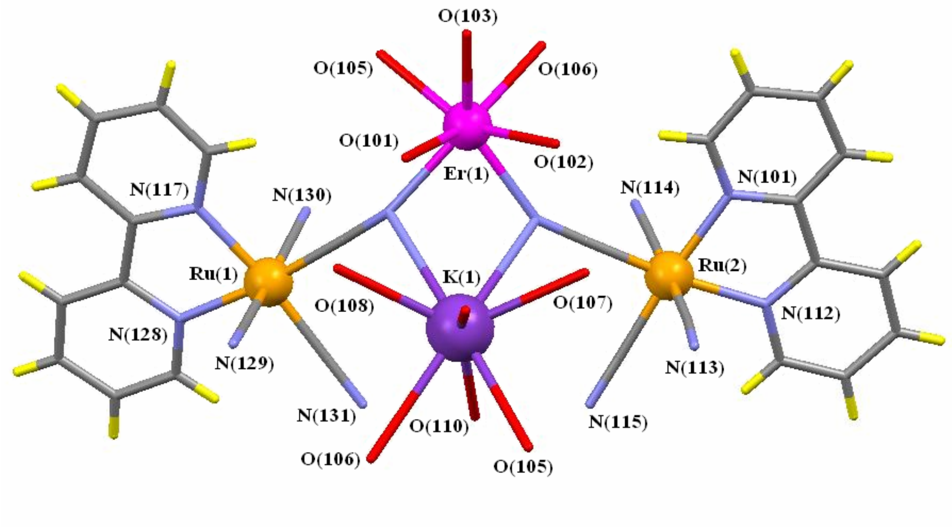

Fig. 4.2.5 – Crystal structure of $[\{Ru(bipy)(CN)_4\}_2\{Er(H_2O)_6\}\{K(H_2O)_4\}]\cdot 5H_2O$
O(106) and O(105) belong to a second Pr atom not in this asymmetric unit

With an eight coordinate environment, the geometry about the Er(III) centre is square antiprismatic, with one plane defined by N(116)/N(132)/O(101)/O(102) and the other by O(103)/O(106)/O(104)/O(105) (average deviations from the mean plane = 0.1233 and 0.3584 Å respectively, **Fig. 4.2.6**). The planes are separated by a distance of 2.609 Å with the Er(III) ion resting approx. 1.30 Å from either plane.

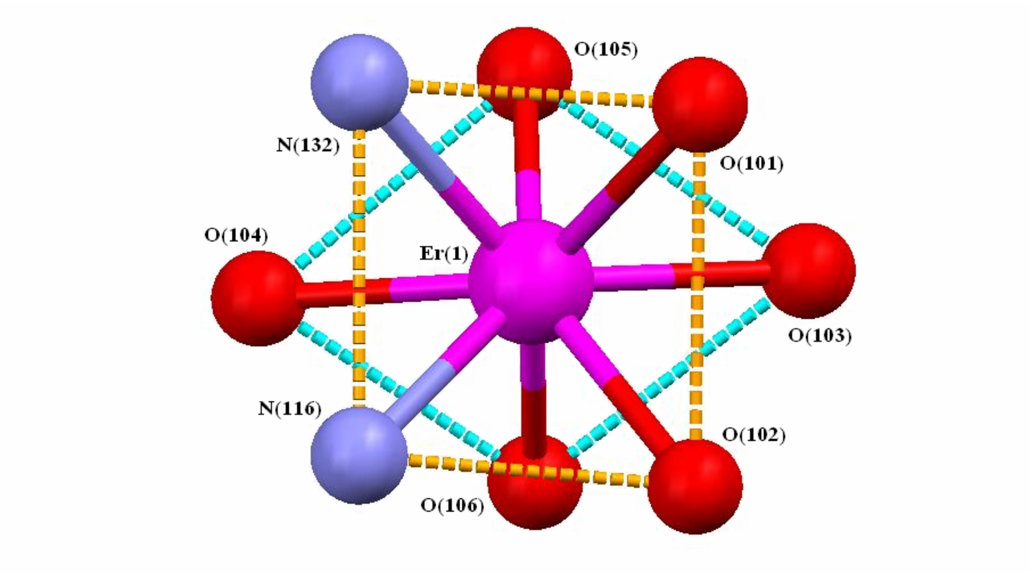

Fig. 4.2.6 – Square antiprismatic geometry about the Er centre in $\mathbf{Ru_2ErK}$

The main difference between this and the $\mathbf{Ru_2PrK}$ structure is the environment of the associated K^+ ion, for whilst both Ru-based units reside in a *syn* conformation with respect to Er(1), we do not observe the previous π-bonding behaviour of the cyanides. Instead the lone pairs of the two end-on erbium-bound cyanide nitrogens are shared between the Er(III) and K^+ (giving an average Er-N-K angle of 94.3°), with no further cyanide-K bonding apparent (K-C bond length ≈ 3.9 Å). This is because the K^+ ion sits 2.843 Å above the N(115)/N(116)/N(131)/N(132) cyanide plane, compared to 0.336 Å in the equivalent plane of $\mathbf{Ru_2PrK}$. In addition to the two cyanide nitrogens, the K^+ ion has six water molecules in its coordination sphere: four of which are terminal [O(107)/O(108)/O(109)/O(110)] with average K-O distance of 2.842 Å, whilst two [O(105)/O(106)] bridge the adjacent Er(III) ion and so have longer bonds to the K^+ ion (average K···O separation = 3.126 Å). There is no simple describable geometry about the K^+ ion.

The bridging oxygens and cyanide groups linking K and Er give rise to a one dimensional chain that propagates along the **a**-axis (**Fig. 4.2.7**). The average K-N bond length (3.352 Å) is quite long compared to that of $\mathbf{Ru_2PrK}$ indicating a weaker interaction, however it is still sufficient to displace the Ru-CN-Er vector from linearity with the C-N-Er angles ranging from 150-160°.

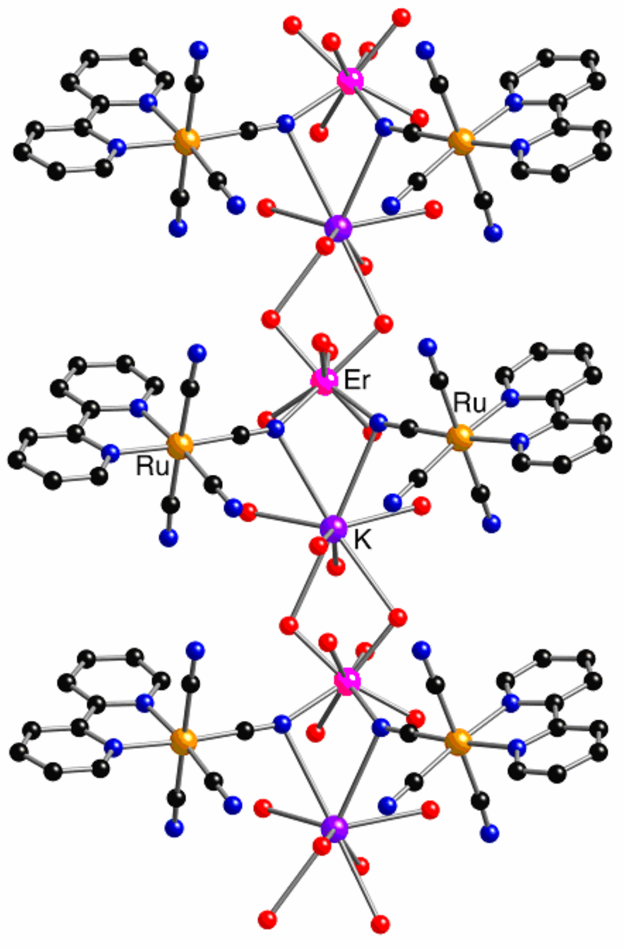

Fig. 4.2.7 – Crystal structure of [{Ru(bipy)(CN)$_4$}$_2${Er(H$_2$O)$_6$}{K(H$_2$O)$_4$}]·5H$_2$O showing the chain propagation through the bridging water molecules O(105) and O(106)

Non-bonded contacts of 2.8-3.0 Å are found for O(103)-N(115), O(107)-N(114), O(109)-N(114) and O(108)-N(130) indicative of hydrogen bonding interactions between adjacent chains, showing how they are associated within the crystal.

All of the previous comments apply to the second tetranuclear complex in the asymmetric unit as well, with bond lengths differ by negligible amounts between the two units. Ru(3)···Er(2) and Ru(4)···Er(2) distances were found to be 5.345(6) and 5.439(6) Å respectively. Ten water molecules are located within the crystal lattice (i.e. five per **Ru$_2$ErK** unit) which shows numerous O···O and O···N non-bonded distances of 2.6-3.0 Å, again indicative of a substantial hydrogen-bonded network. Selected bond lengths are given in **Table 4.2.2**.

Er(1)-O(106)	2.338(4)	K(1)-O(105)	3.031(5)
Er(1)-O(105)	2.341(4)	K(1)-O(106)	3.222(5)
Er(1)-O(102)	2.343(5)	K(1)-O(107)	2.840(6)
Er(1)-O(101)	2.351(6)	K(1)-O(108)	2.882(7)
Er(1)-O(104)	2.384(6)	K(1)-O(109)	2.846(7)
Er(1)-O(103)	2.386(5)	K(1)-O(110)	2.801(8)
Er(1)-N(132)	2.391(6)	K(1)-N(132A)	3.344(7)
Er(1)-N(116)	2.410(6)	K(1)-N(116A)	3.360(7)
Er(2)-O(1)	2.399(5)	O(5)-K(2)	3.403(6)
Er(2)-O(2)	2.326(5)	O(6)-K(2)	2.964(5)
Er(2)-O(3)	2.405(5)	O(7)-K(2)	2.787(6)
Er(2)-O(4)	2.375(6)	O(8)-K(2)	2.900(6)
Er(2)-O(5)	2.319(5)	O(9)-K(2)	2.778(7)
Er(2)-O(6)	2.354(4)	O(10)-K(2)	2.857(6)
Er(2)-N(32)	2.369(6)	K(2)-N(16A)	3.331(7)
Er(2)-N(16)	2.429(6)	K(2)-N(32A)	3.303(7)
Er(1)-K(1)	4.380(2)	Er(2)-K(2)	4.415(2)
Er(1)-K(1A)	4.267(2)	Er(2)-K(2A)	4.247(2)

Table 4.2.2 – Selected bond lengths (Å) for Ru_2ErK

Previously in our group, Dr Tom Miller had performed the 2:1 reaction with $K_2[Ru(bipy)(CN)_4]$ and $YbCl_3·6H_2O$ respectively, and obtained an identical structure to that of **Ru_2ErK**, with a difference in the number of lattice waters.[21] The Ru···Yb distances for the **Ru_2YbK** complex were 5.32 – 5.44 Å, showing the marked effects of the lanthanide contraction across the **Ru_2LnK** series.

4.2.1.3 Ru_3Ln_2 – (Ln = Nd, Gd)

Despite a 2:1 stoichiometry of the reagents, a 3:2 stoichiometry is observed in the crystalline products formed with Gd(III) or Nd(III) chloride. As the two structures are isomorphous and isostructural, we will restrict our structural discussions to those of the neodymium(III) complex.

The complex crystallises in the monoclinic space group $P2_1/c$ with the asymmetric unit containing three crystallographically unique $[Ru(bipy)(CN)_4]^{2-}$ units and two unique Nd(III) centres. **Fig. 4.2.8** shows the asymmetric unit, depicting a four-member pseudo-square defined by Nd(1)-Ru(1)-Nd(2)-Ru(2) at the corners, with a single cyanide group along each side.

Nd···N distances range from 2.48-2.55 Å, whilst Nd···O distances range from 2.41-2.55 Å, with no distinctions between either Nd(III) centre. The square's side length (and hence Ru···Nd separation) varies between 5.35-5.63 Å (average 5.46 Å) giving a slight increase in separation from the **Ru_2LnK** structures by up to 0.2 Å. Analogous distances decrease slightly in accordance with the lanthanide contraction in the **Ru_3Gd_2** complex (Ru···Gd separation varies between 5.27-5.59 Å). There are no K^+ ions in these complexes, whose overall charge is balanced by the 3:2 stoichiometries, and no side-on π-bonding is observed by the cyanide groups.

Each Nd(III) centre is surrounded by four end-on bound cyanide nitrogen atoms and four terminal water molecules, giving them an eight coordinate geometry and both Nd(1) and Nd(2) centres are found to be square antiprismatic (**Fig. 4.2.9**). The planes of N(57)O(1)/N(55)/O(4), N(42)/N(25)/O(3)/O(2), N(58)/N(24)/O(6)/O(7), O(5)/N(41)/N(26)/O(8) have deviations of 0.291, 0.173, 0.302 and 0.055 Å from their respective means with the relevant Nd(III) ion equidistant of both planes.

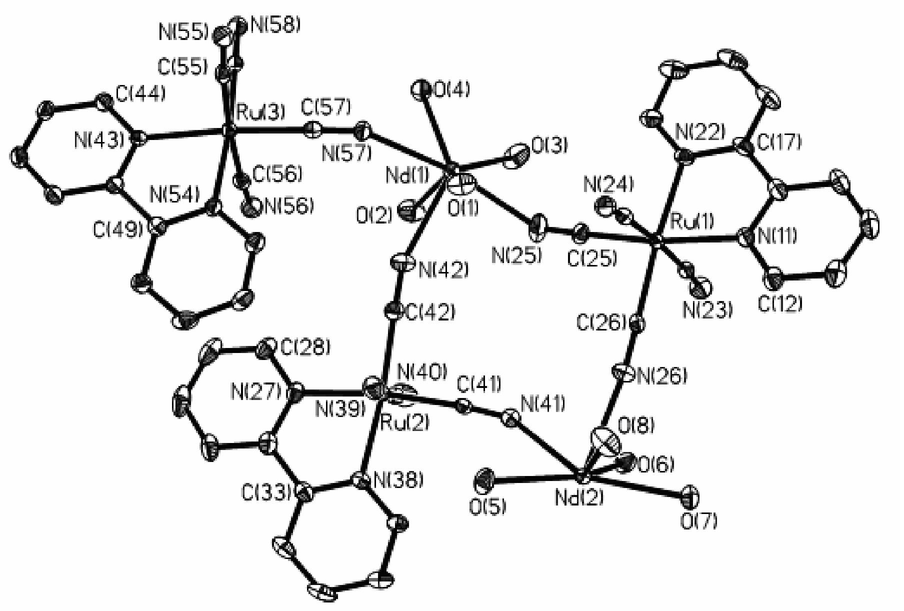

Fig. 4.2.8 – Crystal structure of the asymmetric unit of $[\{Ru(bipy)(CN)_4\}_3\{Nd(H_2O)_4\}_2]\cdot 11H_2O$ Thermal ellipsoids are shown at the 40 % probability level, and the coordination sphere about Nd(2) is completed by N(24) and N(58) from adjacent units.

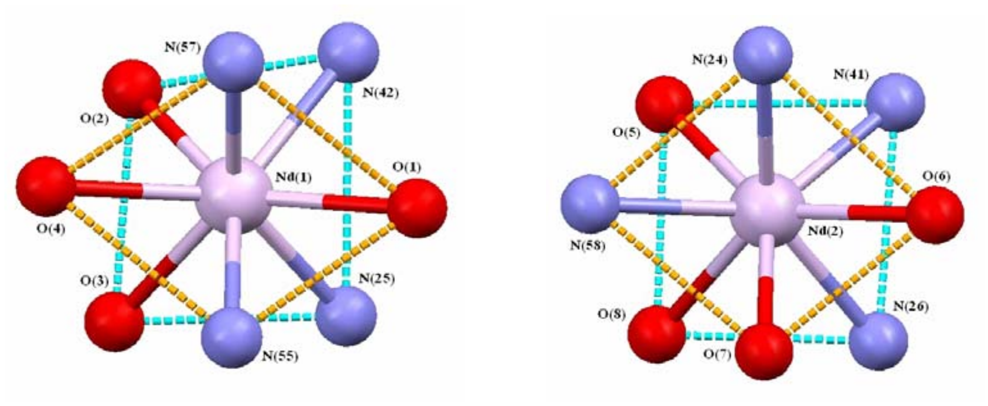

Fig. 4.2.9 – Different geometries about the two lanthanide centres in Ru_3Nd_2

The structure's main repeating unit is a set of five fused rings which propagate to form a complicated two dimensional network (**Fig. 4.2.10**). As shown, the three central rings are each reminiscent of that shown in **Fig. 4.2.8**, and can be considered a 'square' with the Ru(2)/Nd(1)/Ru(1)/Nd(2) and Ru(3)/Nd(1)/Ru(3)/Nd(1) plane deviating 0.0288 Å from the mean; whilst the adjacent Ru(3)/Nd(2)/Ru(1)/Nd(1) plane deviates 0.5021 Å from the mean, and clearly appears buckled, thus adopting a butterfly-style conformation.

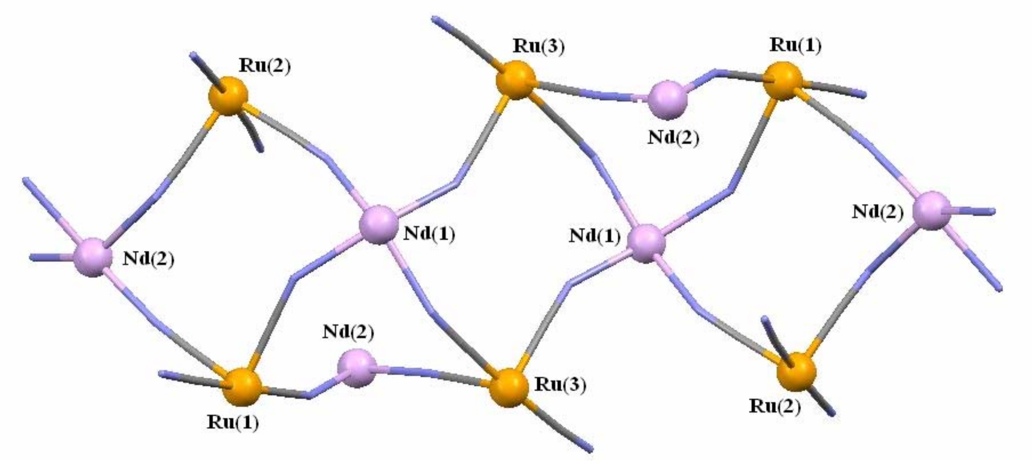

Fig. 4.2.10 – Crystal structure of $[\{Ru(bipy)(CN)_4\}_3\{Nd(H_2O)_4\}_2]\cdot 11H_2O$ showing part of the two-dimensional sheet structure arising from cyanide bridging. Only metal ions and CN bonds are displayed.

These groups of five rings couple to each other through the Nd(2) 'corners' (**Fig. 4.2.11**) to propagate into a two-dimensional sheet parallel to the **bc** face of the unit cell (**Fig. 4.2.12**).

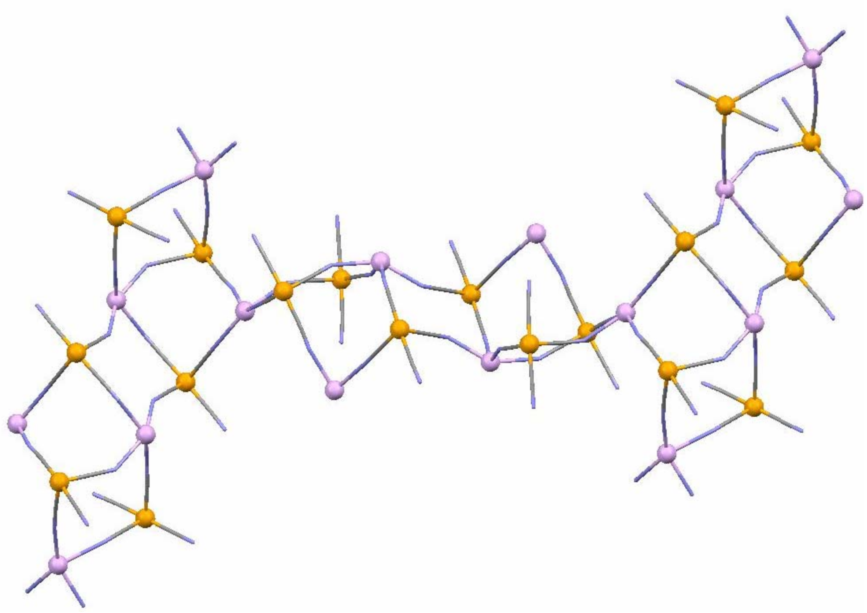

Fig. 4.2.11 – Crystal structure of Ru_3Nd_2 showing three adjacent sets of the five-ring groups. Only metal ions and CN bonds are displayed.

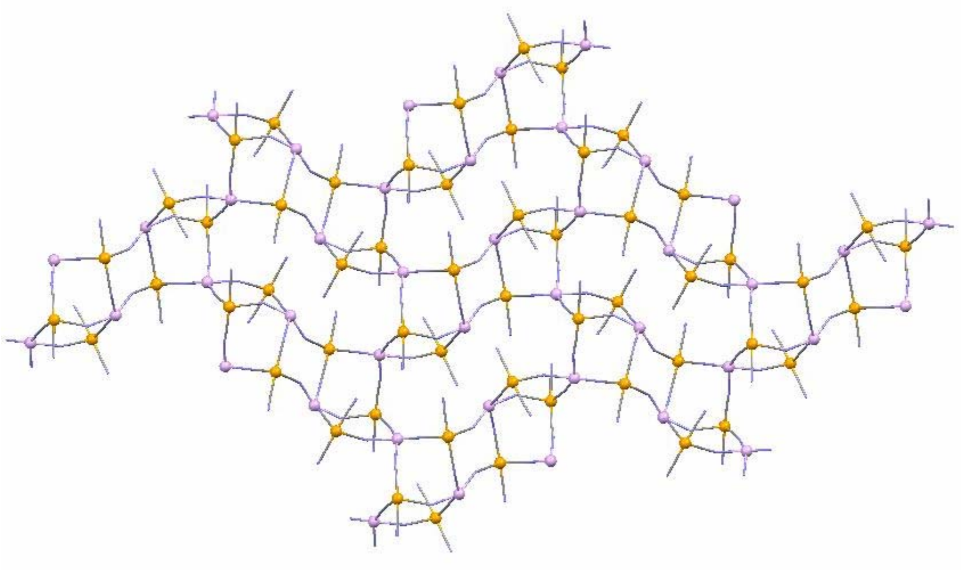

Fig. 4.2.12 – Propagation of Ru_3Nd_2 parallel to the bc face of the unit cell

In viewing down the **b**-axis, **Fig. 4.2.13** illustrates how the two-dimensional sheets are capped on either side by the bipyridine ligands. Selected bond lengths for both **Ru_3Nd_2** and **Ru_3Gd_2** are given in **Tables 4.2.3** and **4.2.4** respectively.

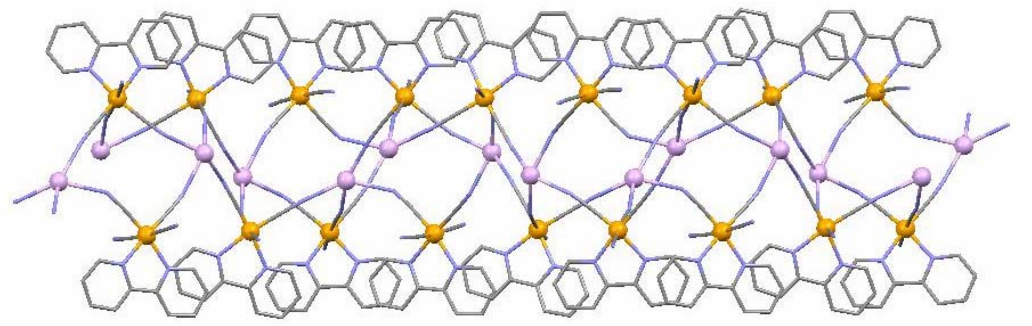

Fig. 4.2.13 – View of Ru_3Nd_2 viewing down the b-axis

Nd(1)-N(25)	2.493(3)	Nd(2)-O(7)	2.425(3)
Nd(1)-N(42)	2.531(3)	Nd(2)-O(5)	2.488(3)
Nd(1)-O(2)	2.405(9)	Nd(2)-O(8)	2.491(3)
Nd(1)-O(3)	2.475(3)	Nd(2)-O(6)	2.499(3)
Nd(1)-O(1)	2.524(3)	Nd(2)-N(58D)	2.506(3)
Nd(1)-N(55B)	2.532(3)	Nd(2)-N(24C)	2.550(3)
Nd(1)-O(4)	2.554(3)	Nd(2)-N(41)	2.533(3)
Nd(1)-O(2A)	2.607(13)	Nd(2)-N(26)	2.521(3)

Table 4.2.3 – Selected bond lengths (Å) for Ru_3Nd_2

Gd(1)-N(58)	2.461(7)	Gd(2)-O(8)	2.338(6)
Gd(1)-O(3)	2.409(7)	Gd(2)-O(7)	2.414(6)
Gd(1)-O(1)	2.439(13)	Gd(2)-O(5)	2.418(6)
Gd(1)-N(39A)	2.448(8)	Gd(2)-O(6)	2.436(6)
Gd(1)-O(4)	2.450(5)	Gd(2)-N(57C)	2.462(8)
Gd(1)-O(2)	2.481(6)	Gd(2)-N(25C)	2.469(7)
Gd(1)-O(1B)	2.485(19)	Gd(2)-N(24A)	2.501(7)
Gd(1)-N(41)	2.412(8)	Gd(2)-N(42)	2.446(7)

Table 4.2.4 – Selected bond lengths (Å) for Ru_3Gd_2

In the previous work by Dr Miller,[22] slow evaporation of the reaction mixture generated multiple crystal types that were distinguishable by colour and shape, (four types were isolated by the time the solvent had completely evaporated). The samples of **Ru_2PrK Ru_2ErK**, **Ru_3Nd_2** and **Ru_3Gd_2** in this work all had their respective crops of crystals looking identical in shape and colour, with the same unit cell observed for several crystals in each sample.

However, in the case of **Ru_2PrK**, whilst the sample contained the given structure as small orange crystals, the sample also contained a single, much larger yellow crystal which was found to have the structural form **Ru_3Pr_2**. There is very little difference between this structure and those of the other **Ru_3Ln_2** complexes, with the exception that one Pr centre [Pr(1)] has five water molecules in its first coordination sphere because of its larger ionic radius. Consequently, the geometry about the two lanthanide centres is square antiprismatic for Pr(2) and capped-square antiprismatic for Pr(1) (**Fig. 4.2.14**).

The same five-membered set of rings pack in the same manner as those of **Ru_3Nd_2**, with the Pr···N and Pr···O distances lying in the ranges of 2.50-2.57 and 2.44-2.91 Å respectively, and Ru···Pr separations varying between 5.37-5.65 Å, on average less than the **Ru_2PrK** system, but consistent with the other two **Ru_3Ln_2** systems. Selected bond lengths are given in **Table 4.2.5**. For the purposes of photophysical studies, only the orange **Ru_2PrK** crystals were analysed as the only **Ru_3Pr_2** crystal had been contaminated during X-Ray studies.

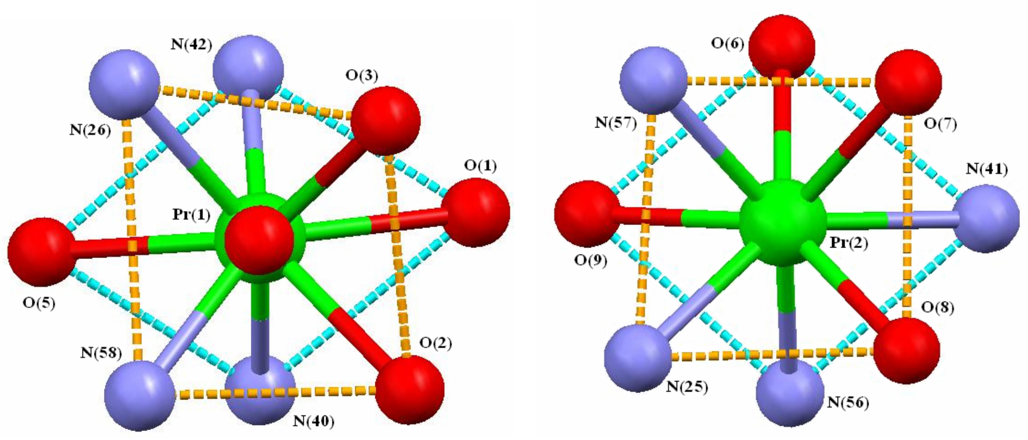

(a) **(b)**

Fig. 4.2.14 – Coordination geometries about the two crystallographically independent lanthanide centres in Ru_3Pr_2: (a) capped square antiprismatic and (b) square antiprismatic

In all three **Ru_3Ln_2** systems, there are 10-11 lattice water molecules in each asymmetric unit (some disordered over two sites) which form hydrogen bonds between themselves, terminal cyanide nitrogen lone pairs, and the metal-bound water molecules.

Pr(1)-O(1)	2.578(2)	Pr(2)-O(6)	2.444(2)
Pr(1)-O(2)	2.491(3)	Pr(2)-O(7)	2.507(3)
Pr(1)-O(3)	2.529(4)	Pr(2)-O(8)	2.506(3)
Pr(1)-O(4)	2.906(6)	Pr(2)-O(9)	2.519(3)
Pr(1)-O(5)	2.545(2)	Pr(2)-N(41)	2.520(3)
Pr(1)-N(26)	2.553(3)	N(57)-Pr(2)	2.538(3)
Pr(1)-N(40)	2.558(3)	Pr(2)-N(56)	2.567(3)
Pr(1)-N(42)	2.499(3)	Pr(2)-N(25)	2.552(3)
Pr(1)-N(58)	2.503(3)		

Table 4.2.5 – Selected bond lengths (Å) for Ru_3Pr_2

4.2.2 Photophyscial Studies: $[Ru(bipy)(CN)_4]^{2-}$ - Ln(III)

All photophysical studies were performed on solid state samples as it was deemed the coordination polymers would break up into their component parts in solution.

4.2.2.1 Energy Transfer Theories

There are two well-known theories that have been suggested to explain the mechanism of energy transfer *via* the antenna effect: The theory of Förster and the theory of Dexter.

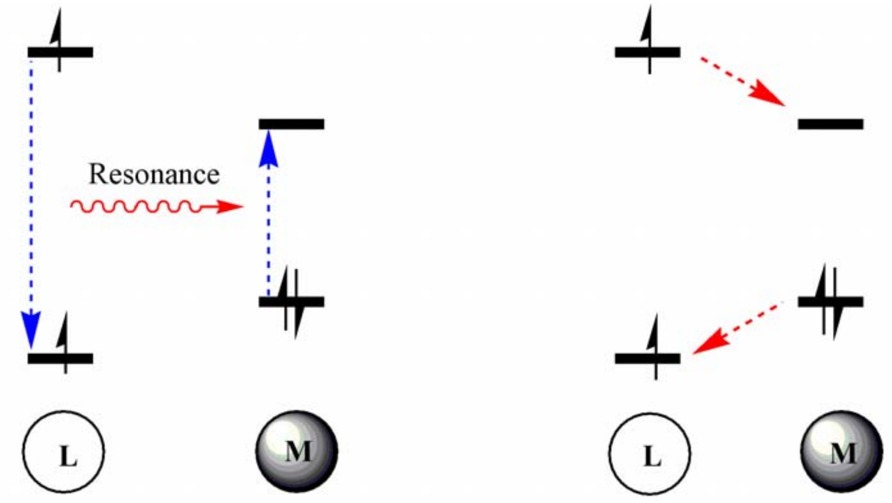

(a) (b)

Fig. 4.2.15 – Energy transfer mechanisms: (a) Förster and (b) Dexter.

Förster theory suggests a purely through-space energy transfer in which the oscillating electric dipoles of the excited ligand (L) and the metal (M) interact sufficiently to induce the excitation of an electron in the metal to higher energy levels, which subsequently falls back to the lower level(s) generating the luminescence (**Fig. 4.2.15a**). The effect is an energy transfer that occurs over a distance appreciably greater than the sum of the individual components van der waals radii; therefore, whilst its occurrence depends on the strength of the oscillator overlap, it is not dependent on a short L-M separation, with k_{ET} proportional to r^{-6} where r is the L-M separation.

Dexter theory suggests a double electron exchange between the ligand and the metal (**Fig. 4.2.15b**) in which the higher energy levels of the metal are populated by the promoted electron of the ligand (first exchange) which then falls to the lower energy levels of the metal to give the luminescence. At the same time, an electron from these levels is returned to the ground state of the ligand (second exchange) giving a concerted two electron exchange which allows the ligand to return to the ground state after excitation, and the metal to be promoted to an excited state. The Dexter theory has a much stronger dependence on a shorter L-M separation as there must be a reasonable overlap of the L and M electron clouds in order for the double electron transfer to occur, with a k_{ET} relationship proportional to e^{-r}.

A common requirement to both theories is that sufficient overlap occurs between the emission spectrum of the donor and the emission spectrum of the acceptor, in order to favour a matching of the pertinent energy levels of the two units. In order to ensure the process goes to completion, the donor excited state should be slightly higher in energy than that of the acceptor, typically >2000 cm^{-1} at room temperature.[23] Even though our $[Ru(bipy)(CN)_4]^{2-}/Ln(III)$ systems are not isostructural, the presence of different structural types should not cause any problems in performing photophysical studies, as energy transfer rates (k_{ET}) will be dominated by the shortest Ru···Ln contact regardless of the bulk structure. If a Dexter mechanism is occurring, this will exploit the Ru-CN-Ln electronic coupling, leaving any remote lanthanide centres in the crystal to a have minimal contribution to the quenching of a Ru centre.

4.2.2.2 Choosing a Reference

It is widely documented that the photophysical properties of the $[Ru(bipy)(CN)_4]^{2-}$ unit are heavily influenced by its surrounding environment, with the interaction of the cyanide lone pairs with protic solvents increasing the ligand field strength, thus giving rise to higher energy, longer lived ^{3}MLCT states.[12,24] For these reasons, we decided against using $K_2[Ru(bipy)(CN)_4]$ as our reference compound in determining the values of k_{ET} for the Ru-Ln complexes, as the interaction of the cyanide lone pairs with a heavy lanthanide centre needed to be accounted for. The $\mathbf{Ru_3Gd_2}$ complex was the perfect choice for a reference complex as Gd(III) has its lowest excited state lying some 30,000 cm^{-1} higher in energy than its ground state, and some 10,000 cm^{-1} higher in energy than the tail end of the Ru-based emission. Consequently, Gd(III) is unable to quench the Ru-based luminescence of the $[Ru(bipy)(CN)_4]^{2-}$ unit whilst maintaining the general environment of the $[Ru(bipy)(CN)_4]^{2-}$ units in interacting with 3+ metal centres.

Whilst the luminescence of $[Ru(bipy)(CN)_4]^{2-}$ in water occurs at *ca.* 640 nm,[24] prior work by Miller[21] showed that this shifts substantially to 584 nm in solid $K_2[Ru(bipy)(CN)_4]$, and the luminescence for our Ru_3Gd_2 system occurs at a comparable maximum of 580 nm. The interaction of the cyanide lone pairs with an electropositive metal ion clearly blue shifts the Ru luminescence, with the increase in ^{3}MLCT energy attributed to the increasing ability of the cyanide C terminus to act as a π acceptor.

Despite there being three crystallographically unique Ru centres in the crystal structure, the Ru-based luminescence decay for $\mathbf{Ru_3Gd_2}$ could be fitted to a single exponential decay with a half life (τ) of 550 ns, whilst the previous work[21] showed solid $K_2[Ru(bipy)(CN)_4]$ could be fitted to a dual exponential decay with lifetimes of 751 ns and 2955 ns, (*cf.* 100 ns in aqueous solution),[24] and it is here we identify the problems associated with performing such studies in the solid state, in that the crystal may contain defect sites or there may be surface effects in which luminescent centres at the surface of a crystal will be in different environments from those in the bulk.

As the 2955 ns lifetime of $K_2[Ru(bipy)(CN)_4]$ has only a 5 % weighting, it was deemed that this was not representative of the bulk structure and that in fact, 751 ns (with a 95 % weighting) was reflective of the lifetime in the solid state. The decrease in Ru-based luminescence lifetimes between $K_2[Ru(bipy)(CN)_4]$ and **Ru_3Gd_2** (≈ 200 ns) shows that there is a clear quenching effect observed in having the Gd(III) centres coordinated to the cyanides. This preliminary quenching is attributed to a slight vibrational quenching across the Ru-CN-Gd pathway and the easy dispersal of luminescence across the 2-D network in the crystal lattice, as each Ru centre has cyanide bridges to two or three Gd(III) centres.

In all other cases, excitation of the $[Ru(bipy)(CN)_4]^{2-}$ unit by 337 nm energy resulted in sensitised characteristic near-IR luminescence (840 and 1010 nm for **Ru_2PrK**, 1530 nm for **Ru_2ErK**, and both 1055 and 1340 nm for Ru_3Nd_2). 980 nm emission was observed for the **Ru_2YbK** complex by Dr Miller,[21] and we include this result in the following discussion to obtain a complete picture of the $[Ru(bipy)(CN)_4]^{2-}$ - Ln(III) series.

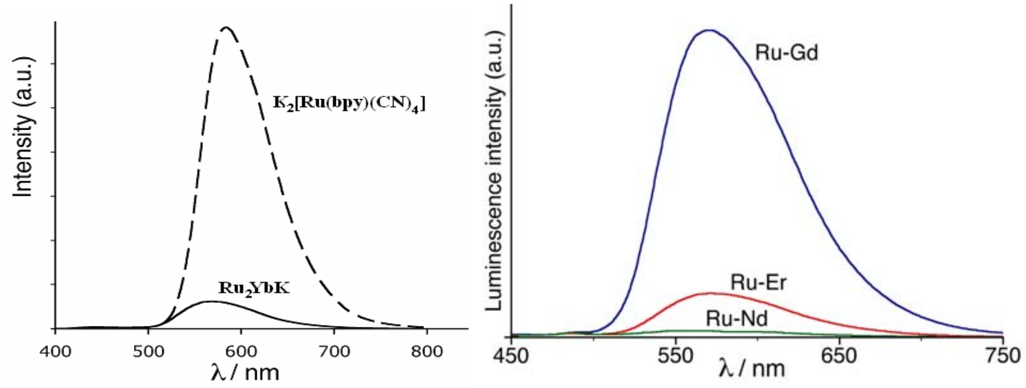

Fig. 4.2.16 – Extents of Ru-based quenching attributed to the Ln(III) ions. Graph intensity scales are arbitrary and not identical to one another.

4.2.2.3 Emission Quenching by the Lanthanides

In each complex there was some residual Ru-based luminescence centred at 570-580 nm that had not been quenched by the lanthanide. **Fig. 4.2.16a** shows the Ru-based luminescence for $K_2[Ru(bipy)(CN)_4]$ (dashed line) and for **Ru_2YbK** (solid line) showing the degree of quenching influenced by the presence of the Ln(III) centres. **Fig. 4.2.16b** shows the comparable degrees of Ru-luminescence quenching exhibited by lanthanide centres in **Ru_3Gd_2**, **Ru_2ErK**, and **Ru_3Nd_2** systems.

Ru_2YbK delivers the smallest degree of quenching of the Ln(III) systems compared to the Gd(III) reference, whilst **Ru_3Nd_2** provides the greatest (i.e. least amount of Ru-based luminescence still apparent). The series then, in order of efficiency of Ru luminescence quenching (and hence the efficiency of energy transfer to the lanthanide) can be reported as Nd > Pr > Er > Yb > Gd with reference to the graphs of **Fig. 4.2.16** (the scales of both graphs are not comparable).

The lifetimes of Ru-based luminescence were recorded for all systems at 700 nm using time-resolved measurements. Only the **Ru_2YbK** and **Ru_3Gd_2** systems could have their Ru-based luminescence lifetime decays fitted to a single exponential decay, whilst the other systems all fitted dual decays with a heavily dominant short-lived component. These minor long-lived Ru luminescences were assumed to come from imperfections in the crystals and were ignored. They actually have lifetimes in the regions of 300-500 ns which is comparable to the unquenched lifetime of Ru-luminescence in the **Ru_3Gd_2** system, and are therefore ascribed to a small proportion of $[Ru(bipy)(CN)_4]^{2-}$ centres that are not coordinated to Ln(III) centres with no means of energy transfer. Such environments may have arisen from defects in the crystal or surface effects as the samples were ground up to a powder prior to analysis. The photophysical data collected are illustrated in **Table 4.2.6**.

Complex	Ru-based emission (weighting) τ, ns[a]	Ln(III)-based emission τ, ns	Ru → Ln(III) energy transfer rate[b] k_{ET}, s^{-1}
Ru_3Gd_2	**550** (100 %)	--	--
Ru_2YbK	**197** (100 %)	**197** [c]	**3×10^6**
Ru_2ErK	**76** (96 %) **437** (4 %)	*d*	**1×10^7**
Ru_2PrK	**22** (97 %) **273** (3 %)	**22** [e]	**4×10^7**
Ru_3Nd_2	**5** (> 99 %) **439** (< 1 %)	**45** [f]	**2×10^8**

Table 4.2.6 – Photophysical data for the $[Ru(bipy)(CN)_4]^{2-}$ - Ln(III) series

[a] Recorded at 700 nm; [b] Determined using Eq 4.1; [c] Recorded at 980 nm – the Yb-based luminescence overlaps with the tail end of the Ru-based luminescence and this value is therefore subject to error; [d] Luminescence too weak to obtain meaningful value for τ;
[e] Recorded at 1010 nm; [f] Recorded at 1055 nm.

Knowing the lifetimes of residual Ru-based emissions in the presence of both a lanthanide which acts as an energy acceptor (τ_q) and Gd as reference, (τ), we can employ **Eq. 4.1** to determine the rate of Ru → Ln energy transfer in the various systems.

$$k_{ET} = 1/\tau_q - 1/\tau \qquad \textbf{Eq. 4.1}$$

Taking τ = 550 ns for the unquenched luminescence of **Ru_3Gd_2**, and employing the values shown in the second column of **Table 4.2.6**, we can deduce that for **Ru_3Nd_2** (i.e. the fastest quenching system):

$$k_{ET(Ru \rightarrow Nd)} = [(5 \times 10^{-9})^{-1} - (550 \times 10^{-9})^{-1}] = 2 \times 10^{8}\ s^{-1}$$

Applying the same data manipulation for the rest of the series generates the values shown in column four of **Table 4.2.6**, which agree with the relative intensities displayed in **Fig. 4.2.16**.

There are relatively few examples of quantified d-f energy transfer rates in the literature, although the work by van Veggel in {$[Ru(bipy)_3]^{2+}$ / Yb(III)} and {$[Ru(bipy)_3]^{2+}$ / Nd(III)} hybrids offers sufficient means for comparison with our systems.[2] The rate of k_{ET} = < 10^5 s^{-1} for their Yb(III) system is an order of magnitude slower than our system, highlighting the combined effects of having a large Ru···Ln separation as well as the absence of a conjugated bridge. A much faster energy transfer rate is observed in their Nd(III) system (k_{ET} = 1.1 x 10^6) as we also observe, although again the absolute value is low.

4.2.2.4 Ru-Ln Overlap

The vast difference in k_{ET} values for our series (spanning a difference of two orders of magnitude across the members) can be explained with reference to **Fig. 4.2.17**, which depicts the relevant energy levels of the near-IR emissive lanthanide ions.

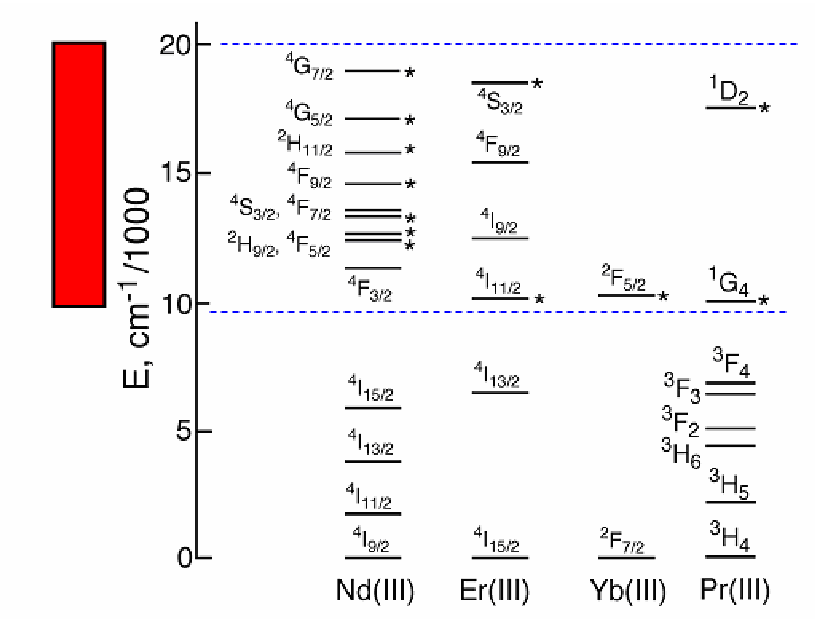

Fig. 4.2.17 – Relevant emissive and ground state energy levels for the luminescent Ln(III) ions. Those marked with an asterisk (*) are capable of accepting energy *via* Förster or Dexter mechanisms.

The range of the $[Ru(bipy)(CN)_4]^{2-}$ emission spectrum is represented by the red box shown to the left of the graph (*ca.* 10,000 – 20,000 cm^{-1}),[9,24] placed in relation to the absorption spectrum of the Ln-acceptor energy levels. As the series member with the shortest Ru···Ln separation (**Ru_2YbK**) gives the slowest rate of energy transfer, it can be deemed that the small variation in Ru···Ln distances across the series will make only a minor contribution to the energy transfer.

Those Ln(III) energy levels encompassed between the dotted blue lines should have sufficient overlap with the Ru-based emission, enabling a facile energy transfer, and we can therefore exclude any energy levels higher than 20,000 cm^{-1} as energy acceptors. Previous studies[25] show that an excited triplet donor should be at least 1000 cm^{-1} higher in energy than the acceptor level of a lanthanide ion to ensure the energy transfer is exothermically driven and no thermally activated backwards transfer occurs at room temperature, and so we can discount any lanthanide energy levels above 19,000 cm^{-1} as facilitators of Ru → Ln energy transfer as well. In addition to this, the low end of the Ru-based emission ends at 10,000 cm^{-1}, enabling us to discount any energy levels below this energy as acceptors of emission.

The emissive level of $^2F_{5/2}$ of Yb(III) in **Ru_2YbK** just overlaps with the low energy tail end of the Ru emission at 10,200 cm^{-1}, and we see the characteristic *f-f* transition of $^2F_{5/2} \rightarrow {}^2F_{7/2}$ at 980 nm.[21] This small overlap accounts for why this lanthanide has the slowest degree of quenching, when compared to **Ru_3Nd_2**, in which we have nine energy levels lying in the 10,000-19,000 cm^{-1} region of the Ru emission. It is thus clear from this high density of acceptor levels why the **Ru_3Nd_2** system is the fastest quencher. The observed luminescence at 1055 and 1340 nm is attributed to the $^4F_{3/2} \rightarrow {}^4I_{11/2}$ and $^4F_{3/2} \rightarrow {}^4I_{13/2}$ transitions respectively.[26]

From looking at **Fig. 4.2.17** one might think that Er(III) would provide a faster rate of quenching than Pr(III), with four energy levels in the 10,000-19,000 cm^{-1} region compared to the two of Pr(III); however the data in **Table 4.2.6** shows the reverse to be the case.

It is worth recalling at this stage that energy transfer can only occur *via* a Förster or Dexter mechanism, and these carry their own selection rules, namely the change in total angular momentum (ΔJ) between the emissive states and the ground states of the *f-f* transitions. Förster pathways require ΔJ values of 2, 4, or 6; whilst Dexter values are 0 or 1,[5] and those levels that can act as energy acceptors whilst also permitting the ΔJ values to change in accordance with either pathway are marked on **Fig. 4.2.17** with an asterisk (*).

In light of this, it is apparent that two of the acceptor levels of Er(III) which have good energetic overlap with the Ru emission ($^4F_{9/2}$ and $^4I_{9/2}$), are excluded from participating in energy transfer as this would give ΔJ a value of 3 from the ground state of $^4I_{15/2}$. This leaves only two viable energy acceptor levels ($^4S_{3/2}$ and $^4I_{11/2}$). In the **Ru$_2$PrK** system, there are also only two viable levels ($^1D_2$ and $^1G_4$), and whilst there is little difference in displacement between the two lower levels of these lanthanide ions, the $^1D_2$ level of Pr(III) lies at about 17,500 cm^{-1} and consequently has a much better spectral overlap with the higher end of the Ru emission compared with the $^4S_{3/2}$ level of Er(III) which lies at about 18,500 cm^{-1}, and gives it a better gradient for energy transfer. This explains the greater degree of quenching observed in **Ru$_2$PrK** than **Ru$_2$ErK**. In fact, the 1010 nm luminescence in **Ru$_2$PrK** arises from the $^1D_2 \rightarrow {}^3F_4$ transition (which we assigned in chapter three), showing that direct population of the $^1D_2$ state does indeed occur to a satisfactory degree, whilst no luminescence is observed in **Ru$_2$ErK** that can be attributed to the $^4S_{3/2}$ state.

However, that is not to say that the $^4S_{3/2}$ level in Er(III) is not populated as it will have a better overlap with the Ru emission than the lower $^4I_{11/2}$ level which only just overlaps with the emission spectrum at 10,000 cm^{-1}. The higher state does however, have a gradient of less than 2000 cm^{-1} from the ^{3}MLCT energy of the Ru unit and may be inefficient at quenching due to back energy transfer at room temperature. The observed luminescence of **Ru$_2$ErK** at 1530 nm is attributed to the $^4I_{13/2} \rightarrow {}^4I_{15/2}$ transition, and whilst the $^4I_{13/2}$ level lies at about 7000 cm^{-1}, it becomes populated *via* the offloading of energy from the higher levels by internal conversion, rather than direct acceptance from the Ru emission.

4.2.2.5 Alternate Transfer Rates

The third column of **Table 4.2.6** illustrates the lifetimes of the lanthanide-based luminescence for all members of the series. The Ru-based emission for **Ru_2YbK** was measured at 700 nm with a lifetime of 197 ns, and measuring the luminescence at 980 nm of the Yb(III) also produced a lifetime of 197 ns for this decay (assuming a single exponential decay component). However, **Ru_2YbK** did show a rise time component for the Yb-based luminescence of 160 ns (i.e. Ru → Yb energy transfer) the reciprocal of which suggests an energy transfer rate of 6×10^6 s^{-1}. This is higher than the value of 3×10^6 s^{-1} calculated using the Ru-based emission, but given the approximations involved in fitting these decays to single or dual exponential components, is within experimental error.[9] Due to the limitations of the instrument, no rise times could be deduced for the other members of the series, although we can predict that the quenching trend of Nd > Pr > Er > Yb will be reproduced.

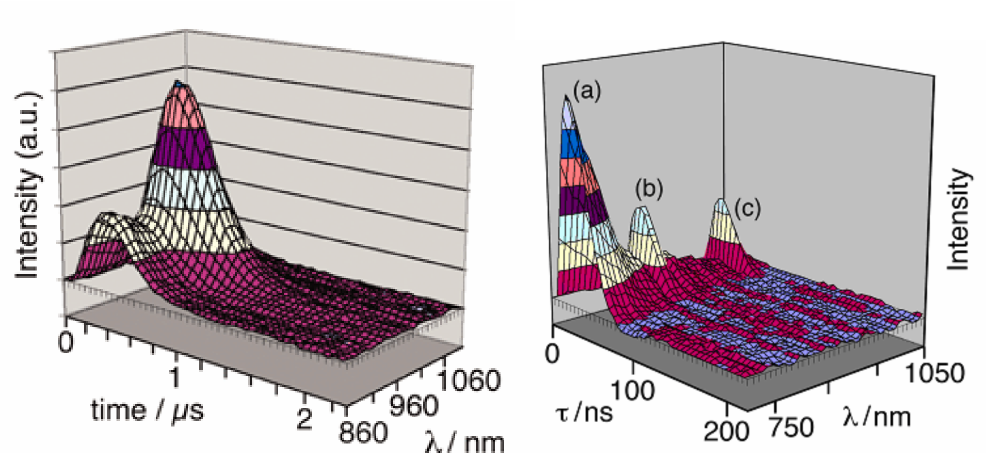

Fig. 4.2.18 – Time-resolved luminescence profile for (i) Ru_2YbK in the region 860-1060 nm and (ii) Ru_2PrK in the region 750-1050 nm.

Fig. 4.2.18 shows the overlapping Ru emission (a) with the 840 nm (b) and 1010 nm (c) components of Pr(III), also highlighting the inherent weakness of *f-f* transitions in comparison to ^{3}MLCT transitions. The longer wavelength component at 1010 nm is not as appreciably 'contaminated' and we can use this value to deduce a decay lifetime of 22 ns for the Pr-based luminescence.

The longer wavelength components in **Ru_3Nd_2** are also free from Ru-based contamination, and both 1055 and 1340 nm emissions (**Fig. 4.2.19**) show a decay lifetime of 45 ns, indicative of emissions occurring from a common excited state (i.e. $^4F_{3/2}$). These values indicate that the excited states of the lanthanides, once populated, are easily quenched by lattice vibrations. In the case of **Ru_2ErK**, the time-resolved emission spectrum (TRES) was noisy, due to the weakness of Er-based luminescence at 1530 nm. An effort was made to fit the signal at this wavelength to a single exponential decay (somewhere between 200 and 100 ns), but all we can confidently say is that the decay lifetime for this luminescence is less than 200 ns.

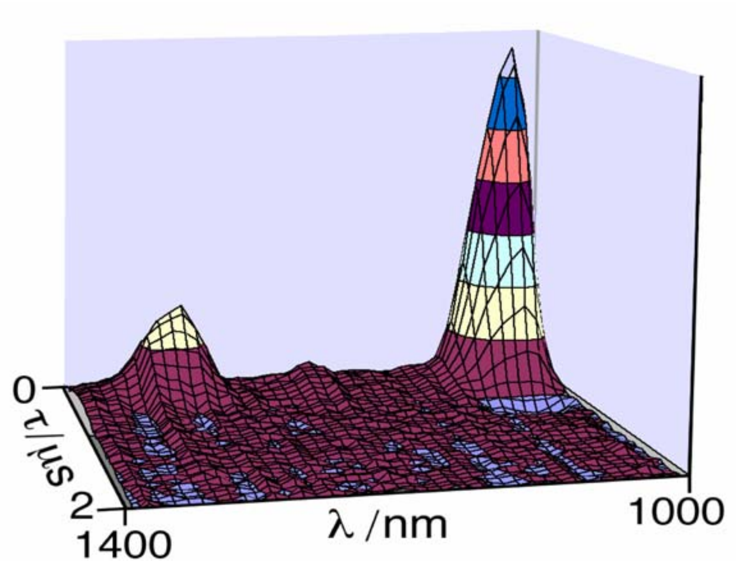

Fig. 4.2.19 – Time-resolved luminescence profile for Ru_3Nd_2 in the region 1000-1400 nm

4.2.2.6 Quenching of Lanthanide Luminescence

All complexes in this series have shown that the lanthanide ions complete their coordination spheres with a mixture of cyanide nitrogen donors and terminal water or D_2O molecules. Despite using D_2O to maximise the lanthanide luminescence by removing O-H oscillators as quenching pathways (**Section 1.2.4.2**), the luminescence lifetimes of these complexes are appreciably less than those obtained for the $[Ln(Bp^{2py})(dbm)_2]$ complexes in chapter three. For example, $[Nd(Bp^{2py})(dbm)_2]$ has a luminescence lifetime of 740 ns in the solid state, whereas that of the Nd(III) centre in **Ru_3Nd_2** is 45 ns.

The previous works of our group[1,4,5,27,28] have shown decay lifetimes of 10–11.5 μs for Yb(III); 1.0 μs for Nd(III); 1.2-1.6 μs for Er(III) and 0.05-0.07 μs for Pr(III) based molecular complexes that are devoid of water molecules in the solid state. In light of this, we can only hypothesise that the weaker luminescence observed in the Ru-Ln series must arise from an alternative quenching mode to O-H vibrations.

The obvious candidate is the C≡N vibrations, however these have relatively low energy vibrations (on a par with that of O-D oscillators),[29] and so it is unclear as to why these should be the culprit. An alternative theory to suggest would be the effect of having an interconnected network in the crystal lattice, which may dissipate luminescence energy by vibrations at a faster rate across the Ru-Ln system than in crystals where complexes reside in isolated locations and are not vibronically coupled to one another.

4.2.3 Crystal Structure of $K_2[(phen)Ru(CN)_4]\cdot 4H_2O$

The complex unit $K_2[(phen)Ru(CN)_4]$ was first synthesised by Horváth in 2002,[30] but has not yet been structurally characterised. The complex was made in identical fashion to that of $K_2[(bipy)Ru(CN)_4]$ using 1,10-phenanthroline for the diimine ligand, and slow evaporation of a concentrated aqueous solution of the complex afforded single crystals suitable for X-Ray studies. The complex was found to contain four water molecules in the lattice, rather than the two that Horváth had originally postulated (**Fig. 4.2.20**). Selected bond lengths for the complex are given in **Table 4.2.7**.

K(2)-O(103)	2.716(8)	K(3)-O(101)	2.714(8)
K(2)-O(103A)	2.751(8)	K(3)-N(6B)	2.775(11)
K(2)-N(5)	2.908(13)	K(3)-N(6A)	2.788(13)
K(2)-N(5B)	2.791(11)	K(3)-N(3)	3.017(14)
K(2)-N(6A)	2.983(13)	K(3)-O(101A)	3.025(9)
K(2)-N(2A)	3.005(13)	K(3)-N(5)	3.029(12)
K(2)-C(16A)	3.046(16)	K(3)-C(13)	3.077(14)
K(2)-C(14A)	3.073(14)	K(3)-C(15)	3.133(15)
K(2)-K(3)#1	4.367(3)	K(3)-O(100)	3.229(7)

Table 4.2.7 – Selected bond lengths (Å) for $K_2[(phen)Ru(CN)_4]\cdot 4H_2O$

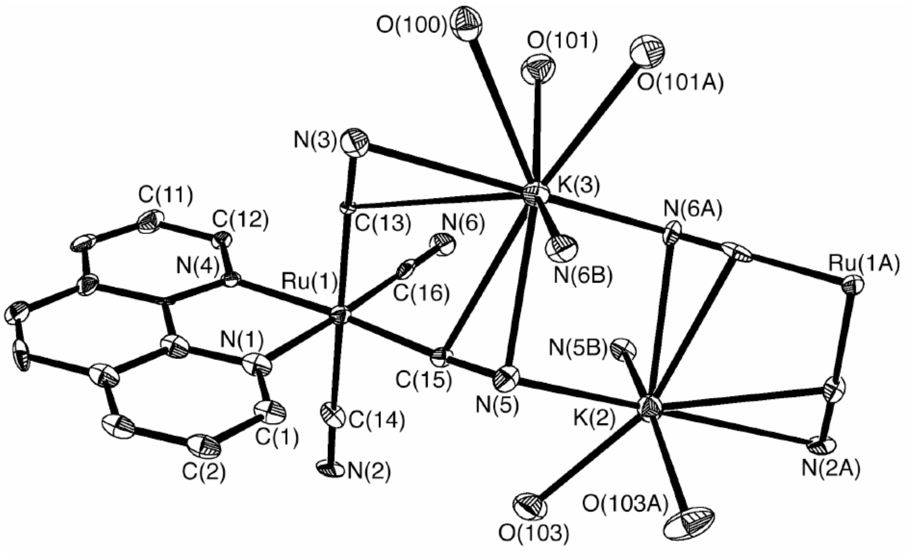

Fig. 4.2.20 – Crystal structure of $K_2[(phen)Ru(CN)_4]\cdot 4H_2O$ with some additional symmetry-equivalent atoms included to complete the coordination spheres about the metal atoms

The Ru(II) metal centre shows an unremarkable pseudo-octahedral geometry with the N-Ru-C and C-Ru-C angles deviating approximately 5° from ideal linear and perpendicular values; the Ru-C and Ru-N bond lengths are typical (Ru···N = 2.10-2.12 Å, and Ru···C = 1.98-2.06 Å). Each cyanide group coordinates to a K^+ ion *via* a side-on interaction reminiscent of that seen in **Ru_2PrK** (**Fig. 4.2.1**). Our average K-C and K-N bond lengths in the $K_2[(phen)Ru(CN)_4]$ complex (3.1 and 3.0 Å respectively) are remarkably shorter than those in the $[Rh(CN)_3]$-based K^+ cages of Rauchfuss (both bond lengths average at 3.74 Å) but comparable with those based on the $[Mo(CO)_3(CN)_3]$ motif.[20] The average C-K-N angle for the complex is 21.9°.

The four cyanide groups exhibit two types of binding in the complex, with the same type shown by those *trans* to each other. The cyanide groups of N(2) and N(3) bond side-on to the one potassium ion [K(2) and K(3) respectively, average bond length = 3.0 Å], whilst those of N(5) and N(6) bond side-on to K(3) and K(2) respectively (average bond = 3.0 Å), but also form two shorter bonds to two separate potassium ions through the cyanide N atoms only (average bond = 2.8 Å).

The potassium ions are also coordinated by two [K(2)] or three [K(3)] water molecules: Thus, K(2) is coordinated by two side-on cyanides, two water molecules, and two additional cyanide ligands *via* the N atoms only; whereas K(3) is in a similar coordination environment but with an additional water molecule.

The extensive bridging coordination behaviour of the cyanide groups of N(5) and N(6) is quite remarkable, being C-bound to the Ru atom, CN side-on to one K^+ ion, and having the terminal lone pair of the nitrogen atom shared between two additional K^+ ions. In addition to this, pairs of K(2) atoms and K(3) atoms are bridged by the water molecules of O(103) and O(101) respectively (average K-O distance = 2.8 Å). This bridging behaviour connects the $K_2[(phen)Ru(CN)_4]\cdot 4H_2O$ units, giving rise to a one-dimensional chain which propagates along the c-axis (**Fig. 4.2.21**).

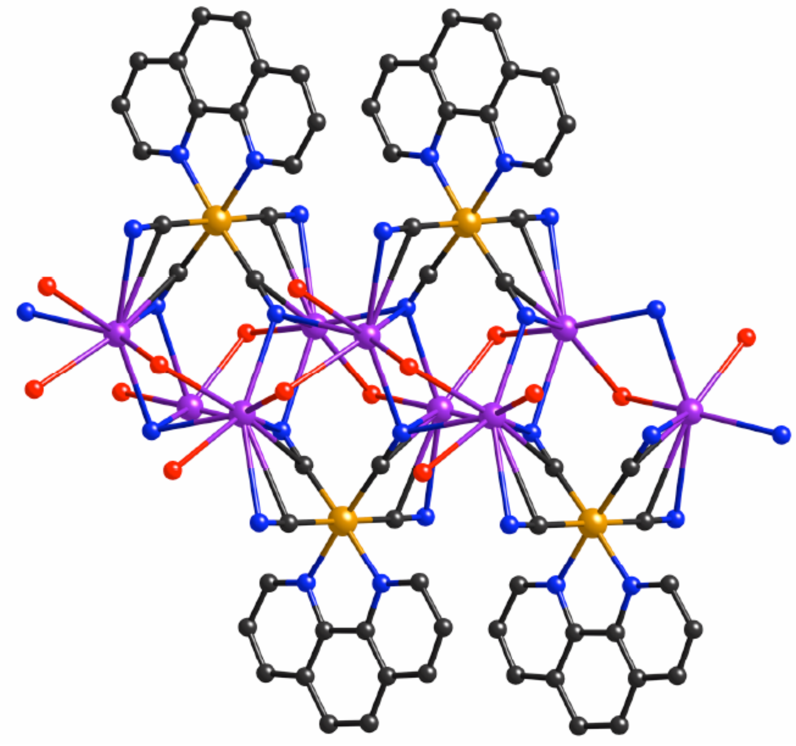

Fig. 4.2.21 – Propagation along the c-axis in $K_2[(phen)Ru(CN)_4]\cdot 4H_2O$ (Ru = brown; K = purple, N = blue, O = red, C = black).

These chains are then associated by hydrogen bonding between a phenanthroline hydrogen [H(7A)] and the oxygen atoms of the lone lattice water molecules [CH(7A)···O(102) = 2.49 Å, C(7)···O(102) = 3.375(15) Å], which in turn form H-bonds to the water molecules with H(103) and H(101) [bond length to O(102) = 2.02 and 2.09 Å respectively].

4.2.4 Studies of [Cr(CN)$_6$]- [Ln(III)] Systems (Ln = Nd, Gd, Yb)

Lanthanide hexacyanometallates have been reported in the literature as early as 1909[31] and to date include series in which cobalt(III),[32] iron(III)[33] and ruthenium(II)[34] take the form of the octahedral metal ion. The combination of hexacyanochromate(III) anions and lanthanide(III) cations has also featured, and first occurred in 1976 when Hulliger and co-workers prepared a full array of $LnCr(CN)_6{\cdot}5H_2O$ complexes to study their magnetic properties.[35] Whilst no crystallographic data was available from this work, it was assumed that the structures were analogous to the $LnFe(CN)_6{\cdot}5H_2O$ complexes determined by Bailey.[36] However, this was subsequently disproved by Seto *et al* when they determined the structures of $LaCr(CN)_6{\cdot}4H_2O$ and $SmCr(CN)_6{\cdot}3H_2O$ *via* powder X-ray diffraction,[37] showing that the number of water molecules in the first coordination sphere of the lanthanide ion appeared to vary.

4.2.4.1 $[Cr(CN)_6][Ln(H_2O)_2]$ (Ln = Gd, Yb)

In an attempt to obtain single crystals of a $LnCr(CN)_6{\cdot}xH_2O$ series member and confirm the structure, we adopted the common method of combining equimolar amounts of $K_3[Cr(CN)_6]$ with the lanthanide(III) chloride in water, allowing the solvent to slowly evaporate. No previously reported works with this method quoted a yield, and in our case only a couple of long, thin crystals were obtained from the resulting deposit; however, these were suitable for X-ray studies. Crystal structures of both Gd(III) and Yb(III) isomers were obtained and both complexes were found to be isostructual with molecular formulas of $LnCr(CN)_6{\cdot}3H_2O$; but for the purposes of structural discussion, we restrict ourselves to the Yb(III) complex.

The complex crystallises in the orthorhombic space group *Cmcm*, giving a better data agreement than the monoclinic $P2_1/m$ that Seto *et al* first proposed for $SmCr(CN)_6{\cdot}3H_2O$ *via* powder analysis.[37] The ytterbium centre is 8-coordinate with a square antiprismatic geometry (**Fig. 4.2.22**) comprising two square planes formed by N_4 and N_2O_2 vertices, perfectly parallel to each other, with the Yb(1) atom sat 1.251 and 1.323 Å from the former and latter plane respectively. The vertices of the N_4 plane are formed by cyanide bonds to four separate $[Cr(CN)_6]^{3-}$ units [Yb(1)···N(1) = 2.394(2) Å], whilst the N_2O_2 plane are formed by bonds to two water molecules [Yb···O(1) = 2.307(3) Å] and two more separate $[Cr(CN)_6]^{3-}$ units.

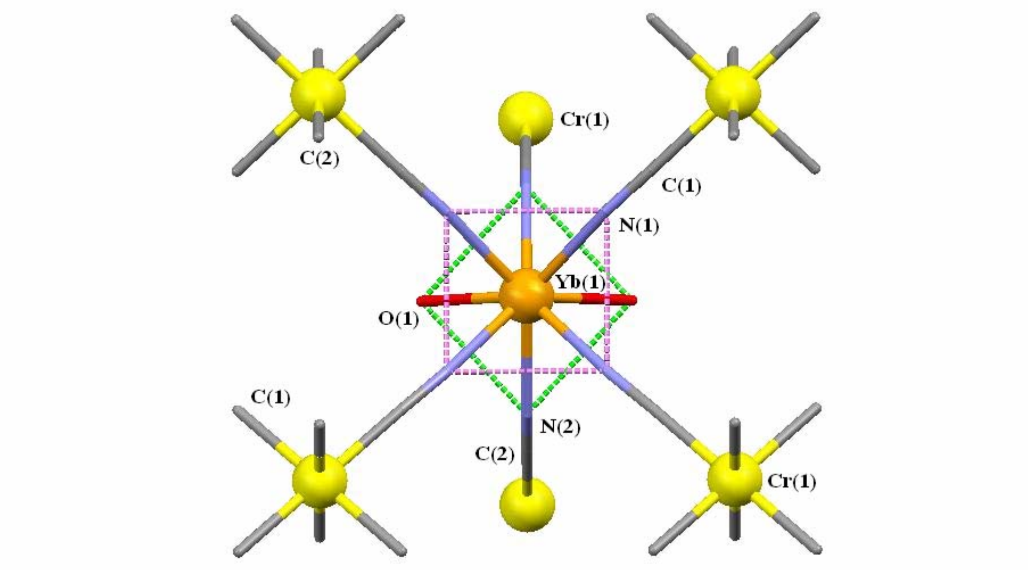

Fig. 4.2.22 – Crystal structure of $Yb[Cr(CN)_6(H_2O)_2]{\cdot}H_2O$ highlighting the coordination geometry about the lanthanide centre. Hydrogen atoms and the lattice water have been removed for clarity.

The structure extends along all three crystallographic axes through the cyanide groups of the Cr(III) unit, with alternate views along the **a**, **b** and **c**-axes shown in **Fig. 4.2.23**, **4.2.24** and **4.2.25** respectively. None of the cyanide-Yb bonds remain linear in the structure, with respective Yb(1)-N(1)-C(1) and Yb(1)-N(2)-C(2) angles at 167.8 and 151.5°, and the bond lengths and angles about the Cr(III) centre unit are unremarkable [Cr-C = 2.068(3) Å, C-Cr-C = 89.9°].

With reference to **Fig. 4.2.25** the Cr···Yb separation is 5.451(1) Å for those metals to the left and right of each other, and 5.581(1) Å for those diagonally related.

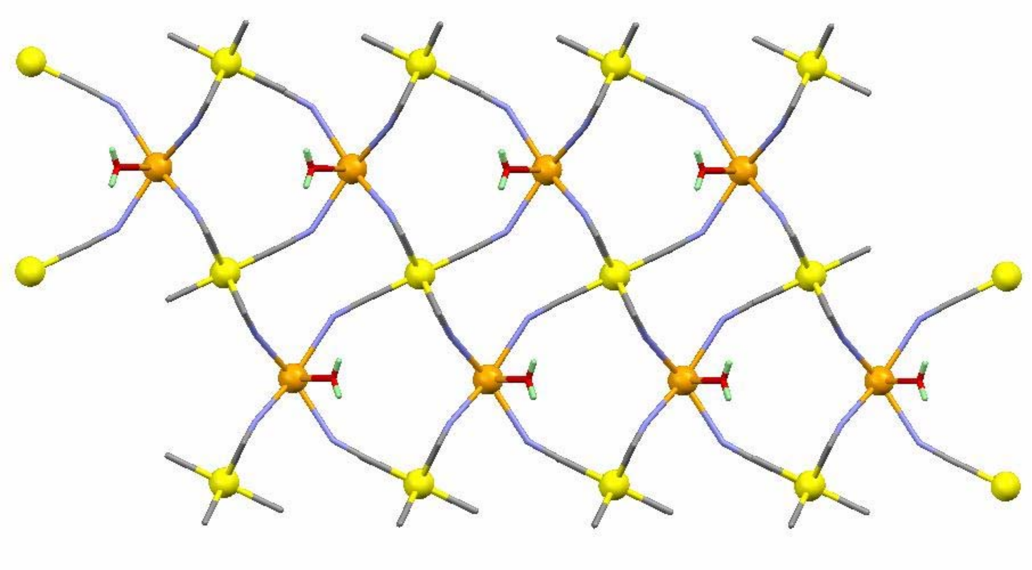

Fig. 4.2.23 – View of Yb[Cr(CN)$_6$(H$_2$O)$_2$]·H$_2$O along the a-axis. Hydrogen atoms and the lattice water have been removed for clarity.

The coordinated water molecule O(1) also helps the propagation of the polymer along the **ac** plane, by hydrogen bonding to the lattice water [OH(1)···O(1S) = 2.136 Å, O(1)···O(1S) = 2.844(4) Å]; which itself is bonded to the axial cyanide group [OH(1S)···N(2) = 2.507 Å, O(1S)···N(2) = 3.269(6) Å] (**Fig. 4.2.26**). Selected bond lengths for both Yb(III) and Gd(III) analogues are shown in **Table 4.2.8** and **4.2.9** respectively.

Cr(1)-C(1)	2.068(3)
C(1)-N(1)	1.157(4)
N(1)-Yb(1)	2.394(2)
N(2)-Yb(1)	2.432(4)
Yb(1)-O(1)	2.307(3)

Table 4.2.8 – Selected bond lengths (Å) for [Cr(CN)$_6$][Yb(H$_2$O)$_2$]·H$_2$O

Cr(1)-C(1)	2.062(5)
C(1)-N(1)	1.155(6)
N(1)-Gd(1)	2.497(4)
N(2)-Gd(1)	2.463(3)
Gd(1)-O(1)	2.374(3)

Table 4.2.9 – Selected bond lengths (Å) for [Cr(CN)$_6$][Gd(H$_2$O)$_2$]·H$_2$O

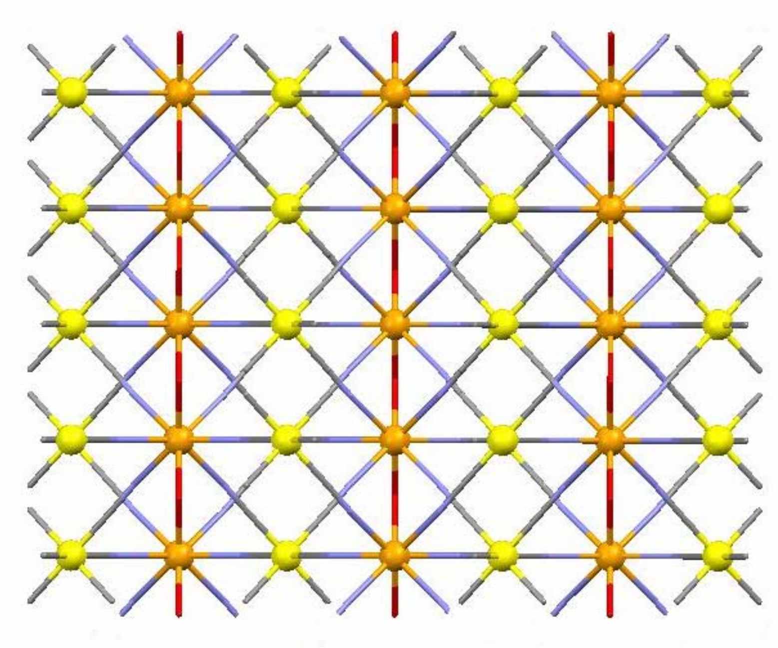

Fig. 4.2.24 – View of Yb[Cr(CN)$_6$(H$_2$O)$_2$]·H$_2$O along the b-axis. Hydrogen atoms and the lattice water have been removed for clarity.

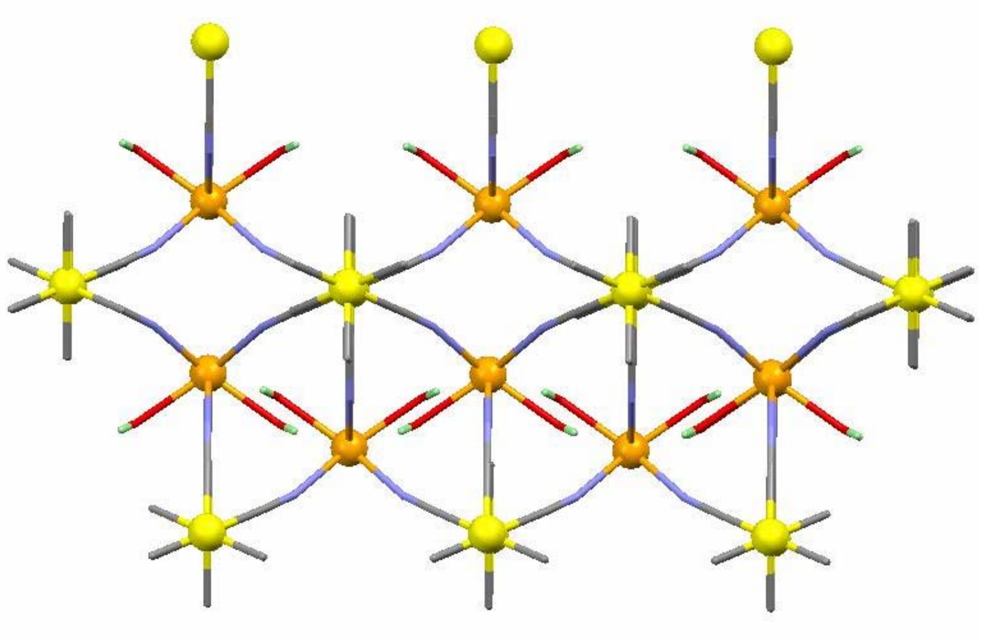

Fig. 4.2.25 – View of Yb[Cr(CN)$_6$(H$_2$O)$_2$]·H$_2$O along the c-axis. Hydrogen atoms and the lattice water have been removed for clarity.

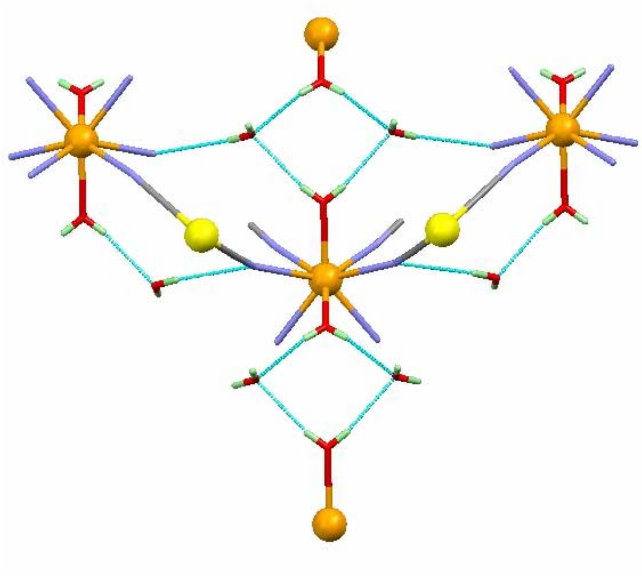

Fig. 4.2.26 – View of Yb[Cr(CN)$_6$(H$_2$O)$_2$]·H$_2$O showing the hydrogen bonded network.

4.2.5 Photophysical Studies of [Cr(CN)$_6$][Ln(DMF)$_4$(H$_2$O)$_2$] Systems

Works by Otsuka,[38] Fujita[39] and Bignozzi[40] *et al* have shown that Cr(III) can be employed in Ru(II)-Cr(III) and Os(II)-Cr(III) systems to accept energy transfer from the group 8 metal once excited, with emission readily being observed from the $^2E_g \rightarrow {}^4A_{2g}$ transition after sensitisation by energy transfer (13,100-14,400 cm^{-1}, **Fig. 4.2.27**).

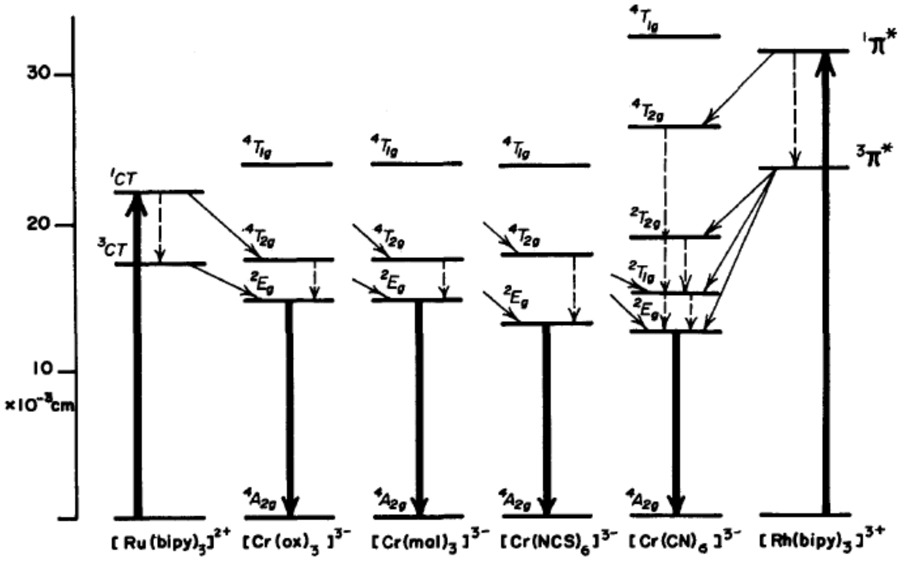

Fig. 4.2.27 – Ru(II)→Cr(III) energy transfer in various hybrid systems. [39]

The ^2E_g level varies in energy depending on the coordination sphere of the Cr(III), and in $[Cr(CN)_6]$ rests at *ca.* 13000 cm^{-1}. Bűnzli and co-workers[41] have shown that the high energy levels of Eu(III) and Tb(III) can also populate the Cr(III) ^2E_g state; however, they[42] and Kaizaki[43] have also showed the reverse can be achieved, with the populated Cr(III) transferring energy from the ^2E_g level to the higher energy levels of near-IR emitting lanthanide(III) ions such as Yb(III) and Nd(III) (**Fig. 4.2.28**). The self-assembled $[LnCrL_3]^{6+}$ helicates used by Bűnzli (where L is a segmental ligand) had typical Cr-Ln separation distances of 9.36 Å and, not surprisingly, accompanying slow energy transfer rates $[k_{(Cr\rightarrow Yb)} = 0.2 \text{ x } 10^3 \text{ s}^{-1}]$, whereas the work by Kaizaki used a much shorter oxalate bridge to hold the components together at a separation of 5.63 Å,[44] although no rate constants were determined for the energy transfer in this work.

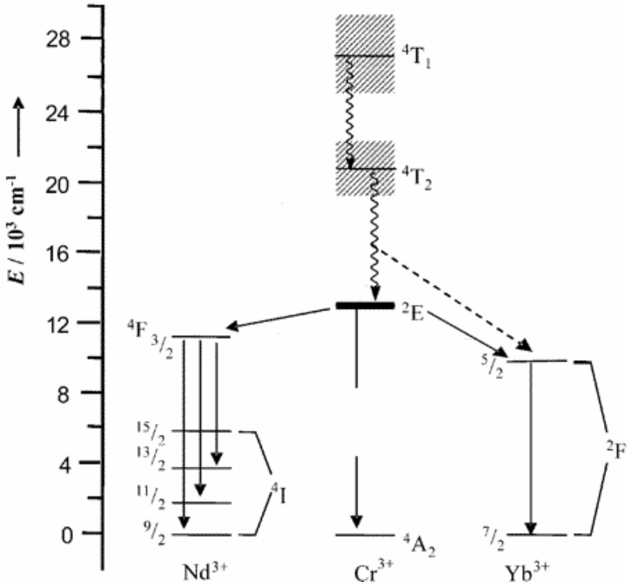

Fig. 4.2.28 – Cr → Ln(III) energy transfer.

As shown in the $[Ru(bipy)(CN)_4]$-Ln(III) systems earlier, the cyanide group is a very attractive bridging unit for promoting energy transfer between metal centres, yet suitable quantities of crystals were not obtainable in our $YbCr(CN)_6{\cdot}3H_2O$ synthesis, leaving us to find another system through which the Cr-CN-Ln bridge could be exploited.

The limitation rests with the lack of solubility for the $K_3[Cr(CN)_6]$ and Ln(III) cation reagents in common solvents making it particularly difficult to obtain sufficient quantities of single crystals. However, a suitable method was found *via* the works of Kautz[45] and Ribas[46] in which the Cr(III) and Ln(III) sources are combined in H_2O and DMF solutions respectively, with slow evaporation generating copious amounts of yellow single crystals of the form $[Cr(CN)_6][Ln(H_2O)_2(DMF)_4]\cdot H_2O$. The effect of luminescence quenching by DMF molecules in the first coordination sphere of the lanthanide ion is much less than for water molecules, but to ensure that the luminescence lifetime of the lanthanide ion was maximised, a D_2O/DMF crystallisation mixture was used in the hope of replacing any coordinated H_2O molecules with D_2O. In these syntheses, we employed $Ln(NO_3)_3$ hydrate salts.

Crystal structures were obtained for $[Cr(CN)_6][Ln(H_2O)_2(DMF)_4]\cdot H_2O$ where Ln = Nd(III), Gd(III), and Yb(III), and yet again we refer to the water molecules as H_2O, although they are mostly D_2O. The complexes were isostructual to the Gd(III) analogue prepared by Ribas[46] (intended for our use as a reference in determining energy transfer rates for these systems), with two water molecules attached to the lanthanide ion.

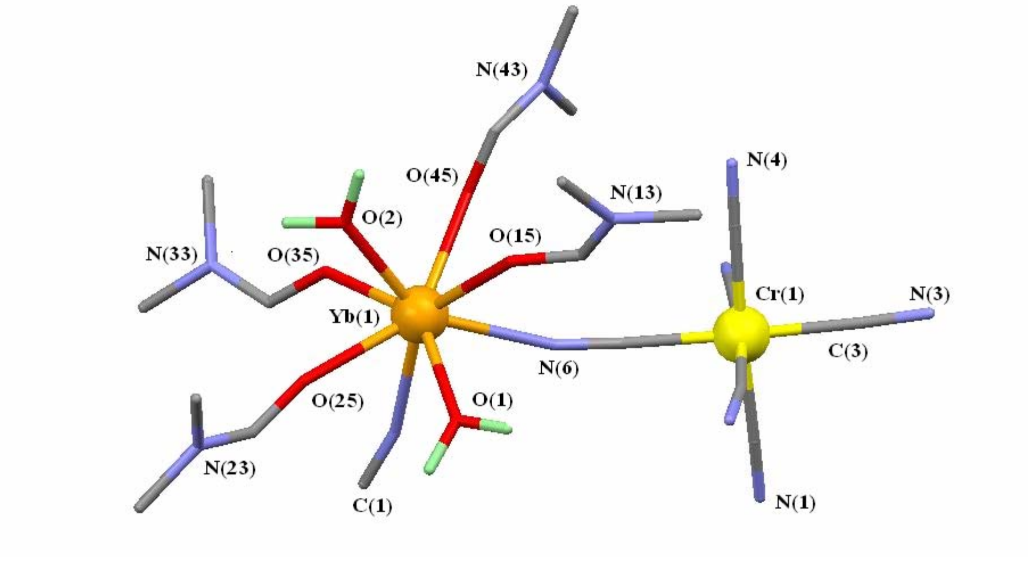

Fig. 4.2.29 – Crystal structure of $[Cr(CN)_6][Yb(DMF)_4(H_2O)_2]\cdot H_2O$

The Yb(III) complex is shown in **Fig. 4.2.29** and shows the lanthanide is in an 8-coordinate N_2O_6 geometry consisting of four Yb-O_{DMF}, two Yb-$O_{D2O,}$ and two Yb-N_{CN} bonds of average lengths 2.312, 2.310 and 2.440 Å respectively. The square antiprismatic geometry is formed by two planes comprising O(15)/O(2)/O(25)/O(1) and N(1)/N(6)/O(35)/O(45) with respective average deviations from the mean of 0.0759 and 0.3739 Å (**Fig. 4.2.30**).

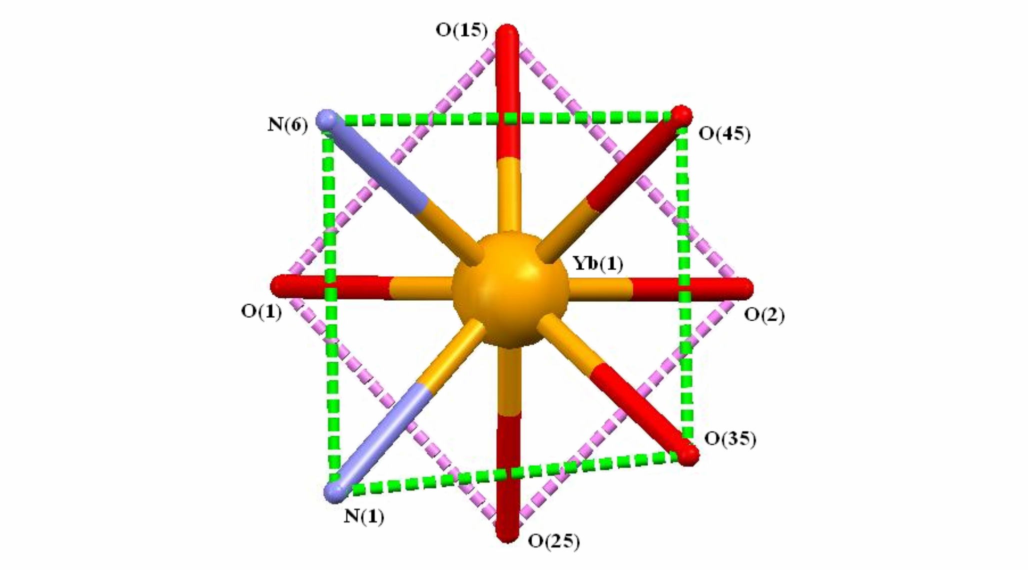

Fig. 4.2.30 – Square antiprismatic geometry about Yb(III) centre in $[Cr(CN)_6][Yb(DMF)_4(H_2O)_2]\cdot H_2O$.

Whilst no immediate effect in ionic radius is observed between Nd(III) and Yb(III) analogues, the Pr(III) analogue of Kautz[45] shows its ability to accommodate an extra water molecule about the lanthanide centre. Selected bond lengths are given for the Nd(III) and Yb(III) analogues in Tables **4.2.10** and **4.2.11** respectively.

N(1)-Nd(1)	2.580(6)
N(6)-Nd(1)	2.560(7)
Nd(1)-O(25)	2.408(5)
Nd(1)-O(2)	2.414(5)
Nd(1)-O(15)	2.415(5)
Nd(1)-O(35)	2.434(5)
Nd(1)-O(45)	2.442(5)
Nd(1)-O(1)	2.458(5)

Table 4.2.10 – Selected bond lengths (Å) for $[Cr(CN)_6][Nd(DMF)_4(H_2O)_2]\cdot H_2O$

N(1)-Yb(1)	2.434(3)
N(6)-Yb(1)	2.445(3)
Yb(1)-O(2)	2.288(2)
Yb(1)-O(25)	2.300(2)
Yb(1)-O(35)	2.308(3)
Yb(1)-O(15)	2.313(2)
Yb(1)-O(45)	2.327(3)
Yb(1)-O(1)	2.331(3)

Table 4.2.11 – Selected bond lengths (Å) for $[Cr(CN)_6][Yb(DMF)_4(H_2O)_2]\cdot H_2O$

Both Cr(III) and Yb(III) units act as bridges to the other metal units forming a one dimensional chain along the **b**-axis with the Cr-Yb-Cr-Yb linkage in a form reminiscent of a sine wave (**Fig. 4.2.31**). Adjacent chains are connected along the **c**-axis by a series of hydrogen bonds such as N(5)-H(21), N(5)-H(22), N(5)-H(1S) and N(2)-H(2S), and whilst the bond lengths and angles about the $[Cr(CN)_6]^{3-}$ unit are unremarkable, the Cr···Yb separation in the polymer is found at 5.58-5.59 Å - slightly shorter than those of Kaizaki's complexes.[43]

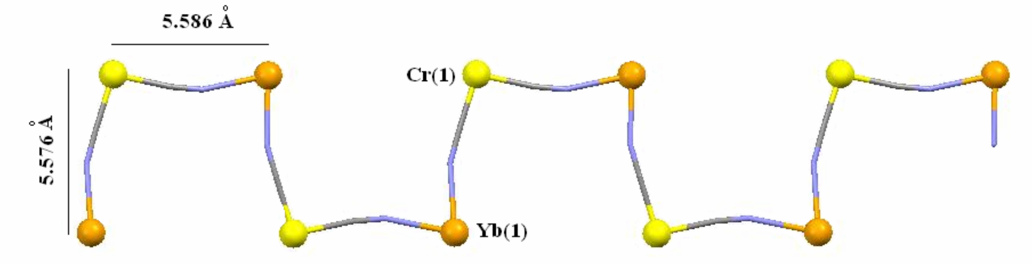

Fig. 4.2.31 – Arrangement of -Cr-Yb-Cr-Yb- chain in $[Cr(CN)_6][Yb(DMF)_4(H_2O)_2]\cdot H_2O$. The same arrangement is observed in Gd(III) and Nd(III) systems.

Sensitised Ln(III)-based emission was observed for both the Yb(III)- and Nd(III)-$[Cr(CN)_6]$ systems upon 337 nm excitation of the Cr(III) unit in the solid state. The Cr(III)-based luminescence is completely quenched by the Ln(III) excited states at room temperature,[42,43] the absence of which meant it was not possible to determine energy-transfer rates for these systems at room temperature, although we can postulate that the shorter internuclear separation and conjugated bridge would provide a faster means of transfer than those of Bűnzli's helicates ($k_{ET(Cr\rightarrow Yb)} = 0.2 \times 10^3\ s^{-1}$).[42]

Both systems displayed single exponential decays for the Ln(III)-based luminescence: the Yb(III)-based $^2F_{5/2} \rightarrow {}^2F_{7/2}$ emission at 980 nm was observed with a lifetime of 612 ns; and the Nd(III)-based emission was observed at both 880 and 1055 nm, with the more intense latter transition ($^2F_{3/2} \rightarrow {}^2I_{11/2}$) used to determine a lifetime of 100 ns. Repeating the measurement on a second sample of the Nd(III)-Cr(III) complex produced a lifetime of 112 ns, indicating the degree of error we can expect to find in recording a lifetime of this magnitude with our instrumentation.

4.3 Experimental

4.3.1 Synthesis of $K_2[Ru(NN')(CN)_4]$ Salts

4.3.1.1 General

3-(2-Pyridyl)pyrazole[47] was prepared according to the previously published methods. MeOH:H_2O solutions were purged with nitrogen for *approx*. 30 min before the addition of reagents. Potassium hexacyanoruthenate was dried *in vacuo* and flushed with N_2 prior to use. Solid State UV (i.e. crystals grinded up and sandwiched between two microscope slide covers), show a weak and broad double hump at approx. 500 – 300 nm corresponding to the MLCT.[48]

$K_2[Ru(bipy)(CN)_4]$

2,2-bipyridine (150 mg, 0.96 mmol) and Potassium hexacyanoruthenate (450 mg, 1.1 mmol) were combined in a 1:1 methanol:water solution (60 ml in total) at pH 3.5 (made from stock solution of 1:1 methanol:water with 5 drops of conc. H_2SO_4 per 100 ml total of solution). The reaction was stirred and refluxed at 120 °C for 3 days to leave an intense orange solution. After cooling to room temperature, the reaction mixture was neutralised to pH 7 with K_2CO_3, and the solvent was removed *in vacuo*. The remaining residue was taken up in the minimum amount of water, and methanol added until all unreacted $K_4[Ru(CN)_6]$ had crashed out. This was filtered through celite and washed with methanol. The filtrate was removed and the residue dissolved in the minimum amount of water. Acetone was then added to generate a yellow precipitate. The mixture was then filtered through celite, and the solid obtained by washing through with water. Removal of the solvent and drying gave $K_2[Ru(2,2\text{-}bipy)(CN)_4]$ as an orange powder in 82 % yield (345 mg). ES-MS (Negative ion, low cone voltage) [assignment]: 363 $[Ru(2,2'\text{-}bipy)(CN)_4H]^-$; 401 $[(Ru(2,2'\text{-}bipy)(CN)_4)K]^-$;. ^1H NMR (D_2O): δ 9.15 (2H, d, *J* 5.2, H^1), 8.22 (2H, d, *J* 7.9, H^4), 7.91 (2H, t, *J* 14.7, 7.3, H^3), 7.47 (2H, t, *J* 13.1, 6.6, H^2).

$K_2[(Phen)Ru(CN)_4]\cdot 4H_2O$

This was made in identical fashion to above with 1,10-phenanthroline (Phen) replacing bipy. Following a three day reflux, the product was obtained in 49 % yield as an orange powder. MS E/S (negative ion) [assignment]: 387 $[(Phen)Ru(CN)_4H]^-$. ^1H NMR (D_2O): 9.44 (2H, dd, *J* 1.4, 5.1, $H^{2,9}$); 8.30 (2H, dd, *J* 1.4, 8.4, $H^{4,7}$); 7.75 (2H, dd, *J* 5.2, 8.2, $H^{3,8}$); 7.64 (2H, s, $H^{5,6}$). IR υ_{CN}: 2037 (s), 2089 (w) cm^{-1}.

4.3.2 Synthesis of Ru(II)-Ln(III) Complexes

D_2O solutions of $K_2[Ru(2,2'\text{-bipy})(CN)_4]$ and lanthanide chloride hydrate (Ln = Pr, Nd, Gd, Er, Yb) in a 2:1 ratio (typically 30-40 mg of Ru-bipy reagent), were combine and the KCl precipitate filtered through celite. Slow evaporation of the filtrate over a period of 2 – 3 weeks, resulted in a crop of crystals in varying yields up to 80%; which were filtered off and air-dried.

Elemental analyses in all cases indicated the presence of several lattice water molecules in addition to the expected water ligands coordinated to the Ln^{3+} centres, in agreement with the crystal structures, although in some cases the number of water molecules detected by analysis was less than found in the crystal structure, indicating partial loss of lattice water molecules on drying the crystals. Note that it is unfeasible to suggest which waters are deuterated 100%, 50% or not at all, and so all water hydrogens have been suggested as non-deuterated. Yields were not optimised as we had found in earlier studies that allowing such solutions to evaporate too near to dryness resulted in a mixture of crystalline materials.[21]

$[\{Ru(bipy)(CN)_4\}_2\{Pr(H_2O)_7\}\{K(H_2O)_4\}]\cdot 7H_2O$.

Found: C, 27.7; H, 3.9; N, 13.2%. Calculated: C, 27.4; H, 4.3; N, 13.7%. (Crystal structure has $10H_2O$). IR (ν, cm^{-1}): 3343 (br, s), 2485 (br, w), 2113 (w), 2037 (s), 1600 (m), 1468 (m), 1444 (m), 1428 (m), 1312 (w), 1242 (w), 1157 (w), 763 (s), 734 (m).

$[\{Ru(bipy)(CN)_4\}_2\{Er(H_2O)_6\}\{K(H_2O)_4\}]\cdot 4H_2O$.

Found: C, 28.2; H, 3.4; N, 14.1%. Calculated: C, 28.5; H, 3.8; N, 14.2%. (Crystal structure has $5H_2O$). IR (ν, cm^{-1}): 3380 (br, s), 2501 (br, m), 2097 (m), 2040 (s), 1599 (m), 1468 (m), 1441 (m), 1421 (m), 1311 (w), 1242 (w), 1152 (w), 763 (s), 733 (m).

$[\{Ru(bipy)(CN)_4\}_3\{Nd(H_2O)_4\}_2]\cdot 11H_2O$.

Found: 29.3; H, 3.3; N, 14.7%. Calculated: 29.4; H, 3.6; N, 14.7%. IR (ν, cm^{-1}): ≈ 3600 (sh), 3290 (br, m), 2100 (m), 2046 (s), 1599 (m), 1468 (m), 1444 (m), 1421 (m), 1312 (w), 1241 (w), 766 (s), 732 (m).

$[\{Ru(bipy)(CN)_4\}_3\{Gd(H_2O)_4\}_2]\cdot 10H_2O$.

Found: 28.6; H, 3.2; N, 14.2%. Calculated: 29.0; H, 3.6; N, 14.5%. (Crystal structure has $11H_2O$). IR (ν, cm^{-1}): ≈ 3600 (sh), 3290 (br, m), 2100 (m), 2046 (s), 1599 (m), 1468 (m), 1444 (m), 1421 (m), 1312 (w), 1242 (w), 766 (s), 732 (m).

4.3.3 Synthesis of Cr(III)-Ln(III) Complexes

D_2O solutions of $K_3[Cr(CN)_6]$ and lanthanide chloride hydrate (Ln = Nd, Gd, Yb) were combined in a 1:1 ratio (30 mg of Cr(III) reagent), and slow evaporation of the solution over a period of 2–3 weeks, resulted in a thick opaque deposit containing a few colourless single crystals of the formulae $[Cr(CN)_6][Ln(H_2O)_2]\cdot H_2O$.

D_2O solutions of $K_3[Cr(CN)_6]$ and DMF solutions of lanthanide nitrate hydrate (Ln = Nd, Gd, Yb) were combined in a 1:1 ratio (30 mg of Cr(III) reagent), and slow evaporation of the solution over a period of 2–3 weeks, resulted in a crop of yellow plate-like single crystals of the formulae $[Cr(CN)_6][Ln(DMF)_4(H_2O)_2]\cdot H_2O$. Again, it is unfeasible to suggest which waters are deuterated 100%, 50% or not at all, and so all water hydrogens have been suggested as non-deuterated.

$[Cr(CN)_6][Gd(H_2O)_2]\cdot H_2O$

50 mg (0.15 mmol) of $K_3[Cr(CN)_6]$ and 56 mg (0.15 mmol) of $GdCl_3\cdot 6H_2O$ were combined in D_2O (10 ml) and the solution allowed to slowly evaporate in a foil-covered sample vial. After several weeks an opaque deposit was formed which contained a one or two thin long crystals which were suitable for X-Ray studies.

$[Cr(CN)_6][Yb(H_2O)_2]\cdot H_2O$

Made in identical fashion the Gd(III) analogue using 50 mg (0.15 mmol) of $K_3[Cr(CN)_6]$ and 58 mg (0.15 mmol) of $YbCl_3\cdot 6H_2O$.

$[Cr(CN)_6][Nd(DMF)_4(H_2O)_2]\cdot H_2O$

30.2 mg (0.093 mmol) of $K_3[Cr(CN)_6]$ was dissolved in D_2O (4 ml) and combined with a solution of 40.7 mg (0.093 mmol) of $Nd(NO_3)_3\cdot 6H_2O$ in DMF (1 ml). The resultant solution was allowed to slowly evaporate in a foil-covered sample vial open to air. After several weeks yellow plate-like crystals appeared to give the product in 42 % yield. Found: C, 30.8; H, 4.8; N, 19.8%. $[Cr(CN)_6][Nd(DMF)_4(H_2O)_2]\cdot H_2O$ requires: C, 30.9; H, 4.9; N, 20.1%.

$[Cr(CN)_6][Yb(DMF)_4(H_2O)_2]\cdot H_2O$

Made in identical fashion to the Nd(III) analogue with $Yb(NO_3)_3\cdot 6H_2O$, giving yellow plate-like crystals in 47 % yield. Found: C, 29.6; H, 4.6; N, 18.9%. $[Cr(CN)_6][Nd(DMF)_4(H_2O)_2]\cdot H_2O$ requires: C, 29.7; H, 4.7; N, 19.3%.

Complex	**$[\{Ru(bipy)(CN)_4\}_2\{Pr(H_2O)_7\}\{K(H_2O)_2\}]\cdot 9H_2O$**	**$[\{Ru(bipy)(CN)_4\}_2\{Er(H_2O)_6\}\{K(H_2O)_4\}]\cdot 4H_2O$**
Empirical formula	$C_{14}H_{29}K_{0.50}N_6O_{10.50}Pr_{0.50}Ru$	$C_{56}H_{92}K_2N_{24}O_{30}Er_2Ru_4$
Formula weight	640.51	2398.54
Temperature	150(2)K	150(2) K
Crystal system	Monoclinic	Tetragonal
Space group	$P2_1/m$	$Pca2_1$
a /Å	9.006(2)	17.226(13)
b /Å	29.787(7)	29.365(2)
c /Å	9.505(2)	17.2263(13)
α /°	90	90
β /°	115.048(4)	90
γ /°	90	90
Volume /Å^3	2310.0(10)	8713.9(9)
Z	4	4
Density (calculated) / Mg/m^3	1.842	1.828
Absorption coefficient / mm^{-1}	1.862	2.764
F(000)	1288	4744
Crystal size / mm	0.37 x 0.33 x 0.23	0.42 x 0.40 x 0.40
θ range for data collection	1.37 to 27.60°	1.37 to 27.53°
Reflections collected	26223	96089
Independent reflections	5376 [R(int) = 0.1236]	19724 [R(int) = 0.1230]
Completeness to θ	98.5 %	99.5 %
Data / restraints / parameters	5376 / 0 / 281	19724 / 1 / 1064
Goodness-of-fit on F^2	S = 1.057	1.031
R indices [for reflections with $I>2\sigma(I)$]	$R_1 = 0.0631$, $wR_2 = 0.1733$	$R_1 = 0.0393$, $wR_2 = 0.1029$
R indices (for all data)	$R_1 = 0.0866$, $wR_2 = 0.1958$	$R_1 = 0.0445$, $wR_2 = 0.1062$
Largest diff. peak and hole	4.151 and -2.348 eÅ^{-3}	2.187 and -2.198 e.Å^{-3}

Table 4A Crystallographic Data for the Complexes of Chapter 4

Complex	**$[\{Ru(bipy)(CN)_4\}_3\{Nd(H_2O)_4\}_2]\cdot 11H_2O$**	**$[\{Ru(bipy)(CN)_4\}_3\{Gd(H_2O)_4\}_2]\cdot 10H_2O$**
Empirical formula	$C_{42}H_{24}N_{18}O_{19}Nd_2Ru_3$	$C_{42}H_{24}N_{18}O_{19}Gd_2Ru_3$
Formula weight	1676.48	1722.66
Temperature	150(2)K	150(2) K
Crystal system	Monoclinic	Monoclinic
Space group	$P2_1/c$	$P2_1/c$
a /Å	15.0504(14)	14.9452(11)
b /Å	13.7872(13)	13.7769(10)
c /Å	29.790(3)	29.611(2)
α /°	90	90
β /°	104.599(2)	104.3020(10)
γ /°	90	90
Volume /$Å^3$	5982.0(10)	5907.9(8)
Z	4	4
Density (calculated) / Mg/m^3	1.861	1.937
Absorption coefficient / mm^{-1}	2.527	3.047
F(000)	3224	3336
Crystal size / mm	0.36 x 0.34 x 0.32	0.23 x 0.14 x 0.08
θ range for data collection	1.40 to 27.57°	1.41 to 27.56°
Reflections collected	66457	67374
Independent reflections	13644 [R(int) = 0.0405]	13563 [R(int) = 0.2392]
Completeness to θ	98.7 %	99.2 %
Data / restraints / parameters	13644 / 0 / 794	13563 / 0 / 746
Goodness-of-fit on F^2	S = 1.042	0.941
R indices [for reflections with $I>2\sigma(I)$]	$R_1 = 0.0290$, $wR_2 = 0.0762$	$R_1 = 0.0567$, $wR_2 = 0.1232$
R indices (for all data)	$R_1 = 0.0403$, $wR_2 = 0.0798$	$R_1 = 0.1119$, $wR_2 = 0.1450$
Largest diff. peak and hole	0.951 and -0.809 $eÅ^{-3}$	1.617 and -1.886 $e.Å^{-3}$

Table 4B Crystallographic Data for the Complexes of Chapter 4

Complex	**$[\{Ru(bipy)(CN)_4\}_3\{Pr(H_2O)_4\}\{Pr(H_2O)_4\}]\cdot 10H_2O$**	**$K_2[Ru(phen)(CN)_4]\cdot 4H_2O$**
Empirical formula	$C_{42}H_{38}N_{18}O_{19}Pr_2Ru_3$	$C_{16}H_{16}N_6K_2O_4Ru$
Formula weight	1683.93	535.62
Temperature	150(2)K	150(2) K
Crystal system	Monoclinic	Monoclinic
Space group	$P2_1/n$	Cc
a /Å	15.0905(13)	10.291(16)
b /Å	13.8011(11)	30.116(5)
c /Å	29.895(3)	6.6628(11)
α /°	90	90
β /°	104.4530(10)	101.862(3)
γ /°	90	90
Volume /$Å^3$	6026.7(9)	2020.9(6)
Z	4	4
Density (calculated) / Mg/m^3	1.856	1.760
Absorption coefficient / mm^{-1}	2.402	1.224
F(000)	3272	1072
Crystal size / mm	0.38 x 0.34 x 0.30	0.20 x 0.10 x 0.10
θ range for data collection	1.39 to 27.55°	1.35 to 27.54°
Reflections collected	66944	11718
Independent reflections	13739 [R(int) = 0.0335]	4539 [R(int) = 0.0847]
Completeness to θ	98.9 %	99.4 %
Data / restraints / parameters	13739 / 2 / 754	4539 / 63 / 281
Goodness-of-fit on F^2	S = 1.050	0.903
R indices [for reflections with $I>2\sigma(I)$]	$R_1 = 0.0284$, $wR_2 = 0.0760$	$R_1 = 0.0548$, $wR_2 = 0.1051$
R indices (for all data)	$R_1 = 0.0360$, $wR_2 = 0.0791$	$R_1 = 0.1008$, $wR_2 = 0.1191$
Largest diff. peak and hole	1.178 and -1.133 $eÅ^{-3}$	1.021 and -0.983 $e.Å^{-3}$

Table 4C Crystallographic Data for the Complexes of Chapter 4

Complex	**$[\{Cr(CN)_6\}\{Gd(H_2O)_2\}]\cdot H_2O$**	**$[\{Cr(CN)_6\}\{Yb(H_2O)_2\}]\cdot H_2O$**
Empirical formula	$C_{1.50}H_2N_{1.50}OGd_{0.25}Cr_{0.25}$	$C_{1.50}H_2N_{1.50}OYb_{0.25}Cr_{0.25}$
Formula weight	109.36	113.31
Temperature	150(2)K	150(2) K
Crystal system	Orthorhombic	Orthorhombic
Space group	Cmcm	Cmcm
a /Å	7.5491(11)	7.4572(17)
b /Å	13.0374(19)	12.948(3)
c /Å	14.022(2)	13.898(3)
α /°	90	90
β /°	90	90
γ /°	90	90
Volume /$Å^3$	1380.1(4)	1341.9(5)
Z	16	16
Density (calculated) / Mg/m^3	2.105	2.243
Absorption coefficient / mm^{-1}	5.565	7.750
F(000)	824	848
Crystal size / mm	0.09 x 0.07 x 0.07	0.30 x 0.10 x 0.10
θ range for data collection	2.91 to 27.45°	2.93 to 27.51°
Reflections collected	4147	7581
Independent reflections	882 [R(int) = 0.0466]	863 [R(int) = 0.0449]
Completeness to θ	99.2 %	99.1 %
Data / restraints / parameters	882 / 3 / 51	863 / 0 / 61
Goodness-of-fit on F^2	S = 1.044	1.138
R indices [for reflections with $I>2\sigma(I)$]	$R_1 = 0.0242$, $wR_2 = 0.0495$	$R_1 = 0.0179$, $wR_2 = 0.0379$
R indices (for all data)	$R_1 = 0.0291$, $wR_2 = 0.0509$	$R_1 = 0.0205$, $wR_2 = 0.0385$
Largest diff. peak and hole	0.663 and -0.857 $eÅ^{-3}$	1.065 and -0.697 $e.Å^{-3}$

Table 4D Crystallographic Data for the Complexes of Chapter 4

Complex	**[{Cr(CN)$_6$}{Nd(H$_2$O)$_2$(DMF)$_4$}]·H$_2$O**	**[{Cr(CN)$_6$}{Yb(H$_2$O)$_2$(DMF)$_4$}]·H$_2$O**
Empirical formula	$C_{18}H_{34}N_{10}CrO_7Nd$	$C_{18}H_{34}N_{10}CrO_7Yb$
Formula weight	698.79	727.59
Temperature	150(2)K	150(2) K
Crystal system	Monoclinic	Monoclinic
Space group	$P2_1/n$	$P2_1/n$
a /Å	13.2206(13)	13.0556(11)
b /Å	12.9636(14)	12.7471(11)
c /Å	18.8369(19)	18.9654(16)
α /°	90	90
β /°	109.538(2)	109.8590(10)
γ /°	90	90
Volume /Å^3	3042.5(5)	2968.5(4)
Z	4	4
Density (calculated) / Mg/m^3	1.526	1.628
Absorption coefficient / mm^{-1}	2.095	3.548
F(000)	1408	1448
Crystal size / mm	0.17 x 0.16 x 0.08	0.25 x 0.23 x 0.11
θ range for data collection	1.65 to 27.55°	1.66 to 27.53°
Reflections collected	34153	33128
Independent reflections	6963 [R(int) = 0.3163]	6779 [R(int) = 0.0487]
Completeness to θ	99.1 %	99.1 %
Data / restraints / parameters	6963 / 10 / 364	6779 / 0 / 364
Goodness-of-fit on F^2	S = 0.910	0.981
R indices [for reflections with I>2σ(I)]	$R_1 = 0.0681$, $wR_2 = 0.1458$	$R_1 = 0.0292$, $wR_2 = 0.0652$
R indices (for all data)	$R_1 = 0.1151$, $wR_2 = 0.1674$	$R_1 = 0.0413$, $wR_2 = 0.0690$
Largest diff. peak and hole	1.871 and -4.251 eÅ^{-3}	2.136 and -1.025 e.Å^{-3}

Table 4E Crystallographic Data for the Complexes of Chapter 4

4.4. References

1. N. M. Shavaleev, G. Accorsi, D. Virgili, Z. R. Bell, T. Lazarides, G. Calogero, N. Armaroli, M. D. Ward, *Inorg. Chem*., 2005, **44**, 61.
2. S. I. Klink, H. Keizer, F. C. J. M. van Veggel, *Angew. Chem. Int. Ed*., 2000, **39**, 4319.
3. N. M. Shavaleev, Z. R. Bell, M. D. Ward, *Dalton Trans*., 2002, 3925.
4. N. M. Shavaleev, L. P. Moorcraft, S. J. A. Pope, Z. R. Bell, S. Faulkner, M. D. Ward, *Chem. Commun*., 2003, 1134.
5. N. M. Shavaleev, L. P. Moorcraft, S. J. A. Pope, Z. R. Bell, S. Faulkner, M. D. Ward. *Chem. Eur. J*., 2003, **9**, 5283.
6. A. Beeby, R. S. Dickins, S. FitzGerald, L. J. Govenlock, D. Parker, J. A. G. Williams, C. L. Maupin, J. P. Riehl, G. Siligardi, *Chem. Commun*., 2000, 1183.
7. S. J. A. Pope, B. J. Coe, S. Faulkner, E. V. Bichenkova, X. Yu, K. T. Douglas, *J. Am. Chem. Soc*., 2004, **126**, 9490.
8. P. B. Glover, P. R. Ashton, L. J. Childs, A. Rodger, M. Kercher, R. M. Williams, L. De Cola, Z. Pikramenou, *J. Am. Chem. Soc*., 2003, **125**, 9918.
9. G. M. Davies, S. J. A. Pope, H. Adams, S. Faulkner, M. D. Ward, *Inorg. Chem.*, 2005, **44**, 4656.
10. H. Adams, W. Z. Alsindi, G. M. Davies, M. B. Duriska, T. L. Easun, H. E. Fenton, J. –M. Herrera, M. W. George, K. L. Ronayne, X. -Z. Sun, M. Towrie, M. D. Ward, *Dalton Trans*., 2006, 39.
11. T. L. Lazarides, G. M. Davies, S. J. A. Pope, H. Adams, S. Faulkner, M. D. Ward, *Manuscript in Preparation.*
12. C. A. Bignozzi, C. Chiorboli, M. T. Indelli, M. A. Rampi Scandola, G. Varani, F. Scandola, *J. Am. Chem. Soc*., 1986, **108**, 7872.
13. N. Simpson. *Ph. D Thesis*, University of Bristol, 2001.
14. K. K. Klausmeyer, S. R. Wilson, T. B. Rauchfuss, *J. Am. Chem. Soc*., 1999, **121**, 2705.
15. M. L. Kuhlman, T. B. Rauchfuss, *J. Am. Chem. Soc*., 2003, **125**, 10084.
16. S. M. Contakes, T. B. Rauchfuss, *Chem. Commun*., 2001, 553.
17. J. Hu, L. J. Barbour, G. W. Gokel, *J. Am. Chem. Soc*., 2001, 123, 9486.

18. G. W. Gokel, *Chem. Commun*., 2003, 2847.
19. J. Hu, G. W. Gokel, *Chem. Commun*., 2003, 2536.
20. S. M. Contakes, T. B. Rauchfuss, *Angew. Chem. Int. Ed*., 2000, **39**, 1984
21. T. A. Miller, J. C. Jeffery, M. D. Ward, H. Adams, S. J. A. Pope, S. Faulkner, *Dalton Trans*., 2004, 1524.
22. T. Miller, *Ph. D Thesis*, University of Bristol, 2004.
23. D. Parker, J. A. G. Williams, *J. Chem. Soc. Dalton. Trans.,* 1996, 3613.
24. N. R. M. Simpson, M. D. Ward, A. F. Morales, F. Barigelletti, *J. Chem. Soc., Dalton Trans*., 2002, 2449.
25. (a) N. Sabbatini, M. Guardigli, J. –M. Lehn, Coord. Chem. ReV. 1993, 123, 201; (b) N. Armaroli, G. Accorsi, F. Barigelletti, S. M. Couchman, J. S. Fleming, N. C. Harden, J. C. Jeffery, K. L. V. Mann, J. A. McCleverty, L. H. Rees, S. R. Starling, M. D. Ward, *Inorg. Chem*., 1999, **38**, 5769.
26. A. Beeby, S. Faulkner, *Chem. Phys. Lett.*, 1997, **266**, 116.
27. G. M. Davies, R. J. Aarons, G. R. Motson, J. C. Jeffery, H. Adams, S. Faulkner, M. D. Ward, *Dalton Trans*., 2004, 1136.
28. G. M. Davies, H. Adams, S. J. A. Pope, S. Faulkner, M. D. Ward, *Photochem. Photobiol. Sci*., 2005, **4**, 829.
29. M. A. Semenov, B. I. Sukhorukov, V. I. A. Maleev, L. I. Shabarchina*, Biofizika,* 1979, **24**, 210.
30. M. Kovàcs, A. Horvàth, *Inorg. Chim. Acta*., 2002, **335**, 69.
31. F. W. Robinson, *J. Chem. Soc. Trans*., 1909, **95**, 1353.
32. (a) C. James, P. S. Willand, *J. Am. Chem. Soc*., 1916, **38**, 1497; (b) F. Hulliger, M. Landolt, H. Vetsch, *J. Solid State Chem*., 1976, **18**, 307; (c) Y. Yukawa, S. Igarashi, T. Kawaura, H. Miyamoto, *Inorg. Chem*., 1996, **35**, 7399.
33. (a) W. Xiaoyu, Y. Yukawa, Y. Masuda, *J. Alloy and Compounds*, 1999, **290**, 85; (b) D. F. Mullica, W. O. Milligan, R. L. Garner, *Acta Cryst*. 1980, B**36**, 2561.
34. D. F. Mullica, P. K. Hayward, E. L. Sappenfield, *Inorg. Chim. Acta*., 1996, **244**, 273.
35. F. Hulliger, M. Landolt, H. Vetsch*. J. Solid State Chem*., 1976, **18**, 283.

36. W. E. Bailey, R. J. Williams, W. O. Milligan, *Acta. Cryst*. 1973, B**29**, 1365.
37. Y. Seto, K. Umemto, T. Arii, Y. Masuda, *J. Therm. Anal. Cal*., 2004, **76**, 165.
38. T. Otsuka, N. Takahashi, N. Fujigasaki, A. Sekine, Y. Ohashi, Y. Kaizu, *Inorg. Chem*., 1999, **38**, 1340.
39. I. Fujita, H. Kobayashi, *J. Chem. Phys*., 1973, **59**, 2902.
40. (a) C. A. Bignozzi, O. Bortolini, C. Chiorboli, M. T. Indelli, M. A. Rampi, F. Scandola, *Inorg. Chem*., 1992, **31**, 172; (b) C. A. Bignozzi, M. T. Indelli, F. Scandola, *J. Am. Chem. Soc*., 1989, **111**, 5192.
41. M. Cantuel, G. Bernardinelli, D. Imbert, J. –C. G. Bünzli, G. Hopfgartner, C. Piguet, *J. Chem. Soc., Dalton Trans*., 2002, 1929.
42. D. Imbert, M. Cantuel, J. –C. G. Bunzli, G. Bernardinelli, C. Piguet, *J. Am. Chem. Soc*., 2003, **125**, 15698.
43. M. A. Subhana, H. Nakatab, T. Suzukia, J. -H. Choia, S. Kaizaki, *J. Lumin*., 2003, **101**, 307.
44. T. Sanada, T. Suzuki, T. Yoshida, S. Kaizaki, *Inorg. Chem*., 1998, **37**, 4712.
45. R. A. Combs, J. M. Farmer, J. A. Kautz, *Acta. Cryst*. 2000, C**56**, 1420.
46. A. Figuerola, C. Diaz, M. S. E. Fallah, J. Ribas, M. Maestro, J. Mahia, *Chem. Commun*., 2001, 1204.
47. P. L. Jones, A. J. Amoroso, J. C. Jeffery, J. A. McCleverty, E. Psillakis, L. H. Rees, and M. D. Ward, *Inorg. Chem*., 1997, **36**, 10.
48. H. Zeng, M. Kira, Y. Segawa, *J. Phys. B: At. Mol. Opt. Phys*., 1999, **32** L225.

A. Bravais

W. Röntgen

W. Wein

M. von Laue

X-ray Crystallography

History, Theory and Technique

P. Ewald

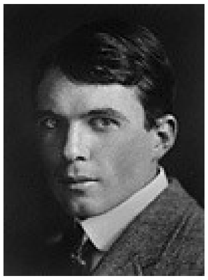

W. Bragg

D. Hodgkin

5.1 Introduction

The application of X-rays to chemistry has enabled us to look into the interior of a molecule, in the solid state, and find out an overwhelming amount of structural information. This chapter discusses the subject of X-ray crystallography, illustrating the theoretical aspects of the relationship with molecules, and the modern day practical procedures themselves that have been undertaken in this thesis. It has been compiled with the aid of several references[1] and websites,[2] and some miscellaneous crystal structures solved by the author are included at the end of the chapter.

5.2 The History

5.2.1 Into Perspective

Today, due to the advancing of computers, the solving of a crystal structure has become relatively routine. The discoveries made by Dorothy Crowfoot Hodgkin offer a stark reminder of how complicated the process actually was: whilst having solved the structures of Penicillin (1945) and Vitamin-B_{12} (1956, **Fig. 5.2.1**), she is mainly credited with solving the structure of Insulin (a 777-atom hormone essential to the efficient metabolism of carbohydrates) a feat which took her 34 years to achieve (1935-1969). The work helped to show how the hormone suppresses the symptoms of diabetes, and such was the value of her work that she was recognised with the Nobel Prize for Chemistry in 1964.

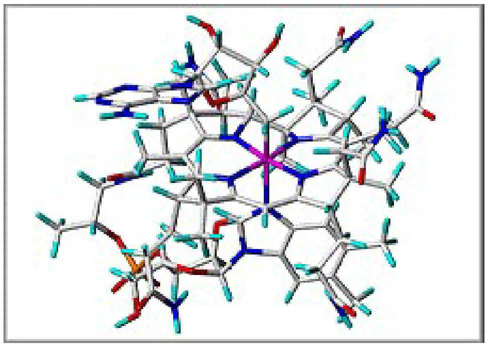

Fig. 5.2.1 - Crystal structure of vitamin B_{12}

5.2.2 In the Beginning…

Whilst it is mainly Laue (1912) and Bragg (1915) that are associated with the application of X-rays to crystallography, there are three other previous events that also play their part:

1890: *The work of Fedorov and Schonflies shows that atoms and molecules in a crystal are arranged in a geometrical pattern with perfect regularity. They calculate that the spacing of such patterns must be in the orders of* 10^{-8} *cm;* **1895:** *X-radiation is observed for the first time on the evening of November 8th when Wilhelm Röntgen observes fluorescence upon discharging cathode rays onto a barium platinocyanide plate. He is later to be awarded the first Nobel Prize for physics in 1901;* **1900:** *Wilhelm Wien uses early quantum theory to deduce that X-rays are a wave phenomena, and suggests they are a form of electromagnetic radiation with wavelengths of* 10^{-9}–10^{-10} *cm.*

The spacing of molecules within a crystal was now seen to be comparable with the wavelengths of X-rays. Later, Max von Laue realised that in a crystal, Nature had provided a perfect diffraction grating for X-rays, and in 1912 Laue and his co-workers; Friedrich and Knipping successfully passed a narrow X-ray beam through a crystal of zinc sulphide to obtain a regular diffraction pattern. Subsequent calculations proved there to be a relationship between the diffraction spots and the symmetry of the underlying crystal. However, only a certain number of the diffraction spots expected for the crystal's symmetry were observed on the photographic plate. Laue hypothesised the X-ray beam contained specific wavelengths and that a diffracted beam only appeared when a certain criteria were met. The work earned him a Nobel Prize in physics (1914).

5.3 The Theory

5.3.1 The Bragg Equation

Points in a crystal lattice can be arranged in series of parallel planes, and in 1915 William L. Bragg suggested that X-Ray diffraction was a reflection of the X-Rays from the planes of the crystal lattice (with the angle of incidence being equal to that of reflection). He later surmised that waves scattered from adjacent lattice planes will be in phase (i.e. the difference in the paths travelled by these waves will be an integral multiple of the wavelength, $n\lambda$) giving rise to constructive interference.

$$n \lambda = 2 d \sin\theta \qquad \textbf{Eq. 5.1}$$

This relationship is summarised as the famous Bragg equation (**Eq. 5.1**), which has become fundamental to the field of modern crystallography winning both Bragg, and his father, the Nobel Prize that year (**Fig. 5.3.1**). Constructive interference accompanies an observable intensity, and because the glancing angle θ corresponds to this intensity, **d** may then be calculated which can in turn be used to derive the unit cell dimensions and crystal symmetry.

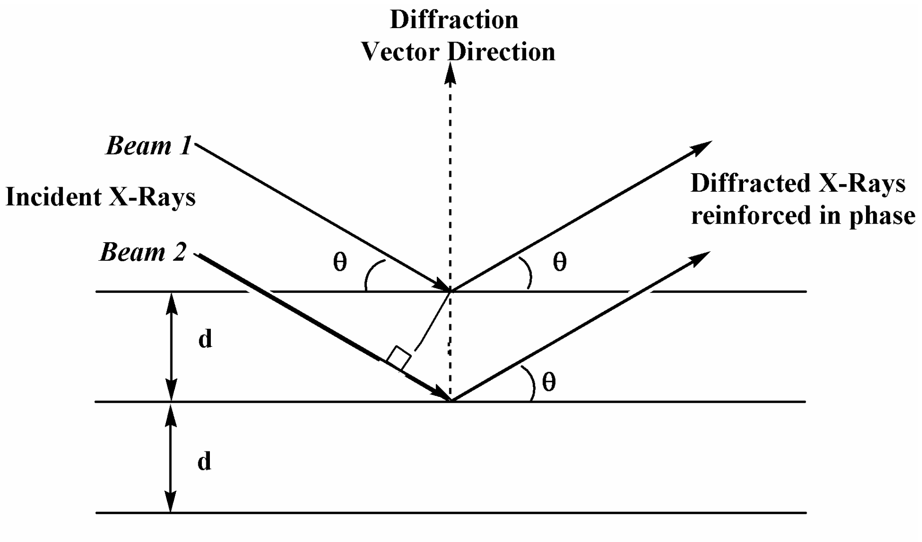

Fig. 5.3.1 - Diffraction between planes of atoms (where d is the perpendicular distance between the lattice planes in the crystal and θ is the angle of incidence of the X-ray beam)

5.3.2 The Generation of X-rays

X-rays are produced whenever matter (for our purposes, a copper or molybdenum anode) is irradiated with a beam of high-energy charged electrons. The interaction is so intense, that an inner orbital electron of the atomic matter is displaced; and an electron from an outer orbital will fall to replace the displaced electron. As energy must be conserved, this results in the generation of an X-ray equal in energy to the energy of the transition.

Fig. 5.3.2 shows the ejected electron is from the K-shell: if the replacement electron comes from the L-shell (i.e. orbital of principal quantum number, n = 2), a strong Kα X-ray is produced; if it is the M-shell (n = 3), a weaker Kβ X-ray is produced.

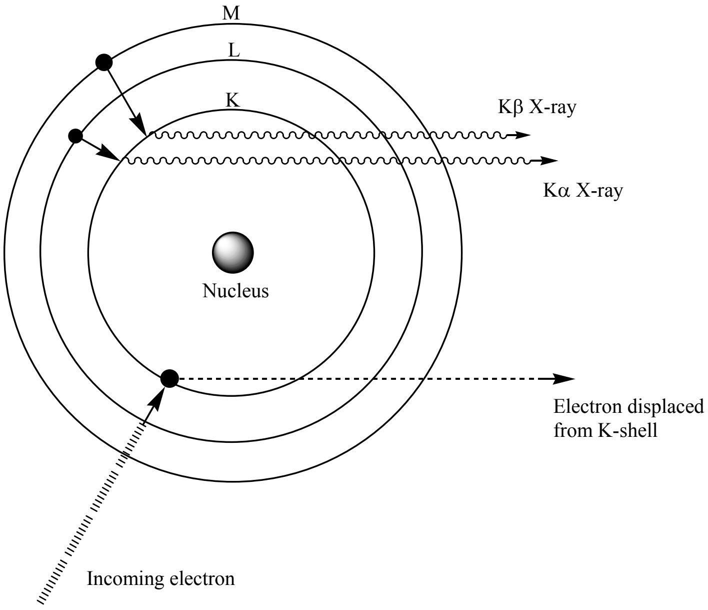

Fig. 5.3.2 - X-ray generation from a copper source

The Kα radiation is of the highest intensity and is therefore used in standard X-ray diffraction work. The availability of conventional sources limits us to using mainly copper or molybdenum metal targets whose Kα transitions generate X-rays with wavelengths of 1.5 and 0.7 Å respectively.

Both Kα and Kβ transitions occur to different extents, and passing the radiation through suitable materials that absorb Kβ radiation can give rise to monochromatic Kα beams. This is an important process as the X-rays used in crystallography need to be as monochromatic as possible, in order to obtain accurate unit cell dimensions (see later). The filtering process works on the basis that the photons emitted upon Kβ emission of the anode have the wavelength corresponding to the energy necessary to eject an electron from the K orbital of the filter's atoms, with the effect that the unwanted Kβ radiation is effectively absorbed without reducing the intensity of the desired Kα radiation. Generally, an element close in atomic number is used as a filter, for example copper anodes (Z = 29) use a nickel filter (Z = 28) and molybdenum anodes (Z = 42) use a zirconium (Z = 40) or Niobium (Z = 41) filter.

5.3.3 The Unit Cell and the Crystal Lattice

Any perfectly crystalline solid material will consist of an effectively infinite number of molecules, arranged in a very precise, regular array in 3-dimensions throughout the crystal. This network is in fact, the repetition of an individual structural unit, known as the *unit cell*, which is a parallelepiped (a solid six-sided block) that contains all the symmetry elements needed to regenerate the whole three dimensional pattern. The contents of the unit cell can be a single atom, molecule, or even an assembly of molecules.

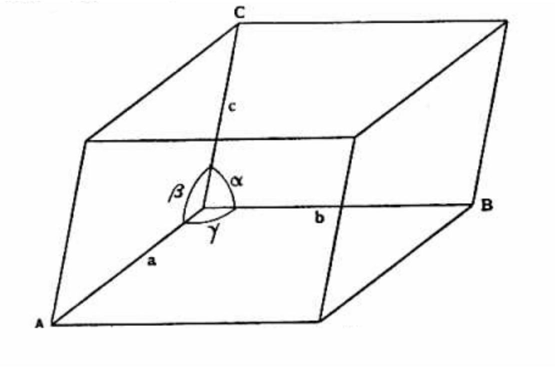

Fig. 5.3.3 - The unit cell

Unit cells are designated by six parameters (**Fig. 5.3.3**): axis length a, b, c; and angles α, β, γ, such that where the angle between a and b is γ, a and c is β, and b and c is α. Symmetry operations impose restrictions upon the values these parameters can take, and we find that because of these restrictions, crystal symmetry is broadly divided into seven types of crystal system (**Table 5.3.1**).

Unit Cell	Edge Lengths	Internal Angles
Triclinic	$(a \neq b \neq c)$	$(\alpha \neq \beta \neq \gamma)$
Monoclinic	$(a \neq b \neq c)$	$(\alpha = \gamma = 90)$ $(\beta \neq 90)$
Orthorhombic	$(a \neq b \neq c)$	$(\alpha = \beta = \gamma = 90)$
Tetragonal	$(a = b \neq c)$	$(\alpha = \beta = \gamma = 90)$
Hexagonal	$(a = b \neq c)$	$(\alpha = \beta = 90)$ $(\gamma = 120)$
Rhombohedral	$(a = b = c)$	$(\alpha = \beta = \gamma \neq 90$
Cubic	$(a = b = c)$	$(\alpha = \beta = \gamma = 90)$

Table 5.3.1 - The seven crystal systems

By placing imaginary dots on the unit cell axes and performing symmetry operations, we can effectively generate a 3-dimensional arrangement of 'points' in real space, known as the crystal lattice. The concept of the lattice is important when diffraction by a crystal is considered, for the condition that must be met in valid lattice symmetry, is that the view in a given direction is the same from each lattice point.

Back in 1848, Auguste Bravais had determined that there were four types of lattice system that would satisfy these criteria, although not all are applicable to each of the seven types of unit cell (**Fig. 5.3.4**).

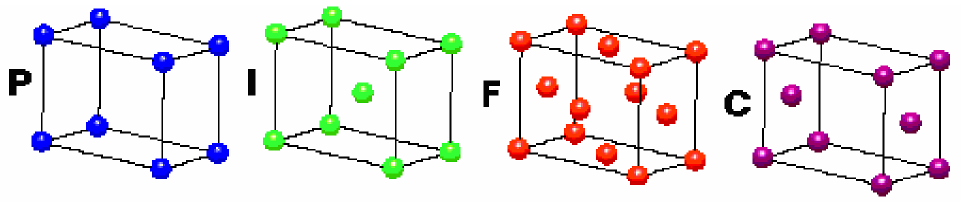

Fig. 5.3.4 – Lattice types

Primitive (P): The same environment is found only at each corner such that there will only be one lattice point per unit cell.

Non-Primitive (I, F, A, B, C): More than one lattice point will be found in the unit cell: *body-centred* (I), where the environments at each corner and the centre of the unit cell are the same; *face-centred* (F), where the environments at each corner and the centre of each face are the same; and finally *centred* (A, B, C) where equal environments are found at the corners, and at the centre of two opposing faces. Assignment of A, B, or C coincides with which two faces are bound (i.e. bound by the ac face gives B). Consequently, there are a total of 14 distinct Bravais lattices (**Table 5.3.2**).

Triclinic	P			
Monoclinic	P	C		
Orthorhombic	P	C	F	I
Tetragonal	P	I		
Hexagonal	P			
Rhombohedral	P			
Cubic	P	F	I	

Table 5.3.2 – The 14 Bravais Lattices

5.3.4 Symmetry and Space Groups

Further discussion of crystallography requires the introduction of the concept of symmetry. An object is said to be symmetrical if after some movement (*operation*) its orientation is indistinguishable from what it was initially. Such movements might include rotation about an axis; reflection in a plane; and inversion through a point. The entity to which the operation is performed (e.g. an axis or a plane) is called a *symmetry element*.

Such operations include: **Rotation -** This is a rotation of (360/n)° about a particular axis. If n = 2, then this means a two-fold rotation because rotating the object 180°, twice, will return it to it's original orientation; **Identity -** This is simply doing nothing to the object – every object has this symmetry operation; **Reflection -** This occurs across a mirror plane (plane of symmetry), converting a left-handed molecule into its right-handed isomer (or *vice versa*), such as changing a point from (x, y, z) to (x, -y, z);

Inversion - In this operation, with the origin of coordinates as the 'centre of inversion', every point (x, y, z) becomes (-x, -y, -z), and the final orientation is centrosymmetrically related to the initial one (i.e. related to the centre of inversion by symmetry). The same inversion operation can also be expressed as the successive performances of other symmetry operations. For example, a two-fold rotation about the **c-**axis, followed by reflection in the **ab** plane will give the same progression as a straight-forward inversion operation

All of the above symmetry operations can be combined in 3-dimensions in 32 ways to form the collective *crystallographic point groups*. But, there are also a few other point groups which are appropriate to other molecules that contain, for example, 5-fold axes.

5.3.5 Space Symmetry

The previous operations all share the same characteristic in that they leave at least one point within the object fixed (hence the name *point groups*). However, there are three more aspects of crystal symmetry which do not have this quality but are still valid symmetry operations.

Translation - This is motion in a straight line along a plane. Although all points in the molecule are translated to a different position in space, it is still in its original *orientation* and is an example of a *space symmetry operation.* Translational symmetry is highly probable in all crystals as a single crystal should contain molecules or atoms arranged in a regular array along successive planes.

Screw Axes - These are a combination of translation and rotation and are given the notation $\mathbf{n_r}$. They involve a rotation of (360/n)°, combined with a translation parallel to the rotation axis by the fraction r/n, such as a 2_1 screw axis involves a 180° rotation and a translation of ½ a unit cell. One or more repeat operations may be needed to bring the molecule back into its original orientation. Other types of screw axes are possible for higher symmetry crystal systems such as 3_1 and 3_2.

Glide Planes - This is the other space symmetry operation which uses translation. In this case reflection in a plane is followed by translation parallel to the plane. The glide plane is referred to as an a-glide, b-glide, or c-glide, depending if the translation is a/2, b/2 or c/2 respectively; or an n-glide if the translation is (a+b)/2, (a+c)/2 or (b+c)/2, - i.e. half way along one of the face diagonals. By default, the b-axis is set as the unique axis - in a monoclinic cell this is because the angle β is unique, and so in a monoclinic cell, it is possible to obtain a-, c- or n-glide planes.

In summary, symmetry operations come under two categories: proper and improper. The former employs a series of operations where more than one is needed to achieve the identity operation. The latter, on the other hand, achieves this with a single operation. The glide planes, screw axes, inversion, rotations and reflections described above can combine with respect to the 14 Bravais lattices to give the 230 possible space groups - the 230 ways that a molecule can arrange itself within a crystal system.

5.3.6 Systematic Absences

The effect of translation in a crystal lattice can have the effect of moving atoms into positions where destructive interference occurs in the diffraction pattern. This ‘systematic absence’ of reflections is easily observed in the data set, and is always considered when selecting the crystal’s space group.

In the case of a C-centred orthorhombic unit cell (**Fig. 5.3.5a**), diffraction from X-ray beams 1 and 2 will be in phase causing constructive interference and satisfying Braggs law. Meanwhile, a body-centred lattice (**Fig. 65.3.5b**) has an interpenetrating set of atoms midway between the other two planes. Therefore, the third X-ray beam is diffracted by this atom (unlike in the previous case).

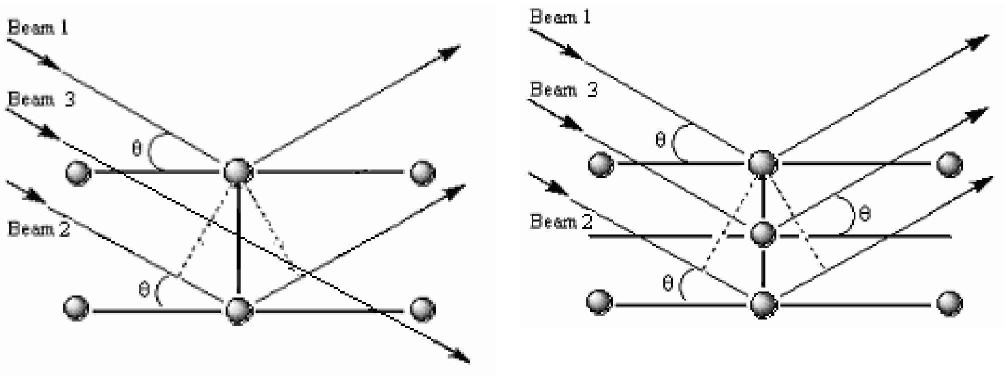

Fig. 5.3.5 – (a) Diffraction in a unit cell (Orthorhombic C-centred, *C*) and (b) Diffraction in a unit cell (Orthorhombic Body-centred *I*)

The path difference of this third diffracted X-ray will be half that of the other two and the net effect of this deflection is to cancel out that of an adjacent beam and no diffraction maxima is observed (i.e. the Bragg law is not satisfied at that particular index). This gives rise to some more limiting conditions for crystallographic lattices (**Table 5.3.3**), where n is any integer (positive, zero or negative), so 2n just means an even number and constructive interference. Thus, for example, for a reflection to be observed in a body-centred unit cell, the sum of all three indices must be even. If the sum is odd, the reflection is zero (i.e. absent).

Bravais Lattice	Absences	Observed intensity conditions
Primitive P	none	none
A-centred A	(0, k, l)	k + l = 2n
B-centred B	(h, 0, l)	h + l = 2n
C-centred C	(h, k, 0)	h + k = 2n
Body-centred I	(h, k, l)	h + k + l = 2n
Face centred F	(0, k, l); (h, 0, l); (h, k 0)	h, k, and l all even or odd

Table 5.3.3 – Systematic absences for centred unit cells

5.3.7 Reciprocal Space

In 1913, Peter Paul Ewald suggested a graphical method to explain the diffraction effects his fellow physicist Max von Laue was observing. This was, without him knowing it, a graphical method of solving the Bragg equation, and has since been used for interpreting diffraction patterns.

In order to do this we must approach the idea that our crystal lattice is, in fact, not real, and not in real space; But treat it as a 'reciprocal lattice' located in 'reciprocal space.' The distance between a stack of planes (d) in the real lattice is inversely related (i.e. the reciprocal of) to the position of a 'point' in reciprocal space. The spacing of different stacks of planes will thus generate a reciprocal lattice structure. Diffraction may now be understood in terms of the relative movement of the 'Ewald sphere' with respect to the reciprocal lattice.

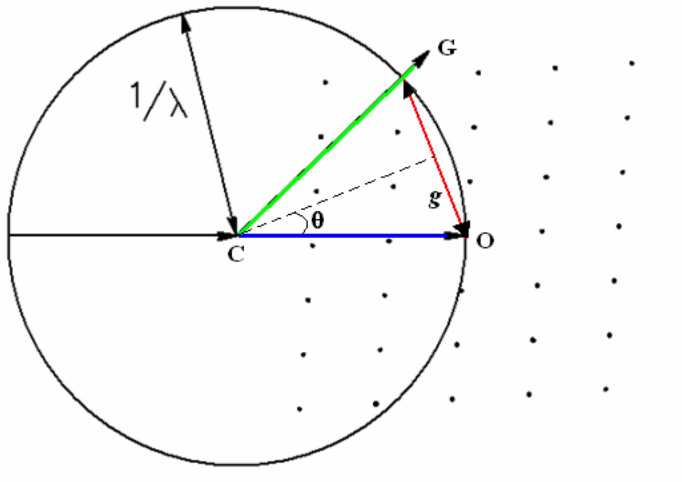

Fig. 5.3.6 – The Ewald sphere in reciprocal space

The Ewald sphere (**Fig. 5.3.6**) has a radius of 1/λ with the incident X-ray beam visualised as passing along its diameter. The origin of the reciprocal lattice is positioned at the point where the incident beam emerges from the sphere, O. Whenever a reciprocal lattice point touches the surface of the sphere, the conditions for a reflected beam (i.e. Braggs' equation) are satisfied.

From the two-dimensional diagram we can see that CO represents the incident beam and CG is a diffracted beam. The angle between them is 2θ. OG is the vector **g** and in reciprocal space has magnitude 1/*d* (with *d* being the distance between planes in the real crystal lattice).

Since CO = $1/\lambda$, and $\mathbf{g} = 1/d$:

$$2 \times (1/\lambda) \times \sin\theta = 1/d \qquad \textbf{Eq. 5.2}$$

Rearranging this gives Bragg's equation (when $n = 1$):

$$\lambda = 2\, d \sin\theta \qquad \textbf{Eq. 5.1}$$

For any orientation of the crystal relative to the incident beam, it is therefore possible to obtain more reciprocal lattice points.

5.4 The Technique

5.4.1 Introduction

This section relates to the practical crystallographic procedures and explains them in detail. Software used for the X-ray crystallographic determinations in this thesis is also discussed. All structures reported in this thesis were carried out by the author, either at the University of Bristol or the University of Sheffield on a Bruker SMART CCD area detector. Any variations of significance particular to a structure determination are detailed in the relevant experimental section(s).

5.4.2 The Instrument

Today, diffractometers are of the CCD area detector type. A charge-coupled device (CCD) detector is a semi-conductor. The instrument operates by incident X-rays diffracting by a crystal and the diffracted radiation falling onto a fluorescent phosphor plate (detector) covered in Ba F Br:Eu^{2+} crystals. When the X-ray photons hit the plate, some of the Eu^{2+} ions are ionised to Eu^{3+} ions with some of the freed electrons becoming trapped in Br vacancies introduced into the crystal (collectively known as 'F centres'). These centres are then excited by a He-Ne laser (633 nm) which liberates the trapped electrons which return to the Eu^{3+} ions to generate excited Eu^{2+} ions.

The electronic transitions in these ions generates a luminescence with intensity proportional to that of the original X-ray. This information is then read and converted into an electrical signal *via* a photomultiplier tube and displayed as a visible signal (reflection) *via* computer hardware. So in fact, the direct recording of X-rays is not actually carried out!

5.4.3 Crystal Growth and Selection

There are many steps between preparing a crystal and interpreting its contents' structure. It goes without saying that the effects of a sub-optimal crystal will propagate through data collection, structure solution, and structure refinement to directly affect the result of the final structure interpretation. Thus, the selection of a crystal of the best possible quality is compulsory!

Crystals were grown from a variety of viable methods each specified in the discussion of the relevant chapter. The importance of slow crystal growth can be understood in terms of molecules arriving at a surface. If they arrive too fast, the less time they have to orientate themselves in relation to ones that are already there, and random accretion is more likely which can lead to non-single crystals (i.e. disordered or twinned) as was seen in the $[Co(4pypz)_4Cl_2]\cdot(MeCN)_4$ complex (**Appendix 3**).

Crystals were initially inspected using binocular microscopes, with those free of defects and with the most isotropic shape selected for analysis (the latter requirement being to reduce absorption errors). In order to obtain satisfactory data, the crystal will have to be completely swamped by X-rays, and as some diffractometers, such as a Bruker SMART,[3] have a maximum X-ray collimator diameter of 0.8 mm, crystals should not have dimensions greater than 0.5 mm. In some cases, crystals were cut to achieve these requirements and dousing them in paraffin or engine oil helped to remove dirt and other unwanted particulates prior to data collection.

5.4.4 Crystal Set-up

The chosen crystal was mounted on a short glass fibre, 1.5-2.0 mm in length, which was then securely attached to the goniometer head, with the tip of the fibre making contact with the crystal 'side-on' in order to minimise the amount of glass fibre in the X-ray beam. For low temperature experiments, a cold stream of nitrogen was passed over the crystal *via* a nozzle delivery system, allowing data collection to occur at temperatures of typically 150 -100 K. The crystal was optically aligned in manual mode with a mechanical driver to be in the centre of the three diffractometer circles. This is necessary as the X-ray beam is extremely narrow. The incident beam of X-rays will then fall onto the crystal in a direction perpendicular to a unit cell axis about which the crystal will be rotated. This axis is, of course, arbitrarily chosen.

5.4.5 Matrix and Unit Cell Determination

Providing that a 60 second 360° ϕ-rotation photograph (**Fig. 5.4.1**) showed a clear diffraction pattern, a set of data 'frames' were collected to determine an orientation matrix; where one frame is a still image of the crystal in a specific orientation relative to the three circles. Generally, three regions of reciprocal space were collected, each consisting of 15-30 frames. The crystal was rotated 0.3° about ω (the angle between the incident beam and the goniometer) between each frame and each frame having an X-ray exposure time of 10 seconds – although this was increased if the crystal was a weak diffractor.

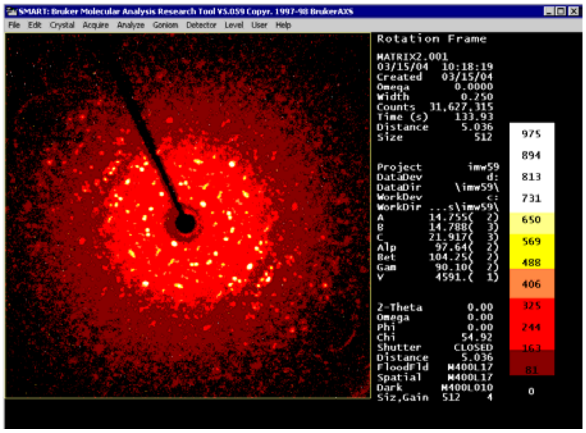

```
Rotation Frame

MATRIX2.001
03/15/04   10:18:19
Created    03/15/04
Omega        0.0000
Width         0.250
Counts   31,627,315
Time (s)     133.93
Distance      5.036
Size            512

Project       imw59
DataDev          d:
DataDir     \imw59\
WorkDev          c:
WorkDir ...s\imw59\
A        14.755(  2)
B        14.788(  3)
C        21.917(  3)
Alp       97.64(  2)
Bet      104.25(  2)
Gam       90.10(  2)
V         4591.(  1)

2-Theta        0.00
Omega          0.00
Phi            0.00
Chi           54.92
Shutter      CLOSED
Distance      5.036
FloodFld    M400L17
Spatial     M400L17
Dark       M400L010
Siz,Gain  512     4
```

Fig. 5.4.1 – a 60 second Φ-rotation photograph

The centroids of each reflection were then computed, with those too low in intensity; too close to the beam stop shadow; and too close to the edge of the detector area being rejected. The remaining 'unique' reflections were then indexed automatically to generate a Bravais lattice before a least-squares calculation was performed on the resultant orientation matrix to suggest a suitable unit cell.

The orientation matrix itself is at the centre of all data collection. In crystallography there are two important sets of dimensional axes: Those that define reciprocal space (a*, b*, and c*) and those that define the orientation of the crystal in real space (x, y, and z). The orientation matrix relates the two. In the former, for any values of (a*, b*, c*) in which the Bragg conditions are met for reflection, are represented as the corresponding Miller indices h, k, and l.

The peak profiles for reflections over sequential frames (points appearing every 0.3°) were next analysed using computer-generated 'rocking graphs'. These plots of intensity against ω to provide any evidence of split peaks (**Fig. 5.4.2**) which indicate poor quality data (**Fig. 5.4.2b**) and which will only serve to make the later treatment of data more taxing.

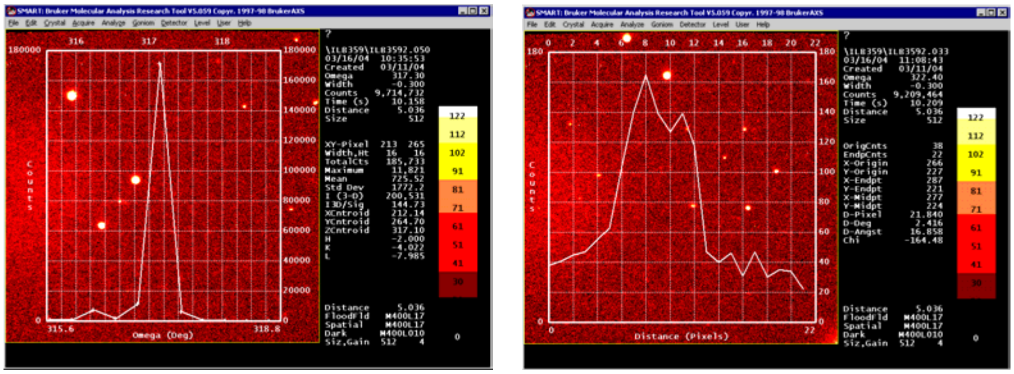

```
\ILB359\ILB3592.050
03/16/04   10:35:53
Created    03/11/04
Omega        317.30
Width        -0.300
Counts    9,714,732
Time (s)     10.158
Distance      5.036
Size            512

XY-Pixel  213   265
Width,Ht   16    16
TotalCts    185,733
Maximum      11,821
Mean         725.52
Std Dev      1772.2
I (3-D)     200,531
I3D/Sig      144.73
XCntroid     212.14
YCntroid     264.70
ZCntroid     317.10
H            -2.000
K            -4.022
L            -7.985

Distance      5.036
FloodFld    M400L17
Spatial     M400L17
Dark       M400L010
Siz,Gain  512     4
```

```
\ILB359\ILB3592.033
03/16/04   11:08:43
Created    03/11/04
Omega        322.40
Width        -0.300
Counts    9,209,464
Time (s)     10.209
Distance      5.036
Size            512

OrigCnts         38
EndpCnts         22
X-Origin        266
Y-Origin        227
X-Endpt         287
Y-Endpt         221
X-Midpt         277
Y-Midpt         224
D-Pixel      21.840
D-Deg         2.416
D-Angst      16.858
Chi         -164.48

Distance      5.036
FloodFld    M400L17
Spatial     M400L17
Dark       M400L010
Siz,Gain  512     4
```

(a) **(b)**

Fig. 5.4.2 – Rocking graphs showing split peak profiles
(a) good data and (b) poor data

In addition to this, the quality of the data (and hence the crystal) was deduced by inspection of the histogram generated in addition to the unit cell. The subsequent indexing process then assigned each 'unique' reflection with an hkl value to define its location in reciprocal space. In theory, all indexes should be perfect integers; yet poor data can result in a 'smearing' from this ideal – the degree of which is determined by the histogram. If a considerable number of reflections deviated more than 0.05 from their integer value, the data was rejected and another crystal tried.

5.4.6 Data Collection

Prior to April 2003, the default no. of frames used to collect a hemisphere of data was 1321, which consisted of four sets of 606, 435, 230 and 50 frames. The initial three sets covered just over one hemisphere of reciprocal space, allowing some overlap of equivalent data. The final set of 50 frames was an identical re-run of the first set of 50 frames of the initial 606, designed to reveal any crystal decomposition, loss of X-ray intensity or detector malfunction that may occur during the data collection.

It was later noted,[4] *however, that this default hemisphere collection setting that accompanies SMART software, was in fact only a complete data set for high symmetry (orthorhombic or higher) and consequently, collecting data in this manner for monoclinic and triclinic systems, always resulted in some data, causing many crystal structures to be rejected for publication.*

The diffractometer was set to collect a complete dataset to 55.0 degrees in 2θ, and the total default number of frames collected for works in this thesis was 1800, consisting of 3 sets of 606 frames with ϕ = 0, 120, 240 for each set and the frames again measured in 0.3° about ω. Frame times were typically 10-30 seconds giving a total data collection time of approximately 6-15 hours depending on the observed intensity of the reflections (**Fig. 5.4.3**).

Whilst increasing the exposure time per frame will increase the intensities observed, it is considered better practice to collect more frames of weakly-diffracted data, than to collect less frames of strongly diffracted data. Specific details of data collection settings are given at the end of each relevant chapter.

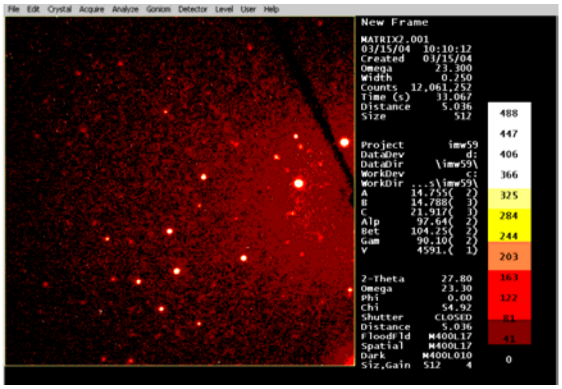

```
New Frame

MATRIX2.001
03/15/04   10:10:12
Created    03/15/04
Omega        23.300
Width         0.250
Counts   12,061,252
Time (s)     33.067
Distance      5.036
Size            512

Project        imw59
DataDev           d:
DataDir      \imw59\
WorkDev           c:
WorkDir  ...s\imw59\
A       14.755(   2)
B       14.788(   3)
C       21.917(   3)
Alp      97.64(   2)
Bet     104.25(   2)
Gam      90.10(   2)
V        4591.(   1)

2-Theta      27.80
Omega        23.30
Phi           0.00
Chi          54.92
Shutter     CLOSED
Distance     5.036
FloodFld   M400L17
Spatial    M400L17
Dark      M400L010
Siz,Gain  512    4
```

Fig. 5.4.3 – one frame of data (10 second exposure time)

5.4.7 Data Reduction

5.4.7.1 Integration

Data was integrated with the Bruker SAINT[5] program, using the orientation matrix to determine the position of all the reflections in reciprocal space. The quality of the integration was measured by monitoring the errors of the spot centroids in x, y and z (i.e. the observed position of a reflection minus the position predicted from the suggested orientation matrix). Ideally, such error values should consistently be ≤ 0.25 degrees with correlation ratios of 0.65-0.8 (65–80 %), and SAINT tracks the gradual shifts of spot centroids from the expected positions and updates the orientation matrix accordingly.

As was the case with unit cell determination, any reflections that fell outside of the boundaries of these ideal centroids, were discarded, giving rise to a collection of 'unique' reflections. The integrated data of each hemisphere were then merged and written to separate raw data files, before being collectively merged to a single raw data file.

5.4.7.2 Data Corrections

The collective merged reflections are recorded in terms of their relative intensities (I_{hkl}) and as X-radiation is an electromagnetic wave, each intensity has its own unique combination of amplitude and phase, known as a *structure factor* (F_{hkl}). Structure factors can be used to calculate electron density maps, and we can then start to see what atoms are present in the structure. However, the conversion is not a straightforward one, and we must apply corrections to the initial intensity data to account for situations which could otherwise contribute to a misleading structure factor:

Lorentz Factor - To use our integrated data to solve a structure, we will require each reciprocal lattice point to make such a contact for the same amount of time with the Ewald sphere, yet unfortunately, data collection is not this ideal, and contact of some points is often prolonged, resulting in reflections with varying intensities.

Polarisation - When the incident X-ray beam is produced by a conventional source and monochromatised using an appropriate filter, the nature of the beam is un-polarised, yet when the beam is diffracted by a crystal it is partially polarised and this affects its resulting intensity.

Heavy Atom - The presence of heavy atoms with high atomic numbers will also scatter the X-rays as their large electron clouds chip away at the beam, subsequently reducing the final intensities.

Absorption - Partial absorption of the X-ray beam by the crystal itself can occur in a manner similar to that of filtering methods, and as the crystal dimensions increase, the resulting intensities drop. Whilst the other factors are instrument specific and self-corrected, absorption is corrected by the Bruker SADABS[6] program.

Once these had been corrected for, structure factors were confidently generated.

5.4.8 Structure Solution and the Phase Problem

When light is diffracted off an object, the lenses in our eyes recombine the resultant light waves enabling our brain to interpret what the object looks like, and in order to achieve this, both the phases and amplitudes of the diffracted waves are required. There is however no lens available that can directly recombine X-Rays, and so this technique works by our collecting diffraction patterns from a crystal and trying to suggest what atomic structure will generate such a pattern.

However, the diffracted waves we have are recorded only in terms of their intensity (which is directly proportional to amplitude), leaving us with only half the necessary information - since I_{hkl} is proportionally related to the square of the structure factor $[F_{hkl}]^2$, it is impossible to tell whether the overall phase of the intensity is $+ F_{hkl}$ or $– F_{hkl}$. This obstacle is overcome by using statistical mathematics to calculate a data set for a proposed structure, which is then compared to what data are actually observed. There are two main techniques for solving this ‘phase problem’, both performed with the Bruker SHELXS[7] programme.

5.4.8.1 Patterson Synthesis

Instead of using the amplitude itself, F_{hkl}, structure factors are replaced by the square of the amplitude (i.e. the square of the structure factor) $[F_{hkl}]^2$ which consequently becomes a phase-less quantity, and can be used to generate a set of peaks (the Patterson map). The peaks do not correspond to the positions of individual atoms but instead to vectors *between* pairs of atoms in the structure (i.e. the position of atoms relative to each other). Thus, for every pair of atoms in the structure with coordinates: (x_1, y_1, z_1) and (x_2, y_2, z_2), there will be a peak in the Patterson map at the position $(x_1\text{-}x_2, y_1\text{-}y_2, z_1\text{-}z_2)$ and also at $(x_2\text{-}x_1, y_2\text{-}y_1, z_2\text{-}z_1)$, each atom giving a vector to the other. The highest Patterson vector corresponds to the inter-atomic distance between the two heaviest atoms, and this peak is always located at the origin of the map. The largest peaks correspond to the heavier atoms and will stand out clearly from smaller peaks if the structure contains few heavy atoms, enabling easy location of any atoms heavier than silicon. The approximate positions of the lighter atoms can then be determined

In structures where there are a few significantly heavier atoms among many light atoms (e.g. metal coordination complexes), the heavier atoms are usually more readily resolved, compared to cases in which all atoms are very similar, and once they have been located, heavy atoms may serve as a phasing model from which the positions of other atoms can then be developed. Thus, in recent years, common practice has been to infuse metal atoms into large structures where all atoms have roughly the same atomic number to aid structure solution (e.g. proteins).

5.4.8.2 Direct Methods

The method attempts to derive structure factor phases and electron locations *directly* from the diffracted X-ray intensities. If a structure generates N reflections, 2^N electron density maps can be calculated which represent all the possible combinations of phase signs for the N independent structure factors. Only one of these 2^N maps must show the true electron density, but it is a case of trial and error to determine which one it is! Thankfully, by applying a number of constraints to the electron density, it is a very possible feat to achieve. The two most important constraints are:

- The electron density map must never contain regions of negative electron density (i.e. the electron density should be zero or above in all regions - as negative electron density is a physical impossibility).

- The electron density should not be smeared all over the map with little variation, but should be effectively zero in most areas and intense and sharp around atoms (i.e. the electron density map should be composed of discrete atoms).

The success of the method is undoubtedly due to the development of computers in recent years, with a small number of initial phases being guessed and then used to calculate the phases of other reflections, based on various mathematical relationships. If the results produce an electron density map that does not conform to the above constraints, then some or all of the initially guessed phases must be wrong.

Various combinations of initial phases are tried until a plausible electron density is obtained. If the phases have been correctly assigned, several initial atom positions can be located. The majority of structures in this thesis were solved using direct methods, and are specified in **Appendix 3** otherwise.

5.4.9 Structure Refinement

Once all atoms had been assigned, a least squares refinement of the structural parameters was taken over the whole dataset between the observed $|F_o|$ and calculated $|F_c|$ structure factors using the Bruker SHELXL[8] programme; with the intention of minimising the sum

$$\Sigma w(F_o^2 - F_c^2)^2 \qquad \textbf{Eq. 5.3}$$

Several cycles of refinement are required before changes in parameters are insignificant and the data converges to a minimum. The programme weights each individual reflection's contribution to the sum according to its reliability based on experimental standard uncertainties. As the relationship between data and parameters (the Fourier transform) is not linear, the weighting scheme, *w*, takes on the form:

$$w = \frac{1}{\sigma_c^2(F_o^2) + (aP)^2 + bP} \qquad \textbf{Eq. 5.4}$$

Where

$$P = \frac{[Max(F_o^2,0) + 2F_c^2]}{3} \qquad \textbf{Eq. 5.5}$$

$\sigma_c^2(F_o^2)$ is the variance in F_o^2, and the values *a* and *b* are constants specific to the dataset, chosen to minimise the variation in S (the goodness of fit) as a function of $|F_o|$.

Residual indices of wR^2 (based on F^2) and S were also calculated:

$$wR^2 = \frac{\sum\sqrt{(w(F_o^2 - F_c^2)^2}}{\sum\sqrt{(w(F_o^2)^2}} \qquad \textbf{Eq. 5.6}$$

$$S = \sqrt{\{\sum(w(F_o - F_c))/(m\text{-}n)\}} \qquad \textbf{Eq. 5.7}$$

Where *m* is the number of observed reflections and *n* the number of parameters.

For historical purposes, a residual R-factor was calculated, based on data of the quality $F_o/\sigma(F_o) > 4$. The lower the R-factor, the better the agreement, and the more the structure geometry is optimised. Therefore, when we 'solve' a crystal structure, we never directly manipulate the collected data, but suggest a model structure to best fit the observed data.

$$R_1 = \frac{\sum|F_o - F_c|}{\sum|F_o|} \qquad \textbf{Eq. 5.8}$$

When changes are made to the calculated 'model' structure, many of the structure's parameters are changed. These can include atomic position; atomic displacement parameters; and site occupancy factors. We can also apply constraints or restraints to aid refinements. Constraints (such as requiring atoms to lie in special positions) are conditions forced upon the refinement calculation by requiring certain parameters to have particular values instead of being free to take those which give the best agreement between observed and calculated diffraction patterns. This is often the case when x-ray diffraction data are poor. Restraints on the other hand, cover acts such as fixing a certain bond length or angle to be a specific value. Applying a restraint will add to the no. of parameters being refined, but still allow the parameters to deviate from the ideal values. Performing any of the above will directly affect the values of $|F_c|$ whereas $|F_o|$ values will remain constant throughout.

5.4.9.1 Anisotropy

One of the most important parameter to refine is the *atomic displacement parameter, U*. Atoms are not 100 % spherical in nature, but vibrate to different degrees about their mean positions in (x, y, z) to have a more ellipsoidal shape.

By making each atom *anisotropic*, we allow it to adopt this geometry to the extent it is comfortable with; this is indicated by the U values we obtain. In addition to x, y, and z, each atom has six U parameters permitting additional axes of vibration and so making atoms anisotropic greatly increases the number of parameters to refine, however, the resulting model structure is far better. The degree of thermal vibration in atoms is drastically reduced by carrying out the data collection at low temperature, giving rise to markedly better data sets. Molecules or atoms that vibrate to the extent that they reside over more than one site (disordered) are treated accordingly with the appropriate amount of occupancy assigned per site.

Once the data has been successfully converged and there are no obvious peaks to assign in the map, the information is summarised in the crystallographic information file (CIF), generated with the XCIF component of the SHELXTL program. By applying a 'CIF checker'programme,[9,10] the CIF files for the structures in this thesis were checked against various criteria to see if they were suitable for publication. Any gross errors were taken on board and dealt with accordingly.

5.5 Summary

On November 8th 1895, Willhelm Röntgen made a valuable contribution to science. His X-rays has benefited all areas of the scientific community, and due to the efforts of many individuals, has resulted in a well developed, accurate, and reliable analytical technique for chemists.

The field of crystallography is still growing however; whilst the development of computers has transformed this technique from the grey days of pen and paper, it appears evident that soon the solving of a structure will become a 'black box' procedure, inevitably leading to a greater production line of solutions and publications. Whilst that may be commercially warranted, it goes without saying that the value of this technique cannot be appreciated without knowledge of Röntgen's discovery, Laue's crystal analogies, Braggs' diffraction hypothesis and the application to modern instrumentation.

5.7 Miscellaneous Crystal Structures

The following crystal structures were solved by the author at the University of Sheffield, yet have been omitted from the main context of this thesis.

5.7.1 [Re(bpym)(CO)$_3$Cl]

The complex was synthesised in accordance to the preparative method[11] by Miss Nina Depperman of the Ward group, and single crystals grown by the slow evaporation of a concentrated MeCN solution of the sample over a 7 day period. The complex crystallises in the monoclinic space group P2$_1$/*c* and was solved by direct methods (shown in **Fig. 5.7.1)**. There is no disorder in the structure and all bond lengths and angles are unremarkable, and on a par with those in the complex [Re(CO)$_3$Cl(*i*-bpym)Ln(fod)$_3$].[12] Selected bond lengths are given in **Table 5.7.1**.

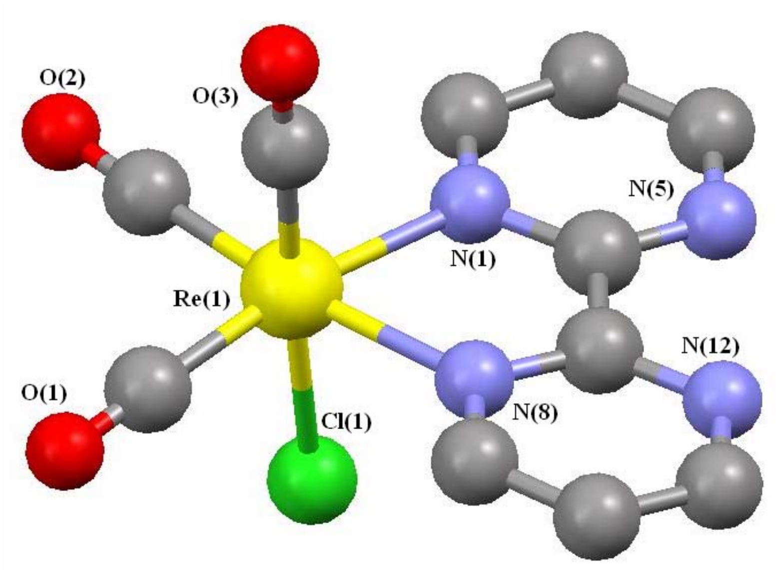

Fig. 5.71. – Crystal structure of [Re(bpym)(CO)$_3$Cl]

Re(1)-C(23)	1.915(6)	Re(1)-N(1)	2.172(4)
Re(1)-C(22)	1.928(6)	Re(1)-N(8)	2.179(4)
Re(1)-C(21)	1.931(6)	Re(1)-Cl(1)	2.4922(16)

Table 5.7.1 – Selected bond lengths (Å) for [Re(bpym)(CO)$_3$Cl]

5.7.2 [Cu(Bp^{2py})(MeCN)][PF$_6$]

In attempts to reproduce the cyclic wheel of $[Co_8(Bp^{2py})_{12}(ClO_4)][(ClO_4)_3]$[13] and study the effects of different templating anions, KBp^{2py} and Cu(II) acetate were combined in a 3:2 ratio in MeOH and stirred at room temperature for a few moments. Subsequent addition of and aqueous solution of KPF_6 resulted in a blue precipitate which was filtered off and washed with copious amount of H_2O. Slow diffusion of diethyl ether into a concentrated solution of the product in MeCN afforded blue prism-like crystals suitable for X-Ray analysis. The complex crystallises in the triclinic space group P-1 and was solved by direct methods.

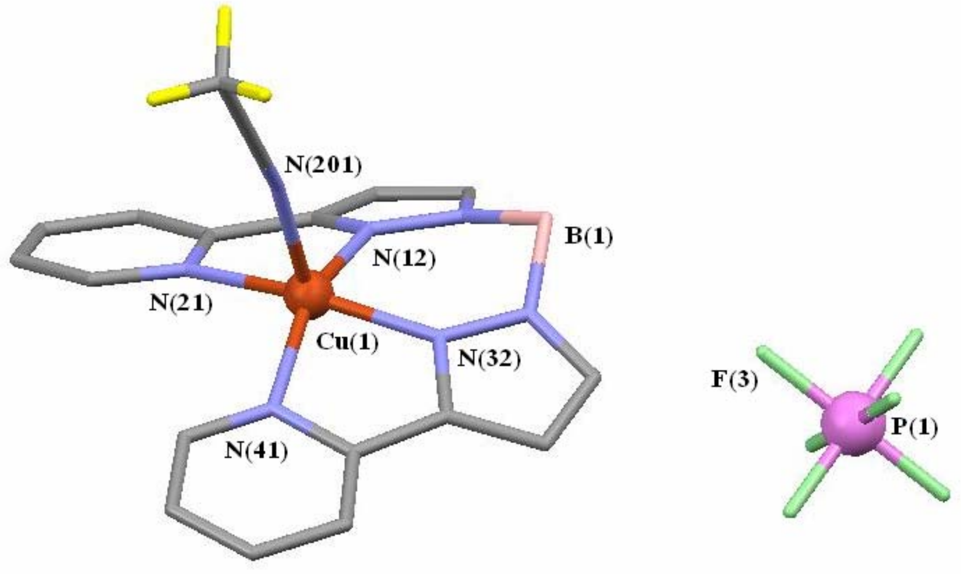

Fig. 5.7.2 – Crystal structure of [Cu(Bp^{2py})(MeCN)][PF$_6$]·(MeCN).
The lone solvent molecule has been removed for clarity.

Fig. 5.7.2 shows the complex with the Cu(II) adopting an N_5 square-based pyramidal geometry with the base formed by the N_4 donor set of the scorpionate and capped by the coordinating solvent molecule. The N_4 donor set consists of N(12)/N(21)/N(41)/N(32) and has an average deviation of 0.0219 Å from the mean, with the Cu(I) atoms sitting 0.325 Å out of the plane. Selected bond lengths and angles are given in **Table 5.7.2**.

Cu(1)-N(32)	1.9438(17)	N(32)-Cu(1)-N(12)	88.00(7)	N(21)-Cu(1)-N(41)	106.90(7)
Cu(1)-N(12)	1.9502(17)	N(32)-Cu(1)-N(21)	160.03(7)	N(32)-Cu(1)-N(201)	101.19(7)
Cu(1)-N(21)	2.0749(17)	N(12)-Cu(1)-N(21)	79.29(7)	N(12)-Cu(1)-N(201)	108.80(7)
Cu(1)-N(41)	2.0783(17)	N(32)-Cu(1)-N(41)	79.75(7)	N(21)-Cu(1)-N(201)	97.47(7)
Cu(1)-N(201)	2.1897(19)	N(12)-Cu(1)-N(41)	158.02(7)	N(41)-Cu(1)-N(201)	91.55(7)

Table 5.7.2 – Selected bond lengths (Å) and angles (°) for [Cu(Bp^{2py})(MeCN)][PF$_6$]

The molecules are associated by a series of hydrogen bonds: the lone MeCN forms bonds to both the fluorine and nitrogen atoms of the anion and solvent molecules respectively [CH(35)···N(301) = 2.529 Å, CH(3B)···F(6) = 2.465 Å, whilst C(35)···N(301) and C(303)···F(6) = 3.456(3) and 3.393(3) Å respectively], with the anion bonding with the boron-end of the scorpionate [CH(45)···F(1) = 2.534 Å, CH(46)···F(2) = 2.651 Å; C(45)···F(1) and C(46)···F(2) = 3.400(3) and 3.419(3) Å respectively].

A similar structure was proposed for the complex [Cu(Bp^{2py})(H$_2$O)][PF$_6$] with the water molecule capping the Cu(II) pyramid,[14] and although analytical data were obtained to support this formulae, no crystal structure was available. However, the previous structure of [Cu(Tp^{2py})(H$_2$O)] suggests this to be the case.[15]

Complex	**[Re(bpym)(CO)$_3$Cl]**	**[Cu(Bp^{2py})(MeCN)][PF$_6$]·(MeCN)**
Empirical formula	$C_{11}H_6N_4O_3ClRe$	$C_{20}H_{20}N_8BF_6PCu$
Formula weight	463.85	591.76
Temperature	150(2)	150(2)
Crystal system	Monoclinic	Triclinic
Space group	P2$_1$/*c*	P-1
a /Å	6.3142(6)	8.1212(14)
b /Å	14.9944(13)	11.996(2)
c /Å	13.5481(12)	12.993(2)
α /°	90	89.760(3)
β /°	102.725(2)	79.100(3)
γ /°	90	75.483(3)
Volume /Å^3	1251.2(2)	1202.1(4)
Z	4	2
Density (calculated) / Mg/m^3	2.462	1.635
Absorption coefficient / mm^{-1}	9.937	1.049
F(000)	864	598
Crystal size / mm	0.22 x 0.16 x 0.11	0.47 x 0.25 x 0.10
θ range for data collection	2.05 to 27.53°	1.60 to 28.31°
Reflections collected	10650	13534
Independent reflections	2836 [R(int) = 0.0546]	5435 [R(int) = 0.0273]
Completeness to θ	98.2 %	90.8 %
Data / restraints / parameters	2836 / 0 / 181	5435 / 0 / 334
Goodness-of-fit on F^2	0.969	1.031
R indices [for reflections with I>2σ(I)]	$R_1 = 0.0299$, $wR_2 = 0.0655$	$R_1 = 0.0344$, $wR_2 = 0.0846$
R indices (for all data)	$R_1 = 0.0412$, $wR_2 = 0.0708$	$R_1 = 0.0432$, $wR_2 = 0.0888$
Largest diff. peak and hole	1.904 and -2.222 eÅ^{-3}	0.611 and -0.400 eÅ^{-3}

Table 5A Crystallographic Data for the Complexes of Chapter 5

5.7 References

1. (a) C. Giacovazzo, H. L. Monaco, D. Viterbo, F. Scordari, G. Gill, G. Zanotti, M. Catti, *Fundamentals of Crystallography, 1st Ed.*, Oxford University Press., 1992; (b) J. P. Glusker, K. N. Trueblood, *Crystal Structure Analysis – a Primer, 2nd Ed.*, Oxford University Press, 1985; (c) J. Hyde, *Ph. D Thesis*, University of Sheffield, 1996; (d) Z. R. Bell, *Ph. D Thesis*, University of Bristol, 2001; (e) W. Clegg, *X-Ray Crystal Structure Determination, 1st Ed.*, Oxford University Press, 1998; (f) G. H. Stout, L. H. Jensen, *X-Ray Structure Determination – a Practical Guide, 2nd Ed.*, Wiley, 1989.
2. (a) http://www.nobel.se;
   (b) http://epswww.unm.edu/xrd/xrdclass/03-GenX-rays.pdf;
   (c) http://www.chem.uwa.edu.au/enrolled_students/MASTsect2/sect2.6.2.html
   (d) http://chemed.chem.purdue.edu/genchem/topicreview/bp/ch13/unitcell.html
   (e) http://jaeger.earthsci.unimelb.edu.au/msandifo/Teaching/Mineralogy2/unitCell.html
   (f) http://www.chem.ox.ac.uk/icl/heyes/structure_of_solids/Lecture1/Lec1.html
   (g) http://www.gly.uga.edu/schroeder/geol6550/millerindices.html
   (h) http://www.matter.org.uk/diffraction/geometry/ewald_sphere_construction_ 2D.html
   (i) http://isites.bio.rpi.edu/bystrc/pub/Xtal/xtal4/img041.gif
   (j) http://lsm-www.nrl.navy.mil/images/ccd01.jpg
3. SMART Siemens Molecular Analysis Research Tool. V4.014. Copyright 1989-1995. Siemens AnalyticalX-ray, Madison, WI, USA.
4. C. Campana, Private Communication.
5. SAINT Siemens Area Detector INTegration Program, Siemens AnalyticalX-ray, Madison, WI, USA.
6. G. M. Sheldrick, SADABS, a program for absorption correction with the Siemens SMART area-detector system; University of Göttingen, 1996.

7. G. M. Sheldrick: SHELXS-97, a program for crystal structure solution; University of Göttingen, 1997.
8. G. M. Sheldrick: SHELXL-97, a program for crystal structure refinement; University of Göttingen, 1997.
9 Louis J. Farrugia: WINGX, a program for viewing and certifying crystallographic structures, *J. Appl. Cryst.* (1999), **32**, 837-838.
10. 'CheckCIF', a program for viewing and certifying crystallographic information files: http://journals.iucr.org/c/ services/ authorservices.html.
11. *A. Vogler, J. Kisslinger*, Inorg. Chim. Acta., *1986, 115, 193*.
12. N. M. Shavaleev, G. Accorsi, D. Virgili, Z. R. Bell, T. Lazarides, G. Calogero, N. Armaroli, M. D. Ward, *Inorg. Chem.*, 2005, **44**, 61.
13. P. L. Jones, K. J. Byrom, J. C. Jeffery, J. A. McCleverty, M. D. Ward, *Chem. Commun*., 1997 1361.
14. P. L. Jones, *Ph.D Thesis*, University of Bristol, 1996.
15. D. A. Bardwell, J. C. Jeffery, P. L. Jones, J. A. McCleverty, M. D. Ward, *J. Chem. Soc., Dalton Trans*., 1995, 2921.

Thesis Summary

Thesis Summary & Suggestions for Further Work

This work in this thesis has explored several areas:

We have described the synthesis and coordination chemistry of several new bis- and tris-poly(pyrazol-1-yl)borate ligands that contain 3- and 4-pyridyl groups in the 3-position of the pyrazole ring. An extensive series of complexes with these new ligands has been structurally characterised and revealed examples of discrete dimeric complexes as well as formation of 1-D chains and cross-linked 2-D and 3-D networks. These ligands offer great scope for development of new metal-organic frameworks, some of which may have practical applications in the areas of second order non-linear optical effects and gas absorption/sensor materials. We have the possibilities of both capsule and larger assembly formation by coordination through the peripheral nitrogen donors of discrete Tp-based ligands; and attachment of additional metal ions at the uncoordinated N_{py} donors in the polymeric species may enable us to synthesise polynuclear assemblies. In addition to this, the pypz arms could be modified with additional donor substituents on the pyridyl rings, or the scorpionates ligand itself could be further developed to contain a mixture of pypz arms. Such changes may lead to the formation of further novel molecular architectures.

In the next piece of work, the straightforward co-crystallisation of $[Ru(bpy)(CN)_4]^{2-}$ anions with Ln(III) salts has led to a range of coordination networks based on Ru-CN-Ln bridging groups. Photophysical studies on these complexes demonstrate photo-induced Ru-Ln energy transfer, with sensitized luminescence from the lanthanide units and simultaneous quenching of the ^{3}MLCT Ru-based luminescence. The efficiency of the energy-transfer process in different Ru-Ln systems has been rationalised by a combination of spectral overlap effects and ΔJ selection rules. The rates of energy transfer span two orders of magnitude, with the effectiveness of the lanthanides' quenching following the order Nd > Pr > Er > Yb.

Despite the replacement of Ln(III)-bound water molecules with D_2O, the luminescence lifetimes of the Ln(III) centres are much shorter than expected, leaving us to the hypothesis that the excess quenching is a direct result of fast phonon delocalisation in the extended coordination lattice.

This economic 'one pot' method of synthesising d-f hybrids may be varied in many ways to produce single crystals of such systems, which in turn may be probed in the solid state for their photophysical properties. It has also proven possible for Cr(III)-CN-Ln complexes, and may therefore lead to more studies on energy transfer within such systems. The rate of crystal formation has also shown to be fundamental in determining the structure of the complex, often giving rise to heterogeneous samples, and offers plenty of scope to obtaining several diverse architectures from the same sample of components.

As a final point, the thesis has also described the syntheses and photophysical properties of Bp^{2py}- and Tp^{2py}–based lanthanide(III) complexes based on metals displaying near-infrared luminescence, especially Pr(III). These scorpionate ligands proved to be effective sensitisers in this manner, resulting in complexes with quite long luminescence lifetimes in the near-infrared region.

Chemicals

All reagents (inc. solvents) were purchased from the usual commercial suppliers (Aldrich, Lancaster, Avocado) and were used as received.

Elemental Analysis

Elemental analysis for carbon, hydrogen and nitrogen were performed by the Microanalytical Laboratories at the University of Sheffield and the School of Chemistry of the University of Bristol. Samples at the former institution were run using the Perkin Elmer 2400 CHNS/ O Series II Elemental Analyser, which uses a combustion method in a pure oxygen environment to convert the accurately weighed sample into the simple gases CO_2, H_2O, N_2, SO_2. After reduction through pure copper, the resulting CHNS gases are then controlled to exact conditions of pressure, temperature and volume where upon the system uses a steady state wavefront approach to separate the controlled gases. This approach involves separating a continuous homogenised mixture of gases through a chromatographic column. The gases eluting off the column are measured as a function of their thermal conductivity.

NMR Analysis

NMR spectra were run on a Bruker AC-250 and Bruker AMX2-400. ^{1}H spectra were measured at 250.13MHz and 400.13MHz respectively, whilst ^{13}C spectra were measured at 62.90 MHz and 100.63 MHz respectively using the attached proton test. Chemical shifts are reported on the δ scale and are accurate to ± 0.01ppm for ^{1}H spectra and ± 0.1ppm for ^{13}C spectra. Spectroscopic grade deuterated solvents were used (*ca*. 0.7 ml) and the spectra were calibrated using the solvent as an internal reference. Typically 10 mg of sample were dissolved for ^{1}H spectra and 20 mg for ^{13}C spectra. ^{11}B spectra were recorded on a Bruker DRX-500 at 160.4MHz and are referred to external boron trifluoride etherate.

UV/VIS Spectroscopy

These were performed on a Cary 50 spectrometer in a quartz cuvet of 1 cm path length. Typical concentrations were 10^{-3} M and solvent background corrections were applied.

Steady State Luminescence

Solid State: Measurements were made using a PerkinElmer LS-55 spectrometer, fitted with a front surface accessory. *Solution*: Weak concentrations of the appropriate complex were made in a suitable solvent and run in a 1 cm path length quartz cuvet, on a Perkin-Elmer LS-50 fluorimeter.

Mass Spectroscopy

Electron Impact (EI), Chemical Ionisation (CI) and Fast Atom Bombardment (FAB) mass spectra were recorded on a VG-Autospec magnetic sector instrument. Negative Ion Electrospray (ES) were recorded on a Waters LCT spectrometer with typically low cone voltages.

Infra Red Spectroscopy

Solid state IR spectra were recorded on a Perkin-Elmer Spectrum RX I FT-IR spectrophotometer, equipped with a SensIR diamond ATR, over the range 4000 – 500 cm^{-1}.

Luminescence Measurements (Solid-State)

Solution: Light emitted at right angles to the excitation beam was focused onto the slits of a monochromator (Spex TRIAX320), which was used to select the appropriate wavelength.

Solid State: Measurements were made using powdered samples packed against a quartz window in a specially prepared die. For time-resolved and near-IR measurements, the whole assembly was held with the plane of the window at 30° to the incident radiation from a dye laser pumped by a pulsed nitrogen laser (PTI-3301). Light emitted at right angles to the excitation beam was focused onto the slits of a monochromator (PTI-120), which was used to select the appropriate wavelength.

General: For all measurements, the sample was excited using a pulsed nitrogen laser (337 nm) operating at 10Hz. The growth and decay of the luminescence at selected wavelengths was detected using a germanium photodiode (Edinburgh Instruments, EI-P) and recorded using a digital oscilloscope (Tektronix TDS220) before being transferred to a PC for analysis. Time resolved emission (TRES) spectra were obtained by measuring the growth and decay of the luminescence at each of a series of wavelengths. Luminescence lifetimes were obtained by iterative reconvolution of the detector response (obtained by using a scatterer) with exponential components for growth and decay of the metal centred luminescence, using a spreadsheet running in Microsoft Excel. The details of this approach have been discussed elsewhere.[1]

1. A. Beeby, S. Faulkner, *Chem. Phys. Lett.*, 1997, **266**, 116.

Crystallographic Instrumentation

For each complex a suitable crystal was coated with hydrocarbon oil and attached to the tip of a glass fibre, which was then transferred to a Bruker-AXS PROTEUM {for $[Eu(L^2)(dbm)_2]\cdot(CH_2Cl_2)_{0.25}$} (Cu-Kα radiation) or SMART-CCD (Mo-Kα radiation) diffractometer (for all other structures) under a stream of cold N_2. An Oxford Cryosystems low temperature system was used to carry out data collection at 150K.

All hydrogen atoms were either calculated, unless stated otherwise and assigned isotropic displacement parameters 1.2 times the U_{iso} value of the parent atom (except methyl hydrogens, which were assigned isotropic displacement parameters 1.5 times the U_{iso} of the parent atom). In such instances, no estimated standard deviations (esd's) are shown for hydrogen bond distances. All π-π interactions (as well as the majority of pictorial representations of crystal structures) were calculated (and constructed) using Mercury.[1] Such calculated distances again, do not contain esd's. Average bond lengths have also not been displayed with esd values.

The structure of $[Re(Tp^{4py})(CO)_3]$ was determined at the University of Southampton on a Nonius Kappa-CCD diffractometer using Mo-$K\alpha$ radiation (λ = 0.71073 Å) from a Bruker-Nonius FR591 rotating anode X-ray generator. The data were absorption corrected using SORTAV,[2] before solution and refinement using SHELXS-97[3] and SHELXL-97[4] respectively The data for this crystal were weak, and SQUEEZE[5] was used to eliminate disordered solvent molecules that could not be modelled.

1. J. Bruno, J. C. Cole, P. R. Edgington, M. K. Kessler, C. F. Macrae, P. McCabe, J. Pearson and R. Taylor, *New software for searching the Cambridge Structural Database and visualising crystal structures, Acta Crystallogr.*, **B58**, 389-397, 2002
2. R. H. Blessing, *Acta Cryst.* 1995, **A51,** 33; (b) R. H. Blessing, *J. Appl. Cryst.,* 1997, **30**, 421.
3. G. M. Sheldrick, *SHELXS-97, a Program for Automatic Solution of Crystal Structures*; University of Göttingen, Göttingen, Germany, 1997.
4. G. M. Sheldrick, *SHELXL-97, A Program for crystal structure refinement;* University of Göttingen, Göttingen, Germany, 1997.
5. A. L. Spek, '*PLATON*: A Multipurpose Crystallographic Tool', *J. Appl. Cryst*., 2003, **36**, 7-13

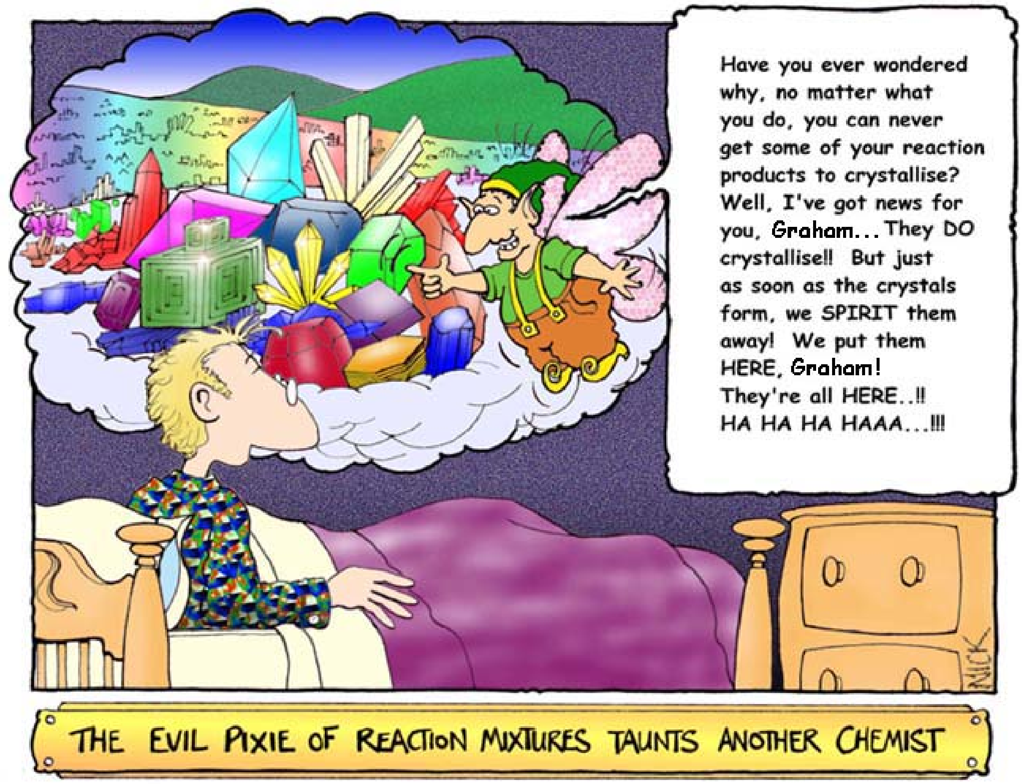

Have you ever wondered why, no matter what you do, you can never get some of your reaction products to crystallise? Well, I've got news for you, Graham... They DO crystallise!! But just as soon as the crystals form, we SPIRIT them away! We put them HERE, Graham! They're all HERE..!! HA HA HA HAAA...!!!
NICK
THE EVIL PIXIE OF REACTION MIXTURES TAUNTS ANOTHER CHEMIST

Alice came to a fork in the road. "Which road do I take?" she asked.
"Where do you want to go?" responded the Cheshire cat.
"I don't know," Alice answered.
"Then," said the cat, "it doesn't matter."

-- Lewis Carroll, *Alice in Wonderland*